Noise and Vibration Characteristics of Dual-Combustion-Mode Gasoline-Direct-Injection Engines

by

Harald Stoffels

Homerton College

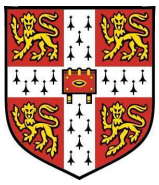

Department of Engineering

University of Cambridge

A dissertation submitted
for the degree of
Doctor of Philosophy

May 2007

"The beautiful simplicity is a dream."

Rolf Dieter Brinkmann

UNIVERSITY OF CAMBRIDGE
DEPARTMENT OF ENGINEERING
I.C. ENGINES - EMISSIONS, MEASUREMENT AND CONTROL

Department of Engineering
Energy Group
Hopkinson Laboratory
Trumpington Street
Cambridge CB2 1PZ
United Kingdom
Telephone: +44-(0)1223-332681
E-Mail: hs360@cam.ac.uk
hstoffel@ford.com

Summary

Spark ignition internal combustion engines with gasoline direct injection can be operated either in homogenous charge or in stratified charge mode. The introduction of full flexible valve trains allows the operation in homogenous charge compression ignition, however, stratified charge mode as well as homogeneous charge compression ignition can only be operated in a limited area of speed and load. This requires switches between the combustion modes. Engines of this type can be characterized as 'Dual-Combustion-Mode engines'. The lack of methodologies to predict the characteristics of noise caused by the different combustion modes of these engines operated in a conventional non-semi-anechoic test cell has governed the present investigation. This thesis closes the gap by providing two innovative methodologies that predict the noise and vibration characteristics based on measured cylinder pressures.

The first method predicts the level of the radiated noise, its spectrum, and the psychoacoustic parameters 'Roughness' and 'Impulsiveness'. In contrast to the currently available methods, the new method processes the data in the time domain from which the combustion and the structure excitation are obtained. The calculation of the structure excitation is carried out using non-linear contact forces. This avoids the hitherto existing usage of so-called 'correlation factors' to achieve an acceptable correlation of the predicted noise spectrum for frequencies above $300 Hz$. Therefore, the calculation of the structure excitation includes the piston induced noise, the forced-response characteristics of the assembly of piston, pin and connecting rod, and the contact force of the crankshaft in the main bearing. This was done by bringing together correlated approaches and methods that were refined and adapted to the engine investigated accordingly. During the development of the forced-response module the sensitivity of the piston-pin-connecting rod assembly to the pressure-rise rate was studied. Accordance with earlier inductively elaborated observations by Ricardo and Pye was found. This novel finding allows a better interpretation of clattering noise from compression engines, occurring above a certain pressure rise rate. In summary this enables the calculation of 'Roughness' and 'Impulsiveness'. In addition, load dependent noise transfer functions were introduced to reflect the change of noise transfer of the structure caused by load. The method predicts the radiated noise with an error lower than 10% compared to measured data. It was used to quantify the impact of gasoline homogeneous charge compres-

sion ignition on engine acoustics under different operating conditions.
The second method evaluates vibrations lower than $32Hz$ that can occur during change of combustion mode. Since known indices to characterize such events reflect just an average excitation that is integrated over a certain time span as is the vibration-dose-value, an index was developed that reflects the amplitude of excitation as well as the duration of the event. The index was used to evaluate different control strategies for combustion mode changes between spark ignition and homogeneous charge compression ignition.

Keywords: Gasoline Direct Injection, HCCI, CAI, Compression Ignition, Pressure Rise Rate, Combustion Noise, Variable Valve Train, Forced-Response, Piston slap, Noise, Vibration, Engine Noise Prediction, Sound Quality, Psychoacoustic, Modulation, Roughness, Combustion Mode Switch, Torque fluctuation, Jerk.

Acknowledgements

Then was then, and now is now. Then was 2004, when Ford Motor Company allowed me to start a company-sponsored PhD study on the HCCI project running at Cambridge University. This would not have happened without Jürgen Klauke and Dr Martin Wirth having initiated the appropriate steps. Now is 2007. Numerous changes have taken place in those three years. Meanwhile the international community has acknowledged that the emission of green-house gases affect the climate change. This has increased the need for automotive propulsion systems emitting less green house gas. Moreover, because of a new legislative regulation in Europe by 2012, the request for lower noise emissions by the automotive sector has moved into increased attention as well. Thus the reason for carrying out the research that forms the basis for this thesis has achieved more importance. Therefore I would like to thank Ford Motor Company for sponsoring my PhD work throughout the three years. In particular, I am grateful to Jürgen Klauke, Bert Pingen, Dr Martin Wirth, Dr Andreas Schamel, Dirk Borrmann and Dr Horst Schulte.

I am greatly indebted to Professor Nick Collings for supervising this work and Professor Dame Ann Dowling for advising me. I have really enjoyed the feedback they gave me on the work, as well as the discussions we had.

In addition, I would like to thank Dr Themi Petridis and Jon O'Neill for their help and support, especially on the logistics. Without their unconventional help the work would not have reached this stage. I am also grateful to my colleague Jens Wojahn and the Ford-Merkenich dynamometer team, not to forget Heinrich Mayer for establishing the testing environment for the measurements during the time-critical combustion development phase. Thanks also go to Jens Dunstheimer for valuable discussions and to Dr Christoph Vorwerk for lending the BEQII-device. I would furthermore like to thank the HCCI steering team at Ford Motor Company. In person these are most of all the colleagues Dr Thomas E. Kenney and Dr Lucien Koopmans. Thanks to Dr Burkhard Pfingsthorn for discussions and for the cylinder pressures, mentioned in Chapter 3.1.4 . The support from colleagues at the modal lab at Ford-Merkenich is also kindly acknowledged.

Special thanks go to the mechanic at Cambridge, Jon Harvey, for setting up an

excellent hardware environment and a timely support when mechanic issues on the test engine needed to be resolved.

I furthermore thank Stelios Karagiorgis for discussions, some beers and the exchange of SAE- and other papers during the last three years. I know now what a real Frappé Coffee is.

Fermín Moscoso del Prado Martín is acknowledged for his support regarding the practical aspects when living in Cambridge.

I would like to thank my friends in Cologne and wherever for the patience with me during the last three years. Special thanks go to my parents in law for providing me with a nice and tasty working environment during last year's Christmas week.

I thank my parents for supporting my early studies in Duisburg and Aachen, thus allowing me to build up the basis necessary for this work. I would also like to thank my uncle Rudi, who died too early. He evoked my interest in mechanical engineering and encouraged it during the important years of my life.

Finally, I would like to thank Katharina Haude, who ensured that even the last three years were very happy years. Her contribution to a happy disposition of mine during writing this thesis was inestimable.

Harald Stoffels
May 2007

Contents

List of Tables

List of Figures

List of Acronyms

Acronyms

ACEA ..... Association des Constructeurs Européens d'Automobiles
AFR ..... Air Fuel Ratio
AGDI ..... Air Guided Direct Injection
ATDC ..... After Top Dead Center
BEM ..... Boundary Element Method
BMEP ..... Brake Mean Effective Pressure
BSFC ..... Brake Specific Fuel Consumption
BTDC ..... Before Top Dead Center
B1090 ..... Burn Duration (10 - 90% Mass Fraction Burned)
CAD ..... Crank Angle Degrees
CAE ..... Computer Aided Engineering
CAI ..... Controlled Auto Ignition
CA50 ..... Crank angle when 50% of total heat is released
CI ..... Compression Ignition (Diesel)
CoG ..... Center of Gravity
CO_2 ..... Carbon Oxides
CPS ..... Cam-Profile Switch
cps ..... cycles per second (equal to [Hz])
CT ..... Closed Throttle
DFT ..... Discrete Fourier Transformation
DFR ..... Dynamic Flow Range, [102]
DI ..... Direct Injection
DoF ..... Degree of Freedom
DOHC ..... Double Overhead Camshaft
DRI ..... Dynamic Response Index
ECU ..... Engine Control Unit
EEOC ..... Estimated end of combustion
EGR ..... Exhaust Gas Recirculation
EHD ..... Elastic-Hydrodynamic Lubrication
Eo ..... Engine Order
EOI ..... End of Injection
EVA ..... Electronic Valve Actuation

EVC ..... Exhaust Valve Closure
EVO ..... Exhaust Valve Opening
FEM ..... Finite Element Method
FFT ..... Fast Fourier Transformation
FMEP ..... Friction Mean Effective Pressure
FRA ..... Forced Response Analysis
FRF ..... Frequency Response Function
FVV ..... Forschungsvereinigung Verbrennungskraftmaschinen e.V.
GDI ..... Gasoline Direct Injection
HC ..... Hydrocarbons
HCCI ..... Homogeneous Charge Compression Ignition
IMEP ..... Indicated Mean Effective Pressure
IMP ..... Index for Impulsiveness
ITDC ..... Ignition Top Dead Center
IVC ..... Inlet Valve Closure
IVO ..... Inlet Valve Opening
JLS ..... Jerk-Level Shape
LHS ..... Left-hand-side
MAF ..... Mass Air Flow
ManiAbs ..... Absolute Intake Manifold Pressure
MBA ..... Multi Body Analysis
MFB(Percent) ..... Mass Fraction Burned
MON ..... Motored octane number
NEDC ..... New European drive cycle
NO_x ..... Nitrogen Oxides
NTF ..... Noise transfer function
NVH ..... Noise vibration harshness
NVO ..... Negative valve overlap
ON ..... Fuel octane number
PCM ..... Powertrain control module
PRF ..... Primary Reference Fuel ($S = RON - MON = 0$)
PT ..... Part-Throttle
RHS ..... Right-hand-side
RMS ..... Root-Mean-Square
RON ..... Research Octane Number

RPM ..... Revolutions per Minute
RRR ..... Rear-roll-restrictor
SAE ..... Society of Automotive Engineers
SBN ..... Structure Borne Noise
SDM ..... Standard deviation, mean value
SGDI ..... Spray-Guided-Direct-Injection (Gasoline)
SI ..... Spark-Ignition
SPL ..... Sound Pressure Level
SOI ..... Start of Injection
TDC ..... Top Dead Center
TDCi ..... Turbo Diesel Common Rail Injection
TRA ..... Torque-roll-axis
VCT ..... Variable Cam-Timing
VDV ..... Vibration Dose Value
WGDI ..... Wall-Guided-Direct-Injection (Gasoline)
WOT ..... Wide open Throttle
WWMP ..... World wide mapping point ($1500 rpm, 2.62 bar BMEP$)

List of Notations

Mechanic and Thermodynamic

A	m^2	Area
a	m	Vert. distance CoG to F_{Skirt}
B	m	Bore diameter
b	m	Vert. distance CoG to F_{Top}
C	$\left[\frac{N}{m}\right]$	Stiffness of spring
c_p	$\left[\frac{J}{kgK}\right]$	Specific heat at constant pressure
c_v	$\left[\frac{J}{kgK}\right]$	Specific heat at constant volume
E	MPa	Young's Modulus
F	N	Force
h	m	Horiz. Dist. CoG to Pin; thickness of oil-film (4.5)
K	$\left[\frac{Ns}{m}\right]$	Damping rate
l	m	Conrod length
M	Nm	Torque (also with the index t)
M	$[kg]$	Mass-matrix
m	kg	Mass
n	$-$	Polytropic exponent
p	Pa	Pressure
Q	J	Heat released
Q_{LHV}	$\left[\frac{MJ}{kg}\right]$	lower heat value, [9]
q	m	Crankshaft offset
R	$\left[\frac{kJ}{kg \cdot K}\right]$	Gas constant
r	m	Crankshaft radius
S	$-$	Fuel sensitivity (RON-MON)
s	m	Lateral piston travel
T	K	Temperature
t	s	Time
V	dm^3	Volume
v	$\left[\frac{m}{s}\right]$	Lateral piston velocity
$\dot{y}_{Piston}$	$\left[\frac{m}{s}\right]$	Piston speed (vertical)
α	deg	Crankshaft angle

β	$-$	Bessel number
Δ	m	Piston-Pin Offset
δ	m	Location of CoG relative to crank-axis
ϵ	$-$	Compression Ratio
η	$Pa \cdot s$	Oil-viscosity
γ	$-$	Specific heat ratio, $\left(\frac{c_p}{c_v}\right)$
κ	$-$	Ratio crankshaft-offset/length conrod, $\left(\frac{q}{l}\right)$
λ	$-$	Bore-stroke Ratio $\left(\frac{r}{l}\right)$
λ	$-$	Relative air/fuel ratio, $(\lambda = \frac{AFR_{real}}{AFR_{\lambda=1}} = \phi^{-1})$
ν	^oC	Oil-Temperature
ϕ	deg	Piston tilt angle
ϕ	$-$	Fuel/air equivalence ratio, $(\phi = \lambda^{-1})$
$\dot{\phi}$	$\left[\frac{rad}{s}\right]$	Piston Tilt Motion
ψ	deg	Conrod tilt angle
ρ	kg/m^3	Density
τ	$msec$	Induction time
ξ	m	Piston Lash
υ	m	Distance CoG to Piston-Pin
ζ	m	Bearing clearance
ζ	rad	Contact length of piston and liner

Noise and Vibration

a	$\left[\frac{m}{s^2}\right]$	Acceleration
c_0	m/s	Speed of sound (ambient conditions)
c	m/s	Speed of sound
f	Hz	Frequency
f_l	Hz	Lower frequency border (Filter)
f_u	Hz	Upper frequency border (Filter)
Δf_G	Hz	Critical Bandwidth
Δf_{to}	Hz	Third Octave Bandwidth
F_0	N	Reference Force Level, $(1N)$
$H_a(\omega)$	$\left[\frac{ms^{-2}}{N}\right]$	Inertance
$H_N(\omega)$	$\left[\frac{Pa}{N}\right]$	Noise Transfer Function

K_t	$-$	Kurtosis
l_{WN}	dB	White-Noise density level
L	dB	Noise Level
L_T	dB	Masking level (threshold)
ΔL	dB	Masking depth
m	kg	Mass
m	$-$	Modulation $(0 \leq m \leq 1), m = 1 \equiv 100\%$
P	Pa	Sound pressure (Time weighted)
p_0	Pa	Reference sound pressure level, $(2 \cdot 10^{-5} Pa)$
p	Pa	Sound pressure
R	$asper$	Roughness
T	s	Periodic time
u	m	Resulting motion of a part
y	m	Motion
z	$Bark$	Critical band
λ	m	wavelength
ω	Hz	Eigenfrequency
ω	Hz	Frequency $(= 2\pi f)$
ϕ	$-$	Eigenvector
σ	$-$	Standard deviation
τ	$msec$	Time constant

Notation and Subscripts

$\bar{}$	Average or mean value
$\hat{}$	Peak value
$\vec{}$	Vector
$\dot{}$	First derivation
$\ddot{}$	Second derivation
$\tilde{}$	Effective value
Δ	Difference
i,j	Indices
x,y,z	x, y, z components
RSS	Root-sum-square

Chapter 1

Introduction

The usage of fossil generated power and its conversion into heat and work has the advantage of being relatively independent from its location of generation and usage. It can be used independently from time and location, it is easy to store and to transport, and it can be consumed 24 hours a day, independent of seasons. As a result, the fossil power generation allows a concentration of economic processes with increased productivity. One such fossil-generated power source is the internal combustion engine, which delivers mobility and decentralized usage: for instance, lawnmowers, chain saws, vehicles, in the private area, and power-plant, boats, lorries and aircraft in the industrial sector. This made the human being independent from the rhythm of daylight and time, leading to a significant rise in productivity and economic power. The actual stability of the world economic system is mostly based on the trade and consumption of fossil resources [5].

However, this development took place only in a part of the world, and the amount of oil is predicted to decrease during the next six decades. Therefore, new strategies have to be developed in order to allow the emerging countries to participate on this development as well, whether based on the consumption of fossil-generated power or not. Due to the change of climate caused by greenhouse gas emissions, in which CO_2 and CH_4 (methane) are the gases with the highest share, numerous discussions were held by local governments and international federations during the last few years, mainly with the aim to reduce the emission of CO_2. Subsequently both CO_2 and CH_4 were declared by the United Nations (UN) as main contributors to the greenhouse effect. A recent press release and the forthcoming fourth report on the climate change issued by the UN and its panel for climate issues, *IPCC*, founded in the late

1980s, has also called for accelerated actions to reduce the emissions of these gases to avoid further climate changes and their impact on the environment [1, 2].

In contrast to such actions, the efforts of the automotive industry to reduce the fuel consumption and thus the emissions of internal combustion engines have unfortunately been negated by the increased weight and driving resistance of the vehicles. This is mainly caused by an increased amount of safety-related countermeasures of the body structure, as well as by the current trend to larger and heavier vehicles such as for instance, off-road vehicles (SUV), which are used privately merely for inner-urban or motor-way driving. In contrast, the potential to reduce greenhouse emission by increasing the efficiency of the thermal insulation of houses in the northern hemisphere or the avoidance of electrical consumers in stand-by mode, can be considered as enormously beneficial. The emission of CH_4 of intensive animal husbandry can be considered as an important contributor, too.

The impact of different countermeasures to control the global warming effect accordingly can also be predicted using simulation models. This was done for instance by Schäfer and Jacoby in [6] investigating the impact of different fuel efficient powertrain technologies on greenhouse gas emissions. They formulated three different scenarios to predict the impact of certain countermeasures on the industrial development, thereby including the future development of emerging countries. Based on this investigation, a forecast of additional costs for automotive propulsion, raised by greenhouse gas reducing legislative countermeasures, was developed. The analysis presented in this paper was done in the light of three different scenarios, too: first a reference scenario was assumed. Hereby the oil-price in 2010 will be on the same level as in 1995, but will then increase in 2030 to about 40% of that of 2010. The second is that the goals of the Kyoto agreement will be reached that greenhouse gas emissions in 2010 will be 7% less than in 1990 and are maintained on this level until 2030. The third scenario was similar to the second, but envisaged that the 7% will be further tightened by 7% in 5-year periods from 2010 onwards. This means then a reduction of CO_2 of 35% below the level of 1990 by 2030. All three cases consider new powertrain technologies, developed under the pressure of future legislation and potential changes of customer's wants and driving patterns.

While the first scenario will not support significantly the further development of powertrain development for less fuel consumption, the second and third scenario show the need for innovative powertrain technologies to comply with the greenhouse gas emission reductions, in the time frame until 2015 latest. This is why powertrain

technologies that decrease fuel consumption and thus lower CO_2 emissions for a relatively low additional vehicle price, should be investigated thoroughly now, so that they can find their way into the market in a timely way.

All things considered, the availability of oil will not be unlimited, and the need for countermeasures to reduce greenhouse-gas emissions will be of increasing importance. Hence, boundary conditions for CO_2 reduction for all European OEM were established by the common agreed ACEA commitment [3]. This ACEA commitment promises to reach the target of 140gr CO_2/km per vehicle in 2008. On top of that the European Union announced a new framework and legislative requirement in January 2007, dictating now the achievement of 130gr CO_2/km per vehicle in 2012, including the use of Bio-Fuels.

Therefore different new powertrain technologies are under development. Beside some current production hybrid powertrain technologies there are, on the one hand, diesel powertrains, which still show an increased market share, while on the other hand, the development of gasoline engine powertrains continues [4, 7]. The reason for this is that modern gasoline powertrains, having direct injection in combination with turbocharging, which are also called 'downsized powertrains', do not have NO_x or particulate matter issues that the diesel still has. From a customer point of view, not only the fuel consumption and the emissions, but also the *noise, vibration and harshness* (NVH) of downsized gasoline powertrains with a higher specific output than a similar gasoline engine with the same power output, but with a larger displacement, will be expected to be equal. It has been shown that this problem can be solved, even when operating the engine in stratified charge mode during low- and part-load operation [34, 36]. As a potential next step on downsizing, the *homogeneous charged compression ignition* (HCCI), also called *controlled auto ignition* (CAI), is currently under intense investigation. Entering this next stage of direct injection gasoline combustion systems, the HCCI, customer concern attributes such as NVH will became a new challenge in noise and vibration engineering. The reason is the un-throttled self-ignition combustion-mode, which leads to higher peak-pressures and pressure-gradients, which in turn can cause an HCCI-gasoline engine to sound like a diesel engine.

However, the gasoline-HCCI engine in its current state is not suitable to cover the whole speed and load range. Therefore it will be necessary to switch between combustion modes. This should be done without any detectable change in noise and vibration. Hence it is necessary to accompany the combustion and controls

development of such dual-mode-combustion engines with the analysis of the NVH during the early development phase. To do this in an efficient way, while bearing in mind cost and accelerated development times, the initial NVH assessment should be carried out during the combustion and control mapping. However, the currently most-used tools to gain first statements on the engine NVH are the FEV-CSL [148] and the AVL-Combustion Noise Meter [149]. Neither of these methods, however, considers the impact of hardware changes, that can take place for example in the power conversion system. For gasoline HCCI such changes can affect the piston design, the valve train or the bearings. Because of the limited hardware available it is not possible to carry out a separate measurement to quantify its impact on the mechanical noise. In addition, the aforementioned noise prediction methods do not provide information on the change of sound quality when operating in the two different combustion modes. Hence it is worthwhile to develop a new method that can predict the engine noise, while allowing the quantification of the trade-off in NVH when doing hardware changes and establishing new or additional combustion systems in already existing engines. If such a method is made available, potential NVH countermeasures during the early development phase can be developed appropriately.

1.1 Thesis Contributions

The aim of the work was to elaborate, to describe and to quantify the impact on engine noise and vibration of an gasoline direct injection engine that can operate in different combustion modes. This should be done based on measured cylinder pressures only. The engine used for the investigations can be operated in conventional *spark ignition* (SI) with a homogeneous charge, and it can also be operated in *homogeneous charged compression ignition* (HCCI) mode. During the necessary combustion mode switch between SI and HCCI, changes of noise patterns and powertrain vibrations occur. These changes were described and quantified accordingly. As a result a general description of the impact of HCCI on engine noise and vibration has been worked out.

Since the engine was driven on a conventional dynamometer without semi-anechoic conditions, the application of an engine noise prediction method, based on measured cylinder pressure signals, was required. It was found out that currently available noise prediction methods [148, 149], mostly based on correlation

analysis, can only deliver a noise level and a third octave spectrum. However, when operating the engine in HCCI mode, an increase in roughness and impulsiveness of the engine noise was observed, as is known from CI engines, too. As a consequence, the noise prediction method was developed in such a way that psychoacoustic variables could be gained from the prediction routine, too. It is because of this that the prediction tool is based on a non-linear excitation model, incorporating a forced response model of the piston-pin-connecting rod assembly, that provides via the application of measured noise transfer functions, extrapolated and adapted to the engine specific load, the radiated noise level, the third octave spectrum, and two psychoacoustic parameters. These parameters are the 'Roughness', processed by a modified method according to Aures [81], and 'Impulsiveness'. The 'Impulsiveness' will be quantified by a parameter derived from a narrow-band modulation analysis. When describing the non-linear sources of excitation of the engine a modal analysis of the piston, pin and connecting rod revealed that the assembly of the parts has a completely different frequency response sensitivity than the individual parts. It should be mentioned that earlier research into this issue was solely focussed on the individual parts. However, in the present study it was found that certain eigenfrequencies of the assembly contribute to the impulsive noise characteristic of the engine when a threshold of the cylinder pressure rise rate is exceeded. This model gives an answer on the root cause of a threshold value, inductively elaborated by Pye [110] in 1937 for the maximum pressure rise rate allowed to avoid rough and impulsive engine noise characteristics. With this knowledge the combustion characteristics can be adapted to the specific eigenfrequencies of the involved parts to achieve a better sound quality, especially for compression ignition engines.

In addition, a new method was developed to quantify the powertrain vibrations that can be caused by torque fluctuations during combustion mode switches. Since former research has shown that the Vibration-Dose-Value (VDV) does not reflect such an event completely [145], a new signal processing method was developed to consider the exposition and sensation of the passenger to such an event in more detail. In contrast to current measures such as the VDV, the Jerk-Level-Shape (JLS) value reflects sharpness and duration of the excitation, too. For this method a European Patent is pending as listed in the separate chapter 'Patents', item one. The technical background forming this patent will be presented in Chapter 3.4.3 .

Based on both the noise prediction method and the mode-switch procedure, suggestions were developed to achieve a refined operation of HCCI combustion under the

umbrella of noise and vibration. The resulting control parameters were incorporated into a control-strategy that forms a pending European Patent as listed in chapter 'Patents', item two. Further details of this patent will be presented in Chapter 4.2 .

1.2 Thesis Outline

This thesis is organized in six chapters.

Chapter 2: the related work of relevant topics treated is elaborated via a literature study. This study focusses on the hardware used while firstly concentrating on Gasoline Direct Injection and its history, and gives a raw outlook on its future usage. Subsequently the current status of research of Gasoline HCCI development is presented. Its history is recapitulated, current issues are discussed, and an outlook on future design trends is summarized. Reasons for choosing HCCI compared to stratified charge combustion are developed. Moreover, different strategies to initiate gasoline HCCI by means of conventional state-of-the-art valve train design are presented. Then the two most popular valve timing strategies to establish the boundaries for the initiation of gasoline HCCI combustion are discussed, and the reason for selecting the negative-valve-overlap strategy is elaborated. The following subsection gives a short overview of the history of research into engine noise and its contributors, mainly focussing on Compression Ignition engines. Results of research into significant engine noise whether it is combustion noise or mechanical noise sources are presented. Subsequently the current status of commercial and published engine noise prediction routines and tools is presented, and the reason for the development of a new method in the light of engines operating in different combustion modes is developed. Low frequency vibrations, caused by torque fluctuations, can be an issue associated with such dual combustion mode engines. Consequently, an overview on the current known procedures to quantify such events is given. Based on the actually published knowledge, the need for the development of a new algorithm is derived.

Chapter 3: a method to predict engine-radiated noise based on combustion- and structure-related noise is developed. The different subsections of this chapter present the different excitation mechanisms in the internal combustion engine while taking measured cylinder pressure. The main forces exciting the struc-

ture are derived. Furthermore, to achieve a better correlation at frequencies above $\sim 300Hz$, the relevant non-linear excitation forces are derived, and their impact on the excitation spectrum is shown. This includes piston slap, the forced response characteristics of the piston-pin-connecting rod assembly, and the main bearing excitation. Separating the sources of excitations, including the valve train forces, and finally considering load dependent noise transfer functions for the structure excitation, a noise prediction routine is developed. Because of the data-processing in the time domain, this makes it possible to consider psycho-acoustic parameters. First, an overview on the hearing mechanism of the human ear is given. Then two important psychoacoustic parameters (Roughness and Impulsiveness) are described. The Roughness is calculated using the algorithm as published by Aures [81], the Impulsiveness is calculated based on a proposal, published in [84]. Different methods to quantify low frequency vibrations of automotive powertrains are presented. Based on the established measure, called 'Vibration Dose Value' (VDV), [16], the necessity of a new measure is identified. The new index is derived and is called 'Jerk-Level-Shape' index (JLS).

Chapter 4: initially the differences in combustion- and mechanical excitation between HCCI and SI combustion are worked out. Afterwards parametric studies on the influence of different engine control settings are carried out, either in HCCI or SI mode. With the focus on HCCI, the impact of spark-supported HCCI combustion, different intake manifold pressures, valve-timing, injection-timing and different ratios of injection split rate is quantified using the noise prediction routine. Settings for a smooth running HCCI operation are identified, and in some cases the trade-off with emissions and fuel economy identified. The psychoacoustic parameters are correlated with results of the statistical combustion analysis. In addition, observations made during engine operation on the dynamometer are also documented by measurements, taken from the operating engine directly.

Chapter 5: while using the noise prediction routine for the combustion mode change, the impact of different control strategies on the combustion mode transition between HCCI and SI is described and quantified using the JLS. The repeatability of combustion mode switches is studied, and the influence of different throttle settings and injection strategies was elaborated. Based on the results

a list of requirements is developed for the further development of mode change control strategies to achieve smooth mode changes.

Chapter 6: this chapter summarizes and reflects the results achieved. In addition, the outlook points out tasks that may be part of further research.

Chapter 2

Literature Review

The current and future development of internal combustion engines with gasoline direct injection systems applied promotes the development of the homogeneous charge compression ignition, too. This will affect engine acoustics and vibration. The following sections will deliver a short overview on gasoline direct injection systems, the development of the HCCI combustion system and strategies to effect HCCI. An overview of the measurement and prediction of engine acoustics and vibrations, including a survey on the evaluation of low-frequency vibrations, is given.

2.1 A short overview on Direct-Injection Gasoline Combustion Systems

Enforced by the need of a high density of power for aircraft under the boundary of operating at high altitudes, the development of the gasoline direct injection (GDI) technology gained increased attention in the 1930's [118], at which first preliminary investigations were carried out by Junkers during World-War I, using a Daimler engine, type *'DIV'*. The most important advantages when applying gasoline direct injection can be listed according to Schmidt [114] and Judge [112] as follow:

- better safety due to less conduit-pipes for the mixture
- increased cam-timing overlap effecting a better scavenging, especially at full-load
- higher knock-limit, allowance of higher pressure levels by super- or turbo-charging, especially when using split- or multi injection.

- better distribution of the mixture to the individual cylinders, because each cylinder receives an equal amount of fuel
- better transient response [116, 153].

Moreover, the direct injection of the gasoline effects a cooling of the incoming air by fuel vaporization during the intake stroke. This improves volumetric efficiency and enhances the knock tolerance. As a consequence e.g. Daimler-Benz was able in 1934 to increase the compression ratio of its aircraft engines types *DB601 A* and *DB603* from 6.5 to 6.9, leading to a better efficiency, and thus allowing a higher level of charge pressure. The charge air pressure was controlled by a full mechanical barometric controlled charge level device, leading to a higher engine power output of 705kW instead of 670kW. This was also accompanied by a reduction of the specific fuel consumption from $225 g/kWh$ to $210 g/kWh$ [118]. The flat top combustion chamber had an opposite arrangement of one multi-hole injector, developed by the company L'Orange, each neighboured by a spark-plug [116]. At the same time similar developments were ongoing at Junkers in collaboration with Bosch, to enhance the power output of the 'Jumo 211D'-type aircraft engine which is discussed thoroughly by Judge [112]. Starting in 1939, BMW developed the '801-Type' 14-cylinder twin-supercharged radial engine, owning direct injection with a fuel-supply pressure between 70bar to 100bar. The injection happened during the intake stroke, whereby the fuel was swirled by a special combination of arrangement and geometry of the half-bowl combustion chamber and inlet valves [113].
In England at that time there was e.g. the Napier Sabre, V-type, having a Hobson RAE fuel injection [119] into the intake ports. In the U.S. the Bendix Aviation Corporation developed a gasoline direct injection system on the base of the Stromberg Injection Carburettor. In this system a high-pressure fuel-pump was employed, delivering $35 bar$ fuel-pressure to feed the outward opening hollow-cone injectors [113]. Besides thermodynamic advantages, the introduction of gasoline direct injection in aircraft engines effected also a reduction of major issues caused by the use of carburettors, for instance icing at high altitudes or a bad mixture formation due to aerobatics [112, 111, 114].
During the early 1950's the gasoline direct injection was discovered to increase the specific power-output of automotive internal combustion engines, accompanied by less fuel consumption. A thorough investigation concerning the applicability of GDI for automotive purposes was done by Schmidt, predicting a benefit in fuel-

consumption of 15-20% [115]. But because of its mechanical complexity and the resulting high additional costs at that time it was a natural consequence that the technology was mainly applied to racing engines. However, even in 1939 there were plans to install a *DB603* aircraft engine with 2800*hp* into a race car for land-speed record purposes. This was suppressed then by the beginning of World War II.
As described by Ludvigsen [120] and Scherenberg [116], first natural aspirated GDI-engines were developed by Mercedes-Benz for the *300SL* in 1952, and in 1955 with the 2.5 litre inline eight-cylinder *M196*-type, allowing a compression ratio of 12.5, leading to a power density of 116.2$bhp/litre$. The side-mounted hollow-cone injector opened at approximately 45bar and supplied the fuel over a certain bowl-piston geometry with a pressure of 70bar into the combustion chamber. In contrast, the average racing engine at that time had a compression ratio of about 9.0. For instance Ferrari's *750-Monza* 3-litre inline four-cylinder from 1955 had a compression ratio of 9.2 and 83.83$bhp/litre$. In 1958 Borgward presented the *RS* 1.5-litre inline four-cylinder, on which a GDI-system was used. The four-valve pent roof combustion chamber had a central mounted injector in the cylinder head, surrounded by two exhaust- and two inlet valves per cylinder. In this engine also a pent-roof piston was used. The mixture was ignited by two spark-plugs per cylinder, arranged between the intake- and exhaust valves [113]. The injector was feed by an electrical fuel-pump for starting, and by a mechanical one during normal operation. Injection-timing was fixed at 62^o after scavenging TDC. In addition this engine was the first to have a kind of variable valve-timing, enabled by joining camshaft and sprocket *'by a coupling, comprised of two conically-tapered rings which, when pressed together by a central clamping bolt, expanded to lock the end of the cam to the sprocket'*, [120] [1]. Driven by the oil-crisis in the early 1980's the development of GDI combustion systems was enforced. The GDI concept promises to operate the engine in stratified operation at part-load condition with full open throttle and a certain amount of exhaust gas recirculation to slow down and phase the combustion. This then would

[1] Most information of this short review of the history of direct injected gasoline engines were concluded from the following publications: a comprehensive overview on piston-engine technology of aircrafts is given in the book by v.Gersdorff et al. [118]. A discussion of GDI aspects of piston aero engines (Rolls-Royce) was found in the book by Rubbra [119], pp. 107 - 116. In addition exhaustive reviews of detailed thermodynamical and mechanical aspects including gasoline direct injection used on aircraft piston engines can be found in the books by Pye [111], Judge [112] or Löhner and Müller [113]. Ludvigsen elaborated an in-depth survey on past and recent developments, including gasoline direct injection, of automotive high-performance engines in [120].

lead to a benefit in fuel consumption. Hereby the combustion system should be able to stabilize the mixture in the center of the chamber to avoid wall wetting, leading to HC emissions, and as well reducing the heat-losses via the cylinder walls [93]. However, when operating a GDI combustion system in stratified-mode, i.e. with a turbulent combustion taking place in a limited zone around the spark plug resulting in an overall air-fuel ratio of e.g. $\lambda = 2.5$, the local temperatures in the reaction zone can be higher than during stoichiometric combustion. Because of the so-called 'Zeldovic-Mechanism' occurring above a temperature of 2200K that generates the NO_x, these temperature conditions are favourable for the generation of NO_x [62, 103]. As a consequence this leads to the necessity of special aftertreatment devices to comply with legislation.

The progress of engine control and -mechanics (a major issue of the early GDI engines was that the high pressure gasoline fuel pump needed separate circuits for gasoline and oil to ensure a proper lubrication, which was in turn possible with Diesel fuel) has led to different categories of GDI combustion systems that are shown in Figure 2.1 [93]. The following is a short discussion of the different principles of GDI

(a) Wall-Guided GDI combustion system, side mounted injector, central mounted spark-plug, bowl-piston (trough-shaped)

(b) Air-Guided GDI combustion system, side mounted injector, central mounted spark-plug, bowl-piston (trough-shaped)

(c) Spray-Guided GDI combustion system, central mounted injector and spark-plug, flat-top piston

Figure 2.1: Survey of different gasoline direct injection combustion systems

systems.

The Wall Guided System (WGDI), Fig.2.1(a): the mixture formation is established via an interaction of the fuel spray and the wall. Usually the spray is guided to the spark plug by a bowl piston design, supported by a certain combination of swirl- and tumble. This bears a risk of unburned hydrocarbons, caused by wall wetting. Also

the relatively long travel of the fuel to the spark plug requires a stabilized charge motion, controlled by injection timing, spray pattern, valve timing, swirl and tumble at each speed and load point.
The Air Guided System (AGDI), Fig.2.1(b): the fuel is brought to the spark plug via a carefully controlled intake air stream whereby the fuel is injected in this airstream directly in the combustion chamber. In contrast to WGDI a contact of the fuel with the walls should be avoided. This lead to a very complex control of fuel-spray pattern and intake air dynamics, i.e. the charge motion, to ensure compliance with emission and power targets.
The Spray Guided System (SGDI), Fig.2.1(c): this system is characterized by a spatial arrangement of fuel injector and spark plug, either a central arrangement or a side mounted injector with a centrally positioned spark plug. The aim is to achieve a compact and ignitible mixture at the spark plug to achieve high air-fuel ratios. This requires, among other things, a fast mixture formation, late injection, especially during low loads and idle and a stable and repeatable spray pattern over the whole injector lifetime.
A thorough discussion of different GDI combustion concepts is given by Fraidl et al. [93] and Zhao et al. [96], but most principles can be referred to one or a combination of these three. However, it can be concluded from Figure 2.1 that the wall- and the air-guided system (Fig.2.1(a),2.1(b)) permit a larger valve diameter and allow a longer time for mixture preparation including less effect of variations in the fuel spray characteristics. In contrast to that, the spray-guided system (Fig.2.1(c)) owns a higher ignition stability, allows a uniform distribution of the fuel in the combustion chamber and thus allows the use of a flat-top piston design. Hence an advantage with respect to NVH of such a spray-guided system is that a flat-top piston can be used instead of the mandatory bowl-shaped for the two other principles. On the one hand, this reduces the oscillating masses (the weight of a flat-top piston is about 15% less than that of a bowl-piston), and on the other hand, it could reduce the effort to minimize piston slap because of a much more homogeneous distribution of its mass around the pin. The GDI-concept found its way to the mass-market in 1995, when Mitsubishi presented its GDI-concept on a 1.8-litre inline four cylinder, followed by Renault in 1999 with a 2.0-liter inline four cylinder. The Mitsubishi had a wall-guided combustion system (Fig.2.1(a)) and was able to operate in stratified charge mode. In contrast to that the Renault system was spray-guided and just operating in homogeneous mode, thus avoiding an expensive NO_x-trap. Both systems

required fuel with less sulfur and higher octane numbers to lower the risk of soot formation on injector and spark plug. Hence there was a likelihood that the savings by consuming less fuel were compensated by increased costs for maintenance.

In 2001 VW introduced its GDI concept, named 'FSI', that can be considered as a combination of an air- and wall-guided system [153].

At the beginning of the 21^{st}-century, then downsizing gained more attraction. Here the combination of homogeneous GDI in combination with super- or turbo-charging is a favorable solution for most OEM's. This allows on the one hand high compression ratios effecting an increased knock-resistance because of the charging, and on the other hand small displacements, delivering low part-load fuel consumption. On most of these new engine-concepts so-called 'second generation GDI systems', i.e. spray guided systems with a central arrangement of spark-plug and solenoid-multi-hole-, or piezo-injector, as shown in Figure 2.1(c), can be found [7, 150].

2.2 Development of the Gasoline-HCCI Combustion System

The application of HCCI on gasoline engines has been published under different acronyms, e.g. as 'ATAC' (Active Thermo-Atmosphere Combustion) in 1979 by Onishi et al. on a two stroke engine [87]. In 1983 Najt et al. presented it on a four stroke engine under the acronym of CIHC ('Compression-Ignited Homogeneous Charge Combustion') [88]. It has also been presented under the abbreviation of CAI (Controlled Auto Ignition) by Lavy et al. in frame of the cross-industrial 4-Space project in 2000 [90]. In addition there are a lot of different acronyms around as e.g. listed by Zhao in [95]. Henceforth the abbreviation HCCI (Homogeneous Charged Compression Ignition) will be used if not otherwise indicated.

All the combustion processes presented in the above-mentioned papers refer to a homogeneous mixture that is ignited by compression near to piston top dead center (TDC). This was first presented by Onishi in 1979 on a two stroke engine. Due to the upcoming legal requirements to reduce the fuel consumption in the near future, the research on HCCI gained more attention. Najt [88] proposed the use of lower compression ratios to achieve the best trade off on ignition requirements and bulk energy release rates. This was also confirmed by Thring in 1989 [89]. Thus,

to achieve a controlled combustion in a gasoline engine with a nearly unchanged compression ratio in the area of 11.5 to 12.5, there are several measures necessary to achieve the temperature level of about $1200K$ to get the combustion started without any emission issues and additional energy consuming devices at the engine, such as e.g. an intake-air heater. One solution to achieve this temperature level in the combustion chamber is to retain the residuals of the combustion that took place before the next cycle. Besides the use of full electronic valve trains, a valve timing strategy was developed, called 'Negative Valve Overlap' (NVO). One instance of the successful application of that strategy was published in [105]. This strategy allows the use of a conventional twin-independent camshaft layout when doing a pre-compression, caused by a low lift cam on exhaust and intake side, accompanied by an early exhaust valve closing and a late intake valve opening. A similar valve timing strategy for HCCI was also published by Law et al. in 2000 [91], employing an electro-mechanical valve train. Moreover, Allen and Law have shown that this strategy is suitable to cover important speed and load ranges to reduce the fuel consumption [92]. Detailed research of HCCI preferring this strategy was done by Koopmans [159]. He presented the impact of different valve timing strategies on the stability and emissions of HCCI, as well as first approaches of doing a mode change between SI and HCCI combustion mode on a multi-cylinder engine [97]. Koopmans also did detailed research on the injection timing, using gasoline direct injection [98]. Accompanied by simulations of the HCCI combustion by Ogink [100], he did investigations while injecting fuel during the negative valve overlap phase to enable a certain pre-combustion during the pre-compression. In this way higher temperatures for the main compression stroke were achieved, resulting in an advanced auto ignition timing. In contrast to the NVO strategy, Fuerhapter et al. [8] presented the AVL-CSI concept, enabling the HCCI mode by re-breathing exhaust gases from the exhaust manifold to achieve the necessary conditions. This strategy has the disadvantage of being dependent on the exhaust manifold gas-dynamics, resulting in a complex control strategy or compromised operation range of the HCCI [99]. An additional issue of this strategy is that the re-breathed gas is cooled in the exhaust manifold.

Most gasoline HCCI engine concepts still have to operate in spark-ignition mode to cover operating points that can not be achieved in HCCI mode. Therefore, the gasoline direct injection [7], due to its cooling effect in the combustion chamber, is the most suitable technology to operate in SI at these relatively high compression ratios without knock issues at full load. A high speed camera analysis of a SI and

a HCCI combustion at same load and speed in the same engine is shown in Figure 2.2 and illustrates the major differences between a SI- and HCCI combustion. The

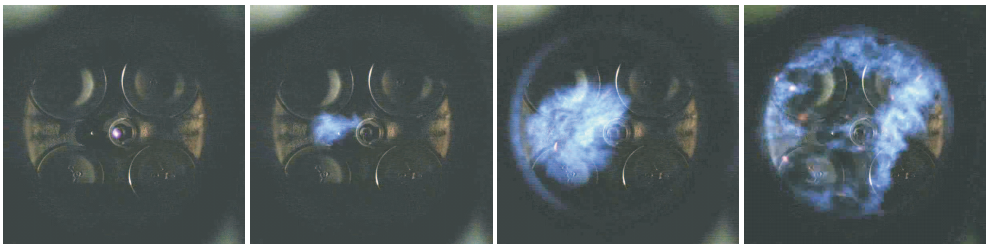

(a) SI combustion, stoichiometric, combustion duration approximately $30deg$ crank-angle

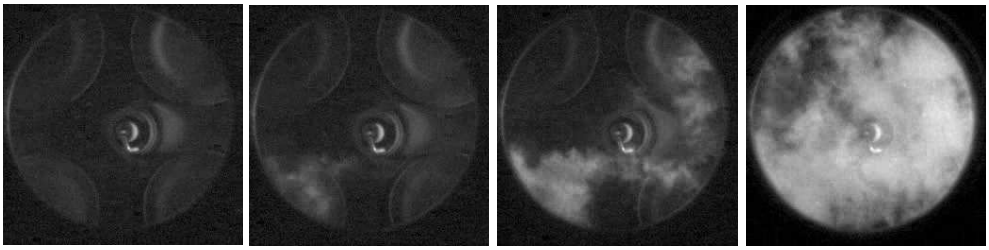

(b) HCCI combustion, $\lambda = 1.9$, 50% residuals, combustion duration approximately $8deg$ crank-angle

Figure 2.2: High speed camera analysis of SI- and HCCI combustion [159]

duration of a stoichiometric SI combustion at same load and speed may be approximately three times longer than a corresponding HCCI combustion. Moreover, Figure 2.2(a) shows the flame front propagation after the spark ignition (first left picture): a propagating flame front develops from the central located spark-plug into the combustion chamber (pictures from left to right). At the very beginning the flame front propagates with a laminar flame speed, then turning into a turbulent flame front with a increased flame speed (third and fourth picture from the left). In contrast to that Figure 2.2(b) shows the controlled auto-ignition combustion without any spark and a propagating flame front: starting with the second picture from the left there is a self-ignition process starting at the homogeneous distributed clouds of mixture, resulting in a sudden homogeneous distributed combustion (right picture). Figure 2.2(b) also shows the absence of fuel-rich zones. In combination with the lean AFR and a homogenisation of the mixture prior to autoignition, such fuel-rich zones can be avoided. This suppresses the generation of soot during combustion, and keeps the combustion temperature low. This is the main advantage of HCCI compared to stratified SI, because of the lower combustion temperature ($< 2200K$) NO_x is not

produced [153].

As was mentioned before the HCCI mode in its current development state can not be employed over the whole load- and speed operating range of automotive applications, and mode changes between SI- and HCCI combustion mode are required. As an example Figure 2.3 shows a possible operation map. It can be seen from

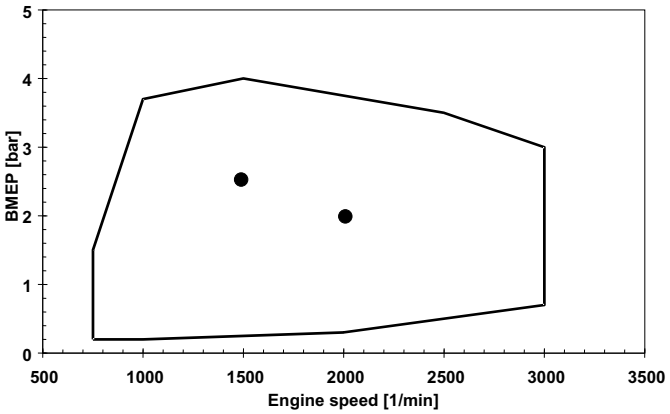

Figure 2.3: Known operation range of gasoline HCCI engines

Figure 2.3 that the HCCI is most suitable for part-load conditions; investigations to enhance the HCCI-mode to idle (e.g. 800rpm, 0.7bar BMEP) are ongoing. This also leads to the challenging task of enabling a very fast mode switch between a throttled SI- and an un-throttled HCCI-operation without any significant load fluctuations, changes in noise level and its frequency contribution, i.e. sound-quality, and resulting torque spikes in the powertrain. The investigations and results presented in the following sections are mostly based on the comparison of SI- versus HCCI operational mode, always at same speed and load point. The two preferred points of operation (1500rpm, 2.62bar BMEP, and 2000rpm, 2bar BMEP) used in this work are also highlighted in Figure 2.3. Both points are in the center of the range of HCCI operation. To underline and quantify the potential trade-off between both modes, in some cases results for the same load and speed of an actual turbo-charged, common rail diesel engine with same displacement are shown in Chapter 4.

2.3 Gasoline-HCCI Operation Strategies

To operate an SI-engine in HCCI mode, a certain amount of hot residual exhaust gases from the previous cycle is necessary to establish a stable HCCI operation mode.

This can be for example established while utilizing different valve lift and -timing strategies for the purpose of retaining residual exhaust gases in the combustion chamber. A survey of such strategies in the light of a fully flexible electro-mechanical valve actuation (EVA) is depicted in Figure 2.4, [94]. But all strategies except the ex-

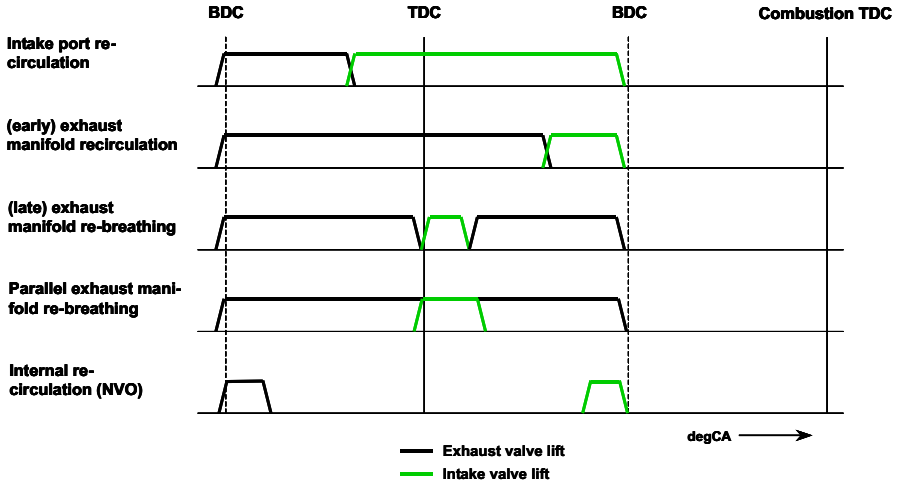

Figure 2.4: Survey of different exhaust gas retaining strategies while utilizing Electro-Mechanical Valve actuation (EVA) to enable gasoline HCCI

haust manifold re-breathing and the parallel exhaust manifold re-breathing strategy, can be enabled using conventional cam-profile-switch techniques such as presented in [171], too. It should be mentioned that all strategies can be combined with a variable valve timing, even when using conventional cam-profile-switch techniques. However, to enhance the window of HCCI operation, a mixture of these different settings can be favourable. This is because each strategy supports HCCI at certain load- and speed combinations, fulfilling the necessary requirements regarding robustness and stability [94].

The most promising strategies which have been published are based on trapping residuals by re-aspirating exhaust gases from the exhaust [8], or establishing a so-called negative valve overlap strategy (NVO) as presented in [105, 159]. Both, the re-breathing and the NVO-strategy will be presented in the following subsections. It should be mentioned that both strategies are discussed under the assumption of a spray guided gasoline direct injection applied to the engine. Moreover, meanwhile both strategies have been demonstrated on a complete engine, including the nec-

essary combustion mode switch between spark ignition and HCCI. No difference of the benefit regarding fuel consumption between both strategies has been found yet [8, 99, 159].

2.3.1 The Exhaust Manifold Re-breathing Strategy

One solution to promote the combustion kinetics (autoignition) for the HCCI combustion is the strategy of manifold gas re-breathing: after the combustion stroke the hot gas is expelled into the manifold, using conventional exhaust valve timing and -lift. Afterwards the exhaust valve is opened for a second time in parallel with opened intake valves during the suction stroke. This will then lead to a mixture to establish the boundaries for the start of the HCCI combustion [8, 99]. However, this strategy has some difficulties.

At low speeds and low loads the expelled exhaust gases lose their temperature level when remaining in the manifold before an exhaust valve is opened for the second time. Once they are re-breathed this can lead to a lower lambda value, which bears the risk of an incomplete combustion, leading to increased HC-emissions, as was observed in [99].

During transient operation this strategy bears the risk of being dependent on the exhaust gas dynamics in the manifold. On the one hand the manifold should keep the temperature of the expelled gases, but on the other hand this should happen independently of the gas dynamics. For instance this could require on an inline four cylinder engines the application of a four into two into one (4-2-1) exhaust manifold. Assuming an ignition order of 1-3-4-2, the runners of cylinder one and four and of cylinder two and three have a separate junction. Just behind the two individual catalysts they are mated into one runner, fitted to the cold end exhaust system. Despite of the advantage of a better scavenging during full-load operation, such a system can lead to lower exhaust gas temperatures, making a stable or transient HCCI operation more difficult. Furthermore, during the required mode transitions from SI to HCCI or vice versa the gas dynamics and the properties of the re-breathed exhaust gas can vary and thus increase the effort to achieve a stable and misfire-free operation.

Ideally, the valve timing can only be realized using electro-mechanical valve actuation (EVA) to enable the second exhaust valve event. Using conventional cam driven valve trains including cam profile switch (CPS), a second separate exhaust

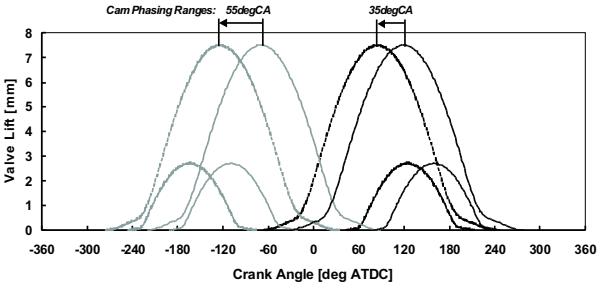

Figure 2.5: Different cam-timing and -lift strategies for HCCI and SI combustion. The exhaust valve lift is represented by the grey line. The HCCI combustion strategy requires the low valve lift curve for both intake and exhaust cam (max. lift of 2.8mm)

valve must be applied. Hence, the application of this strategy ideally requires an individually actuated valve-train, such as EVA. In addition a separation of exhaust runners on the manifold system can be favorable.

2.3.2 The Negative Valve Overlap Strategy

The negative valve overlap (NVO) strategy has been published much more often in conjunction with gasoline HCCI on a complete engine. The NVO-strategy enables HCCI by an early closing of the exhaust valve. Because the exhaust valve closes before scavenging TDC the remaining exhaust gases are compressed to form the chemical reactions for the HCCI combustion. Approximately $85 deg CA$ after TDC the intake valve opens for a period of $120 deg CA$. The mixture of the compressed residuals and the fresh air then form the basis for the reaction to activate HCCI combustion. Figure 2.5 shows the applied two basic valve-timing and valve-lift strategies. Note that the inlet and exhaust valve lift are much less than in SI operation. On the exhaust valve this is to retain the necessary amount of residuals to maintain the temperature in the combustion chamber, and on the intake to keep the amount of fresh air at such a level that the process of combustion is promoted at the homogeneously distributed zones of reaction. During SI-mode, the valve lift can be assumed as a normal SI-engine lift. Contrary to that, the HCCI mode requires a lower valve lift and a cam-timing nearly to the outer boundaries of the exhaust and intake cam timing, accompanied by a shorter event length. This strategy can be enabled with a switch between two cam-profiles. Because of the application of gasoline direct injection each cylinder could be controlled separately to ensure a stable running in HCCI and during mode transition from SI to HCCI. Because of the pre-compression, the boundaries to initiate the HCCI combustion can be con-

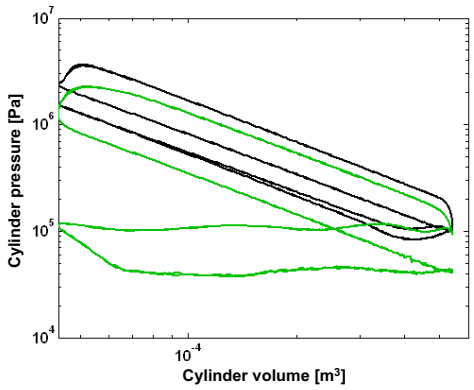

Figure 2.6: pV-diagram of HCCI (black line) using the NVO-strategy, and SI mode at same load and speed (*log-log*)

trolled more easily when applying cylinder individual multiple injection strategies. Moreover, no interaction between exhaust manifold gas-dynamics and residuals is given. This improves the control of HCCI combustion regarding position and duration relative to TDC [99]. A comparison of the particular pV-diagrams of SI- and HCCI mode at the same load and speed is shown in Figure 2.6. It can be seen from Figure 2.6 that the HCCI cycle, represented by the black line, delivers higher peak pressures. Moreover, the HCCI mode using the valve-timing and -lift strategy as shown in Figure 2.5 has significantly lower throttle losses. During all experiments in gasoline HCCI operation in this thesis the NVO-strategy is used.

2.4 Engine Noise and Vibration

Ever since the first internal combustion engine was employed in a vehicle, concerns about its radiated noise were raised. After the main thermodynamic issues were sorted out, the radiated noise came more and more into the focus of research, especially when the Diesel engine was introduced in automotive applications [117, 132]. Ricardo did initial work when defining a maximum pressure rise rate to achieve a smooth running engine [109]. In parallel, there were developments in the interaction of mechanical engine control and NVH, as among others Ricardo, Pischinger and Sass did investigations to achieve a smooth running Diesel engine while varying the injection settings [109, 117, 121]. Pischinger also did initial research on the clattering sound of Diesel engines and identified the shock load on the conrod as the main source [117]. A comprehensive report about Diesel engine acoustics was issued 1959 by Austen and Priede [135]. Furthermore, research on the distribution of noise

in Diesel engines was carried out by Hempel and Pflaum in 1965 [24], who first focussed on the development of the required basic measurement and data evaluation technologies for engine acoustics and then did an acoustic analysis of 17 non-boosted diesel engines of that time.

2.4.1 Experimental Methods

Caused by the increasing legal requirements with the beginning of the 1970's, engine acoustic on both gasoline and diesel, gained more attention. This was also accompanied by a significant step forward on the possibilities of the signal analysis due to the upcoming computer technologies. Thus, Priede gave an overview in his paper on engine NVH in 1980 [140] about the general relationship between cylinder pressure and engine acoustics. Kamal and Hickling published the proceedings of an engine acoustics conference, which contained a detailed account of all theoretical and numerical approaches available at that time for the investigation and improvement of engine NVH and its sources [14]. This proceedings contained also first steps on Finite-Element-Modelling (FEM) for the purpose of dynamic analysis of engine structures. In parallel, mainly starting during the 1980's, research was done while investigating the noise-paths from the cranktrain into the engine structure of an internal combustion engine [26], and identifying the main bearing structure as a central design factor to achieve a low structure-borne noise level. In particular it was pointed out that a high stiffness of the oil-film, caused by a large eccentricity of the shaft in the main bearing, leads to an unfiltered transfer of the gas-forces into the engine structure. Woschni et al. did detailed investigations on the influence of the pressure rise rate on the structure excitation of a diesel engine [47]. One result was that the clattering noise characteristics of diesel engines can be referred to a longitudinal eigenfrequency of the connecting rod. An additional approach was published recently by Göhringer to cascade the radiated engine noise into the contributing sources using correlation methods with the inclusion of load dependent correlation functions [165].

2.4.2 Prediction Methods

Because of the introduction of new pass-by-noise legislative requirements in 1996, powertrain radiated noise, and engine acoustics and vibration in particular, gained much more importance. Moreover, since 1990 a significant rise of the capacity and

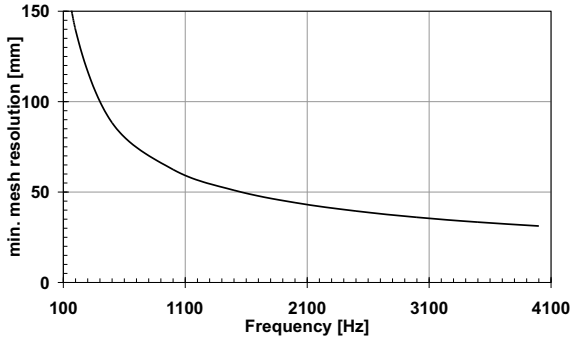

Figure 2.7: Interaction of mesh resolution and frequency to be analysed according to equation (2.4.1) for a plate of thickness $h = 0.01m$, material: steel

calculation time of computers took place. This allowed the use of the Finite-Element-Analysis with meshes of high resolution, such that the wavelength and thus noise and vibration of engines nowadays can be simulated in advance using finite element models in an acceptable running time, for example doing a structure-borne analysis up to a frequency of $4kHz$. However, the requirements to model, for instance a bending wave of a frequency of $4kHz$ appropriately, for example a resolution of a finite element mesh is required. This is demonstrated by the following example: according to the theory of a bending wave of a steel plate of a thickness $h = 0.01m$ with a Young's Modulus of $21 \cdot 10^{10} N/m^2$ and a density of $\rho = 7838kg/m^3$ and $\nu = 0.3$, the velocity c_B can be calculated according to [71] by

$$c_B = \lambda_B \cdot f = \sqrt[4]{\frac{E \cdot h^2}{12\rho(1-\nu^2)}} \cdot \sqrt{2\pi f}. \tag{2.4.1}$$

Choosing $f = 4000Hz$, the wavelength would be $\lambda_B = 0.1568m$. In contrast, the resolution necessary to model a bending wave properly would mean that five nodes are required to describe the wave sufficiently. This results in a wavelength of theoretically $0.03136m$. This yields then a node distance of $0.03136m$, too. Based on equation (2.4.1) the required mesh resolution is drawn over frequency as represented in Figure 2.7. It can be seen that the effort necessary to model the bending wave appropriately decreases progressively at frequencies lower than 100Hz. In contrast, above 100Hz the bending wave of the structure becomes more relevant for acoustics. However, at the very beginning of the product development finite element models of such a high resolution are not available. As a consequence, hybrid models are used to predict the noise and vibration during the advanced product development phase. It is common that such models consists of the combination of analytical mechanics with measured data. Such a hybrid modelling approach is the prediction of

the radiated noise of internal combustion engines, based on measured or calculated cylinder pressures, taking averaged or correlated transfer functions. One method to predict the radiated engine noise was developed based on findings from Wolschendorf, who worked out a correlation of cylinder pressure excitation and acoustics [32] on a Diesel engine. This method was developed further during [27, 28, 31] and is able to predict the radiated noise level and the related third-octave spectrum based on measured cylinder pressures at certain load and speed point while using an averaged structure attenuation. Because of the introduction of lightweight Diesel engines, having aluminium crankcases, these models are not able to predict engine noise as a function of load with great accuracy. One possible solution that is currently under discussion is the introduction of load-dependent transfer functions for the structure excitation [165]. Since modern gasoline engines, especially those with gasoline direct injection, deliver new NVH attributes such as flow induced noise from the intake when being driven un-throttled during stratified combustion mode, this noise prediction method was refined by Heuer considering a simple linear flow noise level approach. He also proposed to distinguish between excitation with gas-force shape and rotating-force shape [28, 31, 148]. However, this refined method still has the issue of not reflecting the time-frequency structure of the noise, i.e. sound quality, such as roughness or clattering. In addition, the dynamic behavior of the engine structure and sub-structure and parts, for example connecting rod, piston and crankshaft, is not considered.

Due to the introduction of *computer aided engineering* (CAE) tools while coupling FEM and flexible *multi-body-analysis* (MBA) and furthermore the introduction of the *boundary-element-method* (BEM), all relevant NVH issues can now be calculated beforehand, which is for example the noise radiation or structure borne noise caused piston slap, considering thermal loaded elastic-hydrodynamic boundaries [29, 38, 42, 130, 160, 164, 166]. All these techniques are suitable for designing an engine to achieve a minimum level of noise and vibrations, but they are often also time consuming, despite the use of advanced computer technologies. This is because of the availability of the necessary design frames during a research phase, or setting up an appropriate FEM-mesh that fits the requirements of resolution as aforementioned for an appropriate model for an analysis of the strength and acoustics in parallel. Hence it will still be necessary to accompany the base engine development, and also the combustion development, with prediction tools which are as simple as possible, but as precise as necessary, to quantify and characterize the NVH during

the pre-development phase of a new engine or combustion system.

2.5 Evaluation of Low-Frequency Vibrations in Automotive Applications

As is already known from current gasoline direct injection engines, the switch between a throttled to an un-throttled running mode can cause low frequency vibrations, excited by torque fluctuations. These vibrations are then transferred into the vehicle interior, i.e. seat and steering wheel, and lead to discomfort. The noise characteristics of the engine changes as well and therefore requires a smooth transition [147]. Since the mode change from SI to HCCI running mode contains a similar problem, the development of a torque control method is required to achieve a comfortable mode switch. In addition, similar low frequency excitations are known, also known as 'jerk' during gear change of automatic or automated transmissions, or as 'shake' when the vehicle is run in start-stop mode. Griffin presented different methods to describe the quality of such low-frequency vibrations and their impact on the human body [16]. Currently, mainly two of these methods are well established in the automotive industry:

1. the Dynamic Response Index (DRI), which is based on the transfer characteristics of the structure from its source to the location of perception by means of an undamped single degree of freedom. Mostly the resonance of the spine of the human body is taken into account.

2. the Vibration Dose Value (VDV), which evaluates the measured acceleration signal at the location of perception, for example at the seat-track.

Since the whole transfer characteristics of a vehicle can be considered strongly nonlinear because of for example rubber elements, which bring frequency-dependent damping effects into the powertrain mounts, the application of the DRI is not widespread. In contrast to the DRI, the VDV is meanwhile a standard to evaluate the gear shift quality of transmissions [146]. However, it has been demonstrated [145] that the VDV neither considers the gradient of the acceleration signal nor its shape during the evaluated time window. It can be the case that a signal with a high peak and a short duration is perceived as being of better quality than an alternating signal with less peak height but a longer duration. Thus, a method should be made

available which not only considers the height and duration of an acceleration signal, but also the shape and envelope of excitation.

Chapter 3

Acoustics of Internal Combustion Engines

The noise radiated by an internal combustion engine can be generated by different sources. However, the prediction of the radiated noise requires an appropriate modelling of these sources. Currently available methods for engine noise prediction are either based on correlation factors to achieve a better correlation between measurement and prediction, or on the rather complex coupling of finite-element method and multi body system simulation, combined with the boundary-element method to retrieve the distribution of the radiated noise. Therefore, the application of such combined finite element models is not affordable when a statement regarding the level of the radiated noise is required in a short timescale, when quantifying for example the impact of engine-control parameters on the acoustics. Moreover, current prediction methods based on the correlation of cylinder-pressure and radiated-noise are only able to predict the noise level and its spectrum.

The new method presented in this chapter is based on an approach that takes the dynamic effects into consideration, using load-dependent noise transfer functions. This makes it possible to predict the impact of hardware changes on the engine-radiated noise without carrying out expensive and time consuming experiments. Furthermore, the resulting excitation in the time domain can be used to quantify the sound-quality of the engine noise; this is mandatory if an internal combustion engine is operated with different types of combustion and therefore has different combustion excitation characteristics.

3.1 Engine Noise and its Contributors

There are different sources in an internal combustion engine that contribute to its acoustics. Listing the different sources in the order of process of an internal combustion engine, they can be itemized as follows:

- Combustion noise (dependent on speed of the combustion process, position of 50% mass fraction burned, $CA50$, maximum peak pressure and its position relative to the crank angle (TDC), pressure rise rate and its derivatives.)
- Direct Combustion Noise (Combustion Noise which is directly radiated by the engine structure, detectable directly at the cylinder liner. The according transfer function can be gained by doing an impact or provoking an explosion in the combustion chamber, while measuring the resulting radiated noise, and processing the necessary transfer function. It is important that the engine parts are not in movement which is to separate the mechanical noise sources.)
- Indirect Combustion Noise (Noise which is transferred from the combustion chamber via the structure, for example the power conversion system and the cranktrain, or diesel engine clatter noise; it is finally radiated by the structure.)
- Mechanical Noise (mostly caused by the cranktrain, such as piston, connecting rod, crankshaft including bearings and the valve train. Lashes between the individual parts play a major role. The mechanical noise used to be estimated on a NVH dynamometer by doing a motored run-up)
- Flow Noise (from the orifice, dependent on the duct geometry, speed, load, valve timing and lift)
- Exhaust system noise (mostly flow noises, when a turbo- or supercharger is matched to the engine; additional different noises can occur, for instance turbo whine; can also be filed under the general flow noise, not considered here due to non-representative boundaries of the engine in the test cell environment.)

Figure 3.1 shows the relationship between the significant engine noise contributors. Since the research work is supposed to deliver general aspects and routes to describe the acoustics of dual-mode-combustion, hence the SI-HCCI engines, the intake, direct, indirect, mechanical and exhaust noises are related to the structure of each

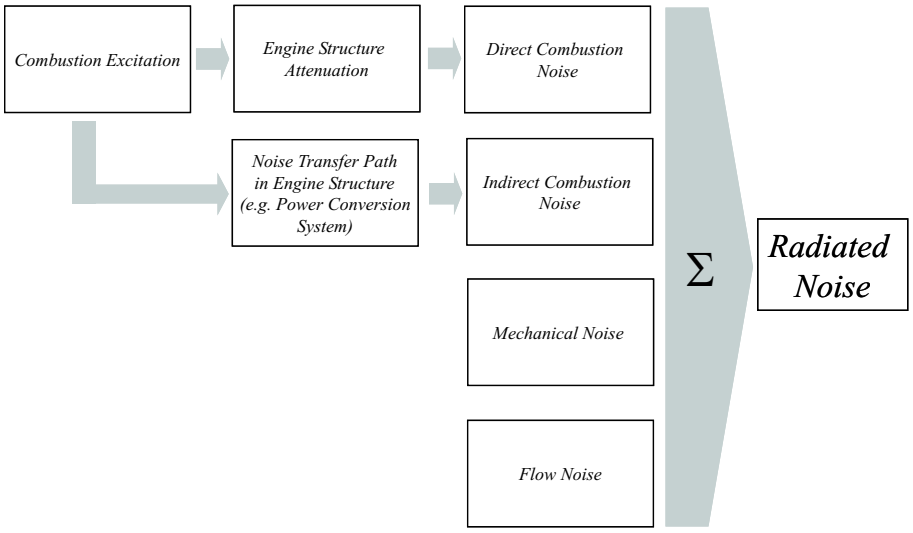

Figure 3.1: Sources and contributors of engine noise

individual type of engine and are therefore difficult to transfer into a general approach. In addition, they are not easy to work out, for instance in comparison with the indirect combustion noise that can be calculated by the difference of the radiated noise level minus the mechanical noise, gained from closed throttle operation without combustion. Also, the investigation of the exhaust system noise is rather difficult to assess on an engine dynamometer because of a non-representative routing of the exhaust system and different muffler positions used there compared to the vehicle installation. By contrast, it is often possible to fit a representative intake system on the engine, installed on the dynamometer. However, taking these uncertainties out of consideration, the prediction routine thus reflects the combustion and the structure excitation, whereby the structure excitation consists of the individual share of indirect and mechanical noise. Hence it is referred to as piston slap, main bearing- and valve train excitation. These particular sources were also identified as the main contributors to structure excitation as published for example in [22, 26, 27, 140, 148]. It will be demonstrated in Chapter 3 that such an approach shows good agreement with measured results when load-dependent transfer functions are used.

3.1.1 Combustion Excitation

During the mode change from SI to HCCI the combustion changes from the exactly controlled spark-ignition mode into the self-igniting homogeneous charge compres-

sion ignition mode that is mainly self-controlled by its chemical kinetics. As the character of the engine noise changes significantly, the relationship between the combustion, which can be best analysed by using the cylinder-pressure traces, and the acoustics need to be investigated. Combustion can be classified as four different types [103]:

Premixed, turbulent. Example: port fuel injected Gasoline engine, stationary gas-turbine. The premixed flame front combusts in a field of turbulent velocity. It has the advantage of generating high temperatures while generating less soot, and it can happen stoichiometric ($\lambda = 1$), rich ($\lambda < 1$) or lean ($\lambda > 1$).

Premixed, laminar. Example: Bunsen burner, gas stove. Such a combustion can be of rich-, stoichiometric-, or lean conditions. A combustion is called stoichiometric when combustible and oxidant are completely dissipated and form CO_2 and water (H_2O). A combustion is called rich when there is more combustible than oxidant. In contrast to the premixed and turbulent combustion the temperatures generated during combustion are lower.

Non-premixed, turbulent. Example: jet-engine, CI-engine, stratified direct injected gasoline engine, coal dust combustion. This type of combustion takes place in a turbulent velocity field, too. In contrast to the premixed and turbulent combustion there is no external mixture formation required that could lead to safety risks.

Non-premixed, laminar. Example: candle, log-fire. Combustible and oxidant are mixed immediately during the combustion process. Hereby a rich combustion would take place rather at the combustible, and a lean combustion would happen rather on the oxidant side.

When restricting attention to the direct injected gasoline engine, operating in SI- and HCCI mode, two different types remain: the premixed turbulent and the non-premixed turbulent combustion. It may be of interest that at the very beginning of a spark-plug initiated combustion, there is often a small laminar flame kernel, developing into a turbulent combustion with the propagation of the flame-front, as already illustrated in Chapter 2.2 .

The combustion of gasoline in internal combustion engines always requires an external initiation such as the spark plug, or certain temperature-pressure and gas

combinations, allowing then the homogeneous charge compression ignition (HCCI). A combustion is always based on a heat release (dQ/dt), consequently leading to a change of the pressure Δp of the surrounding medium, i.e. in most cases a gaseous one. If this change of pressure takes place in the audible frequency range of the human ear one can speak of combustion noise. The pressure change Δp in the combustion chamber of an internal combustion engine is generated by the compression due to the motion of the piston, Δp_v, and the pressure rise, generated by the combustion, Δp_c, thus

$$\Delta p = \Delta p_v + \Delta p_c. \tag{3.1.1}$$

According to [9] the pressure generated by the piston (upwards motion) without combustion taking place during a crank-angle interval $\Delta\alpha$ from i to j can be written as follows:

$$p_i \cdot V_i^n = p_j \cdot V_j^n, \tag{3.1.2}$$

thus

$$\Delta p_v = p_j - p_i = p_i \cdot \left[\left(\frac{V_i}{V_j} \right)^n - 1 \right]. \tag{3.1.3}$$

The variable n is the polytropic exponent which is assumed to be constant during the combustion process.

In absence of measured cylinder pressure data, the combustion pressure p_c must be calculated to gain finally the cylinder pressure. This can be done using three different general methods, which require different efforts and have different levels of complexity. The first method is the so-called *zero-dimensional*, where an ordinary differential equation is solved versus time. Such methods are the heat release model by Vibe, in combination with heat transfer models according to Woschni or Bargende [152]. The disadvantages of this method are the lack of consideration of velocity fields and engine out emissions. The second method is the so called *phenomenological*-approach. Here, ordinary differential equations are solved by using physical and chemical models for the mixture formation, ignition (for example the Arrhenius approach), heat release and emissions. It also includes heat transfer models, and the flow-field is characterized by specific numbers. For instance such a model that includes heat release and flame propagation is the *Entrainment-Model*, [152]. The third method is the *Multi-dimensional*-approach. This requires solving the various partial differential equations as a function of position and time. Based on modified physical and chemical models for the mixture formation, ignition, heat release and emissions, the Navier-Stokes-equations in the appropriate form are solved

in combination with appropriate turbulence- and wall-interaction methods. For example this could be the *Flamelet*-approach to model the turbulent flames in a SI engine. Further details can be found for example in [9, 152]. Nevertheless, it can be concluded that the change of pressure, i.e. the pressure characteristics, measured or calculated in an appropriate time- or crank-angle given resolution, can be taken to characterize the combustion noise further. Research results on the interaction of combustion characteristics and engine noise can be taken from [14, 22, 23]. Figure 3.2 shows an established approach of the relationship between the cylinder-pressure trace, its derivatives and the impact of the particular data and variables on the spectral composition of the combustion noise. Based on Figure 3.2, it can be con-

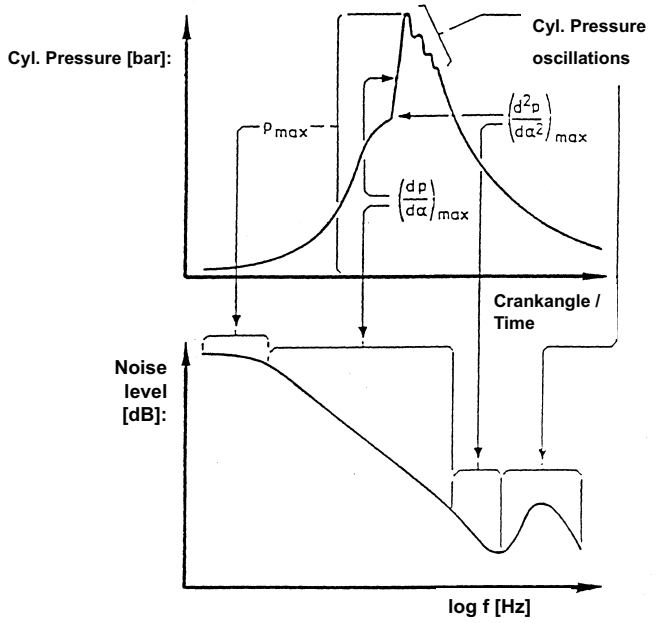

Figure 3.2: Interaction of cylinder pressure and combustion noise excitation [22]

cluded that the relationship between the cylinder pressure excitation and its noise spectrum is as follows [22, 23, 140]:

p_{max}**:** the maximum cylinder pressure has its main impact on the absolute level of the combustion noise excitation. Its frequency range is directly related to the engine order excitation. An In-Line four cylinder four-stroke engine, as it is used for the research here, delivers a 2^{nd}-engine order as main excitation order, therefore this frequency range is mainly in between 20Hz and 240Hz when assuming a cut-off speed of approximately 6500rpm.

$\frac{dp}{d\alpha}|_{max}$**:** the (maximum) pressure rise rate and its dependency on the crank angle α can be used as a measure to describe the combustion noise excitation in the frequency range between 250Hz and 5kHz. It is one of the main contributors to the combustion related engine noise that is perceived in the vehicle interior [14, 22, 140]. The human ear is relatively sensitive to this frequency range [75]. Most complaints on engine noise are referrable to an abnormal rate of pressure rise. The pressure rise rate can be expressed as a function of heat release $dQ_H/d\alpha$ according to the first law of thermodynamics:

$$\frac{dp}{d\alpha} = \left[\frac{(\gamma - 1)}{V}\frac{dQ_H}{d\alpha}\right] - \left[\gamma\frac{p}{V}\frac{dV}{d\alpha}\right]. \tag{3.1.4}$$

In equation (3.1.4) V denotes the volume of the cylinder, and γ the ratio of specific heats. It can be followed that a fast heat release governs a high pressure rise rate. Based on findings by Kalgathgi [154], the change rate of the cylinder volume $dV/d\alpha$ does not affect the pressure rise rate significantly during HCCI. A high pressure gradient, which is higher in compression-ignition (CI) engines because of a faster combustion than in SI-engines, needs to be controlled by developing certain countermeasures. On direct injection Diesel engines, for example, often special injection strategies are used to reduce and control the combustion- and resulting engine noise.

$\frac{d^2p}{d\alpha^2}|_{max}$**:** in self-ignition engines the maximum of the value of the second derivation can be considered as the start of combustion [108]. It also plays an important role in the high-frequency excitation of the combustion noise and, concerning its repeatability of position relative to the crankshaft angle, on noises that could be described as 'Clattering-Noise'. Normally, it corresponds directly to the start and speed of combustion. Moreover it is also related to the location at which 50% of the mass fraction is burned (CA50). This location is defined by the control-settings to achieve a most efficient combustion.

Pressure Oscillations: with the achievement of higher thermodynamical efficiency, the cylinder pressure oscillation plays a more and more important role on the combustion excitation. In addition they can be excited by a knocking combustion in a frequency range between 5kHz to 10kHz. They can often be referred to combustion chamber modes and are always part of a more or less visible intensity in the combustion noise excitation spectrum of a CI-engine [19, 101, 140].

In addition, the pressure gradient ($\frac{dp}{d\alpha}$) and its derivative ($\frac{d^2p}{d\alpha^2}$) have an impact on the noise characteristics of an engine. This includes also the variability of these characteristic values. Normally they correlate with the perceived roughness of the engine noise as well as with knocking or impulsive noise characteristics, known from Diesel engines [19, 22, 75, 140].
Based on Figure 3.2 the excitation spectrum of the combustion can be estimated using an approach developed by Föller in 1971 [72]. This approach is also part of the engine noise predicting tool as described in [148], then combined with transfer functions, obtained from a correlation analysis to estimate the combustion noise. Based on the exciting force in the time domain, the Föller method calculates its integral and its first to third derivation in the time domain. In addition so-called characteristic numbers are calculated, which finally form the estimated excitation spectrum. Hereby the different levels of excitation of the frequency bands are influenced by the characteristic numbers, in turn describing the slope of a linear segment at the particular frequency band in the spectrum. The frequency bands are positioned relative to the frequency by processing the minimum and maximum values of the time signal to detect the dominating frequency. However, this method has the following disadvantages to describe the combustion excitation completely:

1. Narrow band effects are not reflected because of the linear approach to the particular frequency groups. This will affect further time signal analysis of the calculated combustion noise and disregard effects as excited combustion chamber resonances as they can occur in CI-engines.

2. This method leads to a loss of the time-frequency information which is necessary to describe further acoustic effects of the combustion noise. Thus fluctuation effects caused by cylinder-to-cylinder deviation are not reflected.

Especially combustion excitation gained from CI-engines often shows an increase of narrow frequency bands above 5kHz. This can be referred to the first circumferential combustion chamber eigenfrequency [14, 19]. The different frequencies of the combustion chamber modes can be calculated when solving (3.1.5), [22, 106, 156]. The indices m and n represent the number of the circumferential (m) and radial (n) mode:

$$f_{mn} = c_o \sqrt{\frac{T(\alpha)}{273^o K}} \cdot \frac{\beta_{mn}}{d} \tag{3.1.5}$$

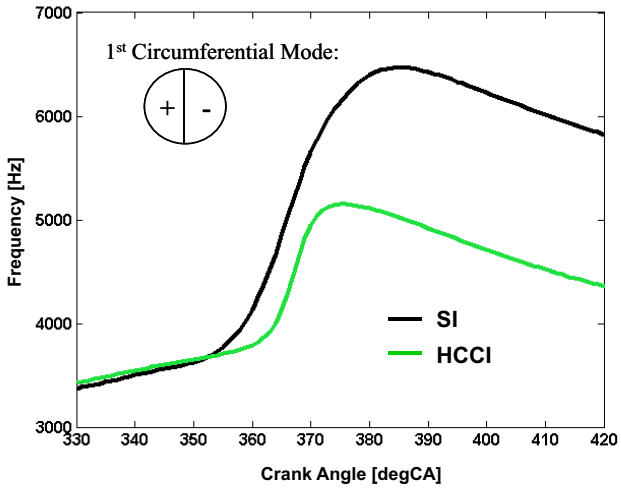

Figure 3.3: Difference of the first circumferential combustion chamber mode frequency around combustion TDC - SI vs. HCCI mode

Hereby the combustion chamber temperature around combustion TDC can be calculated with:

$$T(\alpha) = \frac{p_{cyl}(\alpha) \cdot V(\alpha) \cdot T_0}{p_0 \cdot V_0} \tag{3.1.6}$$

Hence an analysis was carried out comparing the SI- versus HCCI mode. The first circumferential eigenfrequency was estimated during the combustion phase according to equation (3.1.5). This requires the indices m=*1*, n=*0*, and taking β_{10}=0.5861, derived from the roots of the first derivative of the Bessel-function and available via tables as in [66], and c_0 reflecting the sound propagation velocity at 273°K. The results are shown in Figure 3.3 during combustion TDC. During HCCI the entire homogeneously distributed charge, or so-called chemical reaction zones, react at the same time. This infers a faster heat release than generated by SI combustion. Thus, the local temperatures are significantly lower than at a flame front occurring in a SI engine [153]. Hence, as expected, the SI-mode (black line) has higher combustion temperatures and thus leads to about 40% higher frequencies than the HCCI combustion mode at same BMEP and speed. Furthermore it can be inferred from this analysis that the resonance frequency follows the decreasing temperature profile during the combustion stroke as it is also published in [17]. Because of the existence of this mode in Diesel engines Okamura concluded that such an inhomogeneous distribution of the cylinder pressure during the combustion can also lead to an inhomogeneous distribution of the gas force in the combustion chamber, which in turn

then provokes a tilt motion of the piston around its pin [19], finally leading to an increased noise level, caused by piston slap. However, this assumption requires that such modes are taking place with the node line preferably along the piston pin to provoke such reactions. In reality the orientation of this effects takes place randomly orientated in the combustion chamber. This means when detecting a resonance it need not necessarily lead to an incident of piston slap caused by such an excitation.

3.1.2 Forces in the Cranktrain

Besides the combustion excitation as the source the subsequent dynamic loads on the moving parts do have a major impact on the indirect combustion noise excitation and as well as on the mechanical noise. As they are difficult to measure exactly, a simple calculation model was developed as the basis for the prediction model. Hereby the individual forces and torques in an internal combustion engine can be calculated for example as shown in many publications such as [107, 122, 131, 133, 160, 168], assuming an ideal engine with the absence of non-linear effects at piston and liner or conrod, crankshaft and bearings. However, other effects such as lashes and frequency response characteristics of the parts in the power conversion system also play an important role when analysing the dynamic forces in the frequency domain, as will be discussed later in this chapter. Figure 3.4 illustrates a power conversion system, containing the forces considered in the course of this work, acting on piston and conrod. In the following the equations to calculate the relevant forces are written accordingly, while the individual variables are denoted according to Figure 3.4.

Gas Force $F_{Gas}(t)$: acts directly onto the pistons surface, and is initiated by the cylinder pressure, in turn aroused by compression and the superimposed combustion, finally represented as $p(t)$

$$F_{Gas}(t) = p(t) \cdot A_P, \tag{3.1.7}$$

with $p(t)$ denoting the cylinder pressure, and A_P representing the piston surface, id est $A_P = \pi \cdot r^2_{Piston}$.

Mass Force $F_{Mass}(t)$: the mass force $F_{Mass}(t)$ acts opposite to the gas force, and it is evoked by the oscillating mass m_{OP} formed by the piston m_P, the piston-ring packet m_{PR}, the pin m_{PIN} and the contributing mass of the connecting rod m_{CRO} due to the rotation of the cranktrain. The mass m_{CRO} is defined by

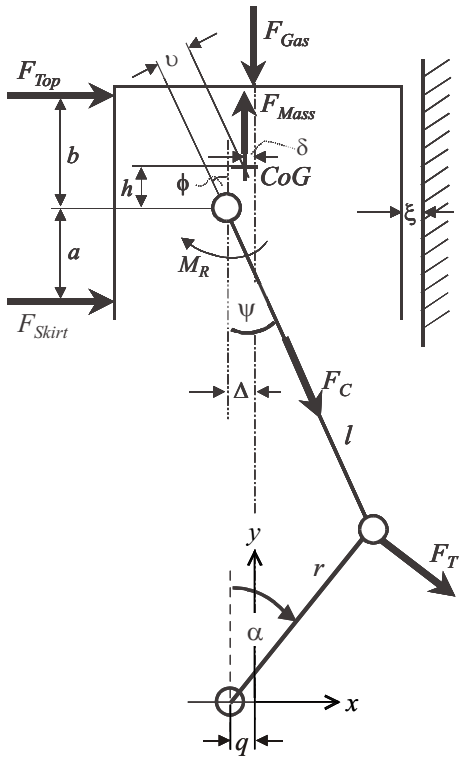

Figure 3.4: Forces and geometric dependencies on piston and connecting rod

$m_{CRO} = m_{CR} \cdot l_{CoG}/l$, with m_{CR} denoting the total mass of the connecting rod, l the length of the connecting rod, and l_{CoG} represents the distance between the axis of the pin and the centre of gravity of the connecting rod. Thus, it can be written $m_{OP} = m_P + m_{PR} + m_{PIN} + m_{CRO}$, and for the mass force caused by the corresponding acceleration $\ddot{y}(t)$ in general:

$$F_{Mass}(t) = m_{OP} \cdot \ddot{y}. \tag{3.1.8}$$

To calculate the acceleration $\ddot{y}$, at first the displacement y of the piston according the geometric dependencies in Figure 3.4 can be derived:

$$y(t) = r \cdot \cos\alpha + l \cdot \cos\psi. \tag{3.1.9}$$

In addition it can be derived from Figure 3.4:

$$r \cdot \sin\alpha = l \cdot \sin\psi + q. \tag{3.1.10}$$

Note that the eccentricity Δ between pin and central axis can be omitted as typical values in automotive engines are less than $1mm$, and the resulting error

can be considered as negligible [133, 168]. Introducing the ratio of crank-radius r and the length l of the connecting rod as $\lambda = r/l$ equation (3.1.9) can be written in the form

$$\frac{y}{r} = \cos\alpha + \frac{1}{\lambda} \cdot \cos\psi. \tag{3.1.11}$$

Introducing λ and $\kappa = q/l$ as the ratio of crankshaft offset and length of the connecting rod in equation (3.1.10), and furthermore, subtracting κ from the right side of the equation this yields:

$$\lambda \cdot \sin\alpha - \kappa = \sin\psi. \tag{3.1.12}$$

By definition it is $\cos^2\psi = 1 - \sin^2\psi$. Hence, it is then considering equations (3.1.12) and (3.1.11):

$$y = r \cdot \left[\cos\alpha + \frac{1}{\lambda} \cdot \sqrt{1 - (\lambda\sin\alpha - \kappa)^2}\right]. \tag{3.1.13}$$

This equation is rather difficult to differentiate. Thus, the root (while also considering the term $1/\lambda$ of equation (3.1.13)) can be expanded into a progression using the following expression [66]:

$$\frac{1}{\lambda} \cdot \sqrt{1-s} = \frac{1}{\lambda} - \frac{s}{2\lambda} - \frac{s^2}{8\lambda} - \dots \tag{3.1.14}$$

with $s = (\lambda\sin\alpha - \kappa)^2$. Most engines have a ratio of the crank-radius and length of the connecting rod, λ, in the range of $1/5 \leq \lambda \leq 1/3$, [122, 133, 168]. Followed by this, all λ^n with $n \geq 3$ can be omitted as this would not affect the result significantly [133]. This can be also stated for κ^n for $n > 1$, since (for example) $\kappa = 0.054$ on the engine investigated here. Hence this yields $s = \lambda^2\sin^2\alpha - 2\kappa\lambda\sin\alpha + \kappa^2$ and $s^2 \approx 0$. Furthermore, the individual terms containing $\sin^n$ can be written in the form $\sin^2 = 1/2 \cdot (1 - \cos 2\alpha)$ and $\sin^4 = 1/8 \cdot (3 - 4\cos 2\alpha + \cos 4\alpha)$, [66]. Inputting the individual equations into the expression for s, one can obtain

$$s = \frac{\lambda^2}{2} \cdot (1 - \cos 2\alpha) - 2\kappa\lambda\sin\alpha + \kappa^2. \tag{3.1.15}$$

With $\kappa^2 \approx 0$ and the consideration of equation (3.1.14) this gives

$$\frac{1}{\lambda} \cdot \sqrt{1-s} = \frac{1}{\lambda} \cdot \sqrt{1 - (\lambda\sin\alpha - \kappa)^2} = \frac{1}{\lambda} - \frac{\lambda}{4}(1 - \cos 2\alpha) - \kappa\sin\alpha. \tag{3.1.16}$$

Inputting equation (3.1.16) into (3.1.13) this delivers then for the displacement y:

$$y = r \cdot \left[\cos\alpha + \frac{1}{\lambda} - \frac{\lambda}{4} + \frac{\lambda}{4} \cdot \cos 2\alpha - \kappa \sin\alpha \right]. \tag{3.1.17}$$

The velocity $\dot{y}$ can be now obtained by $\dot{y} = \frac{dy}{d\alpha}\frac{d\alpha}{dt}$ with $\omega = \frac{d\alpha}{dt}$, thus:

$$\dot{y} = -r \cdot \omega \left(\sin\alpha + \frac{\lambda}{2} \sin 2\alpha + \kappa \cos\alpha \right). \tag{3.1.18}$$

The acceleration $\ddot{y}$ can be obtained similarly by $\ddot{y} = \frac{d\dot{y}}{d\alpha}\frac{d\alpha}{dt}$ with $\omega = \frac{d\alpha}{dt}$, thus:

$$\ddot{y} = -r \cdot \omega^2 \left(\cos\alpha + \lambda \cdot \cos 2\alpha + \kappa \cdot \sin\alpha \right). \tag{3.1.19}$$

Finally combining equations (3.1.8) and (3.1.19) this yields for the mass force F_{Mass}:

$$F_{Mass}(t) = m_{OP} \cdot r \cdot \omega^2 \cdot \left(\cos\alpha + \kappa \cdot \sin\alpha + \lambda \cdot \cos 2\alpha \right). \tag{3.1.20}$$

Resulting piston force $F_K(t)$: this force consists of the gas force $F_{Gas}(t)$ and the mass force $F_{Mass}(t)$, acting opposite to the gas force. Thus $F_K(t)$ is defined as:

$$F_K(t) = F_{Gas}(t) - F_{Mass}(t) \tag{3.1.21}$$

Considering the oscillating mass of the piston, m_{OP}, consisting of the mass of the piston, the pin and mass of the connecting rod, oscillating along the liner axis, the equation to calculate $F_K(t)$ can be re-written:

$$F_K(t) = p(t) \cdot A_P - m_{OP} \cdot r \cdot \omega^2 \cdot \left(\cos\alpha + \kappa \cdot \sin\alpha + \lambda \cdot \cos 2\alpha \right) \tag{3.1.22}$$

In addition, the angular velocity can be expressed as $\omega = 2\pi \cdot n$.

Force in the connecting rod, $F_C(t)$: taking into account the resulting piston force, one can write:

$$F_C(t) = \frac{F_K(t)}{\cos\psi}. \tag{3.1.23}$$

However, it is more convenient to replace the tilt angle of the connecting rod. Furthermore, it is then for $q = \Delta = 0$:

$$\sin\psi = \lambda \cdot \sin\alpha. \tag{3.1.24}$$

In addition it is:

$$\cos^2\psi = 1 - \sin^2\psi, \tag{3.1.25}$$

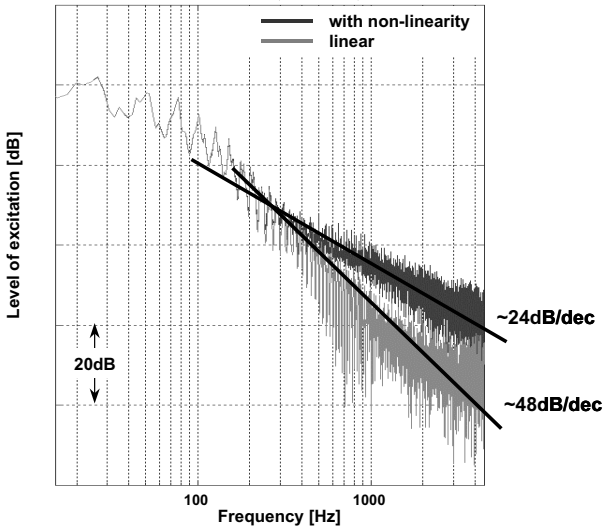

Figure 3.5: Impact of non-linearities on the slope of the excitation spectrum (spectra obtained from simulation results of a piston secondary movement analysis (piston guiding forces) by the author)

thus while considering (3.1.24) and (3.1.25):

$$\cos\psi = \sqrt{1 - \lambda^2 \cdot \sin^2\alpha}. \tag{3.1.26}$$

This yields then:

$$F_C(t) = \frac{F_K(t)}{\sqrt{1 - \lambda^2 \cdot \sin^2\alpha}}. \tag{3.1.27}$$

Tangential Force $F_T(t)$: the tangential force acts perpendicular to the radial force, and is defined as follows:

$$F_T(t) = F_K(t) \cdot \sin\alpha \cdot \left[1 + \frac{\lambda \cdot \cos\alpha}{\sqrt{1 - \lambda^2 \cdot \sin^2\alpha}}\right]. \tag{3.1.28}$$

Impact of non-linear forces in the cranktrain

The usage of linear models as shown in the previous section for calculating the excitation in an internal combustion engine has the deficiency of not achieving a good correlation above 300Hz between predicted and measured vibration values. This is caused by the dynamic loads, caused in the individual lashes and contacts between the parts involved. In turn such contact forces resulting from this can excite higher eigenfrequencies of the structure [15, 22, 141]. The impact of such forces on the excitation spectrum compared to a normal approach is shown in Figure 3.5. For

example a comparison of the force spectra of the piston side force with and without considering the piston slap shows that the excitation spectrum of the conventional solution decreases constantly at $\approx 48dB/decade$. In contrast the spectrum of the force including slap shows a change in slope at about 300Hz from $\approx 48dB/decade$ to $\approx 24dB/decade$. The relationship of the factor of two between the slope of both spectra correlates well with the theory, presented in [22] and confirmed by the experimental results achieved by Priede [140] and DeJong [15]. Both also show the same relationship of high frequency increase when comparing the force spectra of the conventional approach with the non-linear, reflecting also lashes and contacts. Thus to achieve a better quality of the model for load-prediction, the major non-linear effects on the dynamic loads should be incorporated. Based on research done so far [14, 22, 38, 47, 48, 117, 141], these are the piston slap, the dynamic response of sub-components of the power conversion system, and the dynamic loads on the crank-bearings. However, theses forces can also be calculated using software tools as presented for instance in [38, 164] to study all effects in detail using coupled FEM-Multi-Body-System (MBS) analysis approaches. For instance using such an approach the piston slap induced noise can be predicted with a very good accuracy once the bore-distortion of the cylinder-liner is known[1]. But the engine noise prediction model should consider the most important mechanical effects and should thus reflect only the relevant non-linearities, such as for instance the contact conditions or the clearance between individual parts of the excited engine structure. Furthermore it is mandatory that the model processes the data in a low computing time to accompany for example the combustion- or control-system development work efficiently. Therefore these models have to be as simple as possible, but precise enough to be in line with later test results.

3.1.3 Piston Induced Noise by Secondary Movement

The travel of the piston due to its clearance in the cylinder-liner in lateral direction, often combined with a tilt around its pin, is called 'secondary movement'. This movement is caused by the lateral component of the force along the connecting rod. If this force changes its direction, the piston changes its direction of lateral movement, too. The height and direction of this force depends on the actual position

[1] Meanwhile the expensive experimental iterations to achieve a piston slap free engine are mostly replaced by analytical studies, showing high correlation to the reality [verbal communication with Dr M. Voigt, Kolbenschmidt-Pierburg AG, June 2006].

of the connecting rod and the forces acting perpendicular to the axis of the liner at the center of gravity of the piston. These forces, also known as 'piston guiding forces', can again be separated into gas- and mass-forces, either caused by the combustion or by the moving masses. In addition, the forces caused by the combustion, the oscillating masses and the contact forces caused by the lubrication of the piston can influence the secondary movement, too. The particular forces with the focus on the contact force will be studied in more detail in the next few paragraphs.

If a secondary movement of the piston takes place rapidly, the piston hits the liner, leading to a clattering sound of the engine. This effect is known as 'piston slap'. The issue of piston slap has received an increased attention ever since the introduction of light-weight pistons [129], mainly caused by the combination of two materials with different expansion coefficient of the material. Meanwhile different theories are available to model the secondary motion of the piston [124, 163] while considering a different amount of boundary conditions, including thermal expansion of the liner [38] or detailed tribological boundaries [42]. But to ensure an acceptable run-time of the evaluation, the piston slap model was mainly based on results presented by Meier [124, 127] and also verified by Prescher [125] to calculate the secondary movement of the piston, caused by the forces acting on the piston. A similar approach has been employed during a study of the influence of the skirt profile on the secondary movement by Jang [142]. Such a type of model allows prediction of the influence of the piston-to-pin offset and also considers the tilt angle of the piston in the liner.

According to Meier [127] the forces acting on the piston can be calculated under the assumption of a statical analysis referring to Figure 3.4 when the piston is on contact with the cylinder-liner. Thus, the forces acting on the piston skirt F_{Skirt} and top-land, F_{Top} can be calculated while balancing the torque around the center of gravity of the piston, also considering the static frictional torque between piston and pin, M_R:

$$F_{Skirt} = \frac{-F_C \cdot [\nu - (a+h) \cdot \sin\psi] - F_{Gas} \cdot \delta - M_R}{a+b}, \tag{3.1.29}$$

and

$$F_{Top} = \frac{F_C \cdot [\nu + (b-h) \cdot \sin\psi] + F_{Gas} \cdot \delta + M_R}{a+b}. \tag{3.1.30}$$

Applying equations (3.1.29) and (3.1.30), the forces acting on both skirt and top-land can be calculated. The gradient of both forces is comparatively depicted in

Figure 3.6. It can be inferred that both forces are changing from positive to negative values, thus enforcing a lateral movement of the piston. Moreover, because of the eccentricity Δ according to Figure 3.4 of the piston pin relative to its centre of gravity, the lateral movement of the piston takes place in two different phases: firstly the skirt changes from the liner's thrust side to the anti-thrust side, then followed by the top-land. This reduces the impact-force and thus the piston slap noise when the piston contacts the liner by splitting a single impact event into two events with lower impact energy [127, 125]. Figure 3.7 shows the travel and the corresponding tilt-angle of the piston for a complete engine cycle. In addition an example that illustrates the movement of the piston in the liner over crank-angle is depicted in the same Figure 3.7, right half.

The movement of the piston of the mass m between thrust and anti-thrust-side of the cylinder-liner enforced by F_{Skirt} and F_{Top} can be calculated considering Newton's second law:

$$\ddot{s}_{Skirt}(t) = \frac{F_{Skirt}(t)}{m_{Skirt}}, \tag{3.1.31}$$

and

$$\ddot{s}_{Top}(t) = \frac{F_{Top}(t)}{m_{Top}}. \tag{3.1.32}$$

The effective masses for the top and the skirt can be calculated corresponding to Figure 3.4 by $m_{Skirt} = m \cdot a/(a+b)$ and similarly for $m_{Top} = m \cdot b/(a+b)$. However, when the piston reaches the limit of its clearance ξ, for both contact points the following case branches are valid:

$$s(t) = \begin{cases} \xi \cdot sign(s) & \text{for } abs(s(t)) \geq \xi \\ \\ \int \dot{s}(t)dt & \text{for } abs(s(t)) < \xi \end{cases} \tag{3.1.33}$$

$$\dot{s}(t) = \begin{cases} \epsilon \cdot \dot{s}(t - \Delta t) & \text{for } abs(s(t)) \geq \xi \\ \\ \int \ddot{s}(t)dt & \text{for } abs(s(t)) < \xi \end{cases} \tag{3.1.34}$$

The variable ϵ in (3.1.34) denotes the impact value, describing the ratio of velocity of the mass m, i.e. the piston, before and after the impact. This is to reflect the exchange of kinetic energy between the two bodies involved in the impact. According

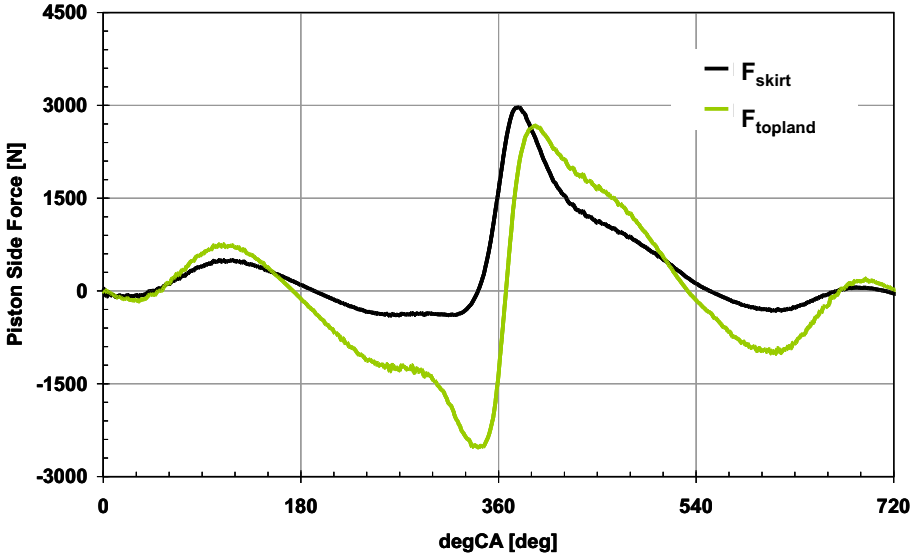

Figure 3.6: Lateral forces acting on the piston with an eccentricity (according to Figure 3.4: $\Delta - \delta$) of the pin relative to the piston's centre of gravity. Note also that the clearance ξ between piston and liner is not yet considered here

to Knoll for the impact number $\epsilon = 0.2$ was chosen [42]. Based on the kinematics resulting from equation (3.1.33) and the schematics illustrated in Figure 3.4, the corresponding tilt angle ϕ of the piston relative to the liner can be calculated

$$\phi(t) = \arctan\left(\frac{s_{Top}(t) - s_{Skirt}(t)}{a+b}\right), \tag{3.1.35}$$

with the boundary condition

$$\phi \leq \phi_{max} = \arctan\left(\frac{\xi}{a+b}\right). \tag{3.1.36}$$

Figure 3.7 shows the kinematic of the piston including the tilt angle of the piston for an interval of $720deg$ crank angle (single cylinder, one complete engine cycle), calculated during SI operation at 2000rpm, 2bar BMEP. The upper border reflects the thrust side.

To consider the tribological boundaries of the piston in the liner and hence modelling the contact forces acting on the piston, it may be useful to separate the particular forces into the different states of piston movement during operation [42]. Figure 3.8 shows the schematics of the particular developed models of piston-motion, representing three different states of motion. In the following the lubrication based forces on the piston occurring during these particular states, will be derived.

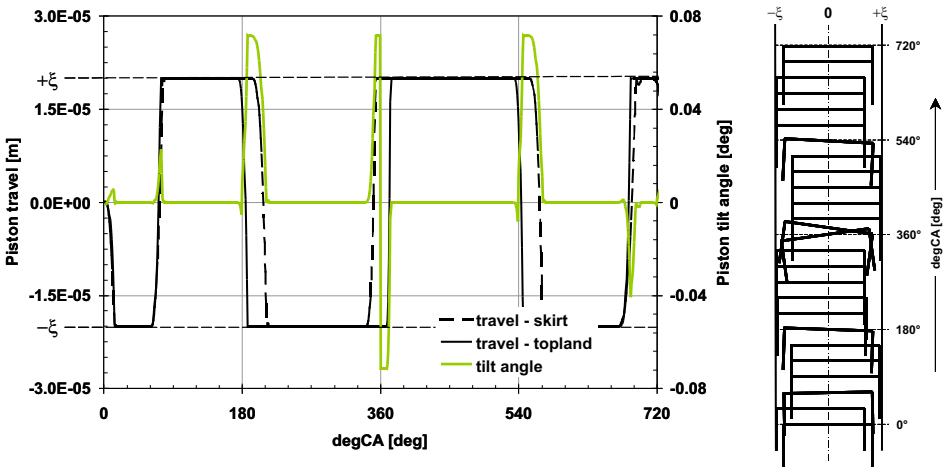

Figure 3.7: Travel of top-land and skirt of the piston, including according tilt angle. Please note the different duration of contacting time between piston and thrust (positive boundary, $+\xi$) and anti-thrust side ($-\xi$). Around $360deg$ crank-angle the kinematics are dominated by the gas-force excitation (combustion). Note also the corresponding trajectory of the piston in the liner, illustrated in the right half

In conjunction with the cylinder liner the skirt of the piston results in a hydrodynamic lubrication regime that can be considered as similar as a journal bearing. Thus, the particular states of lubrication can be described with the equation of Reynolds (3.1.37), while using the appropriate boundary conditions for each of the three particular states.

$$\frac{\partial}{\partial x}\left(\frac{h^3}{\eta}\frac{\partial p}{\partial x}\right)+\frac{\partial}{\partial y}\left(\frac{h^3}{\eta}\frac{\partial p}{\partial y}\right)=6\ \dot{y}_{piston}\ \frac{\partial h}{\partial y}+12\frac{\partial h}{\partial t} \tag{3.1.37}$$

The particular states of motion will be discussed in the following paragraphs.

Vertical movement, parallel/convergent to the liner

If the piston moves in the vertical direction either a parallel gap between piston and liner can occur, or a divergent or convergent gap can happen. But hydrodynamic forces can only be generated by the oil film, when there is a converging gap accompanied by a vertical piston movement in the same direction as illustrated in Figure 3.8(a). This leads to the following condition:

$$\frac{\partial h}{\partial y}\cdot abs\left(sign\left(\dot{y}_{piston}\right)\right)>0 \tag{3.1.38}$$

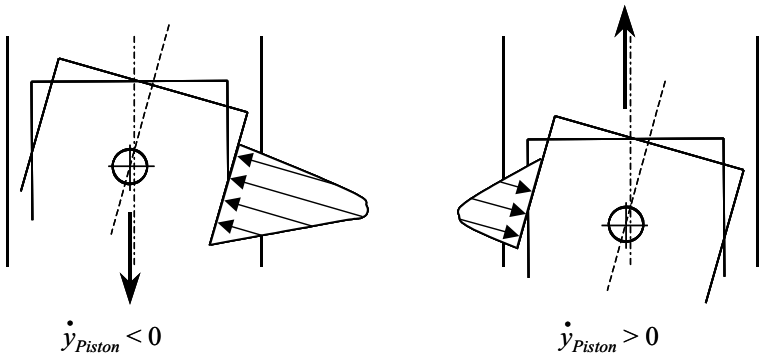

(a) Schematics of hydrodynamic forces, caused by vertical movement of the piston

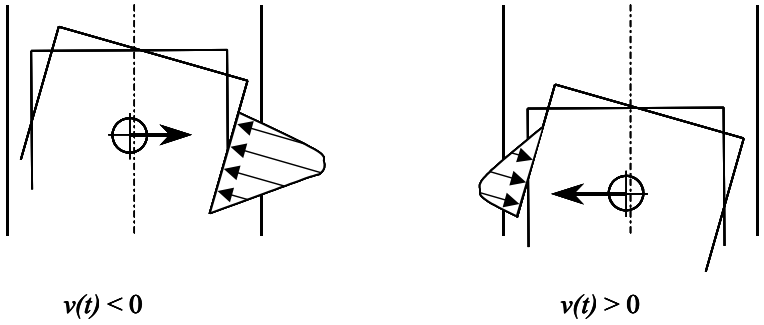

(b) Schematics of hydrodynamic forces (squeeze), caused by lateral movement of the piston

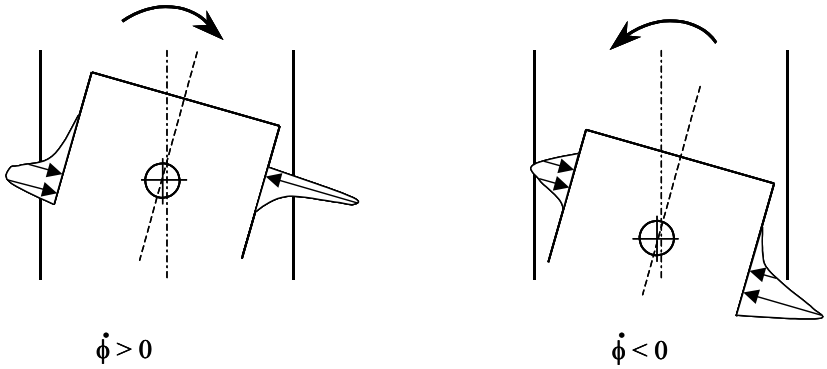

(c) Schematics of hydrodynamic forces, caused by tilt-motion of the piston

Figure 3.8: Schematics of the considered forces on the piston, caused by lubrication during the three different states of motion

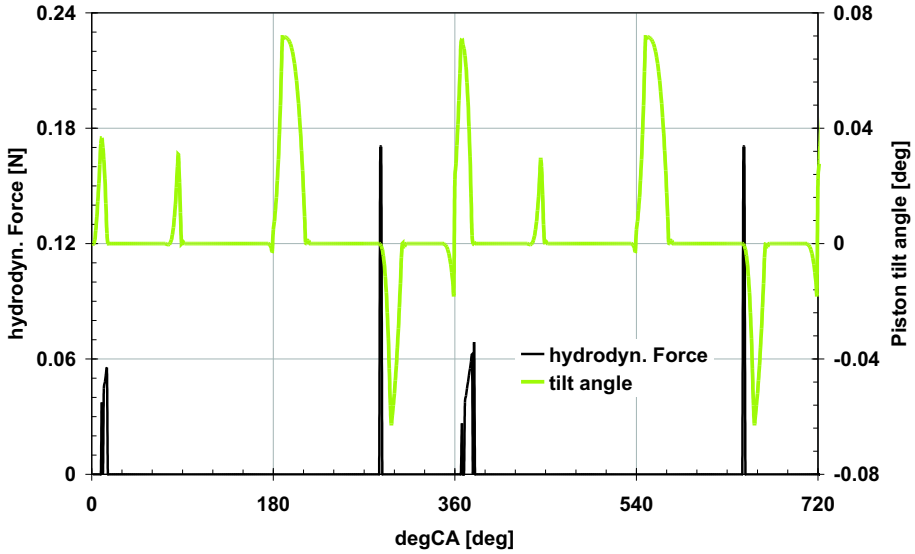

Figure 3.9: F_{Hydr} calculated according equation (3.1.39) and related piston tilt angle during motored condition

Assuming a linear, convergent gap of either the length $L = a$ or $L = b$ of the piston (ref. Figure 3.4), and owning the minimum height $x_0(t) = s_0(t)$ and the maximum height $x_1(t) = s_1(t)$, the resulting hydrodynamic force $F_{Hydr}(t)$, acting in the opposite direction as the gas- and mass-related forces, can be written according to [40]:

$$F_{Hydr}(t) = \frac{6\eta\dot{y}_{piston}L^2B}{(s_1(t) - s_0(t))^2}\left(ln\frac{s_1(t)}{s_0(t)} - 2\frac{s_1(t) - s_0(t)}{s_1(t) + s_0(t)}\right) \tag{3.1.39}$$

Thus, if it is in equation 3.1.39 $s_0(t) = s_1(t)$, i.e. no convergent gap, the resulting hydrodynamic force will disappear. The acting width 'L', or respectively the corresponding arc 'ζ' of the contact is calculated based on the equation for the contact-zone of a conforming pin in a hole according to Johnson [155], considering rigid parts:

$$\zeta = 2 \cdot \arccos\left(\frac{\xi_o}{\xi}\right) \tag{3.1.40}$$

In equation 3.1.40 the variable ξ represents the actual position of the piston inside its absolute lash relative to the liner, labeled ξ_o. The length 'B' of the wedge can be either assumed to be a, b or $a + b$ from Figure 3.4. The following Figure 3.9 shows F_{Hydr} at 2000rpm, 2bar BMEP, SI operation.

Lateral movement, parallel to the liner and piston tilt around the pin

When the piston moves laterally, the gap between piston and liner varies with the time. This is illustrated in Figure 3.8(b). Hence the right side of (3.1.37) can be reduced to the so called 'squeeze term' $12\frac{\partial h}{\partial t}$:

$$\frac{\partial}{\partial x}\left(\frac{h^3}{\eta}\frac{\partial p}{\partial x}\right)+\frac{\partial}{\partial y}\left(\frac{h^3}{\eta}\frac{\partial p}{\partial y}\right)=12\frac{\partial h}{\partial t}. \tag{3.1.41}$$

Combining (3.1.41) with (3.1.34) this yields (3.1.42):

$$\frac{\partial}{\partial x}\left(\frac{h^3}{\eta}\frac{\partial p}{\partial x}\right)+\frac{\partial}{\partial y}\left(\frac{h^3}{\eta}\frac{\partial p}{\partial y}\right)=12\cdot v(t). \tag{3.1.42}$$

An oil-film pressure can be generated only when the piston moves towards the liner. This leads to the following condition (3.1.43):

$$12\cdot sign\left(v(t)\right)>0. \tag{3.1.43}$$

When putting (3.1.43) into (3.1.42) one can write (3.1.44):

$$\frac{\partial}{\partial x}\left(\frac{h^3}{\eta}\frac{\partial p}{\partial x}\right)+\frac{\partial}{\partial y}\left(\frac{h^3}{\eta}\frac{\partial p}{\partial y}\right)=12\cdot v(t)\cdot sign\left(v(t)\right). \tag{3.1.44}$$

In general the force, caused by squeezing the oil-film in a parallel gap of a cylindrical contact can be calculated based on equation (3.1.44) according to Lang or Affenzeller [40, 160] :

$$F_{Squeeze}(t)=\frac{So_V\cdot B\cdot d_{Piston}\cdot\eta\cdot v(t)}{\psi^2} \tag{3.1.45}$$

In equation (3.1.45) B denotes the contacting length between piston and liner, thus $B=a+b$ referring to Figure 3.4. The variable ψ represents the relative bearing clearance, calculated by:

$$\psi=\frac{D_{Bore}-d_{Piston}}{d_{Piston}} \tag{3.1.46}$$

The variable So_V is called 'Sommerfeld-Number', with the index 'V' representing the squeeze effect. This number can either be taken from tables, where So_V is listed as a function of the eccentricity or the relation of width to diameter of the bearing. In contrast to that Butenschön has developed a formula, based on iteration to calculate So_V [40, 160]:

$$\begin{aligned}So_V=4\left(\frac{(a+b)}{d_{Piston}}\right)\left(1-\varepsilon^2\right)^{-\frac{5}{2}}\Big[\left(\frac{\pi}{2}-\frac{1}{2}\arccos\varepsilon\right)\\ \cdot\left(1+2\varepsilon^2\right)+\frac{3}{2}\varepsilon\sqrt{1-\varepsilon^2}\Big]\cdot\frac{a_8(1-\varepsilon)}{-a_9-\varepsilon}\end{aligned} \tag{3.1.47}$$

The variables a_8 and a_9 can be calculated using:

$$a_8 = 0.70038 + 3.2415\left(\frac{(a+b)}{d_{Piston}}\right) - 12.2486\left(\frac{(a+b)}{d_{Piston}}\right)^2 + 18.895\left(\frac{(a+b)}{d_{Piston}}\right)^3 - 9.3561\left(\frac{(a+b)}{d_{Piston}}\right)^4 \tag{3.1.48}$$

and

$$a_9 = -0.999935 + 0.0157434\left(\frac{(a+b)}{d_{Piston}}\right) - 0.74224\left(\frac{(a+b)}{d_{Piston}}\right)^2 + 0.42278\left(\frac{(a+b)}{d_{Piston}}\right)^3 - 0.368928\left(\frac{(a+b)}{d_{Piston}}\right)^4 \tag{3.1.49}$$

The variable ε in (3.1.47) is called 'relative eccentricity' and is defined as follows:

$$\varepsilon(t) = \frac{2 \cdot s(t)}{D_{Liner} - d_{Piston}} \tag{3.1.50}$$

If $\varepsilon = 0$, the piston is concentric with the liner. In contrast to that $\varepsilon = 1$ means a contact of piston and liner. Equation (3.1.50) shows also that the relative eccentricity is a function of time as the eccentricity of the piston in the liner varies with the time, and thus the actual width of the gap. Hence So_V can be generally written (3.1.51):

$$So_V(t) = f\left(\varepsilon(t), \frac{(a+b)}{d_{Piston}}\right) \tag{3.1.51}$$

The squeeze film force according to equation (3.1.51) is depicted in Figure 3.10 during a complete engine cycle in SI-mode operation at 2000rpm, 2bar BMEP. The application of the classical Sommerfeld approach (So_V) will lead to very high contact-, i.e. squeeze-film, forces, as depicted in Figure 3.10. In contrast, the linear calculated maximum piston side force for the operational state considered here would be in the range of $2300N$, as will also be demonstrated later. Also, when comparing these values with measured data, as for example gained by Knoll and Pischinger in [42], the contact forces should be in the range of $1000N$ to $2000N$ for such an engine in part-load or motored condition. This investigation by Knoll and Pischinger revealed that the application of the lubrication theory of Reynolds in the absence of adhesive forces caused by roughness of the contacting surfaces shows a good correlation with measurements. Moreover, when investigating the oil-film behaviour in the diverging gap of a journal bearing Floberg revealed that the oil-film in this section diverges into several streamlines, characterized by the surface tension of the oil itself [161].

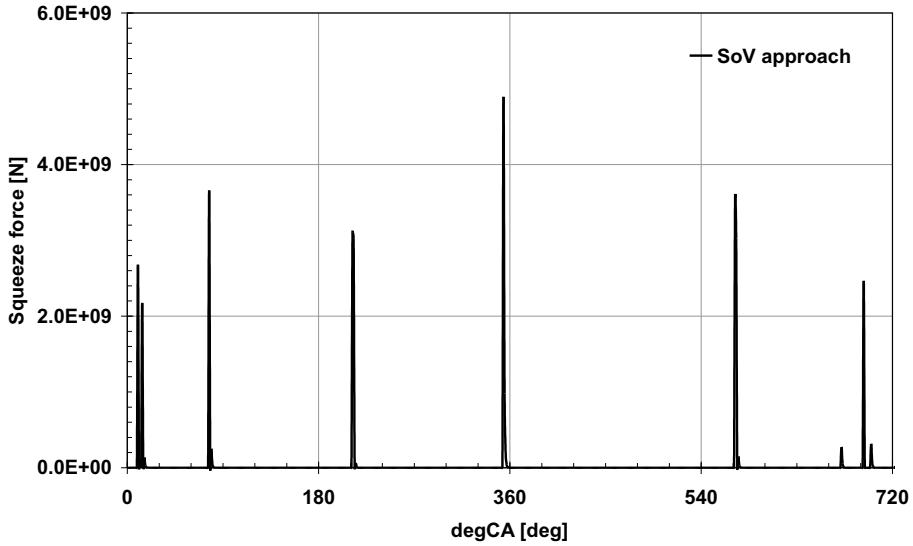

Figure 3.10: Squeeze film forces between piston and liner, using the So_V approach with a rectangular contact pattern. The maximum peak around $360deg$ crank angle is caused by the reaction on the combustion force excitation

This confirmed that the oil cannot sustain suction, if the oil-film fulfills its task to separate the surfaces from each other to minimize friction and fretting. To avoid exaggerated squeeze-film reaction forces by using a rigid piston-liner contact model as shown in Figure 3.11(a) as a boundary for equation (3.1.47), an adaption of the contacting surface should be considered: when looking at the real geometry shape of a piston in a thermal loaded cylinder-liner, Figure 3.11 may illustrate the situation, comparing an ideal rigid and parallel contact (Figure 3.11(a)) with a condition, effected by assuming an elastic, oval piston (along its height) and a thermal loaded cylinder liner (Figure 3.11(b)). This geometry of contact zones can be derived from measurement results, as they were published among others by Knoll, Künzel or Wang [42, 46, 43, 143]. Beside the fact that a real piston shape relative to the liner is oval instead of being ideal-parallel there is mostly a tilt motion superimposed to the lateral movement with the velocity $v_\xi(t)$ of the piston. Thus, in the following the applicability of an hybrid-hydrodynamic contact model, based on the contact zone area of Figure 3.11(b) will be investigated. This model is based on Reynold's theory, too. Hereby the impact forces between piston and liner are gained by reflecting the boundaries according to Figure 3.11(b), without consideration of the thermal deflection of the cylinder-liner. This approach was published by Gerges et al. [162],

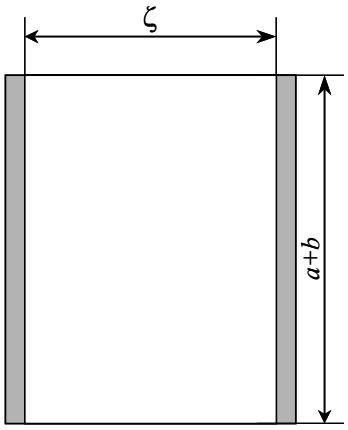

(a) Contact zone model of a rigid piston in a rigid cylinder liner

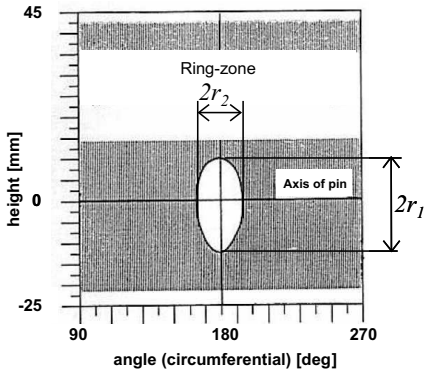

(b) Contact zone model of an oval piston in a cylinder liner; contact pattern taken from measurements by Künzel [43]

Figure 3.11: Side view on different ideal contact-zones (white area) for a piston in a cylinder liner

and supports the intention of a fast data processing.

A tilt motion of the piston around its pin as shown in Figure 3.8(c) leads to similar impact forces as shown in Figure 3.8(b). According to Gerges et al. [162] the impact force F_{Impact}, respectively $F_{Impact-Skirt}$ and $F_{Impact-Top}$, can be calculated using the case branch:

$$F_{Impact-Top/Skirt}(t) = \begin{cases} \frac{\eta \cdot v_\xi(t)}{h^3} \cdot f_{Reynolds} & \text{for } abs(s(t)) \geq \xi \\ \\ 0 & \text{for } abs(s(t)) < \xi \end{cases} \tag{3.1.52}$$

The factor $f_{Reynolds}$ is derived from the Reynolds equation for hydrodynamic lubrication with special respect to the squeeze film term [162]. In [162] this factor reflects the boundaries of a concentric contact. However, it has been revealed that the contact between piston and cylinder-liner is rather of an elliptical than of a concentric shape [43, 143]. Thus a refined contact force will be derived, and the factor $f_{Reynolds}$ is subsequently re-written.

For an elliptical contact pattern according to Figure 3.11, assuming that only a

squeeze of the oil film takes place, the Reynolds equation can be reduced to:

$$\frac{\partial^2 p}{\partial y^2} + \frac{\partial^2 p}{\partial z^2} = -12\eta \frac{dh}{dt} \cdot \frac{1}{h^3} \tag{3.1.53}$$

Introducing $\frac{dh}{dt} = v_\xi(t)$ for the lateral piston velocity and $h = x(t)$ representing the actual lateral position of the piston, and also taking the definition of an ellipsis into account with the two axes radii r_1 and r_2 in the coordinates as already illustrated in Figure 3.4 and 3.11(b), this will lead to:

$$\frac{y^2}{r_1^2} + \frac{z^2}{r_2^2} - 1 = 0 \tag{3.1.54}$$

Moreover, the pressure distribution over the ellipsis gains a function as follows:

$$p(y,z) = C\left(\frac{y^2}{r_1^2} + \frac{z^2}{r_2^2} - 1\right) \tag{3.1.55}$$

Calculating the partial derivations for each coordinate, this yields for the first derivative

$$\frac{\partial p}{\partial y} = C\frac{2y}{r_1^2} \qquad \textit{and} \qquad \frac{\partial p}{\partial z} = C\frac{2y}{r_2^2} \quad , \tag{3.1.56}$$

and for the second derivation:

$$\frac{\partial^2 p}{\partial y^2} = C\frac{2}{r_1^2} \qquad \textit{and} \qquad \frac{\partial^2 p}{\partial z^2} = C\frac{2}{r_2^2} \tag{3.1.57}$$

The substitution of equation (3.1.57) in equation (3.1.53) leads to

$$C = -\frac{6 \cdot \eta \cdot v_\xi}{x^3} \cdot \frac{r_1^2 \cdot r_2^2}{\left(r_1^2 + r_2^2\right)} \tag{3.1.58}$$

When substituting equation (3.1.58) in equation (3.1.55) the pressure distribution $p(y,z)$ in the elliptical piston to liner contact can be calculated:

$$p(y,z,t) = -\frac{6 \cdot \eta \cdot v_\xi(t)}{x^3(t)} \cdot \frac{r_1^2 \cdot r_2^2}{\left(r_1^2 + r_2^2\right)} \cdot \left(\frac{y^2}{r_1^2} + \frac{z^2}{r_2^2} - 1\right) \tag{3.1.59}$$

In addition equation (3.1.59) delivers the maximum pressure p_{max}, occurring at $y = z = 0$, thus

$$p_{max} = \frac{6 \cdot \eta \cdot v_\xi(t)}{x^3(t)} \cdot \frac{r_1^2 \cdot r_2^2}{\left(r_1^2 + r_2^2\right)} \tag{3.1.60}$$

To obtain the resulting force out of equation (3.1.60), an integration over an elliptical area would be required. This integral can only be solved by approximation [66].

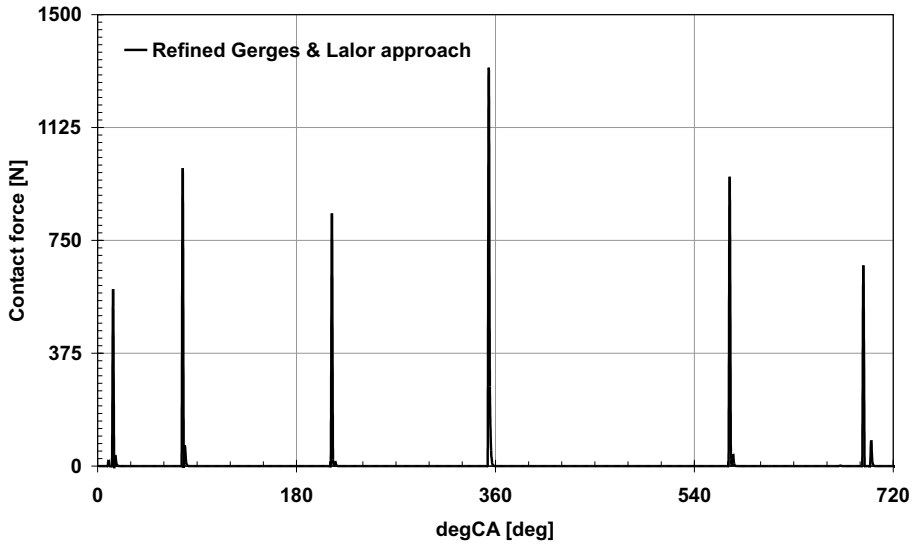

Figure 3.12: Contact force between piston and liner, using the approach according to [162] with a refined elliptical contact pattern according to Figure 3.11(b) and equation (3.1.62)

However, according to Khonsari [41] the load carrying capacity for an elliptically-shaped squeeze contact can be written:

$$F_{Impact}(t) = \frac{3\pi \cdot \eta \cdot r_1^3 \cdot r_2^3 \cdot v_\xi(t)}{\left(r_1^2 + r_2^2\right) \cdot x^3(t)} \quad . \tag{3.1.61}$$

The factor $f_{Reynolds}$ from the case branch (3.1.52) can be extracted from (3.1.61) for the elliptical contact as:

$$f_{Reynolds} = 3\pi \cdot \frac{r_1^3 \cdot r_2^3}{\left(r_1^2 + r_2^2\right)} \tag{3.1.62}$$

Figure 3.12 shows the impact force F_{Impact} at 2000rpm, 2bar BMEP for $r_1 = 8mm$, $r_2 = 5.5mm$ having an average lash between piston and liner of $\bar{\xi} = 20\mu m$. It can be inferred that this approach correlates better with measurement results, showing levels around 1 to $2kN$ for such conditions [42, 162]. Finally, the impact force is superimposed to the piston side force according to equation (3.1.29), thus leading to the resulting piston force $F_P(t)$:

$$F_P(t) = F_{Skirt}(t) + F_{Impact}(t), \tag{3.1.63}$$

further to

$$F_P(t) = \frac{-F_C(t) \cdot [\nu - (a+h) \cdot \sin\psi] - F_{Gas}(t) \cdot \delta - M_R}{a+b} + \frac{3\pi \cdot \eta \cdot r_1^3 \cdot r_2^3 \cdot v_\xi(t)}{\left(r_1^2 + r_2^2\right) \cdot x^3(t)}. \tag{3.1.64}$$

The excitation level of the piston side force, considering the piston secondary movement, can be now written as:

$$L_P(t) = 20 \cdot log\left(\frac{F_P(t)}{F_0}.\right). \tag{3.1.65}$$

Transformed into the frequency domain, for each frequency band i, equation (3.1.65) can be written as a function of frequency. This yields finally

$$L_P(f_i) = 20 \cdot log\left(\frac{F_P(f_i)}{F_0}\right). \tag{3.1.66}$$

It must be noted that the model does not consider entrapped air in the oil, leading to lower values of the contact force. This effect was found by Gerges and Lalor, using a simple test rig, when moving the piston towards the liner upon a certain impact velocity, but without a vertical movement of the piston in parallel. In contrast Knoll, Pischinger et al. proved that the Reynolds theory while assuming a homogeneous oil-film, does reflect the situation with a good correlation of prediction and measurement [42]. The difference between the linear approach and the approach considering the piston slap (F_{Impact}) is illustrated in Figure 3.13. Typical values for the thickness of the oil-film on the liner can be assumed to be 2-6μm for modern automotive gasoline engines [160]. The influence of the temperature ν on the viscosity η of the oil, which has the unit $[Pa \cdot s]$, was considered by Lalor [162] et. al., applying Vogel's equation [40]:

$$\eta = 9.80665 \cdot 10^4 \cdot a \cdot exp\left(\frac{b}{\nu + c}\right). \tag{3.1.67}$$

The table in Appendix *A.3* contains values for the coefficients for different SAE-classifications of engine oil. Gerges et. al. did viscosimeter tests to formulate equation (3.1.67) for SAE 15W/40 oil-type [162]:

$$\eta = 0.94 \cdot e^{-0.057 \cdot \nu}. \tag{3.1.68}$$

In a running engine an oil temperature in the piston-liner contact of $\nu = 100^oC$ can be assumed. The lash between piston and liner was taken as an average tolerance value for the engine used here ($\bar{\xi} = 20\mu m$), and the drag torque between pin and piston can be assumed to be constant (boundary friction) for small tilt angles by $M_R = 0.01Nm$.

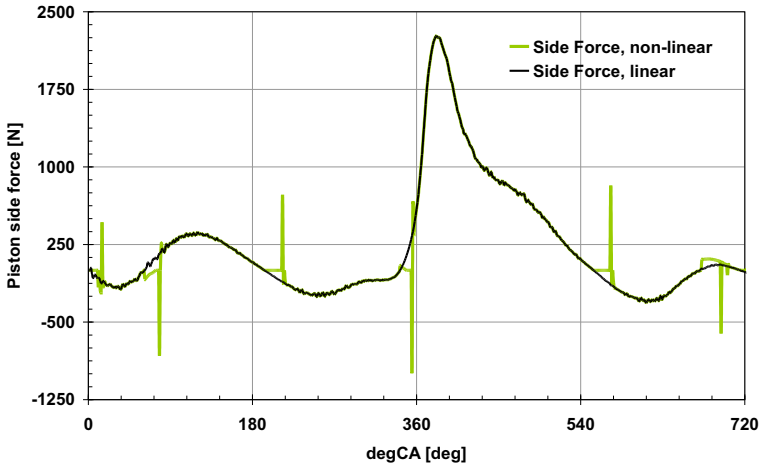

(a) Comparison of the piston side force force 2000rpm, 2bar BMEP. The black curve is the force calculated using equation (3.1.29), and the bright curve reflects the result of the non-linear approach according to equation (3.1.63)

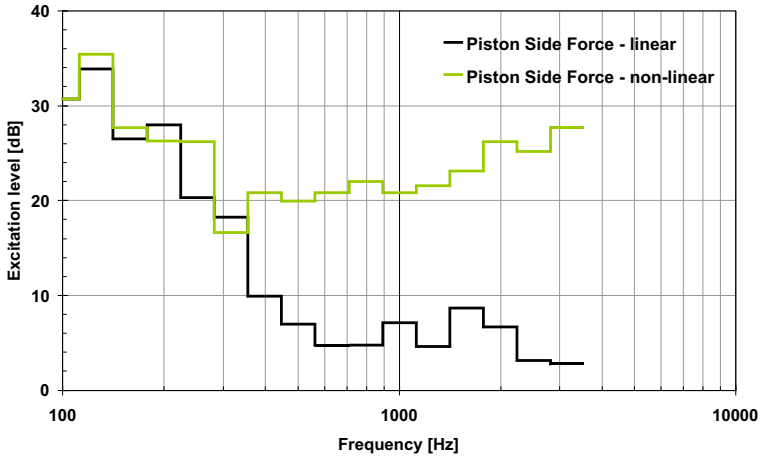

(b) According excitation spectra (third octave) of the forces shown in Figure 3.13(a); please note the increase of the excitation above $400Hz$ of about $10dB$ and higher, caused by the impact force

Figure 3.13: The impact of the non-linear piston side force approach on the force in the time- and frequency domain

3.1.4 A simple Forced-Response-Model to describe the load transfer between Piston and Crankshaft

A first comparison of the excitation mechanisms of HCCI and SI revealed a higher amplitude of the combustion excitation. Moreover, the HCCI combustion delivers a significantly increased pressure rise rate of the cylinder pressure. At first glance, this is obviously not a novel issue, because since the introduction of compression ignition engines research has been conducted to identify the sources of the impulsive noise characteristics of such engines. Research carried out by Ricardo [109] and Pye [110] revealed a certain threshold for the combustion excitation above which the impulsiveness of the engine noise increases dramatically. Pye also determined that the impulsiveness depends on the magnitude of the exciting cylinder pressure gradient, and is independent of the maximum cylinder pressure. This is because a sharper pulse on the structure evokes higher amplitudes of the response of the excited structure than a smooth pulsation, which it is for low pressure gradients during SI mode operation, as for example demonstrated in [50].

Investigations into the root cause of the impulsiveness, carried out in the late 1920's [117] and later in 1987 [47] revealed a strong dependancy of the frequency response sensitivity of the power-conversion system on dynamic bearing loads, especially in the crank-end bearing of the connecting rod. Initial research on the so called 'tertiary movement' of the piston has been done with the aim to characterize the contact zone area between piston and liner when it comes to a lateral piston movement [43]. Also detailed research on the interaction of the lateral piston-movement, combined with the lateral deflection of the connecting rod by the gas-forces [44], has been carried out. It was found that the design of the bearing of the pin in the piston and the fit of the pin between connecting rod and piston have an impact on the lateral movement of the piston under fired engine conditions. However, an interaction between maximum pressure rise rate and its location relative to TDC with the impact forces occurring in the involved clearances when increasing both maximum cylinder pressure and pressure rise rate [44, 141] was revealed while considering the involved parts as rigid.

Surveying the noise spectra emitted by modern lightweight compression ignition engines one can observe an increase at certain frequency bands preferably in the range between $1.5kHz$ to $2.5kHz$. This affects the noise characteristics and thus the sound quality of the radiated engine noise [48, 55, 56, 57, 58, 59, 60]. Most

research into the contribution of the piston, pin and the connecting rod to this noise phenomenon was focussed on the sole parts. In addition, analysis of these parts with regard to other attributes, such as tribology or durability, has revealed effects that could help to interpret the dynamical behaviour of these parts.

Aouichi [48] carried out detailed investigations to search for the cause of diesel-noise characteristics, but still considering the piston and the connecting rod solely. Ishida et al. demonstrated the importance of a bending-mode of the conrod during high-speed operation ($> 6700rpm$) through a frequency analysis of the dynamic stresses in the connecting rod [60] in a running engine when carrying out investigations on durability. Woschni et al. found a correlation between a longitudinal eigenfrequency of the connecting rod and stress-signals, gained by strain gauges fitted on the connecting rod of a light truck diesel engine under high pressure rise rates [47]. Wang et al. carried out a stress analysis of a flexible connecting rod in a high speed engine [51] when investigating bearing lubrication. Although the distortion of the connecting rod during a high speed engine cycle was studied, the eigenfrequencies and flexible modes of the connecting rod were not included, other than the influence of gas- and inertia affected forces. However, this investigation contributed to the understanding of the contact area of the crank-end bearing. In addition, Goudas did a similar investigation while carrying out parametric studies for different engine speeds and length of the connecting rod. He investigated a flexible connecting rod of a constant rectangular profile, studying the first bending mode of the connecting rod and the response at different speeds and for different length of the connecting rod [53]. The slider-crank mechanism was investigated theoretically in a similar way by Fung, who also considered transverse and longitudinal vibratory effects of the connecting rod [54]. This investigation was carried out under the assumption that the dynamic response is dominated by the first transverse and longitudinal eigenfrequencies of the connecting rod, and that the displacement and moment at each end is negligible.

However, because the previous work has treated either the connecting rod or the piston as a single part without the consideration of the linkage to the pin and the piston under various excitation characteristics, a detailed analysis of the system was carried out. A modal analysis of the piston, the conrod and the piston-connecting rod assembly was carried out. Each subsystem was excited by using a modal-hammer and the response was measured at different points on the structure to determine the mode shape of vibration when responding at its eigenfrequency. Thereafter

a forced response model was set up. A parametric study using a representative cylinder pressure and -gradient sweep at a constant load and speed point of operation was carried out [49]. Subsequently the response characteristic of the system was studied under the different forced excitations in a frequency range up to $4kHz$. Figure 3.14 shows the different measurement set-ups. Finally a modal analysis of

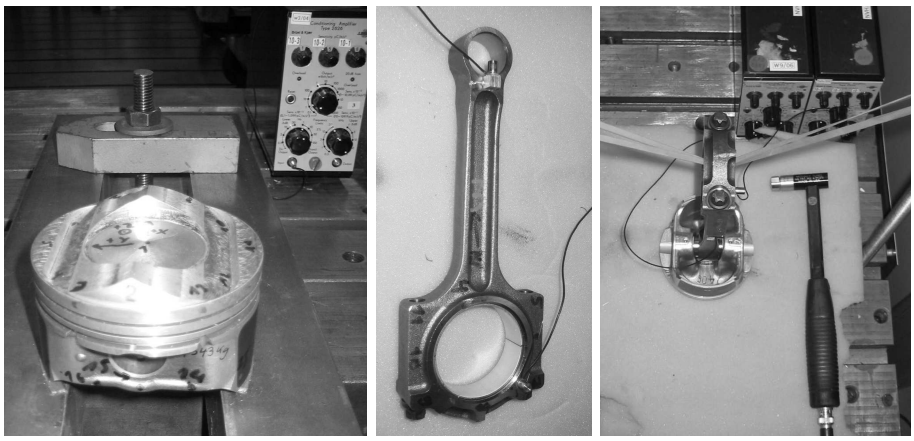

Figure 3.14: Modal analysis set-up for piston, conrod and piston-conrod assembly

the whole power conversion system, suited in the base engine structure, was carried out. Figure 3.15 shows the basic set-up, containing among other things the structure-borne transducers applied at the main bearing caps. Once the eigenfrequencies and

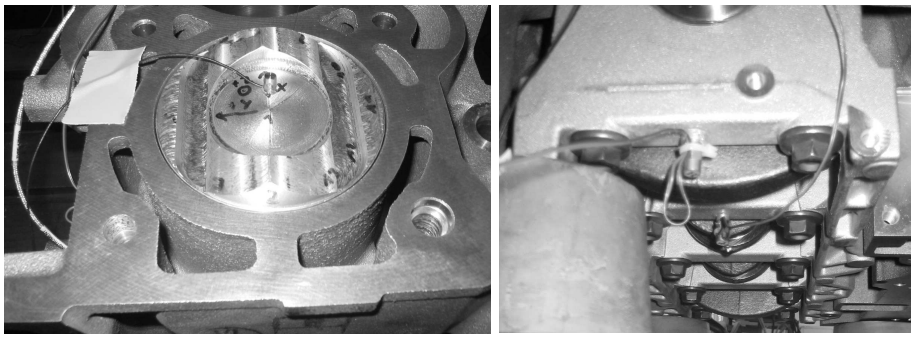

Figure 3.15: Modal analysis set-up of the power-conversion system in its base-engine

the relating mode-shapes of all parts are known, each part can be reduced to a certain number of nodes or points, where e.g. a transducer during the mode-shape measurement was applied, having certain degrees of freedom (DoF). It needs to be ensured that the selected nodes or points describe the interesting mode-shapes up

to a certain frequency correctly.

3.1.4.1 Modal Analysis

After sectioning the part to be investigated into a wire frame mesh with the defined nodes i, a transducer is fitted successively to determine the response at the node $i = j$. The response is $Y_j(\omega)$, when the structure at another node with a force of the frequency spectrum $X_i(\omega)$ is excited. The impulse response is then transformed from the time- into the frequency domain, resulting in the frequency response. The result is a frequency response function of the structure

$$H_{ij}(\omega) = \frac{Y_j(\omega)}{X_i(\omega)}. \tag{3.1.69}$$

However, normally a structure investigated during an experimental modal analysis reveals more than a single mode response or a simple superimposed combination of those. Furthermore, the measured response $Y_j(\omega)$ can not be separated into the single modes easily; a simple summation of the individual responses is not possible because the phases between the particular spectra are random. By definition, the estimation of the resulting FRF, H_{ij}, is usually defined as the fraction of the cross-spectrum between the individual input X_i and output Y_j, G_{XY}, and the auto-spectrum of the input, G_{XX}, thus:

$$H_{ij} = \frac{G_{XY}}{G_{XX}}. \tag{3.1.70}$$

This procedure allows then by averaging the elimination of uncorrelated noise at the measured output [67, 68]. Furthermore, when applying the approach on a system with multiple inputs and multiple outputs, according to [68] the estimated individual FRF's form the frequency response matrix $[H]$ that can be calculated by $[H]^T = [G_{XX}]^{-1}[G_{XY}]$. When carrying out the modal analysis, the force that is brought into the structure with an impact hammer is measured as well as the responding acceleration. Finally the summed frequency response function of the structure is achieved by averaging the particular frequency response functions H_{ij} to one resulting curve with the unit $\left[\frac{m}{s^2 \cdot N}\right]$.

Since the aim of the investigation was to analyse a structure-borne based noise event, the maximum considered frequency was $4kHz$. The relevant eigenfrequencies have the index k. Table 3.1 shows characteristic data of the parts involved. The damping value ϑ of the individual modes can be calculated by using the peak-amplitude method as e.g. derived in [67]. When using this method, the peak at a

Table 3.1: Weight and material of the parts investigated

Part	Weight $[kg]$	Material
Piston	0.343	Aluminium
Pin	0.104	forged Steel
Connecting Rod	0.532	forged Steel
Assembly (incl. pin)	0.979	-

natural frequency k, $\hat{H}_k(\omega)$, of an overall FRF is divided by $\sqrt{2}$, thus $\hat{H}_k(\omega_{ba}) = \hat{H}_k(\omega)/\sqrt{2}$. The indices b and a denote the frequencies one can read from the FRF, if a horizontal line, starting from the ordinate at $\hat{H}_k(\omega_{ba})$ crosses the frequency curve at the peak of k, hence giving the frequencies ω_b and ω_a. According to [67] this yields the damping value of the individual mode k:

$$\vartheta_k = \frac{\omega_a^2 - \omega_b^2}{\omega_k^2}. \tag{3.1.71}$$

3.1.4.2 Formulation of the Forced-Response

In order to calculate the forced-response of the piston-pin-connecting rod assembly, the method of mode superposition was chosen. The advantage is fast data processing even when high frequencies are considered. Moreover, this approach allows the analysis of the system under different excitations in the time domain. According to the approach of the mode superposition the response of the forced structure is calculated by decomposing the structure into a certain number of single-mass systems. The equation of motion for a system consisting of multiple masses can be written as

$$[M] \cdot \{\ddot{u}\} + [D] \cdot \{\dot{u}\} + [C] \cdot \{u\} = \{F(t)\}, \tag{3.1.72}$$

with $[M]$ denoting the mass matrix, $[D]$ the damping matrix, and $[C]$ the stiffness matrix. The vector $\{u\}$ and its first and second derivative denote the deflection, speed and acceleration of the system, respectively. The modal analysis of the structure, as described in the previous chapters, delivers the eigenfrequencies, the mode shape, characterized by $\{\phi\}$ for each particular node, as well as the degree of damping.

In any case, once the considered system is structured into a certain number of nodes i, the degree of freedom N for each node should be chosen in such a way

that the particular mode shape k is reflected by the system accordingly. If the structure has the absolute measured number of eigenfrequencies s, then the number of eigenfrequencies p is considered that occurs in the frequency range of interest. Therefore it should always be $p \leq s$. The final displacement of the node is then determined by the sum of the displacements at the involved eigenfrequencies. Hereby the mode-shape is described by the node-related eigenvector $\{\phi_i\}$, as determined by the experimental modal analysis. This yields then the resulting displacement of each node for the particular coordinates and eigenfrequencies:

$$\{u(t)\} = \sum_{k=1}^{p} \{\phi_{ik}\} \cdot y_{ik}(t), \qquad (p \leq s). \tag{3.1.73}$$

Equation (3.1.73) can be re-written in the appropriate matrix form, reflecting the degrees of freedom, N:

$$\{u(t)\} = [\phi_p] \cdot \{y_N(t)\} \tag{3.1.74}$$

The matrix $[\phi_p]$ is of the dimension $N \cdot p$, and $y_N(t)$ is a vector of the length p. The combination of (3.1.74) and (3.1.72) then yields:

$$[M] \cdot [\phi] \cdot \{\ddot{y}\} + [D] \cdot [\phi] \cdot \{\dot{y}\} + [C] \cdot [\phi] \cdot \{y\} = \{F(t)\}. \tag{3.1.75}$$

Furthermore, it is convenient to multiply equation (3.1.75) with ϕ^T, hence it is:

$$[\phi]^T \cdot [M] \cdot [\phi] \cdot \{\ddot{y}\} + [\phi]^T \cdot [D] \cdot [\phi] \cdot \{\dot{y}\} + [\phi]^T \cdot [C] \cdot [\phi] \cdot \{y\} = [\phi]^T \cdot \{F(t)\} \tag{3.1.76}$$

It must be noted that in the mass matrix $[M]$ in equation (3.1.76), only the diagonals are unequal to zero. Moreover, the modal damping matrix can be derived from the mass- and stiffness matrix. This delivers a damping matrix, which is precisely on the diagonal unequal to zero. Hence the system of equations of (3.1.76) can be expanded into a combination of p single mass systems:

$$\begin{bmatrix} m_1 & & 0 & & 0 \\ & \ddots & & & \\ 0 & & m_k & & 0 \\ & & & \ddots & \\ 0 & & 0 & & m_p \end{bmatrix} \begin{Bmatrix} \ddot{y}_1(t) \\ \vdots \\ \ddot{y}_k(t) \\ \vdots \\ \ddot{y}_p(t) \end{Bmatrix} + \begin{bmatrix} d_1 & & 0 & & 0 \\ & \ddots & & & \\ 0 & & d_k & & 0 \\ & & & \ddots & \\ 0 & & 0 & & d_p \end{bmatrix} \begin{Bmatrix} \dot{y}_1(t) \\ \vdots \\ \dot{y}_k(t) \\ \vdots \\ \dot{y}_p(t) \end{Bmatrix}$$
$$+ \begin{bmatrix} c_1 & & 0 & & 0 \\ & \ddots & & & \\ 0 & & c_k & & 0 \\ & & & \ddots & \\ 0 & & 0 & & c_p \end{bmatrix} \begin{Bmatrix} y_1(t) \\ \vdots \\ y_k(t) \\ \vdots \\ y_p(t) \end{Bmatrix} = \begin{Bmatrix} f_1(t) \\ \vdots \\ f_k(t) \\ \vdots \\ f_p(t) \end{Bmatrix} \tag{3.1.77}$$

Each row of equation (3.1.77) represents a single mass system for each eigenfrequency k:

$$m_k \cdot \ddot{y}_k(t) + d_k \cdot \dot{y}_k(t) + c_k \cdot y_k(t) = f_k(t) \tag{3.1.78}$$

The position of a particular node i is defined by the location at which a transducer was applied during the experimental modal analysis. It needs to be ensured that the selected nodes describe the mode-shapes of interest correctly. The modal analysis delivers all necessary requirements for solving equation (3.1.78). This finally enables the application of the method of mode superposition [69].

The displacement $y(t)$ in each degree of freedom at each node can be either calculated using the method of the finite differences, the Newmark procedure or the Euler algorithm. Then the summation of each node related displacement $y_i(t)$ will contribute to the dynamic force. The semi-implicit Euler-Algorithm was used here. This algorithm captures the damping of the system much better than implicit methods that tend to over-predict the damping. The explicit Euler-Algorithm in turn leads to an under-prediction of the damping [158]. The structure is excited by the cylinder pressure. Hence, the force $f_{(i=1)}(t)$ drives the deflections and then equation (3.1.79), (3.1.80) and (3.1.84) can be used to determine the other forces. The velocity $\dot{y}(t)$ at node i for the eigenfrequency k, excited with the Force $f_i(t)$, can be calculated using the time-step Δt:

$$\dot{y}_{ik}(t + \Delta t) = \dot{y}_{ik}(t) - \Delta t \left(\frac{c_k}{m_{ik}} y_{ik}(t) + \frac{d_k}{m_{ik}} \dot{y}_{ik}(t) - \frac{f_i(t + \Delta t)}{m_{ik}} \right) \tag{3.1.79}$$

In (3.1.79) the variable m_{ik} represents the modal mass of the system [67]. The resulting displacement $y_{ik}(t)$ can then be calculated for the chosen DoF in the cartesien coordinate system:

$$y_{ik}(t + \Delta t) = y_{ik}(t) + \Delta t \cdot \dot{y}_{ik}(t + \Delta t) \tag{3.1.80}$$

To calculate the forced response $F_{ik}(t)$ in the time domain the according stiffness c_{ik} of the system can be derived from the related damping value ϑ_k, which results from the modal analysis test with hardware and occurs at the particular eigenfrequency k:

$$c_{ik} = \frac{d_k^2}{4\vartheta_k^2 m_{ik}} \tag{3.1.81}$$

When considering $c_{ik} = \omega_k^2 \cdot m_{ik}$, the damping constant d_k can be calculated:

$$d_k = 2 m_{ik} \omega_k \vartheta_{ik}. \tag{3.1.82}$$

The Force $F_{ik}(t)$ that acts in each direction can be calculated using also equation (3.1.74) by the product of the individual deflection with its participation factor ϕ_{ik}, which also results from the modal-analysis:

$$F_{ik}(t) = \sum_{p=1}^{k} u_{ik}(t) \cdot c_{ik} \tag{3.1.83}$$

The resulting Force $F_{dyn,i}$ at a particular node can then be calculated considering each particular force acting in the direction defined by the chosen degrees of freedom. This yields:

$$F_{dyn,i}(t) = \sqrt{F_{x,i}^2(t) + F_{y,i}^2(t) + F_{z,i}^2(t)} \tag{3.1.84}$$

In the following sections the response of the assembly of piston, pin and connecting rod will be investigated in greater detail and will form the basis for developing a forced response model. This is done by applying different cylinder pressure excitations on it.

3.1.4.3 The Piston

As depicted in Figure 3.16, the piston was sectioned into a wire frame mesh. A mesh resolution over the circumference with an interval length of the angle of $30deg$ was chosen. Over the height of the piston the attachment of sensors was limited either by the grooves for the three rings or by the geometric shape caused by the skirt. The coordinate system was chosen by aligning the x-axis along the piston-pin-axis. The modal analysis was carried out while placing the piston on a soft foam to achieve free-free conditions and to ensure that the rigid modes of the piston are below the first elastic modes. The particular accelerometer was attached with a thin film of hot glue. Before the measurement it was checked that the hot glue-process did not affect the response of the accelerometer. The frequency response characteristic, represented by showing the resulting inertance versus frequency, is drawn in Figure 3.17. The piston does not have an eigenfrequency below $4kHz$, hence the abscissae were expanded to $7kHz$. It can be inferred from Figure 3.17 that the first natural frequency of the piston is at $4787Hz$. The second eigenfrequency is located at $4962Hz$. The first mode is dominated by a pulsation of the skirt, which is rectangular and vibrates in an elliptic mode shape with the axis of the ellipse as shown in Figure 3.18(a). Figure 3.18(b) shows that the second mode behaves similarly, but the axis of the ellipse is rotated 60degrees counter-clockwise around

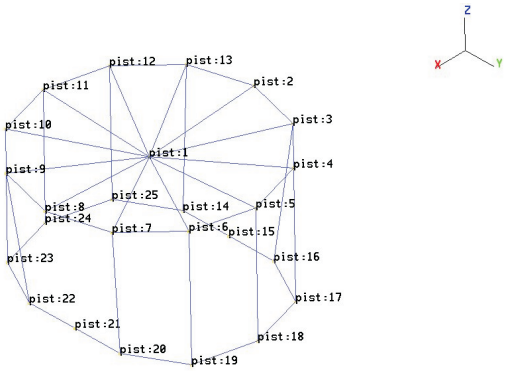

Figure 3.16: Resulting wireframe-model of the piston after sectioning into nodes

the z-axis. Due to the stiffer structure in the direction of the pin, this mode does not show as high a displacement as the first mode. The higher relative damping value ϑ_j of 12% instead of 7% is also due to the increased stiffness of the piston structure at this orientation [2].

3.1.4.4 The Connecting Rod

The connecting rod was modelled as a wire frame in a similar way, as illustrated in Figure 3.19. The inertance versus frequency is shown in Figure 3.20. Four different eigenfrequencies below $4kHz$ are revealed. The first eigenfrequency was identified as the first lateral bending mode at $1112Hz$. Figure 3.20 shows two modes, located close to each other at $2kHz$. The eigenfrequency at $3550Hz$ can be identified as the second lateral bending of the connecting rod. To separate the two frequencies at $2kHz$, the eigenfrequencies of the connecting rod were analysed by using the Finite Element Analysis (FEA). The model consists of tetrahedron type elements. Figure 3.21 shows the calculated first four eigenfrequencies of the connecting rod that were in relation to the degrees of freedom, determined by the pin- and the crank-eye bearing. The results determined by the FEA in Figure 3.21 show clearly the two separated modes at $2228Hz$ (first torsional mode) and at $2320Hz$ (first bending mode). Finally Figure 3.22 shows the correlation of measured and calculated eigenfrequencies, showing that the error is at the $\pm 10\%$ range (dotted lines), which is a common range when comparing simulation and measurement data.

[2] Note also that the high damping values were caused by the experimental set-up for the modal analysis. Thus, the influence of the object sitting on foam during the modal analysis should be taken into account.

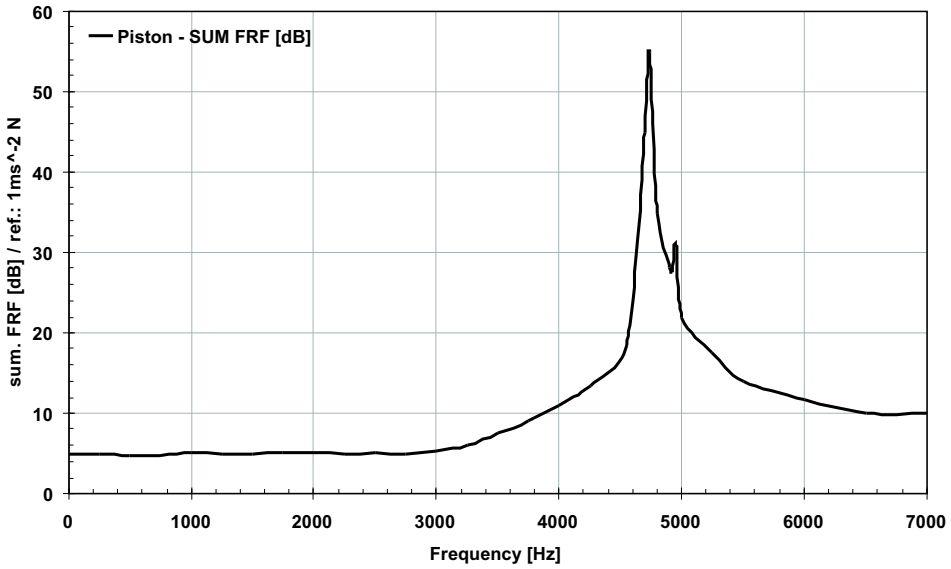

Figure 3.17: Summed Frequency-Response-Function (*sum FRF* according to equation (3.1.70)) of the piston

3.1.4.5 Assembly of Piston and Connecting Rod

When fitting piston, pin and connecting rod into an assembly, the individual eigenfrequencies of each individual part can shift in frequency or even be suppressed by damping. This can happen because the real boundary conditions in the joint differ from the free-free boundary conditions. In addition, the pin influences the stiffness of the assembly itself [44]. The design investigated here has a press fit of the pin into the small eye of the connecting rod and a floating pin design on the piston. The frequency-response curve of this system is shown in Figure 3.23. This analysis revealed that the assembly has different inertance values and higher degrees of damping at its eigenfrequencies than its individual components. All relevant eigenfrequencies f_e and their particular mode shape characteristics are listed in Table 3.2 and illustrated in Figure 3.24. It was decided not to incorporate the eigenfrequency of $386Hz$ into the model, because this mode shape is a rigid torsional mode of the entire assembly around the vertical axis of the connecting rod. This was also confirmed by carrying out modal analysis tests of the assembly when installed in the liner: the test revealed that this particular frequency was not detected in the signal. Hence this mode was not incorporated into the model. Figure 3.24 depicts the three relevant mode shapes of the analysis and delivers a description of the

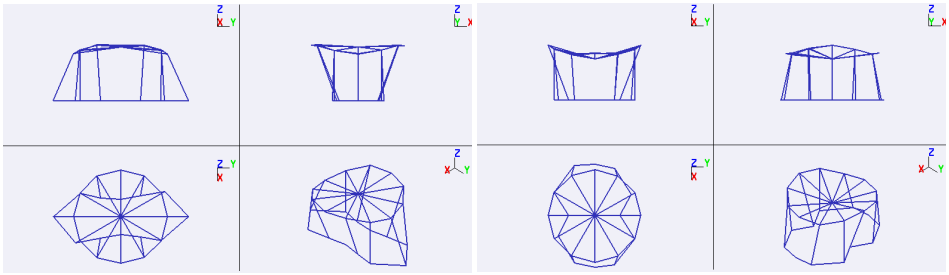

(a) Deflection of the piston at its first eigenfrequency at $4787Hz$

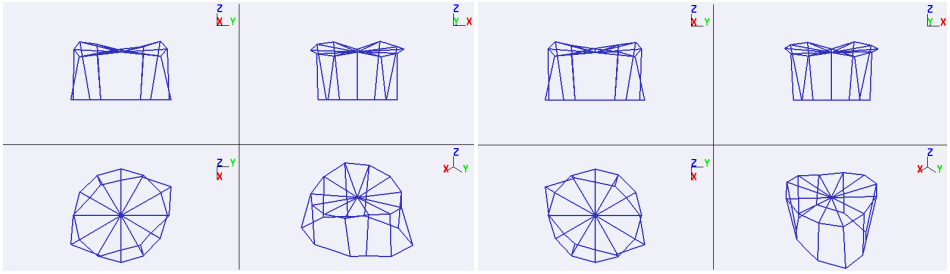

(b) Deflection of the piston at the second eigenfrequency at $4962Hz$

Figure 3.18: Deflection (amplified) of the piston during its first and second natural frequency

Table 3.2: The first four different natural frequencies of the piston-pin-connecting rod assembly and the description of the associated mode shape

Frequency $f_e[Hz]$	Damping $\vartheta_j[\%]$	Description
571Hz	7.51	lateral mode of the connecting rod relative to the piston, the connection between small eye and pin acts as a hinge
1571Hz	7.19	lateral bending mode of the connecting rod with the piston and the pin out of phase
2154Hz	14.58	pumping mode of the piston in vertical (i.e. direction of the cylinder liner) direction, inducing a lateral deflection (bending) of the connecting rod via the pin
2386Hz	15.8	First bending mode of the connecting-rod, similarly to the mode of the connecting rod as a single part (Figure 3.21)

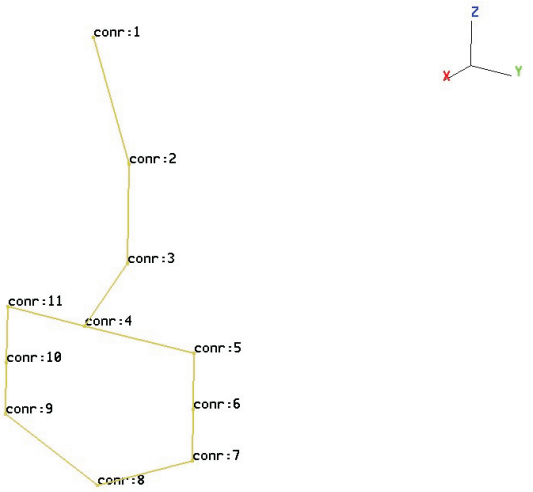

Figure 3.19: Wireframe-model of the connecting rod after sectioning into nodes

individual mode shape. When inputting the frequency values, the individual participation factors and damping values from the modal analysis into equation (3.1.83), the individual dynamic forced response of the system can be calculated.

3.1.4.6 Sensitivity to Pressure Rise Rate

As mentioned earlier and already noted by Ricardo [109] and Pye [110], above certain cylinder pressure gradients the noise characteristics of a CI-engine can change. To study this effect, different cylinder pressure characteristics where calculated, based on two superimposed cylinder pressure traces. Hereby the first pressure trace characterizes the pre-combustion phase, and the latter one the main ignition. This was done to achieve different pressure gradients, but maintaining the same load of 2bar BMEP at 2000rpm with the same peak pressure for all pressure traces. These generated pressure traces and according pressure gradients are shown in Figure 3.25. Based on equation (3.1.84) the resulting dynamic force F_{dyn} in the connecting rod was calculated. Its response to the particular excitations is shown in Figure 3.26(a). To quantify the influence of the individual mode-related forces, Figure 3.26(b) shows the bandpass filtered excitation F_{dyn}. This was processed while choosing the frequency borders of $f_l = 0.5kHz$ and $f_u = 3kHz$. Based on Figure 3.26 it can be concluded that an increase of the pressure gradient will evoke a higher amplitude of the dynamic response of the system. In addition Figure 3.26(b) shows that the increase of the maximum amplitude of the response obviously rises linearly with an

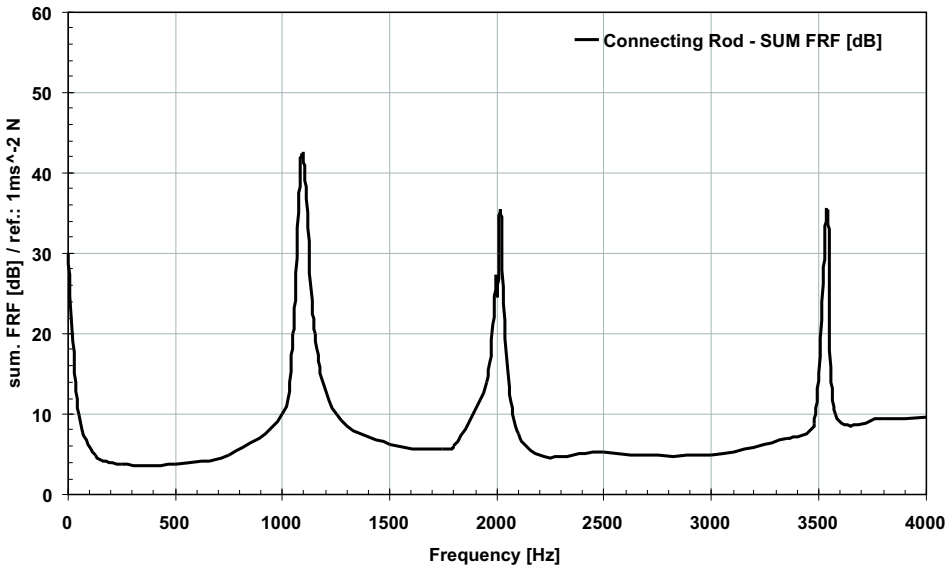

Figure 3.20: Summed Frequency-Response-Function (*sum FRF* according to equation (3.1.70)) of the connecting rod

increase of the pressure gradient. However, taking into account the relative position of the force, caused by the cylinder pressure only, and adding the frequency response of the system, the absolute level of F_{dyn} must not rise necessarily in a linear way with an increase of the pressure rise rate, as will be revealed later.

To evaluate the contribution of each particular mode to F_{dyn}, the mode related forced-responses for the chosen four different excitations were drawn separately, as depicted in Figure 3.27. It can be seen that an increase of the pressure rise rate need not necessarily provoke an increase of the amplitude of the forced-response, as shown for the response of the f_{e1}-mode. In addition the response of the particular modes behaves differently because of the individual degrees of damping. Moreover, it can be concluded that the dynamic response of the system is dominated by the f_{e2} and f_{e3} related modes, both owning the highest level of excitation. In any case, the individual dynamic force component can be transferred via the contacts and lashes into the bearings, then in turn into the structure, until there is a constant contact between connecting rod and crankshaft. Once there is a significant change of the direction of the resulting bearing force, the transfer of this force is interrupted. To analyse this behaviour, the mode related force versus the tilt angle of the connecting rod, as it is depicted in Figure 3.28, were drawn for four different pressure gradients. This analysis reveals that the higher the frequency, the more cycles of the individual

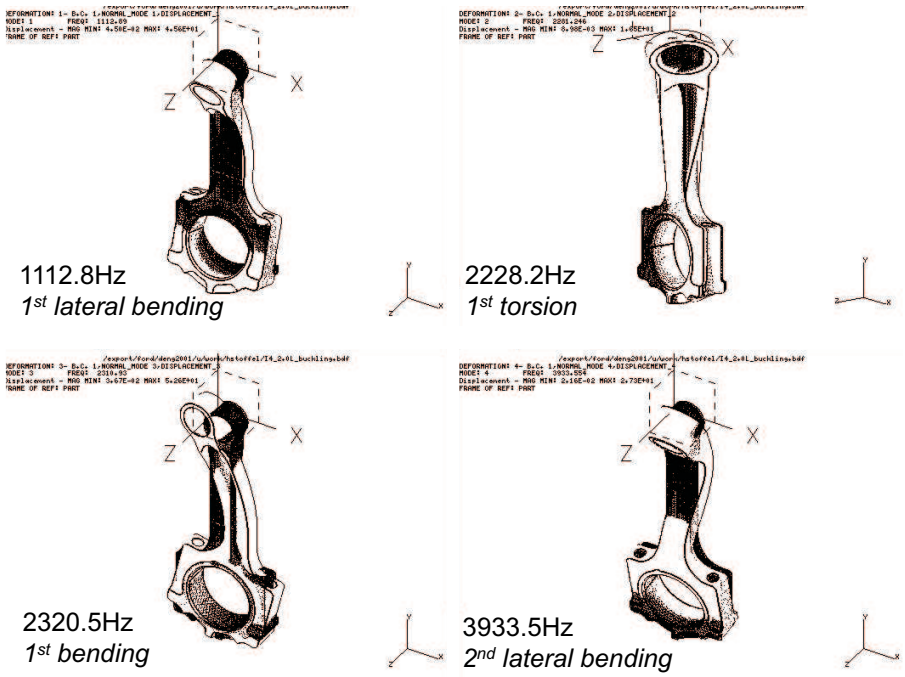

Figure 3.21: The eigenfrequencies of the connecting rod, calculated by the FEM

mode-related force can excite the structure until the connecting rod arrives at $90deg$ after TDC, which means the maximum tilt angle. During this phase no significant change of the contact pattern in the bearings takes place, and the structure is excited according to the dominating eigenfrequencies [3]. This is in accordance with the theory, published in [117] that the nearer the maximum pressure rise rate takes place at combustion TDC, the higher is the excitation and thence the impulsiveness. Furthermore, the analysis reveals that low eigenfrequencies of the assembly, or high eigenfrequencies with high degrees of damping, can allow higher pressure gradients, leading to less impulsive noise characteristics. Subsequently the system was feeded with all calculated cylinder pressure excitations at 2bar BMEP at 2000rpm, starting with the characteristics of $1bar/deg$ and increasing the pressure rise rate up to $7bar/deg$ with an interval length of $0.5bar/deg$. This was done to describe the resulting dynamic response as a function of pressure rise rate and level, as well as to detect the thresholds of the individual mode related responses. Accordingly the following

[3] To ensure an acceptable run time of the engine noise analysis routine, it was decided to omit the detailed contact pattern analysis including lash of the affected bearings in the connecting rod. Moreover, in the assembly investigated, the pin is connected with the connecting rod via a press-fit.

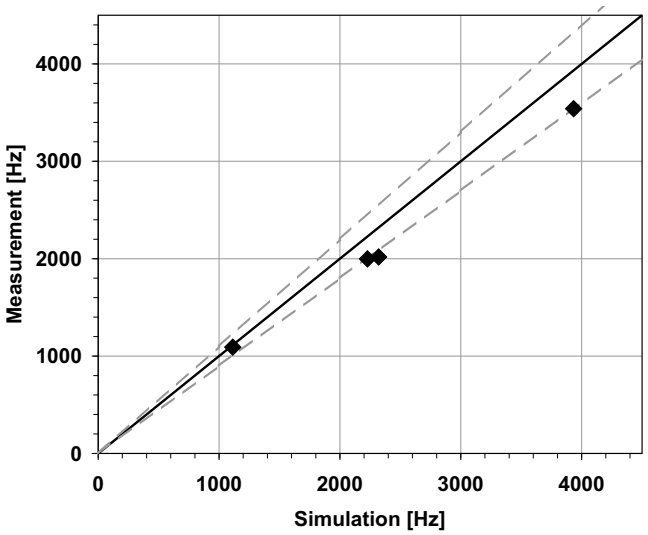

Figure 3.22: Correlation of calculated and measured eigenfrequencies of the connecting rod; the dotted lines represent the upper and lower border of the acceptable mismatch, which is assumed to be $\pm 10\%$.

Figure 3.29 shows the minimum to maximum amplitude of the resulting force F_{dyn} as a function of the pressure rise rate. To illustrate the level of the cylinder pressure excitation, the maximum peak pressure is shown with a second ordinate at the right. It can be seen that the force difference, also called relative force, shows three different slopes versus the cylinder pressure gradient. First the rise can be explained with the also increasing peak pressure. Above $3.5 bar/deg$ the slope increases slightly, and it increases further above $5 bar/deg$. Obviously these different slopes are affected by the eigenfrequencies, excited by the increased sharpness of the cylinder pressure as already illustrated in Figure 3.26 as discussed earlier. Based on these results, a parameter study was carried out while feeding the system successively with all thirteen different pressure traces and -gradients. The result is depicted in one diagram, showing the dynamic force F_{dyn} (upper half) and the bandpass filtered force (lower half) in the connecting rod over crank angle during combustion TDC. The according pressure gradient is written along the ordinate (Figure 3.30). As expected, the upper diagram in Figure 3.30 reveals an increased excitation of the system for higher pressure gradients even while the peak pressure of the cylinder pressure excitation is maintained. However, above a pressure gradient of $4.5 bar/deg$ there is a second peak visible. This can be referred to the increased sharpness of the pressure rise rate, thus exciting the related eigenfrequencies. Furthermore, when applying a bandpass filter with $f_l = 0.5 kHz$ and $f_u = 3 kHz$ on the force F_{dyn}, this effect is revealed as being even more significant. The filtered force shows the characteristic of a free vibrating

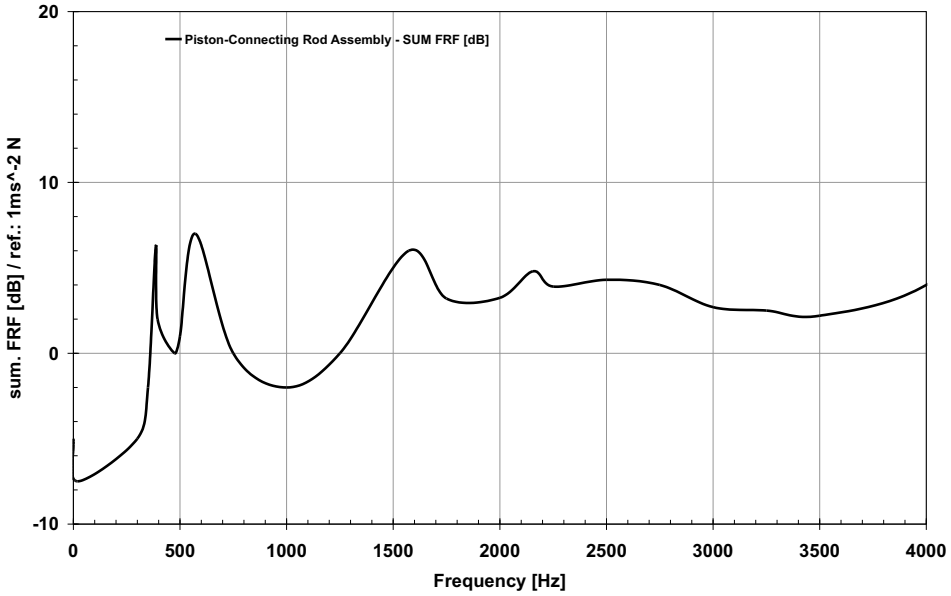

Figure 3.23: Summed Frequency-Response-Function (*sum FRF* according to equation (3.1.70)) of the piston-connecting rod assembly

damped response, which is caused by the superimposition of the four responding eigenfrequencies of the system, as is already shown for selected pressure gradients in Figure 3.26(b). To study this for the individually considered modes incorporated in the model, a similar analysis of each eigenfrequency was carried out. The results are depicted in Figure 3.31. It can be inferred from Figure 3.31(a) that the 571Hz mode does not show a significant vibrational response on the increased excitation. In contrast both $f_{e2} = 1573Hz$ and $f_{e3} = 2154Hz$ (Figure 3.31(b) and (c)) modes show the highest level of excitation, and also a second excitation peak at $368deg$ and $370deg$ for pressure gradients higher than $3.5bar/deg$ and $4bar/deg$. Moreover Figure 3.31(c) shows also a third excitation peak, followed by the according time span of this mode at $374deg$, excited by pressure rise rates higher than $5.5bar/deg$. A similar effect can be observed for the eigenfrequency at $f_{e4} = 2368Hz$ in Figure 3.31(d), that occurs at a significantly lower force level. However, it can be followed that the two changes in the slope of the relative force in Figure 3.29 can be referred to the individual contributing eigenfrequency that is superimposed on the resulting excitation F_{dyn} in the model. With respect to the different eigenfrequencies the responding frequencies will then lead to a certain frequency response characteristic of the piston-pin-connecting rod assembly. It might be of interest that already in

1937, Pye recommended for the CI-research engine he employed for his testing, to maintain the maximum pressure rise rate below $50\frac{lb}{in^2}/deg = 3.45bar/deg$ to avoid impulsive noise characteristics [110].

3.1.4.7 Verification with a running Engine

To validate the model, a structure-borne noise measurement was carried out in SI- and clattering HCCI-operation at 2000rpm, 2bar BMEP. During SI-operation a pressure rise rate of $1.2bar/deg$ was monitored. Operating the engine in HCCI delivered a pressure rate of $4.3bar/deg$. Based on a former modal analysis of the engine structure the transducer was fixed at a stiff location of the engine block nearby the bottom end to avoid influences of local mode shapes of the engine structure itself. The resulting spectra are shown in both sub-figures of Figure 3.32: as a conventional spectrum in Figure 3.32(a), and as a time-frequency analysis in Figure 3.32(b). An increase of amplitudes at certain frequencies can be observed when the engine is operated in HCCI-mode. The measurement reveals that these amplitudes correspond well at $580Hz$, $1500Hz$ and in the range from $2100Hz$ to $2300Hz$ with the measured frequency-response-function of the piston-connecting rod assembly from Figure 3.23. Thus, to describe the structural response completely during HCCI-operation, the dynamic forces of the assembly have to be taken into account. This not only characterizes the noise difference between SI- and HCCI-mode, but also quantifies the potential of optimization of the structure, loaded by HCCI combustion, with regard to noise and vibration. Finally, the observation of these individual frequencies can be interpreted in such a way that internal combustion engines have an optimum of the individual cylinder displacement: below $0.4dm^3$ the friction loss will rise, and above $0.6dm^3$ knock sensitivity or emission related issues will increase, thus deteriorating either fuel consumption or violating emission-legislation [62]. Taking this into consideration, a volume of a combustion chamber within this range requires similar geometric dependencies, hence leading often to similar dimensions and materials of the components investigated. In turn this can infer a similar range of eigenfrequencies.

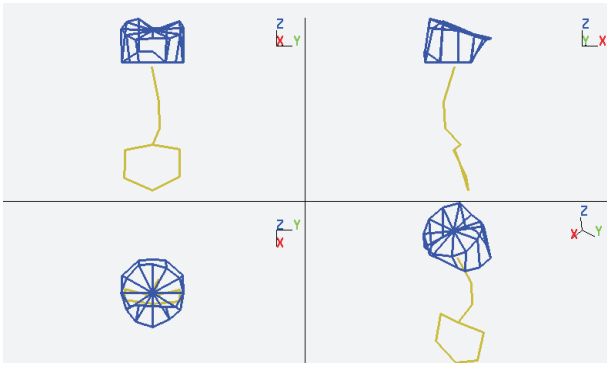

(a) $f_{e1} = 571Hz$: lateral mode of the connecting rod relative to the piston, the connection between small eye and pin acts as a hinge

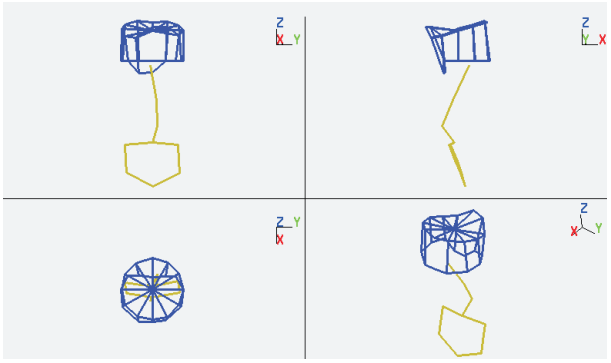

(b) $f_{e2} = 1573Hz$: first lateral bending mode of the connecting rod with an opposite phase mode of the piston relative to the pin

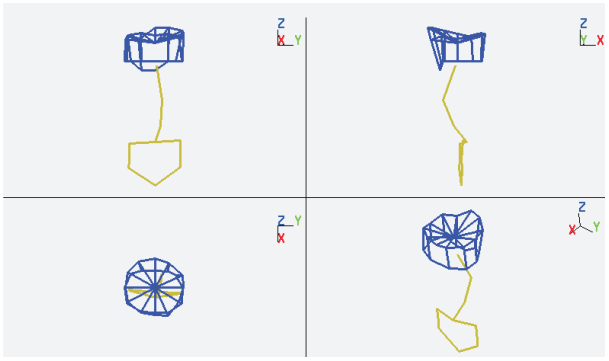

(c) $f_{e3} = 2154Hz$: pumping mode of the piston in vertical (i.e. direction of the cylinder liner) direction, inducing a lateral deflection (bending) of the connecting rod via the pin

Figure 3.24: Measured mode shapes of the piston-pin-connecting rod assembly under free-free boundary conditions

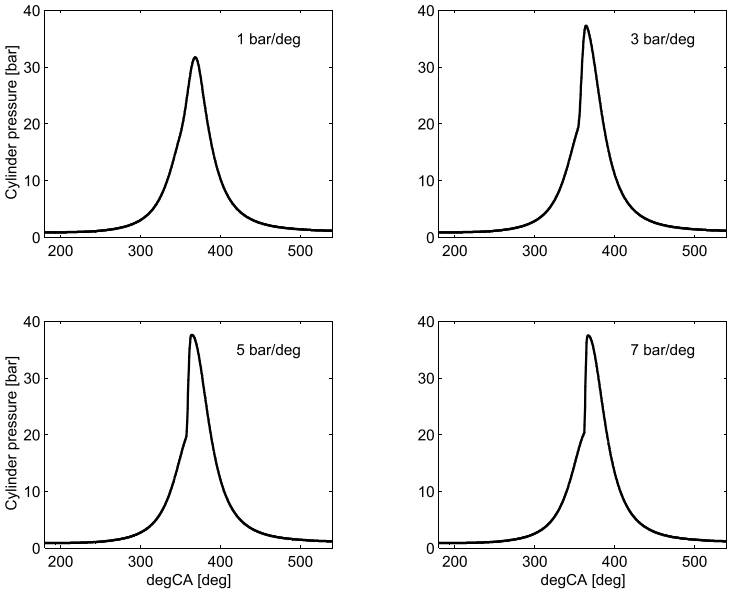

(a) Generated cylinder pressures at 2000rpm, 2bar BMEP, owning different pressure gradients

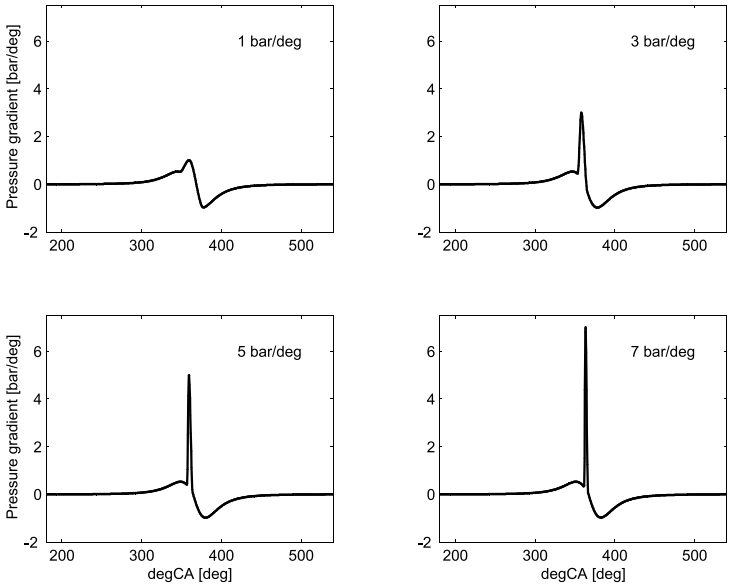

(b) Corresponding pressure gradients of the individual cylinder pressures, depicted in Figure 3.25(a)

Figure 3.25: Artificially generated cylinder pressures and according pressure gradients (2000rpm, 2bar BMEP) for the sensitivity analysis of the Forced-Response model of the piston-pin-connecting rod assembly

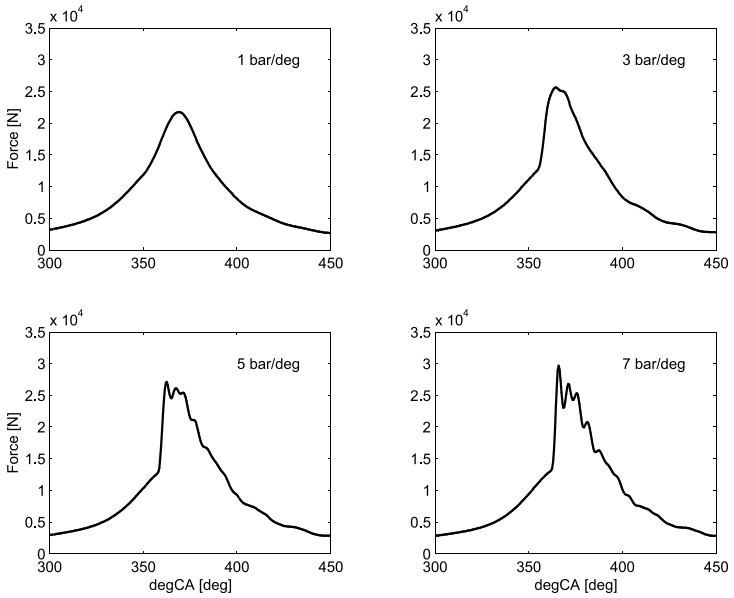

(a) Response of the force F_{dyn} in the connecting rod on the individual cylinder pressure characteristics, depicted in Figure 3.25

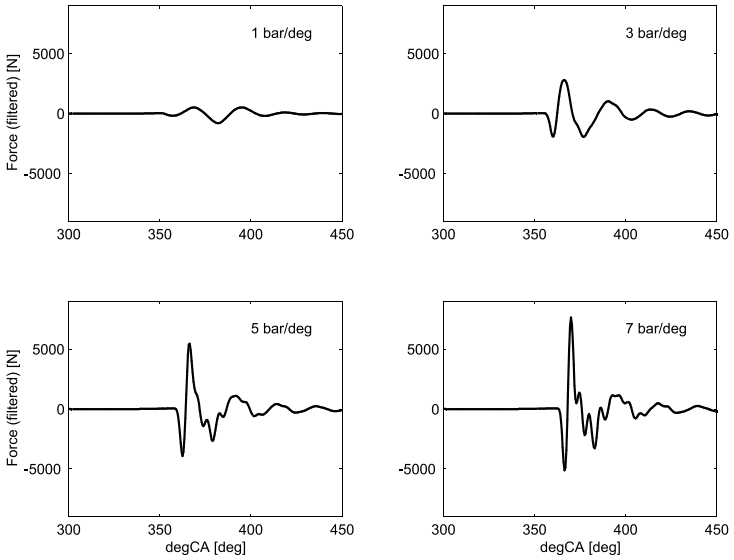

(b) Bandpass filtered response ($f_l = 500Hz, f_u = 3kHz$) of the force in the connecting rod according to the different excitation characteristics

Figure 3.26: Response of the Forced-Response model of piston-pin-connecting rod assembly on the excitation, shown in Figure 3.25

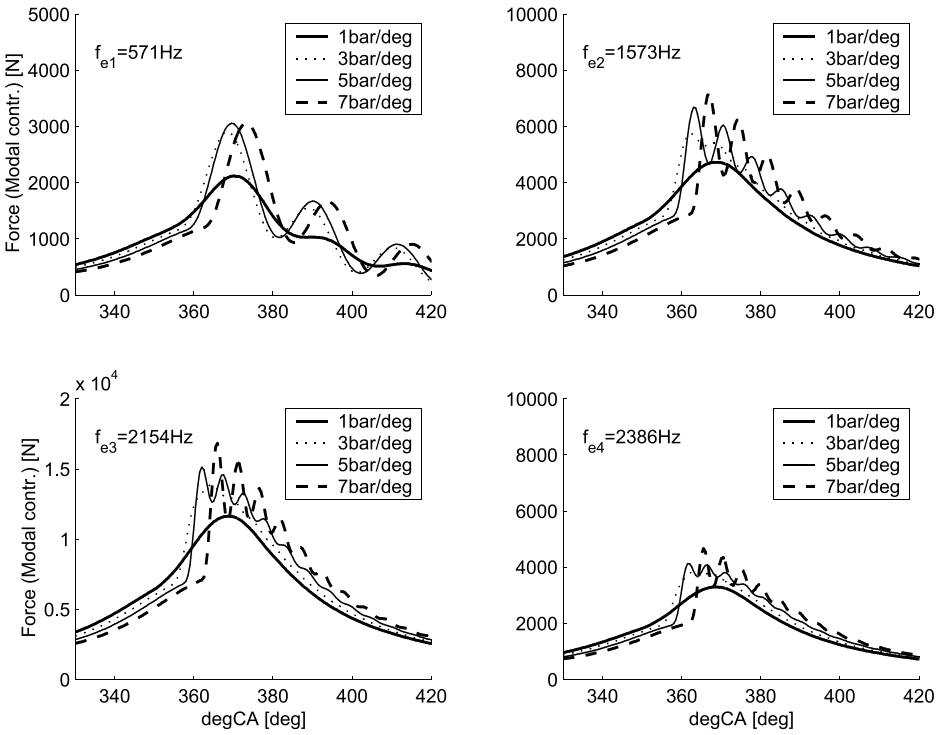

Figure 3.27: Piston-connecting rod assembly: the particular four eigenfrequencies $f_{e1\ldots4}$ related force components as shown in a superimposed manner in Figure 3.26 for the different excitation characteristics according Figure 3.25; note the different scaling of the individual ordinates

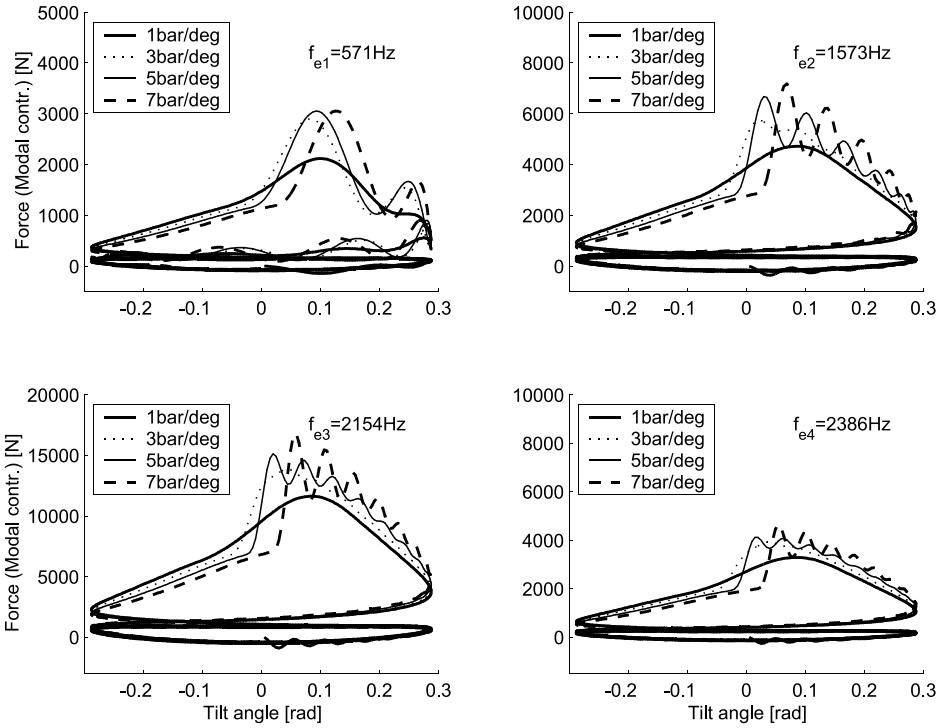

Figure 3.28: The particular four eigenfrequencies $f_{e1\ldots4}$ related force components as shown in a superimposed manner in Figure 3.26 for the different excitation characteristics according Figure 3.25. The forces are drawn versus the tilt angle of the connecting rod; note the different scaling of the individual ordinates. The vibrations for the $1bar/deg$ excitation during the suction stroke are owed to the boundaries at the start of the calculation.

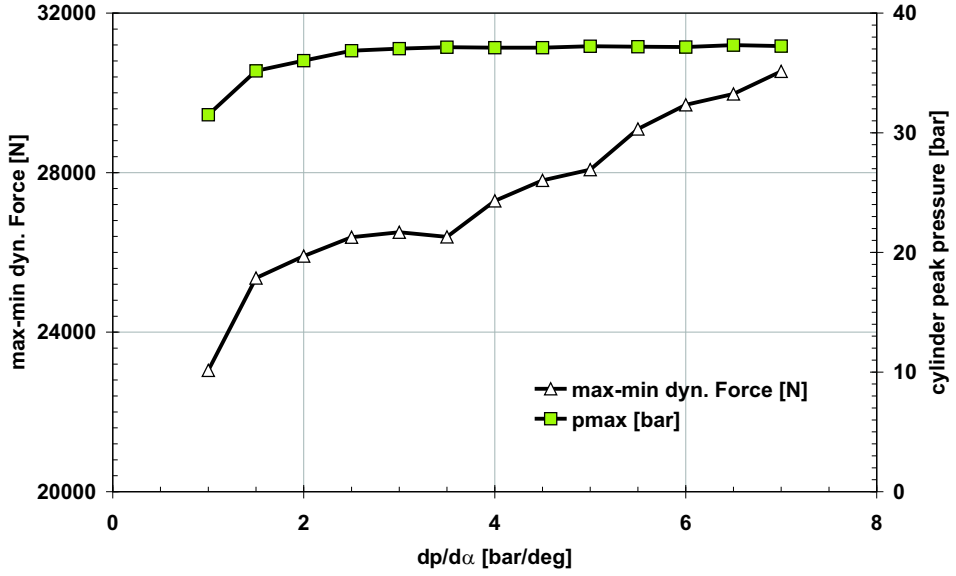

Figure 3.29: Difference of maximum and minimum of the forced response F_{dyn} in the connecting rod for the individual pressure gradients. Also shown is the according peak pressure, gained by simulation

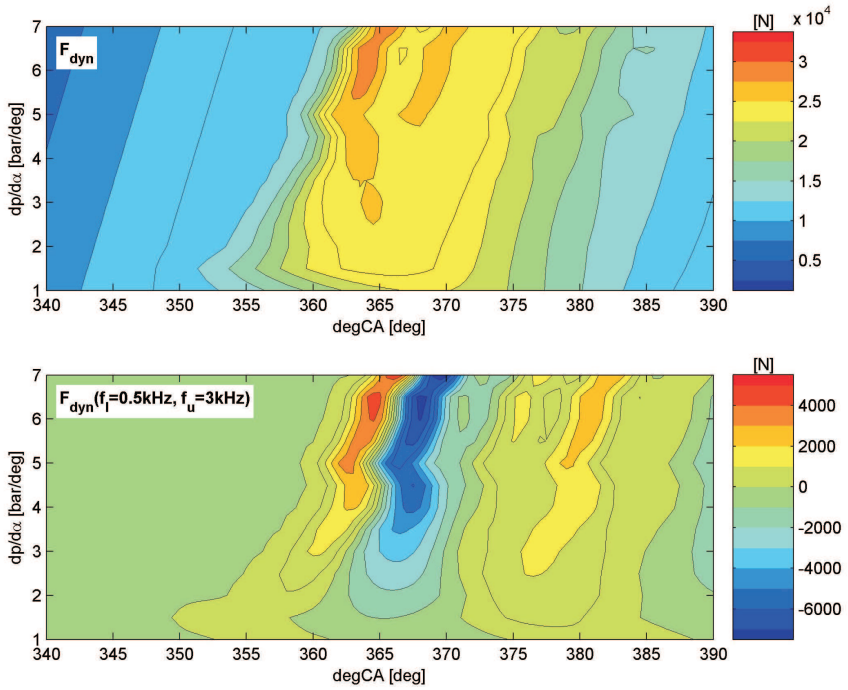

Figure 3.30: Dynamic force in the connecting rod versus crank angle and pressure gradient $\frac{dp}{d\alpha}$ during combustion TDC. Upper half: F_{dyn} as calculated; lower half: a bandpass filter characteristic was applied on F_{dyn} with $f_l = 0.5kHz, f_u = 3kHz$. Please note the different scaling of the individual colorbars, indicating the level of the force in [N]

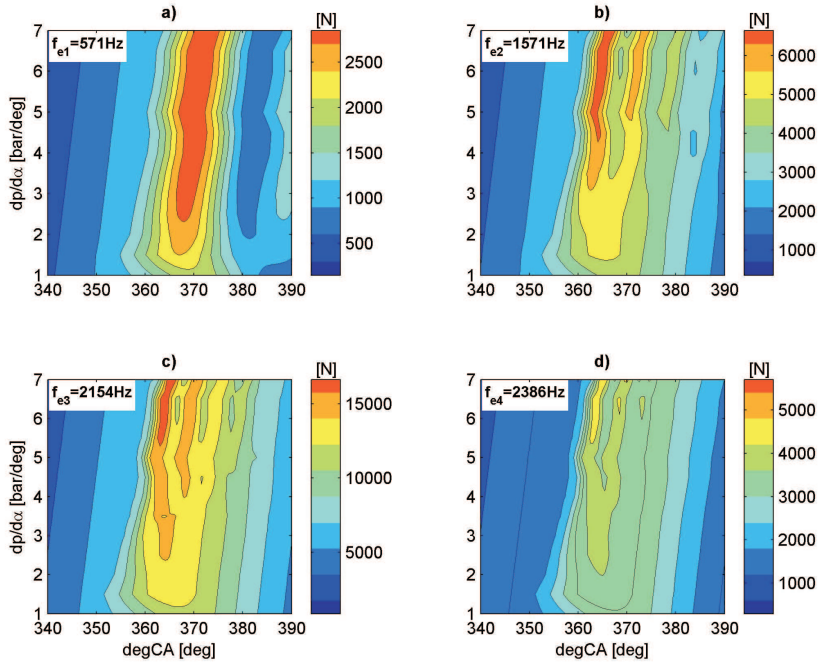

Figure 3.31: The mode related force components contributing to the resulting dynamic force in the connecting rod versus crank angle and pressure gradient $\frac{dp}{d\alpha}$ during combustion TDC. Please note the different scaling of the individual colorbars, indicating the level of the force in [N]

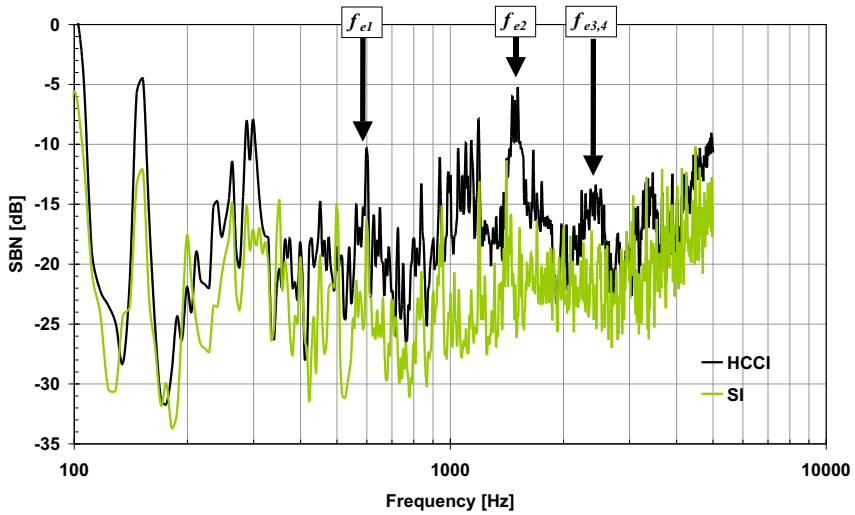

(a) Frequency analysis of a structure-borne signal during SI and HCCI combustion operation; the arrows refer to the frequencies as listed in Tab. 3.2

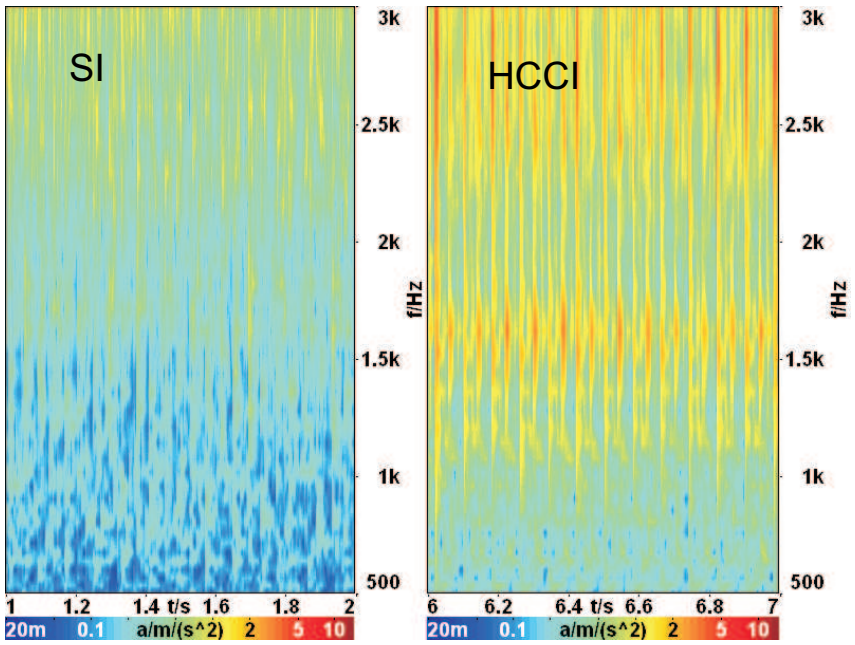

(b) Time-frequency analysis of the structure-borne signal during SI and HCCI combustion operation

Figure 3.32: Structure-borne noise analysis, measured at a stiff location (nearby bottom end at cylinder one), comparison of SI- and HCCI-mode operation at 2000rpm, 2bar BMEP

3.1.5 Excitation of the Main-Bearing

Based on research by Priede [141] it can be assumed that at lower and mid-range engine speeds, i.e. in our case affecting the HCCI operation range, the dynamic force causes elastic impacts in the engine structure, as for example in the crankshaft main-bearing. Moreover, this dynamic force is superimposed on the main bearing force, calculated using the linear approach. Hence the resulting excitation in the main bearing consists of the force component $F_{MBC}(t)$ and the dynamic component $F_{MBdyn}(t)$, which reflects the excitation by the lash and the oil film stiffness in the individual main bearings. The resulting main bearing excitation can then be written as

$$F_{MB}(t) = F_{MBC}(t) + F_{MBdyn}(t). \tag{3.1.85}$$

The force $F_{MBC}(t)$ can be cascaded into gas- and mass-force caused components. Also the dynamic transfer characteristics of the piston-pin-connecting rod subsystem, represented by the force F_{dyn} according to equation (3.1.84) is considered. Thus one can write generally:

$$F_{MBC}(t) = \sqrt{\left(F_{CF}(t) + F_{RAD}(t)\right)^2 + F_T(t)^2}. \tag{3.1.86}$$

The particular forces can be calculated according to equation (3.1.28), (3.1.87) and (3.1.88) as follows:

Centrifugal Force $F_{CF}(t)$: acting at the crank, caused by the mass m_{CRBE} of the big end bearing end of the connecting rod, and the residual unbalanced mass Δm_{UBCR} as the difference of the mass m_{CRP} of the crank-pin and the mass of the opposite counterweight, m_{CW}, i.e. $\Delta m_{UBCR} = m_{CRP} - m_{CW}$:

$$F_{CF}(t) = r \cdot \omega(t)^2 \cdot \left(m_{CRBE} + \Delta m_{UBCR}\right). \tag{3.1.87}$$

Radial Force $F_{RAD}(t)$: this radial force acts along the the crank to the center of the crankshaft:

$$F_{RAD}(t) = -F_{dyn}(t) \cdot \left(\frac{\cos(\alpha + \psi)}{\cos\psi}\right). \tag{3.1.88}$$

In equation (3.1.88) the parameter ψ reflects the tilt angle of the connecting rod relative to the liner. The tilt angle is defined as follows [122]:

$$\psi = \arcsin(\lambda \cdot \sin\alpha). \tag{3.1.89}$$

The dynamic force component $F_{MBdyn}(t)$ of the crankshaft, acting on the bearings, is considered as a spring-mass system with linear damping. According to the theory of an ideal elastic impact [155], the energy balance for a mass m with a velocity of v at the point of impact, hitting a spring of stiffness c, can be written as according to the three phases depicted in Figure 3.33(a) to Figure 3.33(c):

$$\frac{1}{2} \cdot m \cdot v^2 = \frac{1}{2} \cdot \hat{F} \cdot \hat{x} = \frac{1}{2} \cdot \frac{\hat{F}^2}{c}. \tag{3.1.90}$$

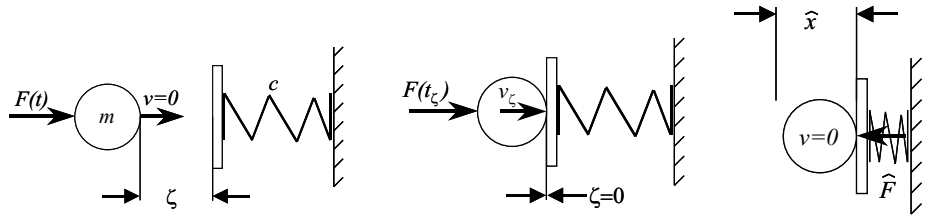

(a) Force $F(t) = 0$, thus $v = 0$

(b) Point of time, when mass traveled through the complete clearance, thus $x = \zeta$

(c) Point of maximum of the impact force: $\hat{F} = \hat{x} \cdot c$

Figure 3.33: Model of the elastic impact

Hence the amplitude of the impact force can be calculated (3.1.91):

$$\hat{F} = \sqrt{m \cdot v^2 \cdot c}. \tag{3.1.91}$$

To calculate the impact velocity v_i of the mass during the contact-time t_ζ reaching the clearance ζ, Newton's law $m \cdot \ddot{x} = \frac{dF}{dt} \cdot t$ can be taken. Thus, the first integration delivers

$$\dot{x} = \left(\frac{\frac{dF}{dt}}{2 \cdot m} \right) \cdot t^2. \tag{3.1.92}$$

and the second integration then yields the actual position x:

$$x = \left(\frac{\frac{dF}{dt}}{6 \cdot m} \right) \cdot t^3. \tag{3.1.93}$$

At the time $t = t_\zeta$ the mass has traveled along the distance $x = \zeta$, which means the mass hits the other border of the clearance ζ at the time t_ζ (Figure 3.33(b)). Thus one can write for the time-span t_ζ, during which the mass m travels through the clearance, using equation (3.1.93):

$$t_\zeta = \left(\frac{\zeta \cdot 6 \cdot m}{\frac{dF}{dt_\zeta}} \right)^{\frac{1}{3}}. \tag{3.1.94}$$

However, the velocity $v_\zeta = \dot{x}_\zeta$ when reaching the end-stop of the clearance can be written according to equation (3.1.92):

$$\dot{x}_\zeta = \left(\frac{\frac{dF}{dt_\zeta}}{2 \cdot m} \right) \cdot t_\zeta^2. \tag{3.1.95}$$

Inserting equation (3.1.94) in (3.1.95) yields

$$\dot{x}_\zeta = \frac{\frac{dF}{dt_\zeta}}{2 \cdot m} \cdot \left(\frac{6 \cdot \zeta \cdot m}{\frac{dF}{dt_\zeta}} \right)^{\frac{2}{3}}, \tag{3.1.96}$$

or alternatively one can write

$$\dot{x}_\zeta = \left(\frac{\left(\frac{dF}{dt_\zeta} \right)^{\frac{3}{2}} \cdot 6 \cdot \zeta \cdot m}{2^{\frac{3}{2}} \cdot m^{\frac{3}{2}} \cdot \frac{dF}{dt_\zeta}} \right)^{\frac{2}{3}}. \tag{3.1.97}$$

Simplifying (3.1.97) yields

$$\dot{x}_\zeta = \left(\frac{\left(\frac{dF}{dt_\zeta} \right)^{3} \cdot 6^2 \cdot \zeta^2 \cdot m^2}{2^3 \cdot m^3 \cdot \left(\frac{dF}{dt_\zeta} \right)^{2}} \right)^{\frac{1}{3}}, \tag{3.1.98}$$

and finally, introducing the gradient of the excitation F_{MBC}:

$$v = \left(9 \cdot \frac{\frac{dF_{MBC}}{dt_\zeta}}{2} \cdot \frac{\zeta^2}{m} \right)^{\frac{1}{3}}. \tag{3.1.99}$$

Combining (3.1.91) and (3.1.99) one can calculate the impact force $\hat{F}$:

$$\hat{F} = \left(\frac{81}{4} \cdot \left(\frac{dF_{MBC}}{dt_\zeta} \right)^2 \cdot \zeta^4 \cdot m \cdot c^3 \right)^{\frac{1}{6}}. \tag{3.1.100}$$

It should be mentioned that the model is formulated under the assumption of an ideal elastic impact. During such an event the force obeys the shape of a half-sinus-wave. Also the duration of the impact τ is short and independent of the impact velocity, thus it is at the moment of the impact (Figure 3.33(b)): $\tau \propto \sqrt{m/c}$. Because of the short impact time the resulting spectrum has constant amplitudes until high frequencies [70]. Hence the amplitude can be estimated by a coefficient A:

$$A = \int_0^\tau F_{Impact}(t) dt. \tag{3.1.101}$$

However, considering the maximum amplitude of the half-sinus-wave one can write:

$$A = \frac{2}{\pi} \cdot \hat{F} \cdot \tau. \tag{3.1.102}$$

Hence it can be written:

$$A \propto \hat{F}. \tag{3.1.103}$$

When considering the exciting force in the time domain independently from the point of time of the impact, equation (3.1.100) can also be written as a general function in the time-domain t. This yields equation (3.1.104) to calculate the force in the main bearing, F_{MBdyn}:

$$F_{MBdyn}(t) = \left(\frac{81}{4} \cdot \left(\frac{dF_{MBC}}{dt} \right)^2 \cdot \zeta^4 \cdot m \cdot c^3 \right)^{\frac{1}{6}}. \tag{3.1.104}$$

To quantify the impact of the non-linear force, a comparison between $F_{MBC}(t)$ and $F_{MBdyn}(t)$ was carried out. The result, simulated for two cycles, is shown in Figure 3.34. When comparing the level of the main bearing force $F_{MBC}(t)$ with

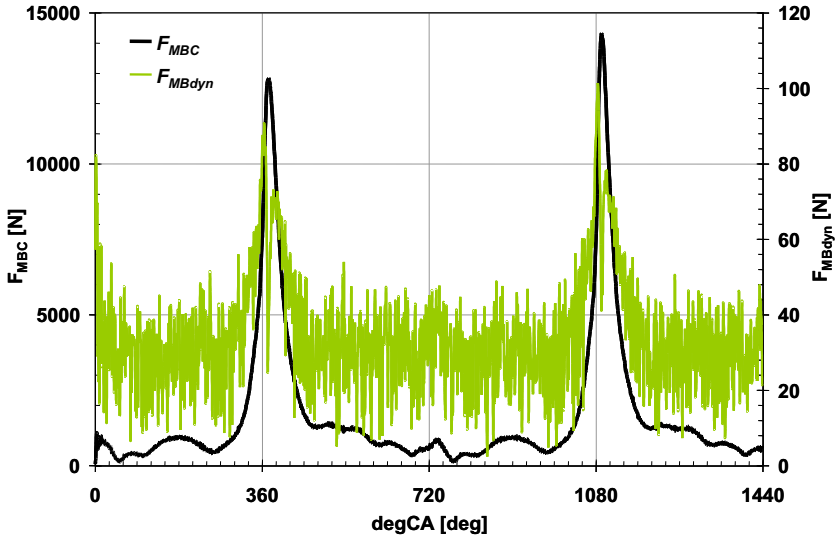

Figure 3.34: Forces in the main bearing: comparison of the force F_{MBC} according to equation (3.1.86) and the non-linear contribution of $F_{MBdyn}(t)$ according to equation (3.1.104). Time traces calculated for SI-operation at 2000rpm, 2bar BMEP, dp/dα =1.5bar/deg

the non-linear force component $F_{MBdyn}(t)$, the contribution of $F_{MBdyn}(t)$ can be considered low. However, to quantify its impact on the resulting force $F_{MB}(t)$ and its importance for the excitation spectrum, the resulting main bearing force is

compared to the complete linear approach as shown in the following Figure 3.35(a). Finally the exciting force-level L_{MB} in the crankshaft bearing can be calculated, assuming a reference force $F_0 = 1N$:

$$L_{MB}(t) = 20 \cdot log\left(\frac{F_{MBdyn}(t) + F_{MBC}(t)}{F_0}\right) = 20 \cdot log\left(\frac{F_{MB}(t)}{F_0}\right). \qquad (3.1.105)$$

Furthermore, transforming (3.1.105) into the frequency domain, for each particular frequency band i one can finally write

$$L_{MB}(f_i) = 20 \cdot log\left(\frac{F_{MB}(f_i)}{F_0}\right). \qquad (3.1.106)$$

The resulting excitation spectra when processing the linear- and the non-linear calculated main bearing force are depicted in Figure 3.35(b). It can be concluded that this approach leads to a share of excitation level at frequencies above 400Hz. When comparing the results achieved by equation (3.1.106) with results based on the Föller approach as published in [148], the excitation spectrum achieved with equation (3.1.106) shows a higher excitation level at frequencies above 500Hz than the Föller approach. This is because the method used in [148] considers the force without considering any impacts, thus neglecting the decrease of slope in the excitation spectrum above a certain frequency as described in Chapter 3.1 and by Müller et al. in [72], where the slope of the spectrum is considered independently of lash and contact force. However, this particular contribution can be considered as significant when using the excitation data for further signal processing, as for example in an analysis of a sound-quality parameter.

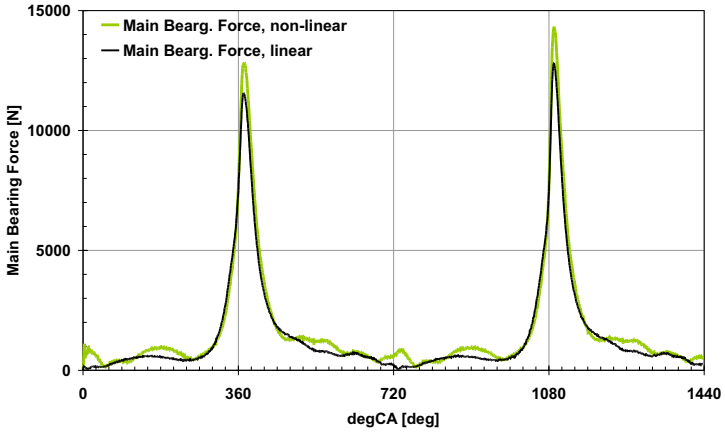

(a) Comparison of the linear- and the non-linear main bearing force

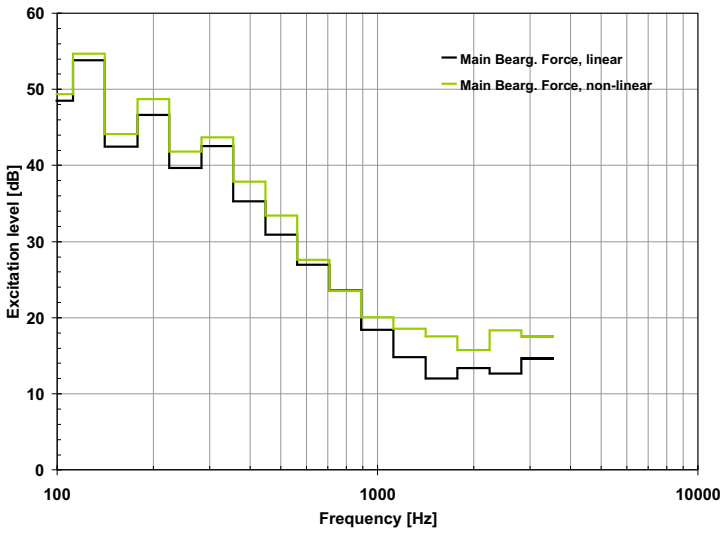

(b) Resulting third octave spectra of the linear and the non-linear approach

Figure 3.35: The impact of the non-linear force approach on the main bearing excitation during SI-operation at 2000rpm, 2bar BMEP

3.1.6 Valve Train Noise

Noise caused by the valve train originates from forces occurring in the contact of tappet and cam. Due to the acting forces and involved masses, which are low compared to piston, connecting rod or crankshaft, it contributes to the engine noise mostly at frequencies above $1kHz$ [63]. To investigate the impact of valve train geometry and involved masses and stiffness, Suh developed a simple one degree of freedom (1 DoF) model to predict the valve train excitation [63]. Figure 3.36 illustrates a sketch of a typical overhead cam drive (Figure 3.36(a)) and an according model (Figure 3.36(b)) that was derived as a base for detailed valve train dynamic investigations by Phlips et al. [64]. The kinematic force $F_{VT}(t)$ in the system can be

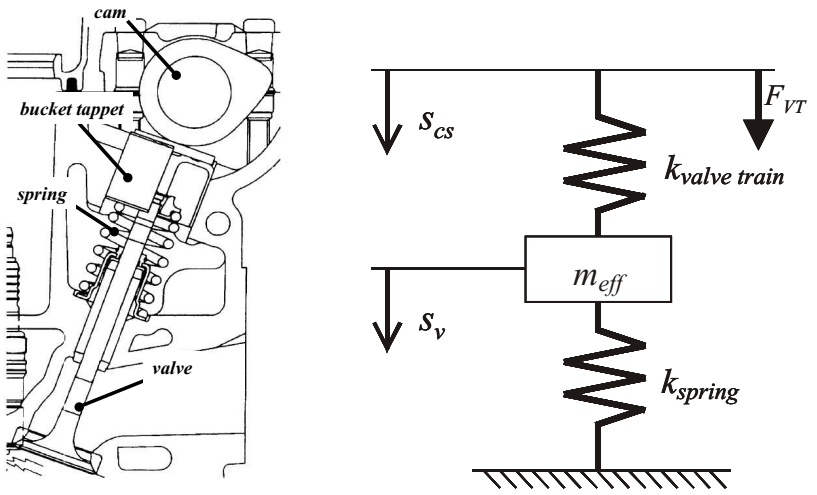

(a) A typical overhead cam drive with direct actuated bucket tappet

(b) Simple model of a valve train with one DoF according to [63] and [64] to calculate the kinematic force $F_{VT}(t)$ in the valve train

Figure 3.36: Sketch of a modern valve train and according 1 DoF model

written considering the displacement of the valve-spring S_0 due to pre-compression:

$$F_{VT}(t) = m_{eff} \cdot \frac{\partial^2 s_{cs}}{\partial t^2} + k_{spring} \cdot (s_{cs} + S_0)\,. \tag{3.1.107}$$

Introducing the resulting displacement s_{res}, which is defined by

$$s_{res}(t) = s_v(t) - s_{cs}(t), \tag{3.1.108}$$

and re-writing the stiffness to effective mass ratio as the natural frequency of the system ω_V, one can write instead of equation (3.1.107) for the kinematic force the

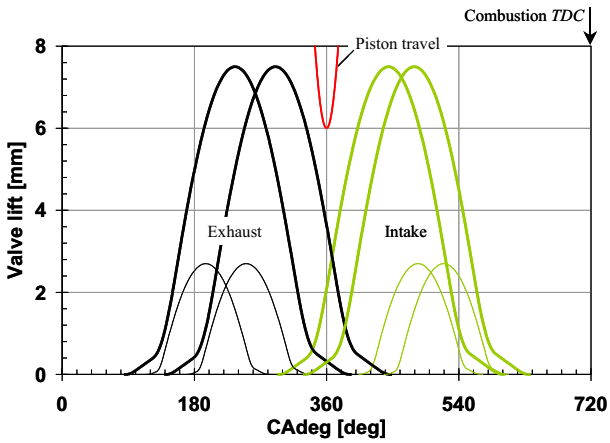

Figure 3.37: Valve lift for low profile (HCCI operation, thin line) and high profile cam for SI-operation. Please note that the individual cam lift curves are representing the range in which both cams can be varied with the cam phasers; black represents the exhaust cam, the bright line-color the intake cam profile

following equation:

$$F_{VT}(t) = m_{eff} \cdot \left[\frac{\partial^2 s_{res}}{\partial t^2} + \omega_V^2 s_{res}(t) \right]. \tag{3.1.109}$$

The displacement s_v is represented by the cam-lift curve, and the natural frequency-induced displacement s_{cs} can be gained from a forced response analysis of the camshaft in its journal bearings. Usual values for the natural frequency of modern double overhead camshaft in-line four cylinder engines are in the region of 2000Hz [64]. Thus, it is expected that this particular eigenfrequency plays only a minor role during low speed operation of the engine here. However, once the natural frequency of the camshaft system is known one can calculate the system dynamics using the forced-response method as already used for the piston-connecting rod model. Finally, for a directly actuated bucket tappet valve train the effective mass m_{eff} can be gained by adding the mass of the bucket-tappet and one third of the individual valve mass [122]. As was already mentioned, a two profile and -lift valve train system is suited on the cylinder head to effect HCCI using the NVO-strategy (Figure 3.37). Note that both intake and exhaust shaft have the same cam profiles.
Evaluating the individual deflection, velocity and acceleration of a valve at an engine speed of 2000rpm, the individual resulting valve dynamics acting during SI- and HCCI-operation are shown in the following Figure 3.38. Processing equation (3.1.109) and transferring the results into the frequency domain, the level of the

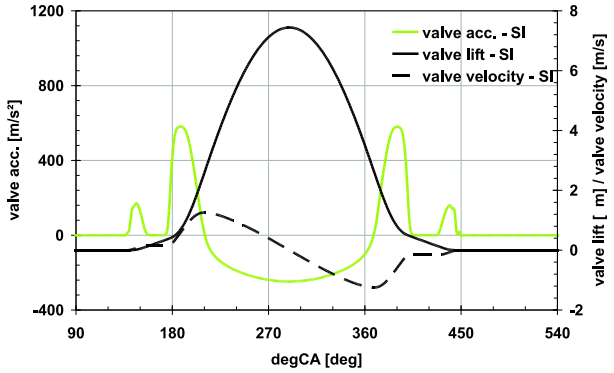

(a) SI-cam profile: valve displacement, velocity and acceleration at 2000rpm

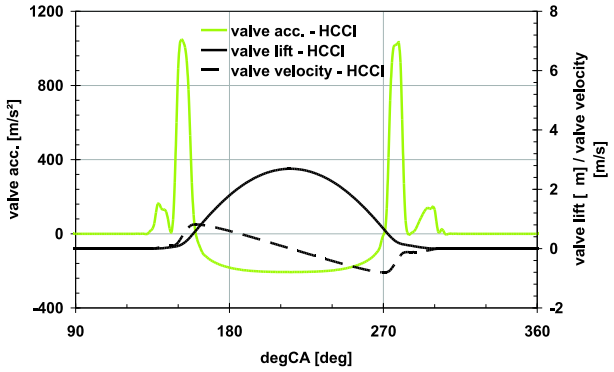

(b) HCCI-cam profile: valve displacement, velocity and acceleration at 2000rpm

Figure 3.38: Comparison of valve dynamics during SI- and HCCI-operation

valve-train excitation L_C of each individual frequency i band can be written:

$$L_C(f_i) = 20 \cdot log\left(\frac{F_{VT}(f_i)}{F_o}\right). \tag{3.1.110}$$

When using equation (3.1.110), the difference between the excitation at 2000rpm engine speed of the SI compared to the HCCI cam can be calculated, as shown in Figure 3.39. In contrast to the lower lift during HCCI, which leads to a lower harmonic of the engine-speed related amplitude at 142Hz, the increased level of valve acceleration due to the higher slope of the cam at the beginning of the valve opening and closing leads to a higher level of excitation for the HCCI cam, and consequently to an increased contribution at frequencies above 300Hz.

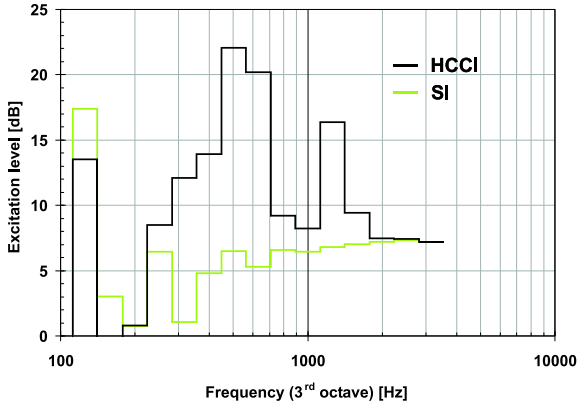

Figure 3.39: Excitation level of SI and HCCI cam profile at 2000rpm engine speed

3.2 Engine Noise Analysis

The engine noise prediction method should be able to predict the radiated noise level, the noise spectrum and relevant psychoacoustic parameters. This should be gained from the information delivered by the cylinder pressure, the structure attenuation, load dependent transfer functions and geometric data. In detail, the prediction method delivers:

Sound Pressure Level. The sound pressure level is the most common and simplest approach to judge whether the engine acoustics are changed when for instance a new combustion system is applied.

Third-Octave Spectrum. The third-octave spectrum is calculated to characterize the cylinder pressure excitation, the internal forces and the radiated noise level.

Roughness. The value of Roughness will be gained from the calculated engine noise. This is done according to the algorithm published by Aures [81].

Impulsiveness. This sound quality aspect characterizes the impulsiveness of the engine noise, such as the clattering sound of compression-ignition engines. This characteristic has been chosen to weight the noise trade-offs during HCCI combustion development compared to SI-operation.

According to Figure 3.1, Figure 3.40 below shows the sub-process of calculation of the two particular noise contributors, the combustion- and the indirect combustion noise. The individual signal processing is described and discussed in the following

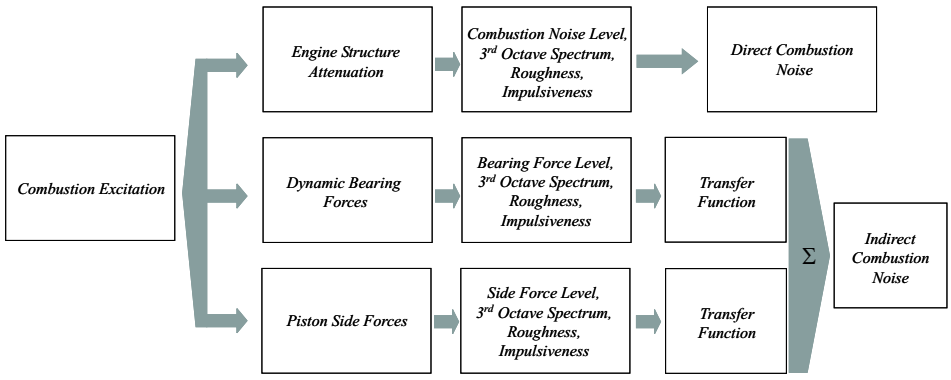

Figure 3.40: Sub-process to calculate the direct and indirect combustion noise based on measured cylinder pressures

subsections.

3.2.1 Noise Level and Third-Octave Spectrum

The noise level, as for example the sound pressure level, can be estimated when the attenuation level of the engine structure is known. As a first measure, this value can provide information about whether a modification of the engine would have an impact on the engine-radiated noise. But it can be shown easily that a decision of whether the radiated noise can be considered as acceptable or not is not just a question of its noise level [85]. Hence it is important to know the spectral content of the noise. Normally this can be done by processing a spectral analysis of the noise, using Fast-, or Discrete-Fourier-Transformation (FFT, DFT; [69]) or, for impulsive signals, as it is a single combustion excitation event, the wavelet analysis [12]. Based on such data processing, further investigations can be carried out to analyse whether certain frequencies will change due to modifications of the engine structure or combustion system. For example the impact of structure refinement can be assessed using this information. However, to achieve a better visibility of the calculated results while bearing in mind the data processing time of the noise prediction routine, these spectra are used to be calculated in third-octave resolution.

Due to its characteristics, the human ear not only receives the amount of noise and sound as a level and its frequency content. Therefore, it is necessary to develop a metric to describe the transient time-frequency characteristics of the engine noise, i.e. a sound-quality metric. Such important metrics for internal combustion engines are mainly the roughness for gasoline engines, and the impulsiveness, mostly perceived from diesel engines, especially during cold start conditions. Thus a main aspect in the field of Psychoacoustics is to develop metrics that reflect the necessary spectral and time resolution of signals to model the sensitivity of the human ear appropriately. Two models of such a type are shown in the following two sections.

3.2.2 Psychoacoustic Parameters

The psychoacoustic parameters derived in the following section are based on two different signal-processing procedures. The Roughness is gained by the approach published by Aures [81], and the Impulsiveness is derived based on the Narrow-Band-Modulation approach [84]. Both methods are well correlated with the perception of the human ear as for example shown in [30, 81, 84]. This is important because the prediction method delivers a time signal indeed, and even though it is processed using the transfer functions, its quality is not suitable for a proper binaural assessment

later. This is mainly linked to the sample rate, dependent on the chosen crank-angle resolution of $1 deg CA$, which would mean for example an upper frequency border of $4.5 kHz$ at 1500rpm. Therefore both measures are intended to give a direction of the evolution of the engine noise regarding sound quality during the combustion system and control strategy development on the dynamometer. However, based on current knowledge, for instance represented by the publications [30, 35, 81, 84], the break-down of psychoacoustic parameters to combustion parameters apparently requires further research. Subsequently to Chapter 3, the analysis of the combustion data in Chapter 4 will diminish this gap appropriately.

3.2.2.1 Roughness - Signal-Envelope Analysis

Based on published results of experiments, e.g. by [74, 75, 80, 81, 82], roughness can be perceived by the human ear as a modulation of a noise signal. Figure 3.41 shows a modulated noise signal, whereby ΔL reflects the "masking depth", and f_{mod} its frequency of occurrence. However, below a modulation frequency of f_{mod}=4Hz

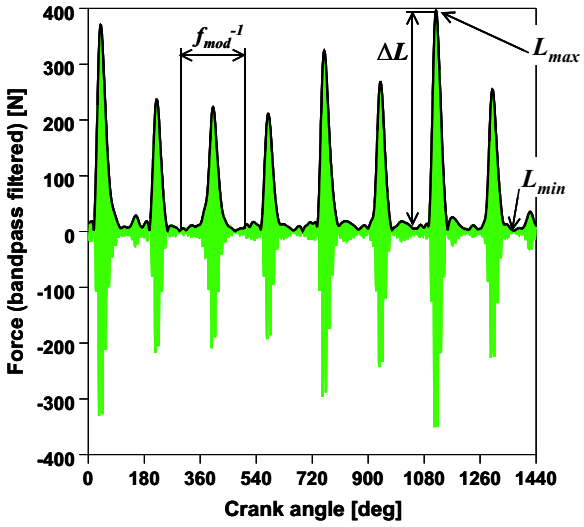

Figure 3.41: Noise signal, modulated with the frequency f_{mod} and definition of masking depth ΔL with according L_{max} and L_{min}; the black line represents the envelope

the human ear perceives the signal as fluctuation, above 15Hz, until its resolution capability at approximately f_{mod}=300Hz, it is called "Roughness" [75]. Above 300Hz the fluctuations are not perceived anymore. As a result of the characterization of the modulated signal presented in Figure 3.41, the roughness R is proportional to

the modulation frequency f_{mod} and the level of the amplitude of its envelope or masking depth, ΔL:

$$R \propto f_{mod} \cdot \Delta L. \tag{3.2.1}$$

However, Zwicker did also investigations to describe the ability of the human ear with regard to frequency resolution. This was done because psychoacoustic experiments had shown that experimental results correlated better with the sensation of the test persons when introducing frequency bands, that are more related to the ability of the human ear to distinguish between individual frequencies and masking noises [73, 74, 82].

On the basis of the ear model from Helmholtz in 1863, Trendelenburg published a principal model of the human ear in 1939, as illustrated in Figure 3.42. At this the human ear transfers noise, i.e. a pressure fluctuation of the air, into a sensation as described as follows: the sound pressure, denoted by Δp, excites the ear drum, which in turn transfers the excitation via malleus and incus into the cochlea. The vibrating incus then excites the stapes, which in turn leads to pressure fluctuations of the lymph fluid in form of a propagating wavefront in the cochlea (the pressure fluctuations of the liquid are compensated by the elastic oval window). Furthermore, the fluctuation of the lymph fluid provokes vibrations of the basilar membrane. Depending on the wavelength of the pulsation, the basilar membrane responds with an amplitude at a certain location. This vibration then is picked up by the nerve cells of the Nervus Akusticus, finally transforming the mechanical vibrations into electric signals. Békésy carried out experiments on cochlea cadavers to search for

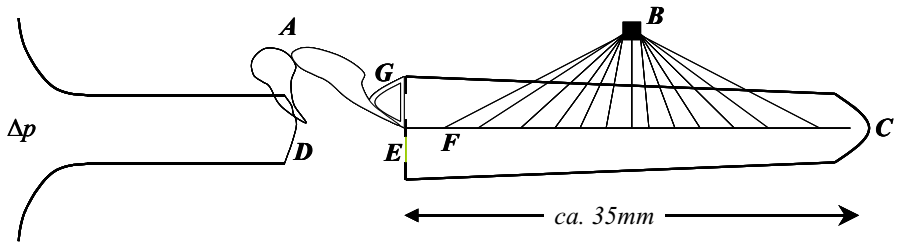

Figure 3.42: Simplified schematics of the anatomy of the human ear according to [73]: Δp - pressure fluctuation (sound pressure), occurring in the external auditory meatus, A - Malleus and Incus, B - Nervus Akusticus, C - Cochlea, filled with lymph fluid, D - Ear Drum, E - Round Window, F - Basilar Membrane, G - Stapes, connected to the Oval Window

the dependency of exciting frequency and location of perception along the basilar

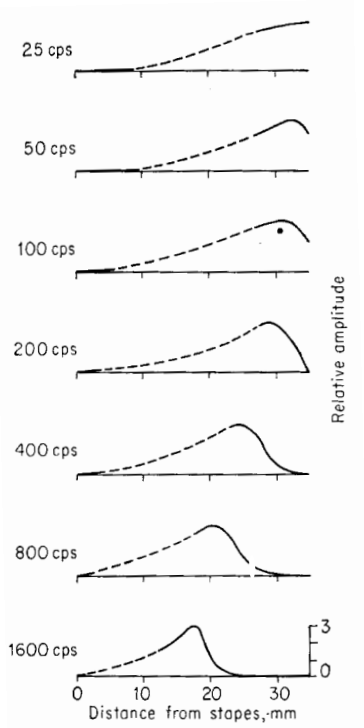

Figure 3.43: Location of sensation at noises (sinusodial pure tone) of different stimulating frequencies along the basilar membrane by the Nervus Akusticus, taken from [74]. The higher the stimulating frequency, the nearer is its perception at the oval window. Please note that the unit '*cps*' is similar to 'Hz'. The individual signals are characterized by the according envelope of the propagating wavefront

membrane. He revealed that the higher the frequency, the nearer is the response to the oval window, as depicted in Figure 3.43, taken from [74]. According to the findings by Békésy it was concluded that the human ear can be considered as a parallel arrangement of bandpass filters, having different bandwidths. However, the dependency of the intensity of vibration of the basilar membrane on different sound pressure intensities was then published in 2000 by Eguíluz et al. [83]. Based on experiments with a laser-vibrometer on an inner ear of a chinchilla they found out that the basilar membrane responds essentially nonlinear to a linear variation of the noise intensity. They assumed that this may be evoked by chemical fluid reactions taking place in the membrane. This reaction then stiffens the membrane at higher sound pressure intensities to prevent it from getting damaged, but also lowers its stiffness to increase the ability of receiving signals with a very low intensity. This is in contrast to the results of Békésy in 1960, who stated a linear vibrational behavior of the membrane [74]. Thus, to adapt the auditory signal processing better to the ability of the human ear in the field of Psychoacoustics, the critical band width 'Δf_G' was introduced. The critical band width can be written as dependent of the

frequency (3.2.2) according to [75], as it is also possible with the critical band rate 'z', owning the unit 'Bark' [4], (3.2.3).

Critical bandwidth $\Delta f_G(f)$:

$$\Delta f_G(f) = 25 + 75 \cdot \left(1 + \frac{f^2}{1.4}\right)^{0.69} \tag{3.2.2}$$

Critical band rate $z(f)$:

$$z(f) = 13 \cdot arctan(0.76 \cdot f) + 3.5 \cdot arctan\left(\frac{f}{7.5}\right)^2 \tag{3.2.3}$$

Please note that in (3.2.2) and (3.2.3) the frequency is of the unit 'kHz'. Furthermore it should be noted that the critical band rate $z(f)$ preferably refers to an integer number in the interval between 1 to 24. This follows that equation (3.2.3) should be re-arranged such that the critical band is an integer number, following then the corresponding centre frequency f. As shown in Figure 3.44(a) the critical bandwidth Δf_G as a function of frequency remains constant from 100Hz until f =500Hz. Above the slope is approximately of $0.2 \cdot f$, which is similar to that of a third octave filter with a slope of $0.23 \cdot f$. Grouping the particular bandwidths leads to the Bark-scale. The Bark-scale is defined by equation (3.2.3), and is shown as a function of frequency in Figure 3.44(b). Again, it can be seen that the human ear has a linear scale until 500Hz as it can be drawn from the step-width of 100Hz until 500Hz. Above that, it follows a logarithmic sensitivity scale. To calculate the roughness from a given signal different procedures are known such as from Zwicker and Terhardt [75, 82], or as published later by Aures in 1985 [81]. However, it has been demonstrated by Essers et al. that the Aures approach shows a better correlation of the calculated and the perceived auditory roughness [30]. Consequently this approach was chosen to calculate the roughness for the calculated engine noise. The signal flow of the according calculation procedure is depicted in Figure 3.45.

Firstly the calculated excitation will be weighted with the according noise transfer function. Secondly an A-weighting will be applied to consider the sensitivity regarding frequencies of the human ear. Thirdly the signal will be bandpass-filtered according to the critical band criterion. Then its envelope $h_{E,i}$ at each critical band

[4] 'Bark': Physicist Heinrich *Bark*hausen (1881 - 1956).

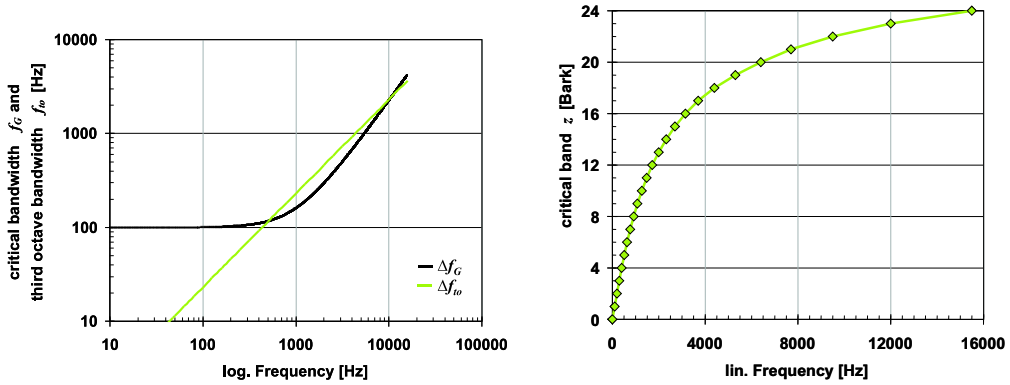

(a) Critical bandwidth Δf_G and bandwidth of third octave band Δf_{to} versus frequency

(b) Critical band rate z (Bark) versus frequency

Figure 3.44: Relationship of critical bandwidth Δf_G and critical band rate z with the frequency

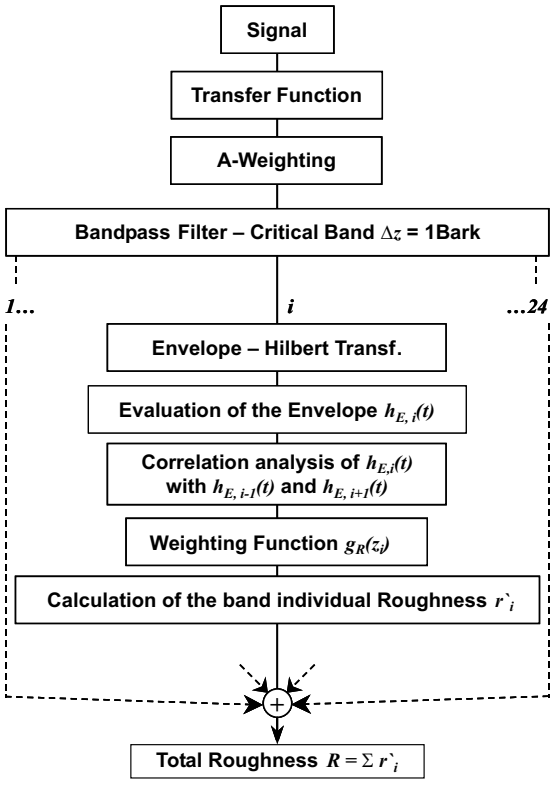

Figure 3.45: Signal flow for the calculation of roughness as proposed by Aures [81]. Please note: in contrast to Aures the envelope is now calculated using the Hilbert transformation

z_i is calculated. It is common in the field of signal processing to calculate the envelope by using the Hilbert-transformation [11]: by definition the Hilbert transform or also so-called Hilbert transform filter of a signal $x(t)$ is its convolution with $1/\pi t$. The result is denoted as $\hat{x}(t)$:

$$\hat{x}(t) = \frac{1}{\pi \cdot t} * x(t) \tag{3.2.4}$$

According to Fahy et al. in [11] this means that for example the Hilbert transform of $\cos \Omega t$ is $\sin \Omega t$, or that of $\sin \Omega t$ is $-\sin \Omega t$. Furthermore, more complicated signals can be expressed as a sum of sinusoids. Thus, when applying the Hilbert transform filter H_t each sinusoid component is shifted by a quarter of a cycle. It is worthwhile to mention that the filter has the magnitude of 1 at all frequencies. In addition, the filter applies a phase shift of $-\pi/2$ at each positive frequency, and a phase shift of $+\pi/2$ at each negative frequency. Furthermore, the Hilbert transform is also applicable in the frequency domain, so it can be then generally written for a Hilbert-transformed signal $\hat{X}(\omega)$:

$$\hat{X}(t) = H(\omega) \cdot X(t), \tag{3.2.5}$$

with the following case branch:

$$\begin{array}{lll} H_t(\omega) = j & \text{for} & \omega < 0, \\ = -j & \text{for} & \omega > 0, \\ = 0 & \text{for} & \omega = 0\ . \end{array}$$

To calculate the envelope, i.e. the 'instantaneous frequency' of a signal $x(t)$, it is combined with its Hilbert-transform $\hat{x}(t)$ as already written in equation (3.2.4). This leads to the so called 'pre-envelope' signal $\sigma_x(t)$ of $x(t)$ in the time domain:

$$\sigma_x(t) = x(t) + j\hat{x}(t). \tag{3.2.6}$$

Equation (3.2.6) can be also expressed as:

$$\sigma_x(t) = A_x(t) \cdot e^{j\phi_x(t)}. \tag{3.2.7}$$

The instantaneous amplitude of the signal, thus its envelope $A_x(t)$, can be extracted, and it can be written for the envelope signal:

$$A_x(t) = \sqrt{x^2 + \hat{x}^2}. \tag{3.2.8}$$

However, this means that when a Hilbert-transform of a signal $x(t)$ is processed, the absolute of the real part of the Hilbert transformed $\hat{x}(t)$ reflects its envelope signal. The following Figure 3.46 illustrates an analysis of the individual critical bands and the according envelopes. Moreover, in our case one can write assuming an input signal $f(t)$:

$$h_{E,i}(t) = \sqrt{f_i^2 + \hat{f}_i^{\,2}}. \tag{3.2.9}$$

The degree of modulation m of a signal can be defined as (Figure 3.41):

$$m = \frac{L_{max} - L_{min}}{L_{max} + L_{min}}, \tag{3.2.10}$$

which means in our case for each band i:

$$m_i = \frac{L_{max}(h_{E,i}) - L_{min}(h_{E,i})}{L_{max}(h_{E,i}) + L_{min}(h_{E,i})}. \tag{3.2.11}$$

However, it will be shown that the degree of modulation can be processed by the fraction of effective- and the mean-value of the signal, too. This method has the advantage of a better reflection of the fluctuations over time of the signal during the time-window analysis of the effective-value. Once the degree of modulation is known, the according masking depth ΔL can be derived. Based on results of a study carried out by Vogel [80] the degree of modulation and the related masking depth ΔL has a non-linear characteristic with regard to the perception by the human ear. Thus it can be calculated by using the equation as published for example in [75, 76, 80]:

$$\Delta L = 20 \cdot log\left(\frac{(1+m)}{(1-m)}\right). \tag{3.2.12}$$

The evaluation of (3.2.12) for different parameter settings reveals a non-linear interaction between degree of modulation and masking depth upon a degree of modulation above 70%, as illustrated in Figure 3.47. In contrast, this sensitivity infers that at a degree of modulation above 70%, the intensity of a superimposed signal must have a progressive increasing level to achieve the threshold of perceiving of the human ear. Based on listening studies, Aures recommended to use the linear signal state to calculate the masking depth, which means the sound pressure fluctuation [81]. In contrast to Zwicker, the roughness analysis according to Aures is able to consider modulated broadband noise and narrow band modulation effects, i.e. typical noise signals: the perceived roughness of an arbitrary noise increases if its frequency content gets broader. To avoid this effect, a weighting factor k_i for the critical band

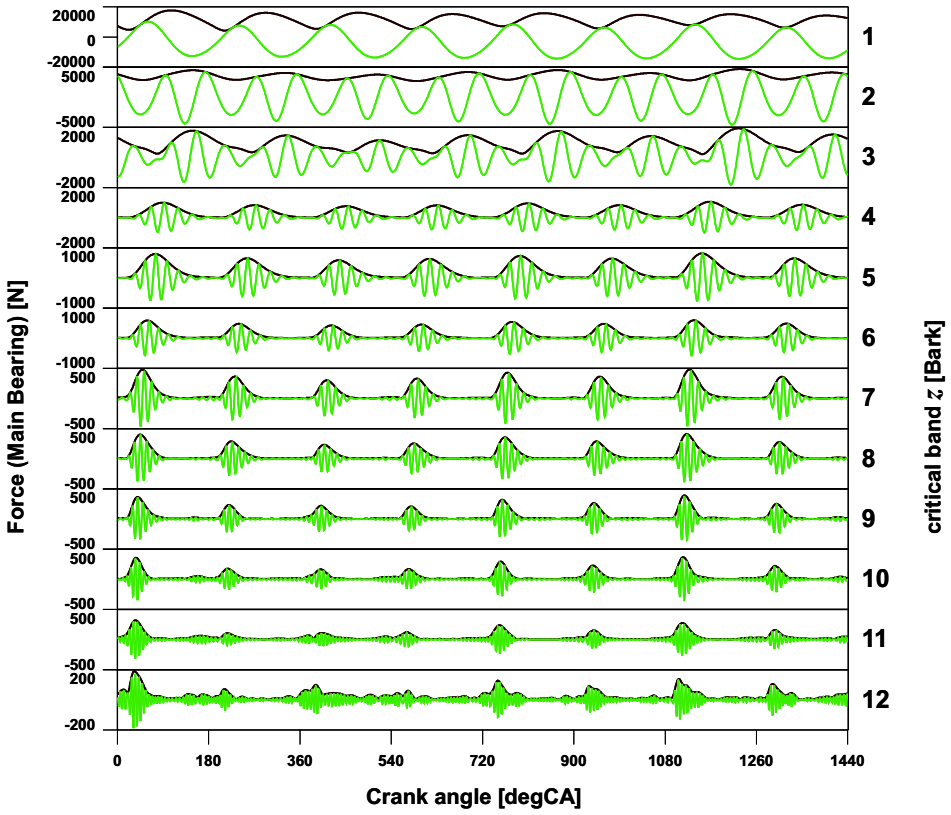

Figure 3.46: Bandpass filtered main bearing force for individual critical bands ($z = 1 \ldots 12 Bark$), and the according envelope signals (black lines), calculated using equation (3.2.8)

related roughness $r_i^{'}$ is calculated. The resulting correlation factor $C_{F,i}$ is calculated by processing the cross-correlation of the adjacent envelope signals, consisting of the number of samples n, $h_{E,i-1}$ and $h_{E,i+1}$ with $h_{E,i}$. For example one can write for the correlation factor k_i:

$$k_i = \frac{\sum h_{E,i} h_{E,i+1} - \frac{1}{n} \left(\sum h_{E,i}\right) \left(\sum h_{E,i+1}\right)}{\sqrt{\left[\sum h_{E,i}^2 - \frac{1}{n} \left(\sum h_{E,i}\right)^2\right] \left[\sum h_{E,i+1}^2 - \frac{1}{n} \left(\sum h_{E,i+1}\right)^2\right]}}, \tag{3.2.13}$$

and similar for k_{i-1} one can write:

$$k_{i-1} = \frac{\sum h_{E,i} h_{E,i-1} - \frac{1}{n} \left(\sum h_{E,i}\right) \left(\sum h_{E,i-1}\right)}{\sqrt{\left[\sum h_{E,i}^2 - \frac{1}{n} \left(\sum h_{E,i}\right)^2\right] \left[\sum h_{E,i-1}^2 - \frac{1}{n} \left(\sum h_{E,i-1}\right)^2\right]}}. \tag{3.2.14}$$

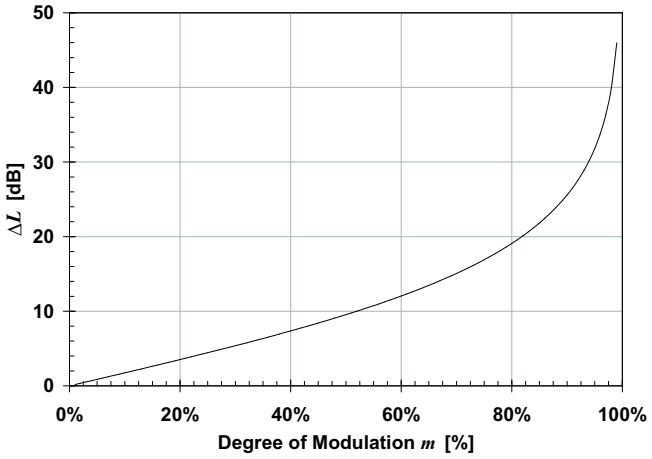

Figure 3.47: Relationship between masking depth ΔL and degree of modulation m according to Zwicker [76]

The correlation factor $C_{F,i}$ can be calculated by taking k_{i-1} and k_i:

$$C_{F,i} = \frac{(k_{i-1} + k_i)}{2}. \tag{3.2.15}$$

Please note that it is by definition $k_0 = k_1$, and $k_{24} = k_{23}$. In addition, the band individual roughness is weighted with a critical band factor $g_R(z_i)$ to reflect the frequency related roughness. The spectral weighting factor is depicted in Figure 3.48. However, also the degree of fluctuation of the individual envelope is calculated

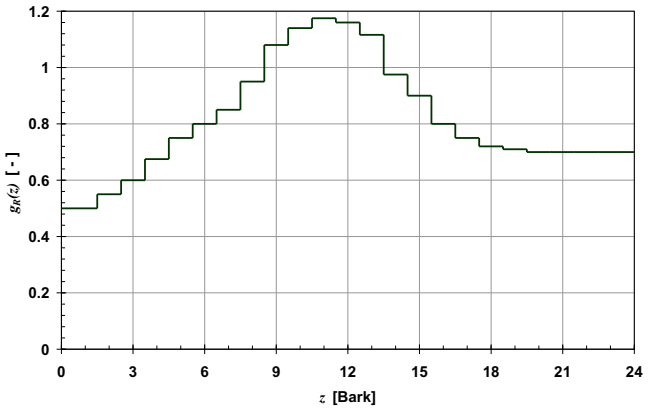

Figure 3.48: Weighting factor $g_R(z_i)$ for the individual critical band z according to [81]

by processing the ratio of the effective value $\tilde{h}_{Eff,i}$ and the mean value $h_{E0,i}$ to consider the non sinusodial signal characteristics. The length of $h_E(t)$ shall be T, which can be for instance chosen as the according time for $720 deg CA$. This yields an alternative approach for the calculation of the band individual degree of modulation

m_i^*:

$$m_i^* = \frac{\tilde{h}_{Eff,i}}{h_{E0,i}} = \frac{\sqrt{\frac{1}{T}\int_0^T h_{E,i}^2(t)dt}}{\frac{1}{n}\sum_{s=1}^{n} h_{E,i}}. \tag{3.2.16}$$

The denominator in equation (3.2.16) is the arithmetic mean value of the envelope according to the chosen interval of the length T. At last the constant c must be calculated as such, as it leads to $r_i^{'} = 1asper$ [5] for a sinusodial tone of $1kHz$, modulated with $70Hz$, and a level of $60dB$. Thus the critical-band related Roughness can be calculated as follows:

$$r_i^{'} = c \cdot \left(g_R(z_i) \cdot m_i^*\right)^2. \tag{3.2.17}$$

Adding then the individual $r_i^{'}$, the value of Roughness can be calculated:

$$R = c \cdot \sum_{i=1}^{n} r_i^{'} \cdot \Delta z \cdot C_{F,i}. \tag{3.2.18}$$

3.2.2.2 Impulsiveness - Narrowband Modulation

Engine knocking noise can also be characterized as 'impulsive'. In this work it is not interpreted as conventional engine knocking, caused by uncontrolled self-inflammation in the combustion chamber. To characterize the impulsiveness of engine noise such as clattering, as known from Compression-Ignition engines especially during cold start conditions, different approaches are published. Maeda et al. [18] applied the fluctuation level L_{FL}.

$$L_{FL} = 20 \cdot log\left(\frac{1}{T} \cdot \int_0^{\tau} \frac{|P_{As} - P_A|}{P_A} dt\right). \tag{3.2.19}$$

According to equation (3.2.19), T represents the duration of one engine cycle, τ is the time window constant, P_A is the root-mean-square (RMS) value of the A-weighted sound pressure, having a time constant of $\tau = 1sec$, and P_{As} represents the RMS value of the A-weighted sound pressure, but calculated using a time constant of $\tau = 20msec$. In contrast, Hughes [20] proposed to use an adapted Kurtosis K_t that correlates with measured signals and subjective ratings for a diesel engine, but just when operating in idle [16, 21]:

$$K_t = \frac{1}{N \cdot \sigma^4} \cdot \sum [x(i) - \bar{x}]^4. \tag{3.2.20}$$

[5] asper (lat.): rough

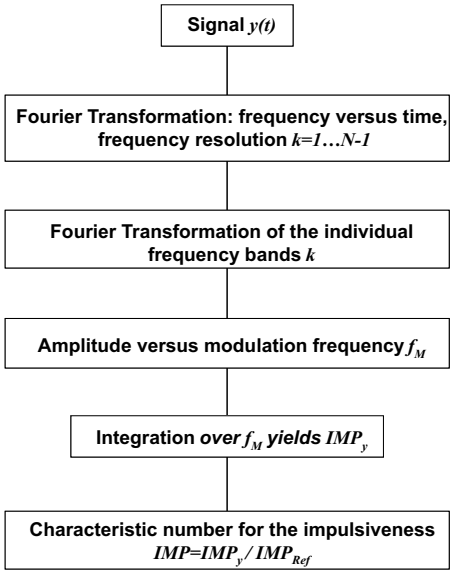

Figure 3.49: Development of the index IMP, describing the impulsiveness: signal flow for the narrow band modulation analysis

In equation (3.2.20), the variable $x(i)$ represents the time series, N the number of values of the taken time-series, σ is the standard deviation of the time series, and $\bar{x}$ reflects the mean value of the series. However, both methods are based on a statistical evaluation of the combustion-induced signal, gained during steady state conditions. Bearing in mind mode changes between SI and HCCI, this can lead to the issue that a smooth SI-mode operation can have a worse Fluctuation Level or Kurtosis than a stable, but impulsive sounding, HCCI operation due to the higher combustion variability of the SI cycles, as will be shown in chapter 4. Thus, to avoid the risk of misinterpretation of such signals, the approach of the narrow band modulation analysis is chosen to describe the impulsiveness of the engine noise. In addition, former psychoacoustic studies have shown that such an approach correlates well with the human perception of impulsive signals [35, 84]. The signal flow of the narrow band modulation analysis, as implemented in the prediction routine is depicted in Figure 3.49. According to the flow chart, first a discrete Fourier Transformation of the signal or vector $y(t)$, for instance representing the engine noise excitation in the time domain, is carried out [13]. The signal consists of a total number of discrete samples N, sampled with a constant interval of Δt, thus it is of a total interval length of $T = \Delta t \cdot N$. The discrete Fourier Transformation can be then written under the consideration of the Nyquist criterion $0 < k < \frac{N}{2}$ to avoid

aliasing [13, 70]:

$$Y_I(k) = \sum_{n=0}^{N_I-1} y_n \exp^{-j \ \frac{2\pi nk}{N_I}} \quad , \quad 0 < k < \frac{N}{2}. \tag{3.2.21}$$

However, equation (3.2.24) delivers just one spectrum for the entire signal $y(t)$. To gain a frequency versus time spectrogram the signal is windowed into a number of $n = s$ segments of the individual length N'. In other words, one can write $N = N' \cdot s$. Similarly this leads then in the time domain to $T_s = \Delta t \cdot N'$. In addition let the windowed segment of the vector be $y'_s(t)$, the equation (3.2.24) can be re-written:

$$Y_I(k) = \sum_{n=0}^{N'_I-1} y'_n \exp^{-j \ \frac{2\pi nk}{N'_I}} \quad , \quad 0 < k < \frac{N}{2}. \tag{3.2.22}$$

Each sectioned signal y'_n can be analysed using different types of windows, describing the ramp-in and -out of the section [70, 69]. Therefore the following case branch should be considered then for the section, defined by its lower border N'_l, and its upper border, N'_u:

$$y'_n(s) = \begin{cases} y_n(t) & \text{for } N'_l \leq s \leq N'_u \\ \\ 0 & \text{for } s < N'_l \wedge s \geq N'_u \end{cases} \tag{3.2.23}$$

It must be noted that the resulting spectrum consists of the successively processed numbers of individual spectra, s. Subsequently a second discrete Fourier Transform of the individual envelopes is processed. This yields the Amplitude $Y_{II}(k_M)$ at a modulation frequency f_M, hence one can write:

$$Y_{II}(k_M) = \sum_{n=0}^{N_{II}-1} Y_I(n) \exp^{-j \ \frac{2\pi nk}{N_{II}}} \quad , \quad 0 < k < \frac{N}{2}. \tag{3.2.24}$$

The surface, defined by $Y_{II}(k_M)$ over f_M represents the amount of modulation. Hence one can integrate $Y_{II}(k_M)$ over f_M from $f_M = 0$ to the maximum modulation frequency, $f_M|_{max}$ to gain an index that quantifies the content of the impulsiveness IMP_y. Therefore one can write:

$$IMP_y = \int_{f_M=0}^{f_M|_{max}} Y_{II}(k_M) df. \tag{3.2.25}$$

Thus, the higher the impulsiveness of a signal, the higher is the value of IMP. However, in psychoacoustic a signal is often taken for reference that shows less occurrence of the effect to be described. Assuming a reference signal that has been rated by a jury as 'smooth', thus perceived without any impulsiveness by an auditorium and named IMP_{Ref}, one can write for the calculated impulsiveness IMP of a signal $y(t)$:

$$IMP = \frac{IMP_y}{IMP_{Ref}}. \tag{3.2.26}$$

Following equation (3.2.26) one can gain indices of the impulsiveness higher than '1' when having a signal showing a higher degree of modulation and thus impulsive content.

3.3 Prediction of Engine Acoustics

3.3.1 Structure of the Prediction Model

To estimate the engine radiated noise without running the engine under semi-anechoic conditions, a separation of the noise into its sources is required. Considering these individual sources, it is useful to structure such a prediction model into the three aforementioned noise sources:

- the combustion excitation, characterized by the cylinder pressure as input, as shown in Chapter 3.1.1.
- the indirect combustion noise, caused by the response of the mechanical engine structure directly by the combustion. The model considers the noise contribution by piston slap (Chapter 3.1.3), the dynamic transfer characteristic of the piston-conrod unit (Chapter 3.1.4), and the main bearing excitation (Chapter 3.1.5).
- the mechanical noise. Since the valve noise is a main contributing noise source in a motored engine, the model considers the dynamic forces, acting in the valve train and derived in Chapter 3.1.6.

Figure 3.50 shows the signal flow of the model, reflecting the structure of the sources and transfer functions. The result consists of the absolute noise level at the individual load-speed points, the related third octave spectrum and of the sound quality

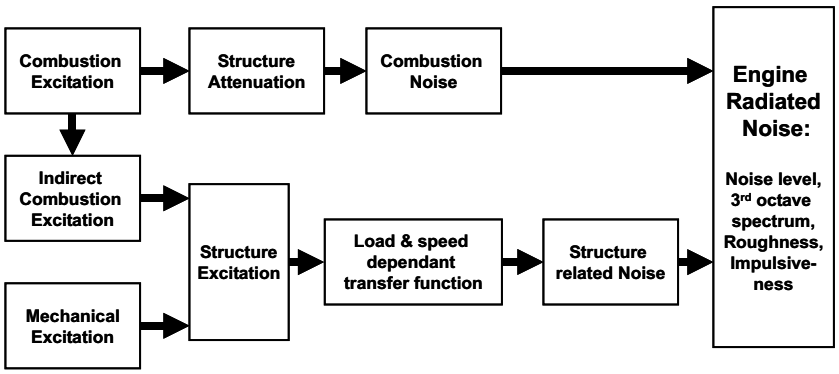

Figure 3.50: Signal flow of the engine noise prediction model

analysis. The combustion and structure excitation are transferred into the individual third- or critical bands in the time domain. Based on the third octave bands versus time, the resulting level of the radiated noise L_{Rad} is then re-assembled while adding the resulting average sound pressures of each band i of all considered bands n accordingly, using the following relationship:

$$L_{Rad} = 10 \cdot \log \left(\frac{\sum_{i=1}^{n} \bar{p}_i^2}{p_0^2} \right), \tag{3.3.1}$$

or according to Figure 3.50

$$L_{Rad} = 10 \cdot \log \left(10^{(0.1 \cdot L_{CN})} + 10^{(0.1 \cdot L_{StN})} \right). \tag{3.3.2}$$

The individual paths of the signals to obtain L_{CN} and L_{StN} are presented in the next sections in greater detail.

3.3.2 Radiated Noise effected by Combustion

The combustion event is a sudden pressure pulse loaded on the engine structure. When processing a sound pressure analysis of such a combustion pressure pulse, noise levels of *180dB* and higher can be expected. This noise event is damped by the attenuation characteristics of the engine structure. This structure-attenuation function is normally gained from experiments by exciting the combustion chamber with pressure pulses, and measuring the response using microphones. Such attenuation functions are available for different engine structures, as grey-cast-iron or aluminum-engine structures. Figure 3.51 shows measured attenuation functions for

five different in-line four cylinder aluminum engine structures by different manufacturers in a displacement range from 1.6 to 2.0 litres. The individual attenuation curves were achieved by measuring the airborne noise, while provoking a detonation in the combustion chamber in a non-rotating engine in absence of disturbing indirect combustion- and mechanical noise. The detonation in the combustion chamber is measured with a pressure transducer. The radiated noise caused by the detonation then is measured in parallel with a microphone and the signal is A-weighted, and put into relationship with the excitation level of the combustion chamber. Therefore the structure attenuation function for the combustion noise has the unit $dB(A)$. This procedure is repeated for each individual cylinder. Finally, an average structure attenuation curve is calculated from the individual functions as is depicted in Figure 3.51. Beginning at approximately *200Hz*, all five attenuation functions show

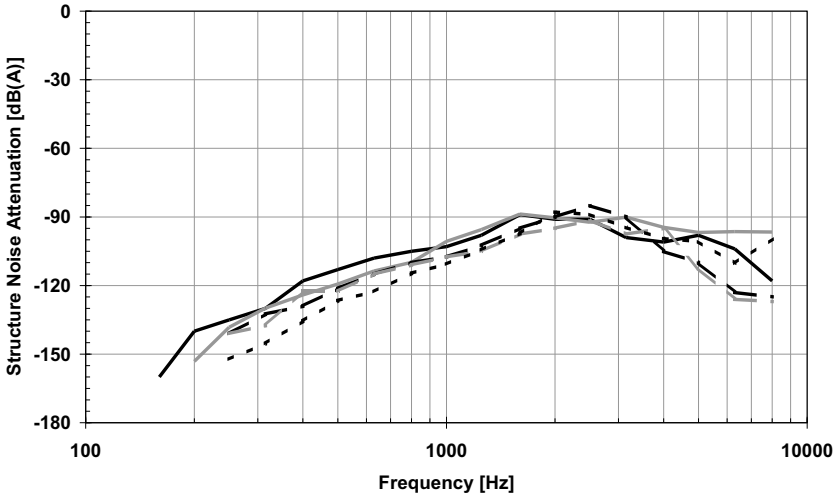

Figure 3.51: Structure attenuation functions for five different inline four cylinder gasoline engines, range of displacements from 1.6 to 2.0 litres

a similar characteristic. Thus, an average attenuation function for aluminum engine blocks was calculated and incorporated in the model for the calculation of the combustion noise. However, taking the structure attenuation function L_{Atn} into account when calculating the sound pressure level L_{CN}, raised by the combustion pressure p_{Comb} only, for each frequency band f_i:

$$L_{CN}(f_i) = L_{Comb}(f_i) - L_{Atn}(f_i). \tag{3.3.3}$$

Re-writing equation (3.3.3) as a function of the sound pressure only yields:

$$p_{CN}(f_i) = p_0 \cdot \left(10^{(L_{Comb}(f_i)/20)} - 10^{(L_{Atn}(f_i)/20)}\right). \tag{3.3.4}$$

Hence for the resulting sound pressure level, raised by the combustion excitation, one can write:

$$L_{CN}(f_i) = 20 \cdot log\left(\frac{p_{CN}(f_i)}{p_0}\right). \tag{3.3.5}$$

3.3.3 Structure Excitation related Engine Noise by means of load dependent Transfer Functions

Actual simple engine noise prediction methods have the issue that the predicted radiated noise level at low engine load levels is less precise. One reason for this is the increase in excitation, caused by modern combustion systems such as CI and GDI, combined with lightweight engine structures. This has also been revealed by measurements on an automotive Diesel engine in [165]. Also the calculated structure excitation cannot be taken directly for the engine-radiated noise calculation. This is because the noise radiation and -transfer characteristics of the engine structure need to be considered, too. Furthermore, caused by an increased load, the temperature in the engine will rise, which leads to a change of the lashes and contact forces. Hence load-dependent transfer functions for the individual third octave bands are introduced for individual engine speeds to reflect this effect. But in order to facilitate the requirements of fast data processing, the complexity of the prediction routine is kept low. Hence load-dependent transfer functions for the individual third octave bands are introduced for individual engine speeds to reflect this effect.

According to Ewins [67] the noise transfer function $H_{Ntf}(f)$, which is written in the linear scale and that considers the excitation force $F_{Exc}(f)$ and the radiated sound pressure $p_{StN}(f)$ as the output, can be written for each frequency band i :

$$H_{Ntf}(f_i) = \frac{p_{StN}(f_i)}{F_{Exc}(f_i)} \tag{3.3.6}$$

Based on the derivation of the individual forces, as already done in Chapters 3.1.1 to 3.1.6, the excitation force $F_{Exc}(f)$ finally is the sum of the main bearing force $F_{MB}(f)$, the piston-induced force excitation $F_P(f)$ and the valve train force excitation $F_{VT}(f)$. Thus, one can write for each frequency band i:

$$F_{Exc}(f_i) = F_{MB}(f_i) + F_P(f_i) + F_{VT}(f_i). \tag{3.3.7}$$

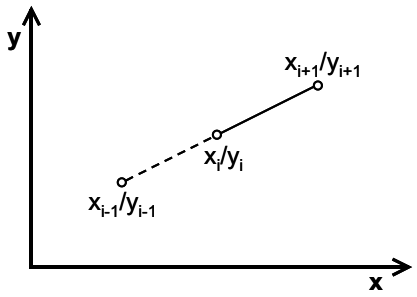

Figure 3.52: Principle of the linear extrapolation for the individual octave bands of the weighting functions

Once a measured full- and a part load noise spectrum of the radiated noise level of an engine is known, the radiated noise can be split up into the direct combustion noise and the structure excitation. Beforehand the overall noise level is transferred into the linear environment using the re-written sound-pressure level definition (3.3.8).

$$p = p_0 \cdot 10^{(L_p/20)}. \tag{3.3.8}$$

However, the sound pressure level, generated by the structure excitation can be generally written:

$$L_{StN}(f_i) = 20 \cdot log\left(\frac{p_{StN}(f_i)}{p_0}\right), \tag{3.3.9}$$

which can be re-written considering (3.3.6):

$$L_{StN}(f_i) = 20 \cdot log\left(\frac{H_{Ntf}(f_i) \cdot F_{Exc}(f_i)}{p_0}\right). \tag{3.3.10}$$

It is known that the noise level of a natural aspirated engine has a nearly linear slope versus load. This is because of the individual lashes increase linearly by an increased thermal load. Followed by that the load dependent transfer functions depend linear on the load, too. As a consequence, the noise transfer factors for each frequency band must be estimated for two load points at a constant engine speed first. After the synchronous measurement of cylinder pressures and the radiated noise in a semi-anechoic chamber at constant speed at two different loads, the structure excitation F_{Exc} according to (3.3.7) is calculated. Because of the measurement of the radiated noise p_{StN} is also known. For example p_{StN} can be the four microphone average sound pressure. The so-called reference transfer functions H_{Ntf} can be then calculated. Finally all other load points at a certain engine speed can then be linearly extrapolated using equation (3.3.11). However, if the engine structure reveals non-linear characteristics, the interpolation can be carried out using cubic- or spline-interpolation, too. According to Figure 3.52, one can calculate the noise

transfer value of the individual 3^{rd} octave band y_{i-1}, assuming a known load x_{i-1} at this point:

$$y_{i-1} = y_{i+1} - \left[\left(\frac{y_{i+1} - y_i}{x_{i+1} - x_i} \right) \cdot (x_{i+1} - x_{i-1}) \right]. \tag{3.3.11}$$

Hence the transfer function $H_{Ntf(i-1)}$ for the new load $BMEP_{(i-1)} = L_{(i-1)}$ can be calculated by substituting x and y in (3.3.11). This leads then to:

$$H_{Ntf(i-1)} = H_{Ntf(i+1)} - \left[\left(\frac{H_{Ntf(i+1)} - H_{Ntf(i)}}{L_{(i+1)} - L_{(i)}} \right) \cdot \left(L_{(i+1)} - L_{(i-1)} \right) \right]. \tag{3.3.12}$$

It must be noted that equation (3.3.12) could also be re-written accordingly if the transfer function $H_{Ntf(i+1)}$ is required. To give an example, the resulting noise transfer functions for four different loads at 2000rpm are illustrated in Figure 3.53. Hereby the transfer functions were calculated based on reference functions, attained from 4bar and 8.2bar BMEP load reference points. As expected, the lower the

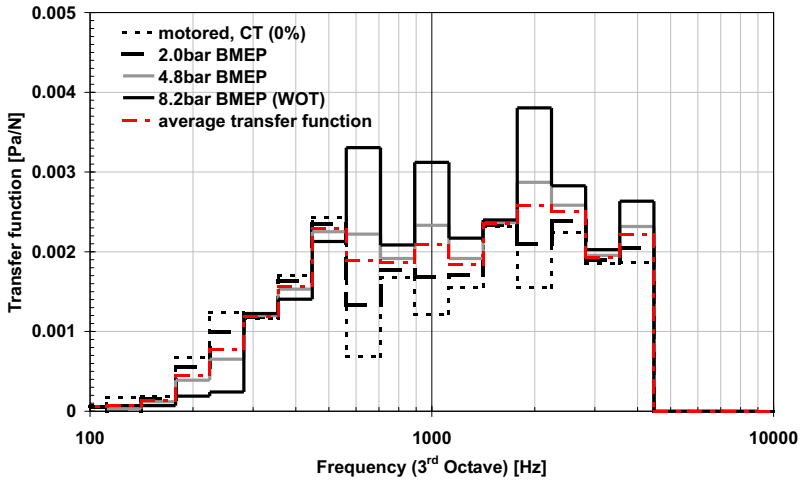

Figure 3.53: Load dependent transfer function $H_{Ntf}(f_i)$ for the structure excitation, linearly extrapolated for different loads at 2000rpm, aluminum engine block. Please note that the cut-off at the 4kHz frequency band is due to the sampling rate, which is linked to the chosen crankshaft angle resolution ($1deg$) for the cylinder pressure measurements

load, the lower is the transfer of the noise. However, a further result is that the frequency bands between 0.6 and $2.5kHz$ show the highest sensitivity to engine load. Therefore, to get a complete overview of the sensitivity of each frequency band, a parametric study with an interval length of 0.2bar BMEP was carried out. Figure 3.54 below depicts the noise transfer functions from motored operation with closed throttle (CT) until full load (WOT) (8.2bar BMEP) at 2000rpm engine speed. In

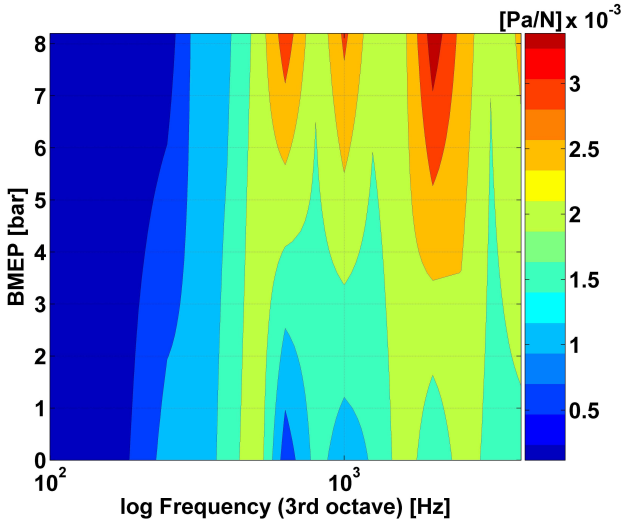

Figure 3.54: Transfer function $H_{Ntf}(f_i)$ versus frequency (third octave bandwidth) and load (BMEP) at 2000rpm

addition to the transfer functions depicted in Figure 3.53 the result of the parametric study depicted in Figure 3.54 reveals a high sensitivity of the transfer characteristic of the engine structure investigated here at the particular third octave bands at $600Hz$, $1000Hz$ and $2000Hz$. However, compared to the the $600Hz$ and $2000Hz$ band, the transfer function of the $600Hz$ band shows an even higher sensitivity to engine load.

3.3.4 Verification of the Prediction Method

According to Figure 3.50, the resulting radiated noise level can be calculated by adding both contributors, the combustion-induced noise and the structure excitation. Thus, the sound pressure of the overall radiated noise is raised by the sum of the combustion-induced and the structure-excitation induced sound pressure:

$$p_{Rad}(f_i) = p_{CN}(f_i) + p_{StN}(f_i) \tag{3.3.13}$$

Re-writing this equation in the sound pressure level definition form, it yields for each frequency band i:

$$L_{Rad}(f_i) = 10 \cdot log\left(10^{\frac{L_{CN}(f_i)}{10}} + 10^{\frac{L_{StN}(f_i)}{10}}\right) \tag{3.3.14}$$

To adapt the level L_{Rad} to the sensitivity of the human ear, the A-weighting scale is a commonly used attenuation. In accordance to [72], the following definition can be used to calculate the A-weighted noise level L_{RadA} from the un-weighted noise

level L_{Rad} as a function of frequency $f[Hz]$ [6]:

$$L_{RadA}(f_i) = L_{Rad}(f_i) - 11.15 \cdot [log(f_i)]^2 + 75.2 \cdot [log(f_i)] - 125.25 \qquad (3.3.15)$$

Writing equation (3.3.15) as a function for each frequency band i this yields for the resulting overall radiated noise level L_{SPL}, owning then the unit $dB(A)$:

$$L_{SPL} = 10 \cdot log \left(\sum_{i=1}^{n} 10^{\frac{L_{RadA}(f_i)}{10}} \right) \qquad (3.3.16)$$

The verification of the prediction model was carried out for the operation point 4bar BMEP at 2000rpm engine speed. While feeding the measured cylinder pressures for each individual cylinder into the model, the direct combustion noise and the structure excitation were calculated. The 3^{rd} octave spectrum of each noise contributor is shown in Figure 3.55. Both direct combustion noise and structure excitation are

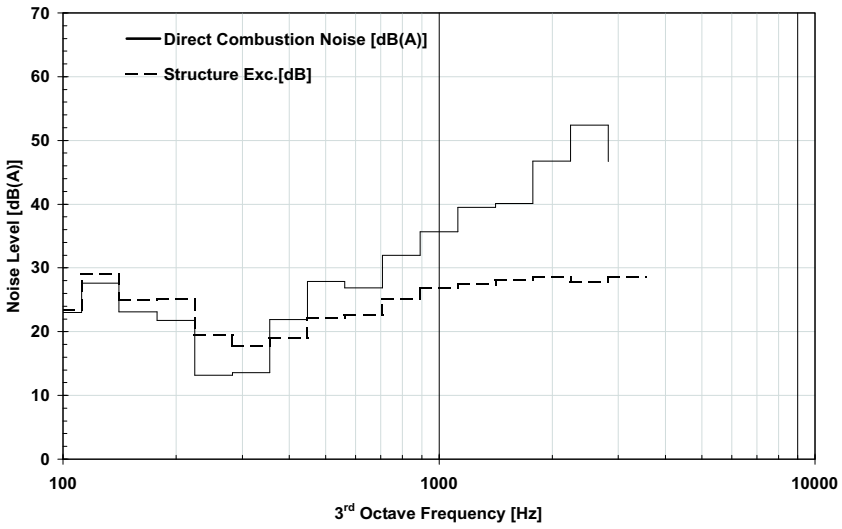

Figure 3.55: Calculated individual noise contribution of combustion and structure excitation at 4bar BMEP, 2000rpm

showing similar noise levels for frequencies lower than *300Hz*. This is due to the A-weighting of the direct combustion noise that reduces the amplitudes of harmonics of the second engine order *(66Hz)*. The direct combustion noise dominates the radiated noise especially at frequencies greater than *500Hz*. Also the incorporation

[6] Note that this equation between quantities differs from the definition published in the international standard IEC651. However, the error of the the A-weighting levels achieved with equation (3.3.15) compared to IEC651 can be considered as negligibly low.

of the non-linearities when calculating the structure excitation will lead to an increased level of the structure excitation at frequencies higher than *500Hz*. Finally, the transfer function was applied and the radiated noise level and its third octave spectrum were calculated. The result, compared with the measured four microphone average, gained in a semi-anechoic chamber at same load and speed, is shown in Figure 3.56. It can be concluded that the model predicts the radiated noise level of all

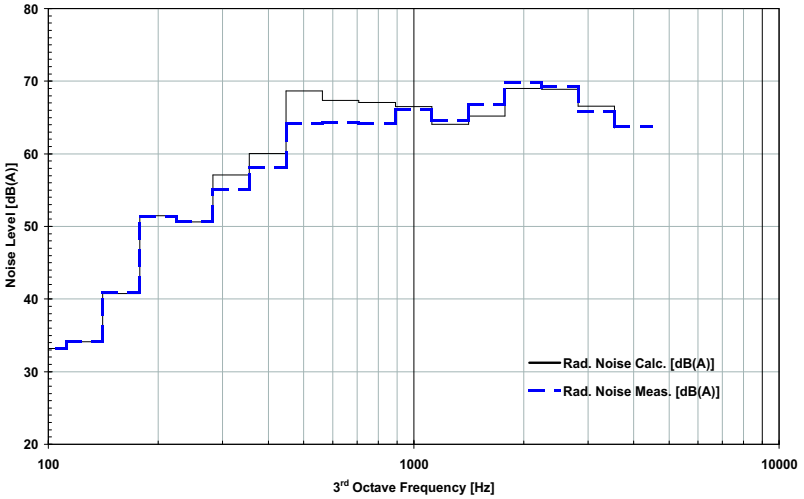

Figure 3.56: Engine radiated noise prediction at 4bar BMEP, 2000rpm: comparison of predicted and measured 3^{rd} octave spectrum

third octave bands below *200Hz* very well; this can be also noticed for frequencies above *800Hz*. The correlation of prediction and measurement in the frequency range *300Hz* to *1000Hz* can be considered as acceptable. This is because the deviation of the individual bands from the measurement is lower than $5dB(A)$ [7]. The difference of prediction and measurement is higher for the frequency bands that display the highest sensitivity on load of the transfer function, as already shown in Figure 3.54 above. This can be referred to a certain sensitivity of the engine structure and its noise radiation in these particular frequency bands. To correlate measured and predicted results, the levels of all individual frequency bands are drawn in a correlation chart, that shows the measured band-levels versus the calculated ones, as illustrated in Figure 3.57. Once the values coincide with the dotted, diagonal

[7] The repeatability of engine noise measured in a semi anechoic chamber is usually in the range $\pm 0.5dB(A)$ in the overall level, but can vary at certain frequency bands in the range of $\pm 1.5dB(A)$, especially for turbo-charged engines.

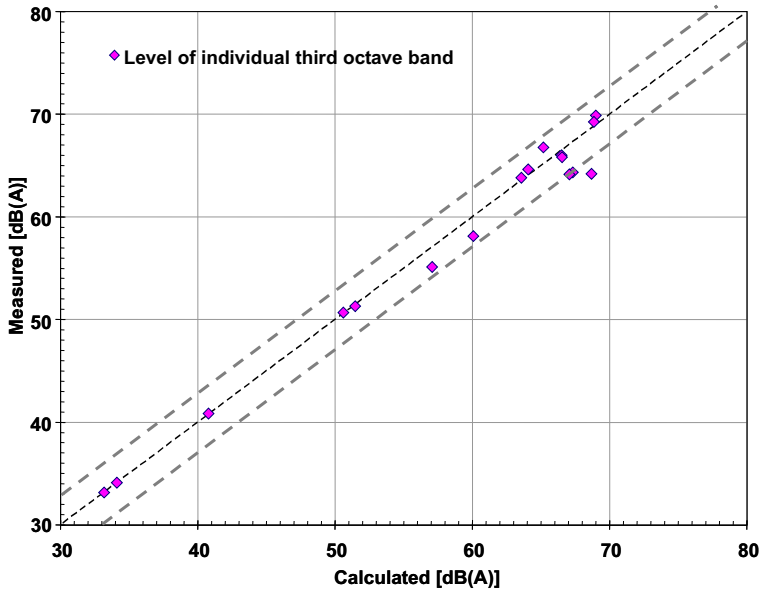

Figure 3.57: Correlation of predicted and measured individual 3^{rd} octave band noise levels at 4bar BMEP, 2000rpm

line, the correlation is 100%. When the point is below the line, the calculated value is higher than the measured level, or vice versa. The two grey dotted lines denote an upper and lower tolerance threshold of $\pm 3dB(A)$, meaning an error less than $3dB(A)$ for most of the individual third octave bands (there are two bands deviating with a maximum value of $4.5dB(A)$ from the measurement: these are the *500Hz* and *630Hz* third octave band). However, this can be considered as acceptable when comparing it with results gained from current prediction methods, e.g. by Heuer in [31], page 50, were deviations of up to $5.5dB(A)$ for individual frequency bands are considered as acceptable. Thus, it can be concluded that the prediction model can be considered as applicable for predicting the engine radiated noise. This will be done in Chapter 4.

3.4 Assessment of different Methods to quantify Vibrations during Mode-Switch

The current methods to evaluate low frequency vibration and their effect on the human body was already outlined in Chapter 2.5 . The following two subsections recapitulate the physics according to Griffin, [16] behind two important indices, the Dynamic-Response-Index (DRI) and the currently most common index, the Vibration-Dose-Value (VDV). A new index is proposed that incorporates also the duration of exposure to low frequency events while considering the shape, i.e. its sharpness, of the excitation, too. Based on the signal processing, necessary to calculate this index, this method has been called Jerk-Level-Shape (JLS). For this method a patent is pending.

3.4.1 Dynamic Response Index - DRI

The theory of the DRI is based on the combination of the theory of a peak stress $\hat{\sigma}$, occurring on a spine of a certain area A of the human body. In addition the spine is assumed as an undamped single degree of freedom system. According to [16] one can write for the peak stress $\hat{\sigma}$

$$\hat{\sigma} = \frac{\hat{F}}{A}. \tag{3.4.1}$$

Furthermore it is assumed that the area A is proportional to the effective mass m_{eff}. Thus one can write

$$\hat{\sigma} \propto \frac{\hat{F}}{m_{eff}}. \tag{3.4.2}$$

However, the peak force can be written as the product of stiffness c and the peak value of the deflection, δ_{max}. This yields then

$$\hat{\sigma} \propto \frac{c}{m_{eff}} \cdot \delta_{max}. \tag{3.4.3}$$

Moreover, the undamped natural frequency ω_n of a system is defined by:

$$\omega_n = \sqrt{\frac{c}{m_{eff}}}. \tag{3.4.4}$$

To give an example, a typical value of the natural frequency of the spine of a human being is given by Griffin [16] as $8.42Hz$. Finally, combining equation (3.4.3) and (3.4.4), the DRI can be written as follows:

$$DRI = \omega_n^2 \cdot \delta_{max}. \tag{3.4.5}$$

A disadvantage of the DRI is that no damping of the system is considered. This can result in a too high DRI-value once there is a short pulse applied to the system or the object is subjected to continuous vibration. Moreover, it is more handy to measure acceleration than deflections.

3.4.2 Vibration Dose Value - VDV

The VDV is a well-established measure of the vibration and shock received by a person during the measurement time span. Using the measured and frequency weighted acceleration $a_w(t)$, the VDV over a period T can be written [16]:

$$VDV = \left(\int_{t=0}^{t=T} a_w^4 dt \right)^{1/4} . \tag{3.4.6}$$

The variable $a_w(t)$ is the acceleration signal, gained from measurements or calculations, filtered by a bandpass with a window of 1 to 32Hz. However, this value is based on the acceleration integrated over an interval and does neither reflect the sharpness of excitation, nor the duration of exposition of the object to the fluctuating acceleration signal.

3.4.3 A Method to quantify Powertrain-Vibrations during Mode Change of the Combustion - JLS

In contrast to the VDV, the proposed evaluation method, which leads to the Jerk-Level-Shape (JLS), will not only consider the height of the peak weighted in a certain period. It also considers the duration of the excitation and its shape. Thus, the following calculation procedure, consisting of four steps, was developed:

(a) Define the event of the measured or calculated acceleration signal. The Figure depicted here contains a calculated acceleration at the rear-roll-restrictor in x- and z-direction.

(b) Calculate the average acceleration level after applying a bandpass filter of 1 - 32Hz and processing the resulting acceleration vector $a_{\vec{RSS}}$. The resulting vector of acceleration $\vec{a}_{RSS}$ is calculated by

$$\vec{a}_{RSS} = \sqrt{\vec{a}_x^2 + \vec{a}_y^2 + \vec{a}_z^2}. \tag{3.4.7}$$

The individual crank-angle interval $\Delta\alpha$ and the time-interval ΔT correspond to the sample rate f_s as follows:

$$\Delta T = \frac{1}{f_s} = \frac{\Delta\alpha}{n \cdot 360}, \tag{3.4.8}$$

with n denoting the rotational speed of the crankshaft in s^{-1}. The level of acceleration is then calculated by using a time window ΔT such that a crank-angle interval of $\Delta\alpha = 180deg$ is considered. This means that the time window contains one combustion event when analysing data gained from an in-line four cylinder four stroke engine. This is because of the individual cylinder combustion controller, typically used at spray-guided-direct-injection engines. Thus, this step provides the band-pass filtered level of acceleration,

$$a_L(t) = \frac{1}{\Delta T} \int_{t=0}^{\Delta T} \vec{a}_{RSS}(t)dt. \tag{3.4.9}$$

(c) The derivation of the acceleration is called jerk. During this step the derivative $j_L(t)$ of the acceleration level $a_L(t)$ is calculated by

$$j_L(t) = \frac{da_L(t)}{dt}. \tag{3.4.10}$$

The jerk $j_L(t)$ is used to describe the sharpness of an acceleration signal, as is also its purpose here.

(d) Similarly to step (b), the level of the jerk, JLS is calculated, using a crank-angle related time window for $\Delta\alpha = 180deg$:

$$JLS(t) = \frac{1}{\Delta T} \int_{t=0}^{\Delta T} j_L(t)dt. \tag{3.4.11}$$

Figure 3.58 shows the evolution of the analysis for simulated acceleration signals, taken from a SI to HCCI transition simulation. The items as listed correspond to the individual sub-figures of Figure 3.58. One advantage of the JLS-method is the use of the derivation of the acceleration signal because the human body is more sensitive to the change of acceleration than to its peak [16]. However, it is useful to develop values, based on the JLS that describe the event accordingly.

It is known that the peak of the event contributes to the perception. The higher the peak, the more discomfort is the excitation [86]. Hence, the peak value of $JLS(t)$

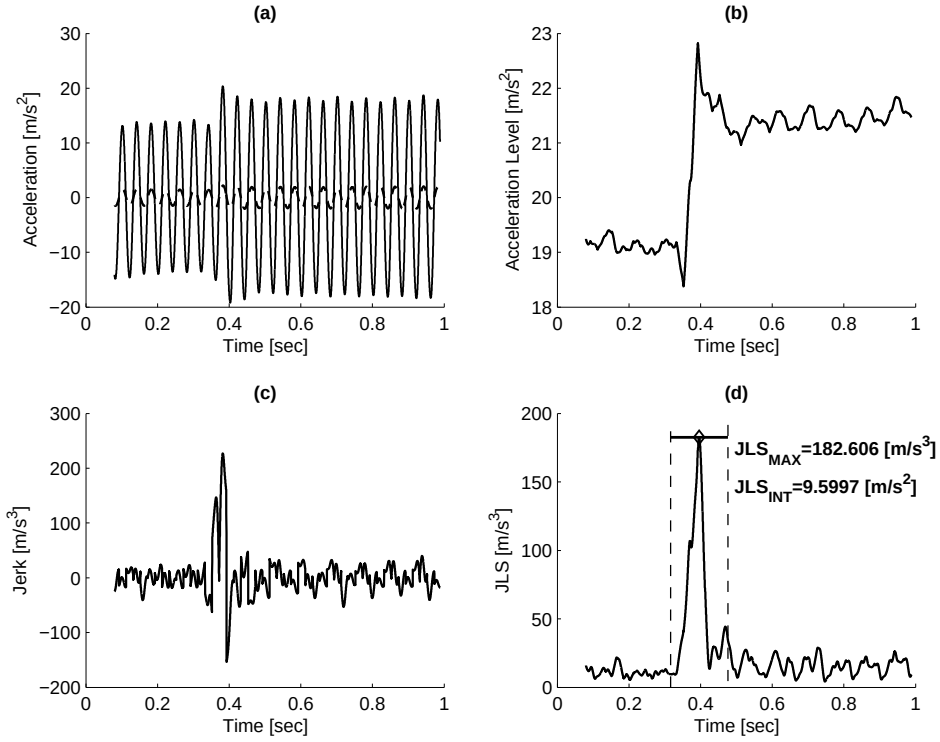

Figure 3.58: Calculation-history of the JLS

occurs during the mode switch from SI into HCCI, i.e. in the example provided her around $t = 0.39s$. The height of the peak is also written in sub-figure (d) of Figure 3.58, and is named JLS_{MAX}, which is also marked at the curve with the diamond symbol. Furthermore, it is also known that the duration of the event has an impact on the perception. The longer the duration of the jerk-event, the worse it will be perceived. Subsequently a window has been defined to integrate over $JLS(t)$ while centering the window around JLS_{MAX}. According to the controller of the engine, the total window length was defined over eight combustion events, thus $\Delta\Omega = 2 \cdot 720 degCA = 1440 degCA$. Hereby the engine speed n, the time Δt and the crank-angle α correspond as follow:

$$\Delta t = \frac{\Delta\alpha \cdot 60}{n \cdot 360} \cdot \Delta\Omega. \tag{3.4.12}$$

Note that in equation (3.4.12) the engine speed is of the unit min^{-1}, and the crank-angle has the unit deg. The crank-angle resolution chosen is $\Delta\alpha$, and the length of the crank-angle interval is denoted as $\Delta\Omega$ in deg. However, it should be mentioned that the corresponding time of the eight combustion cycles will decrease

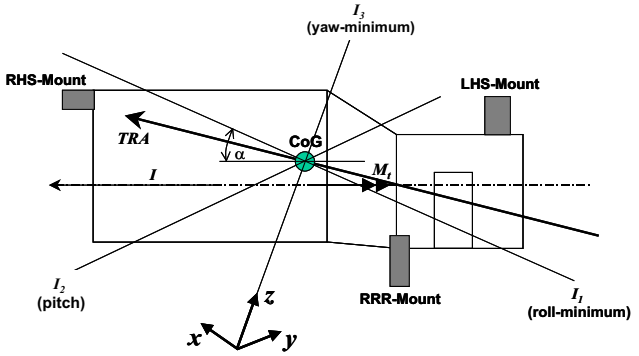

Figure 3.59: Simple rigid model of an east-west installed front-wheel drive automotive powertrain

when the engine speed increases. This could affect the correlation between analysis and sensation, especially at higher engine speeds [8]. The resulting limits at $(-\Delta\Omega/2) \leq t(JLS_{MAX}) \leq (\Delta\Omega/2)$ respectively for the integration are marked in sub-figure (d) by the two vertical dotted lines, with the duration highlighted by the horizontal line, centered relative to the time at which JLS_{MAX} occurs. The resulting value, denoted JLS_{INT} can be calculated then:

$$JLS_{INT} = \int_{t(-\frac{\Delta\Omega}{2})}^{t(\frac{\Delta\Omega}{2})} JLS(t)dt. \tag{3.4.13}$$

In addition, the resulting value JLS_{INT} for the example presented here is depicted in sub-figure (d) of Figure 3.58. However, since the engine is not operating in a vehicle, the accelerations to evaluate the mode switch quality need to be gained from a model, fed with measured cylinder pressure signals. Thus, a powertrain with its inertia I around its central axis as depicted by the dashed line in Figure 3.59, is subjected to the engine torque M_t. When the powertrain is unrestrained, then it rotates, excited by the resultant torque M_t, around its torque-roll axis, denoted as TRA in Figure 3.59, which results in the principal axis of inertia $I_{1...3}$. If the center of gravity, denoted as CoG, is located in a plane of symmetry, the TRA lies within this phase. The resultant engine torque is calculated using equation (3.1.28) and the radius of the crank, r:

$$M_t(t) = r \cdot F_T(t). \tag{3.4.14}$$

However, in an ideal case the TRA and the x-axis can interfere. Based on such an assumption, the equation of motion for the system around the principal axis of

[8] The difference of the duration of the eight combustion cycles between the investigated points of operation at 1500rpm and 2000rpm was calculated to 0.04sec.

inertia I_1, I_2 and I_3 can be written:

$$[M] \cdot \{\ddot{\theta}\} = \{M_t\} \tag{3.4.15}$$

Expanding the matrix yields:

$$\begin{bmatrix} m_1 & & & & & \\ & m_2 & & & & \\ & & m_3 & & & \\ & & & I_1 & & \\ & & & & I_2 & \\ & & & & & I_3 \end{bmatrix} \begin{Bmatrix} a_x \\ a_y \\ a_z \\ \ddot{\theta}_x \\ \ddot{\theta}_y \\ \ddot{\theta}_z \end{Bmatrix} = \begin{Bmatrix} 0 \\ 0 \\ 0 \\ M_t \cdot \cos\alpha \\ 0 \\ M_t \cdot \sin\alpha \end{Bmatrix}. \tag{3.4.16}$$

Because the only non-zero components of the acceleration around the principal inertia axis I_1 and I_2 are $\ddot{\theta}_x$ and $\ddot{\theta}_z$, one can write for the resulting acceleration in x-, and z-direction at the Rear-Roll-Restrictor (RRR-Mount):

$$\ddot{\theta}_x = \frac{M_t \cdot \cos\alpha}{I_1}, \tag{3.4.17}$$

and

$$\ddot{\theta}_z = \frac{M_t \cdot \sin\alpha}{I_3}. \tag{3.4.18}$$

Introducing the length of the lever l from the central axis of the powertrain to the location, where the RRR is linked to the vehicle structure, the resulting accelerations in $[m/s^2]$ can be calculated:

$$a_{\ddot{\theta},x} = l \cdot \left(\frac{M_t \cdot \cos\alpha}{I_1} \right), \tag{3.4.19}$$

and

$$a_{\ddot{\theta},z} = l \cdot \left(\frac{M_t \cdot \cos\alpha}{I_3} \right). \tag{3.4.20}$$

The resulting acceleration vector can be calculated for further processing with the JLS, or VDV routine:

$$a_{\ddot{\theta},RSS} = \sqrt{a_{\ddot{\theta},x}^2 + a_{\ddot{\theta},z}^2}. \tag{3.4.21}$$

This approach supports a fast data processing and allows a further transformation of the calculated acceleration onto the left- and right-hand side mounting, leading to a non solely diagonal assigned mass-matrix in equation (3.4.16). A comparative analysis between the VDV and JLS for a mode switch from SI into HCCI operation is illustrated in Figure 3.60. The upper diagram shows the calculated accelerations of

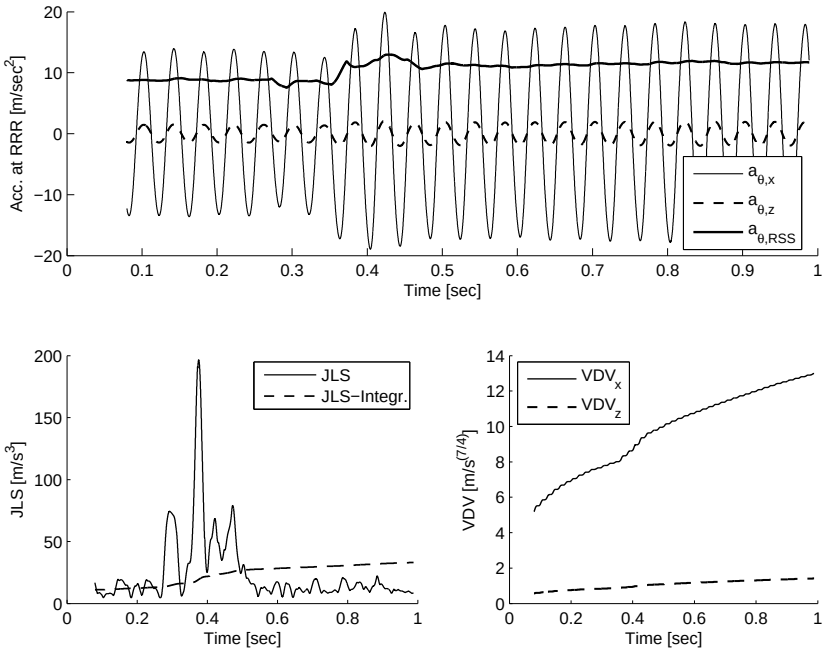

Figure 3.60: Analysis of SI to HCCI mode switch at 1500rpm, 2.62bar BMEP. The JLS-Integr. and VDV are cumulative integrated values

the powertrain during a simple mode transition. It can be seen that the powertrain accelerations will increase when the engine operates in HCCI mode. This takes place at approximately $t = 0.34sec$, showing the highest powertrain vibrations at $t = 0.395sec$, caused by the higher cylinder pressures during HCCI. Furthermore, the first HCCI cycle leads to an increased negative peak of $a_{\ddot{\theta},x}$ at $t = 0.36sec$. In contrast to the VDV analysis, depicted in the lower right diagram, the JLS analysis is able to identify this event. This diagram also shows the cumulated integrated JLS to achieve a better comparison with the VDV, depicted in the lower right graph that is also shown as a cumulative integrated value. In addition, the mode switch-related vibrations and jerk of the powertrain are described by single peaks of certain amplitude and duration. In contrast, the VDV analysis shows an increased slope during the mode switch event, which cannot be directly related to a certain event and duration of the effect. For the JLS this is on the one hand caused by the derivative of the acceleration, the jerk, and on the other hand by the shorter time window as for the VDV. Furthermore, the JLS is able to identify each jerk event, while characterizing its amplitude and duration. In contrast, the VDV as a cumulative

measure consists of a time-windowed level that does not allow such an analysis of such a resolution. It should be noted that the VDV owns the unit of $[m/s^{(7/4)}]$, which is not as practical as the unit of the JLS_{MAX}, $[m/s^3]$ or JLS_{INT}, $[m/s^2]$. This simplifies the understanding during target setting and further data processing.

Chapter 4

Impact of HCCI on Engine Acoustics

A significant change of the engine noise must be avoided when switching from one combustion mode into the other or vice versa. Hence detailed studies of the different excitation sources of engine noise need to be investigated thoroughly. Subjective assessments of engines, running in HCCI operation have shown the following issues compared to SI operation:

- higher noise level than in SI-mode
- a tonal noise of a low frequency at the orifice of the intake system, and
- a rough and particular impulsive sound.

The investigations and results presented in the following are mostly based on the comparison of SI- versus HCCI-operation, always at same speed and load, using the noise prediction methodology developed in Chapter 3. To underline and quantify the potential trade-off between both modes, in some cases results of a turbo-charged common rail diesel engine with the same displacement, operating at same load and speed are shown.

4.1 Comparative Analysis of SI- and HCCI-operation induced Noise and Vibrations

For the baseline analysis, measurements and predictions were carried out while operating the engine in steady state conditions in the individual combustion modes. Mainly two speed load points were preferred, 1500rpm, 2.62bar BMEP, and at 2000rpm, 2bar BMEP. The first one represents the so-called world-wide-mapping point (WWMP), which is a common point of operation at most engine manufacturers to enable an easier comparison of different engines and to simplify benchmark studies.

4.1.1 Combustion Excitation

A comparison of the cylinder pressures of SI- and HCCI-mode versus a common rail turbo-charged diesel with the same displacement is shown in Figure 4.1. It can be

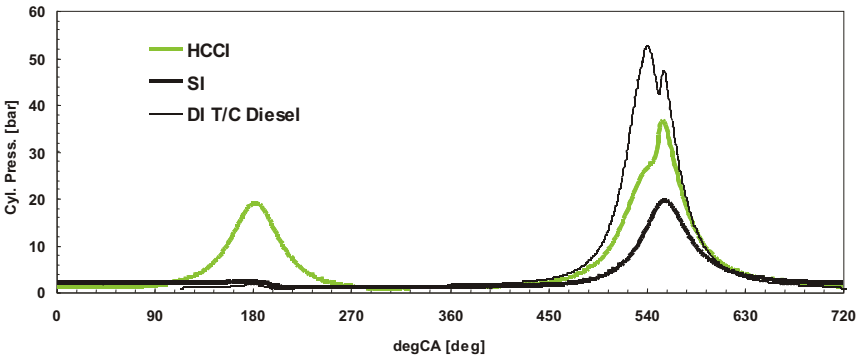

Figure 4.1: Cylinder pressure traces for HCCI-, SI- and DI-Diesel-combustion at 2000rpm, 2bar BMEP

seen that the diesel has the highest peak pressure and the highest excitation level. In contrast, the gasoline SI-mode shows the lowest excitation. HCCI combustion reaches nearly the maximum pressure level of the diesel engine, but delivers also an excitation for its pre-compression phase, that is nearly on SI-level at this speed and load. A comparison of the cylinder pressures, the pressure-gradients and a frequency versus time analysis (Wavelet, [12]) of SI- and HCCI-mode versus a common rail turbo-charged diesel, 'TDCI') with same displacement is shown in Figure 4.2; the spectrogram was averaged and calculated over 60 consecutive cycles, and is depicted

in Figure 4.2, right half. This Figure shows in its left half the in-cylinder pressure and its related pressure gradient for three combustion processes, SI, HCCI, and TDCI. The related frequencies and their amplitude versus time content, is also shown on the right half of Figure 4.2 (the corresponding colorbar illustrates the particular noise intensity at the certain time-frequency point). It can be concluded

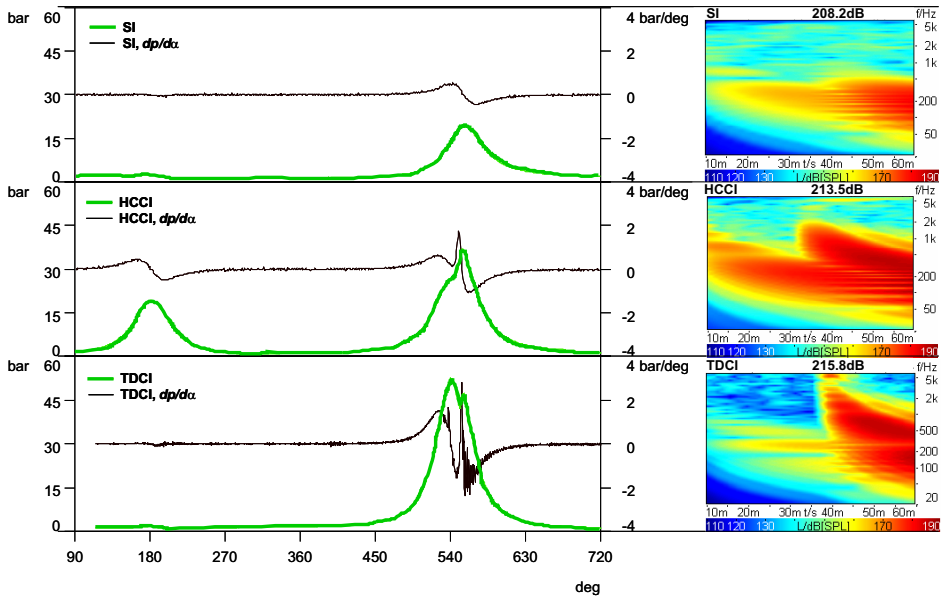

Figure 4.2: Comparative analysis of the combustion excitation at 2000rpm, 2bar BMEP of SI-, HCCI- and a CI-combustion excitation

that SI operation has the lowest excitation level ($208.2dB$) and an accompanying pressure gradient that is nearly on the level of the pre-compression of the HCCI cycle. In contrast, the Diesel (TDCI) shows the highest excitation level ($215.8dB$) and pressure gradient. The combustion excitation level of the HCCI is just $2.3dB$ lower than the TDCI at this particular load and speed. The HCCI combustion was operated with a single injection strategy. The magnitude of the pressure gradient of the HCCI combustion at this particular load and speed is also between the SI- and the TDCI-value. However, both the HCCI and the TDCI combustion pressure traces and their according pressure rise rates show typical compression ignition shapes, whereby the TDCI exhibits a more significant one due to a certain pre-injection strategy. The pressure rise rate of the TDCI shows first a smooth rise rate because of the compression, followed by a sharp pressure rise rate due to the premixed combustion, subsequently followed by a smoother main combustion as is typical for

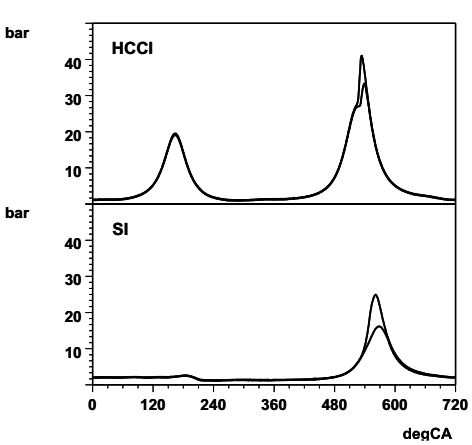

(a) Comparison of the variance of the cylinder pressure traces for HCCI and SI combustion at 2000rpm, 2bar BMEP

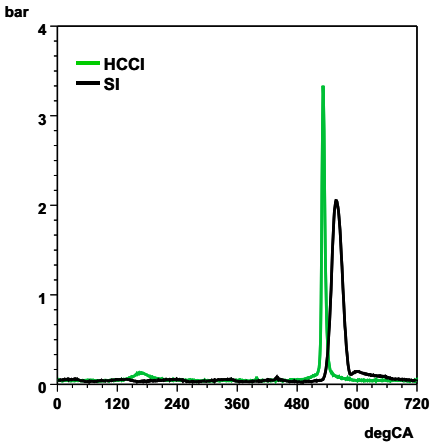

(b) Variance of the maximum cylinder peak pressure and its location for HCCI- and SI mode at 2000rpm, 2bar

Figure 4.3: Spread of individual cylinder pressure traces of SI- and HCCI combustion at part load; analysis processed from 60 consecutive cycles. Note that the combustion during HCCI takes place around $540 degCA$, and for SI around $360 degCA$. This was done to illustrate the impact of the pre-compression caused by the NVO.

such combustion systems [153]. In contrast the HCCI shows similar characteristics, but no distinct rise rate because of a main combustion phase. Because of the single event injection strategy in HCCI there is just one sharp main combustion. But this is not as sharp as the TDCI-combustion due to a lower compression ratio and a slower combustion characteristic, shown by the lower pressure rise rate.

Looking at the stability and repeatability of SI- and HCCI-mode, Figure 4.3(a) shows the spread of the cylinder pressure time history for a HCCI-cycle and the SI-cycle, averaged over 60 consecutive cycles. In each graph the lower black curve reflects the minimum envelope of the analysed pressure traces, and the upper curve the maximum envelope. It can be seen that HCCI has a higher spread regarding its peak pressure, but a better stability of its location than the SI-mode. To underline this, the difference of the envelopes was calculated. These are shown in Figure 4.3(b). Figure 4.3(b) shows a much earlier location relative to ITDC of the maximum peak pressure for the HCCI combustion than the SI-mode. Moreover, the first and the second derivative of the cylinder pressure as a measure for the high frequency excitation [22, 109, 141] of both modes were calculated, as can be seen in Figure 4.4. In each diagram depicted in the two sub-figures of Figure 4.4, the two individual

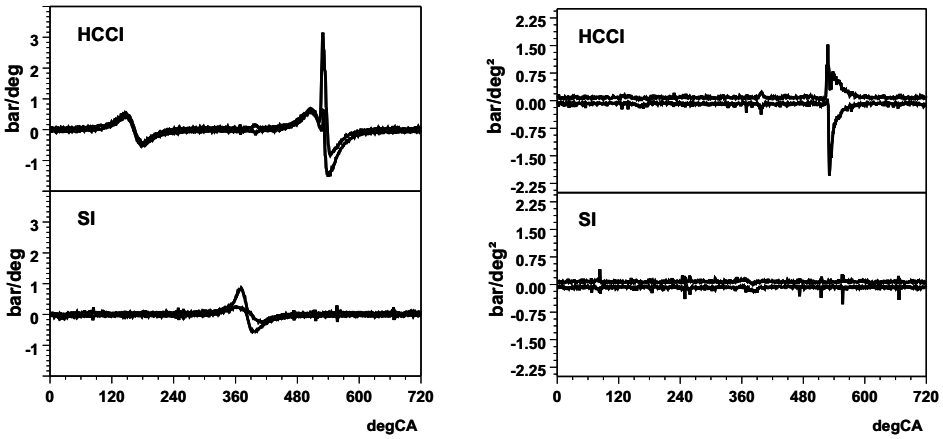

(a) Comparison of the variance (minimum and maximum envelope) of the cylinder pressure gradients ($dp/d\alpha$) of HCCI- and SI combustion at 2000rpm, 2bar BMEP

(b) Spread (envelope analysis) of the second derivation of the cylinder pressure ($\frac{d^2p}{d\alpha^2}$) for HCCI- and SI combustion at 2000rpm, 2bar

Figure 4.4: Analysis of the spread of the cylinder pressure rise rate of SI- and HCCI combustion at part load; analysis processed from 60 consecutive cycles. Note that the location of combustion is similar to Figure 4.3

graphs represent the upper and lower envelope of 60 consecutive cycles. Here HCCI-operation shows even during the pre-compression a pressure gradient similar to that of SI-mode during its combustion. In addition, HCCI has a significantly higher spread regarding the pressure gradient. According to Figure 4.4(b) it can be followed that the SI combustion does not show any significant second pressure gradient as a measure for the high frequency contribution to the combustion noise. However, the HCCI combustion has one: the positive and negative envelope curve is caused by the different ignition delays. If the cylinder pressure caused by the compression only shows a negative slope, but with the combustion starting immediately after TDC this second derivative, and its peak respectively, is negative, hence $\frac{d^2p}{d\alpha^2} \leq 0$. In turn, the second derivative has a positive peak with the main combustion starting before TDC.

4.1.2 Structure Excitation

Based on the models and equations derived in Chapter 3.1., the mechanical excitation was calculated also using the cylinder pressure data from the 2000rpm, 2bar BMEP operation, considering the non-linearities, caused by the lashes in the power

conversion system and lubrication effects. Based on the results the impact of the different combustion types can be studied now with regard to gas-force, piston-guiding force, force in the connecting rod and the force, acting on the main-bearing.

Gas Force: Figure 4.10 shows a comparison of the force $F_{Gas}(\alpha)$, initiated by the combustion over one cycle, comparing SI- versus HCCI-mode. The HCCI combus-

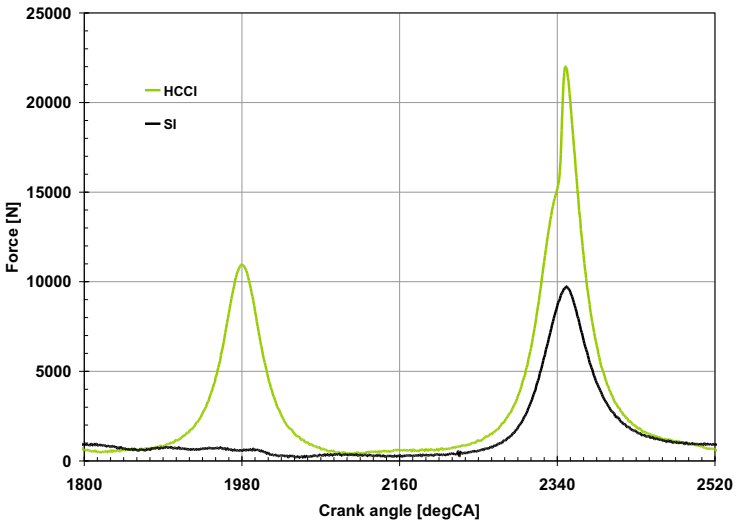

Figure 4.5: Comparison of combustion induced force - SI vs. HCCI at 2000rpm, 2bar BMEP

tion, represented by the bright line, delivers even in the pre-compression phase at $\approx 1980 degCA$ an excitation that is as high as the SI combustion generates around the combustion TDC at $2340 degCA$. However, superimposing the individual combustion HCCI excitation on a multi-cylinder engine, the impact of the pre-compression excitation can be neglected as long as it is hidden by the combustion in a cylinder, having its combustion in parallel. For example this would not be the case for an in-line five cylinder engine architecture. Furthermore, HCCI combustion at this particular point of operation leads to more than twice as much level of peak force than an equivalent SI combustion. Note also the increasing slope at $\approx 2340 degCA$ of the gas-force for the HCCI, caused by the compression ignition characteristics.

Piston-Guiding Force: a comparison of the guiding force of the piston and travel is depicted in Figure 4.8. The acting force and the related piston travel in the cylinder liner for the SI-excitation is shown in Figure 4.6(a), whilst the according data for the HCCI-excitation are shown in Figure 4.6(b). Because of the shape of the

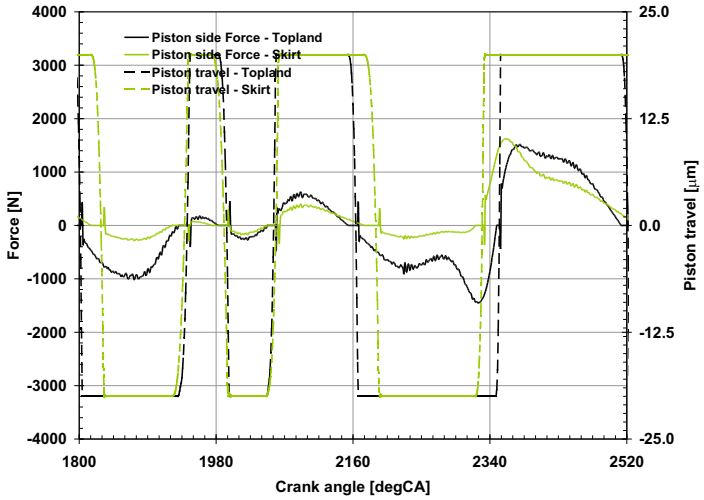

(a) Piston side force and travel during a SI cycle

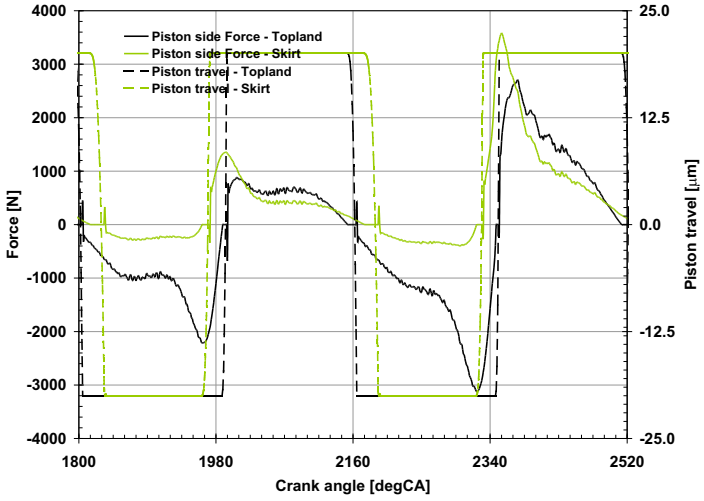

(b) Piston side force and travel during a HCCI cycle

Figure 4.6: Comparative analysis of piston side forces and -travel during SI- and HCCI-operation at 2000rpm, 2bar BMEP; combustion takes place around 2340*deg* crank angle (ITDC)

piston guiding force follows the rotational force characteristics, the piston changes its position from the thrust to the anti-thrust side, depending on the direction of the force. In contrast to the HCCI-mode operation, the intake stroke of the throttled SI-mode operation at 2000rpm, 2bar BMEP leads to an additional travel of the piston during SI-mode around 1980$degCA$ because of the change of the direction of the acting guiding force, hence leading six times during one cycle to a change of the lateral position of the position of the piston. As a result of the pre-compression, maintaining always a positive cylinder pressure, the piston just changes its lateral position four times during HCCI-operation. Moreover it can be seen from Figure 4.8 that the travel of piston-skirt and piston-topland is separated because of the non centrally positioned pin. As a result such a design is intended to lower the piston slap excitation. However, the magnitude of the acting guiding forces during HCCI are twice as high as during SI-operation. Assuming the same friction coefficient during both mode of operation, this would double the friction-force between piston and liner during HCCI-operation, too.

Force in the Connecting Rod: the force in the connecting rod has the shape of the gas-force. Figure 4.7(a) shows the force for both combustion modes versus crank-angle, and Figure 4.7(b) depicts the same forces over two consecutive cycles versus tilt angle of the connecting rod. According to Figure 4.7(a) HCCI operation leads to a significantly higher force in the connecting rod than during SI-operation. The maximum magnitude of the force during combustion is more than twice as much than during a SI-operation. But operating the engine in SI-mode the force is turning into a slight negative range, resulting in a traction-force loading of the connecting rod. This is due to the throttled aspirating stroke happening around 1980$degCA$, also denoting intake TDC. In contrast the force remains a pressure-force during HCCI-operation due to the pre-compression. Similar to the gas-force excitation, the magnitude of the pre-compression generated force is similar to the force, occurring in the connecting rod during SI-operation. When drawing both forces versus crank-angle it can be seen that the maximum force occurs closer to TDC during HCCI-operation than during SI-mode. The maximum of the SI-mode related force is retarded relative to combustion TDC, compared to the re-compression effected force, generated during HCCI-operation. Moreover, the maximum gradient of the force during HCCI-mode occurs just at or immediately before TDC, too. As already described in Chapter 3.1.4 this can excite natural frequencies of the piston-pin-connecting rod assembly. Hence the following Figure 4.8 shows the forced-response of the particular eigenfrequencies

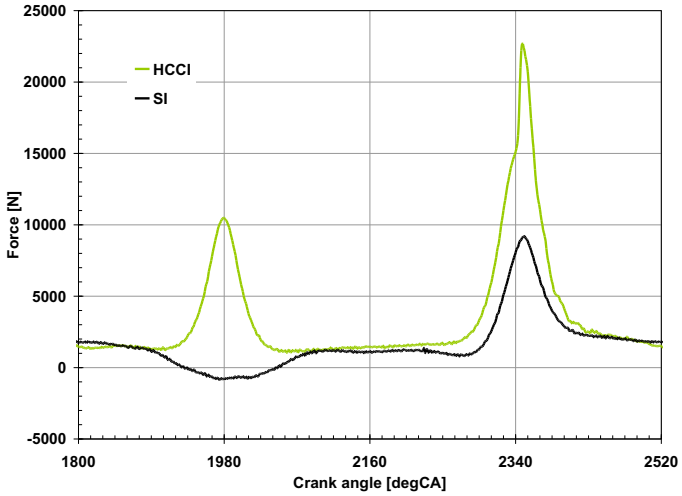

(a) Force in the connecting rod versus crank-angle: SI compared to a HCCI cycle

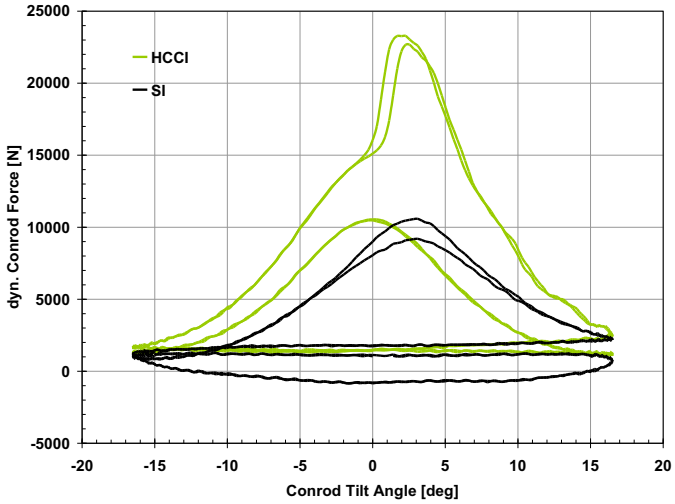

(b) Force in the connecting rod versus tilt-angle: SI compared to a HCCI (two consecutive cycles)

Figure 4.7: Comparative analysis of force in the connecting rod during SI- and HCCI-operation at 2000rpm, 2bar BMEP; combustion takes place around 2340deg crank angle (ITDC)

during SI-operation (Figure 4.8(a)), and during HCCI-operation (Figure 4.8(b)). In accordance with the forced-response model, derived in Chapter 3.1.4, during

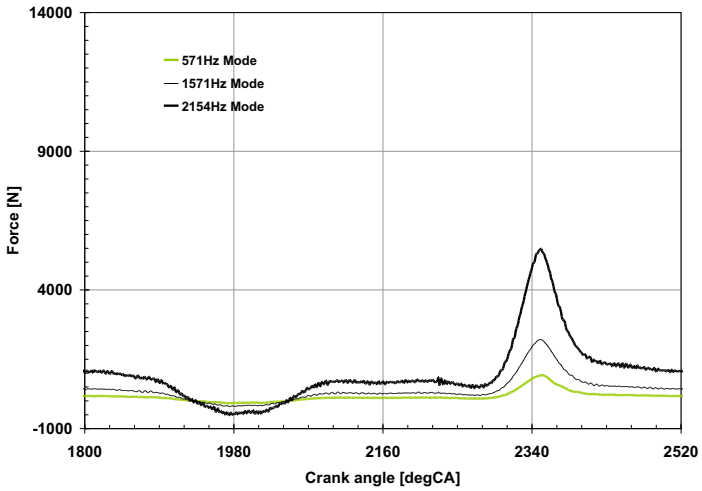

(a) Individual forced response of the considered eigenfrequencies; time response of the model, subjected to SI combustion

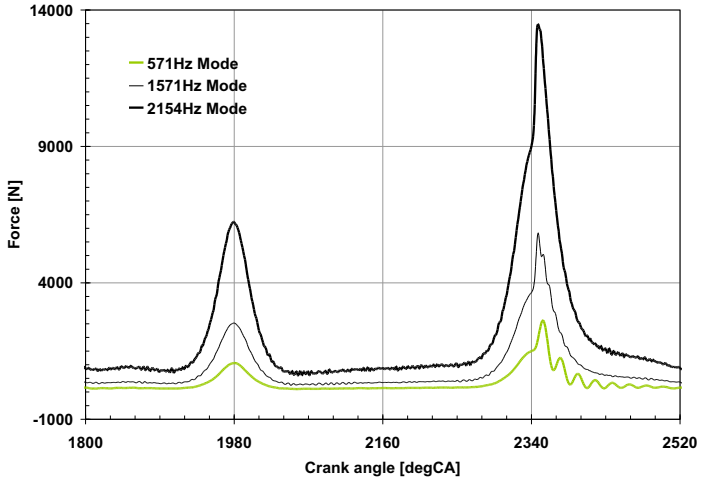

(b) Individual forced response of the considered eigenfrequencies; time response of the model, subjected to HCCI combustion

Figure 4.8: Comparative analysis of the time response of the forced response model of the connecting rod during SI- and HCCI-operation at 2000rpm, 2bar BMEP. Please note: combustion takes place around 2340deg crank angle (ITDC)

both combustion modes the ranking of the individual contribution of the enforced

eigenfrequencies is the same, which follows that the $2154Hz$ mode has the highest contribution, followed by the eigenfrequencies at $1573Hz$ and $571Hz$. However, because of the higher peak-pressure, and subsequently a higher force gradient, the HCCI-operation evokes the eigenfrequencies more significantly as it can be drawn from Figure 4.8(b) for the forced-response component of the $571Hz$ eigenfrequency. In addition the magnitude of the individual forces is attributed to the particular cylinder pressure characteristics, thus the HCCI-operation leads to a force level that is approximately twice as high as enforced by SI-operation.

Force in the Crankshaft Bearing: similar to the results depicted in the previous Figures, the maximum magnitude of the force $F_{MB}(\alpha)$, acting on the crankshaft, is as twice as high for the HCCI-operation than for the SI-mode at this particular speed and load. The characteristic of both forces follows the shape of the gas-force, too.

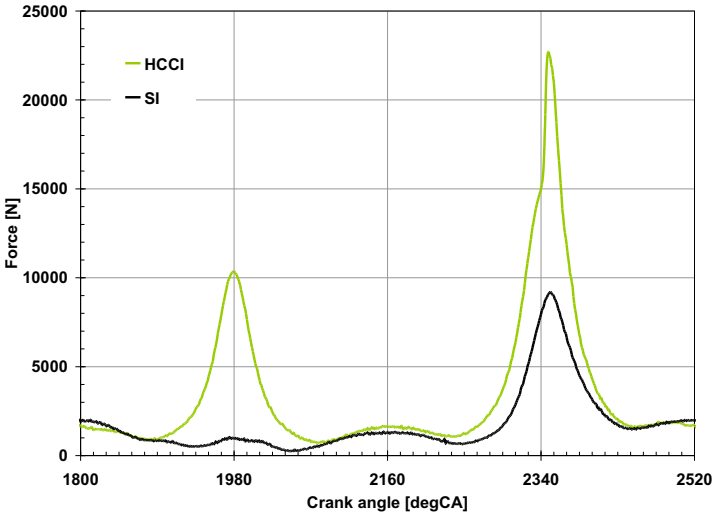

Figure 4.9: Comparison of force, acting on the crankshaft bearing - SI versus HCCI at 2000rpm, 2bar BMEP

Rotational Force: in contrast to the force acting on the crankshaft bearing, the rotating force $F_T(\alpha)$ according to equation (3.1.28) as a measure for torsional vibrations is depicted comparatively between SI- and HCCI-operation in the following Figure 4.10. Assuming the same geometric dependencies and inertias during both combustion modes the level of torsional vibrations effected by HCCI-operation will follow the increase of the magnitude of the force accordingly. Subsequently

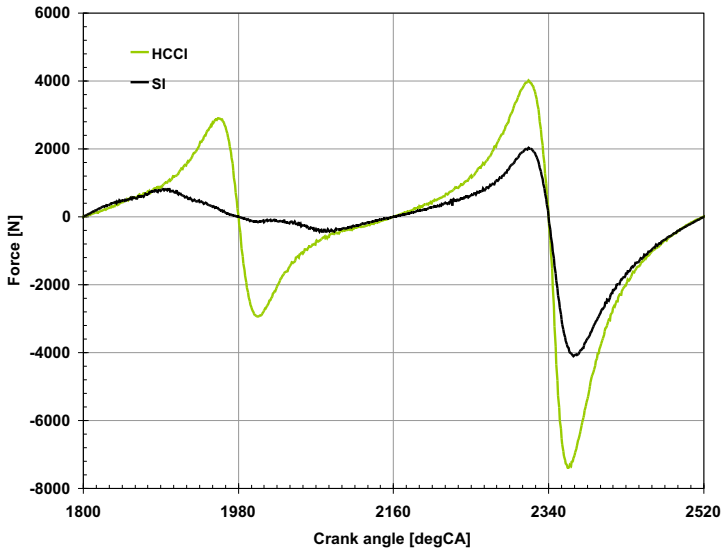

Figure 4.10: Comparison of rotational force - SI vs. HCCI at 2000rpm, 2bar BMEP

operating an engine in HCCI requires a reinforcement of the crank-train and powertrain structure to take on the increased level of torsional vibrations, as they are for example proposed in [17, 37].

4.1.3 Radiated Noise and Sound-Quality

According to the structure of the prediction model, the individual contributions to the structure excitation of the radiated noise, and the radiated noise itself of both combustion modes were assessed. Figure 4.11 depicts the individual piston guidance force excitation in Figure 4.11(a) and Figure 4.11(b) shows a comparison of the third octave spectra of the main bearing excitation of both combustion modes. The resulting third octave spectrum of the radiated noise of each combustion mode is depicted in Figure 4.11(c). Operating the engine in SI leads to a lower level of both piston guidance force and main-bearing force excitation. Moreover, operating the engine in HCCI leads to an increased magnitude of the fourth engine order related third octave band ($125Hz$) because of the higher cylinder peak pressures. In addition, because of the higher pressure rise rate an increased contribution of the frequencies between $200Hz$ and $1000Hz$ can be noticed. In summary, the magnitude of the individual third octave frequency bands during HCCI-operation exceeds the levels generated by SI combustion significantly. When looking at the resulting third octave spectra of the calculated radiated noise, the HCCI operation leads to a

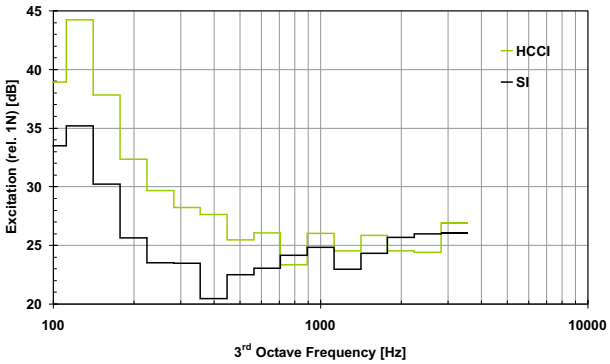

(a) Comparison of the excitation, effected by the piston guidance force

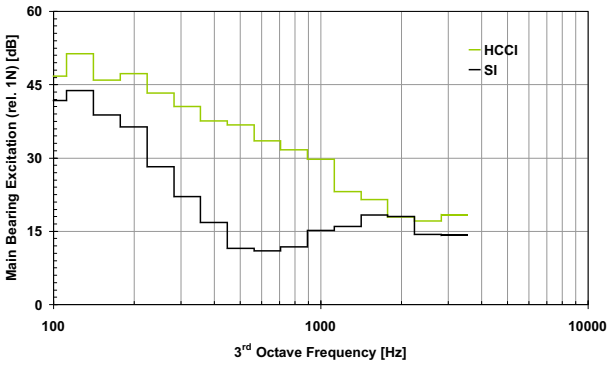

(b) Comparison of the excitation, acting on the main bearing

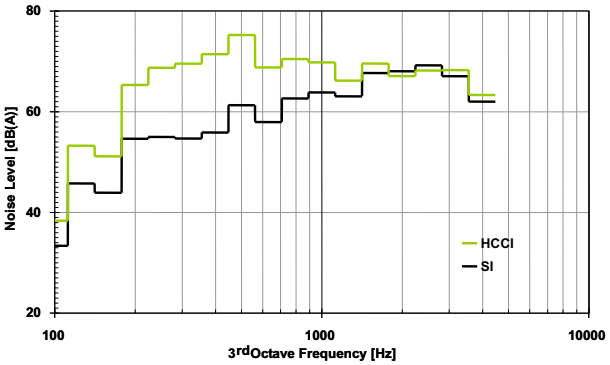

(c) Predicted radiated noise: third octave spectra of SI- and HCCI combustion

Figure 4.11: Comparison of the main contributors to the structure excitation, and the calculated radiated noise of SI- and HCCI-operation at 2000rpm, 2bar BMEP

significant rise of the third octave bands between $200Hz$ and $1500Hz$ which is again governed by the higher pressure rise rate. The increased magnitude of the $125Hz$ band can be explained with the higher excitation of the fourth engine order, whereby this order corresponds with the second engine order which in turn has an amplitude that is direct proportional to the maximum peak pressure of the combustion. The frequency f_{EO} of an individual engine order N itself can be calculated by:

$$f_{EO} = \frac{n \cdot N}{60}. \tag{4.1.1}$$

In equation (4.1.1) the variable n denotes the engine speed in min^{-1}, and N is the chosen order. The frequency has the dimension Hz. Furthermore, the data gained from both states can be analysed further regarding their sound quality, using the two metrics *Roughness* and *Impulsiveness*. The roughness was analysed as it was presented in Chapter 3.2.2.1, thus Figure 4.12 depicts the individual roughness values versus critical band for the data in Figures 4.12(a) and 4.12(b). Compared to the individual roughness values at SI-operation, an increase of the roughness for the critical bands at $z = 11Bark$ and $z = 12Bark$ with the the according center-frequencies of $1480Hz$ and $1720Hz$ can be noticed for HCCI-operation. The increase at these particular bands can be referred to the higher pressure gradient occurring in HCCI, which in turn evokes the eigenfrequencies of the piston-connecting-rod assembly, lying in these frequency bands. Subsequently these frequencies can then be observed in the radiated noise, too. However, the analysis reveals also slightly higher levels of roughness for the critical bands of 6 to $8Bark$ during SI-operation. According to equation (3.2.17), this increase is governed by a higher standard deviation of the burn duration, $B1090|_{SDM}$, accompanied by a higher standard deviation of the location of the maximum peak pressure, $p_{max}|_{SDM}$. The resulting roughness values for both combustion modes according to equation (3.2.18) are shown in Figure 4.12(c), revealing a slightly higher roughness value R_{SPL} for the SI-mode operation, which is governed by the higher particular roughness value of the critical bands 6 to $8Bark$.

The result of the comparative analysis of the impulsiveness IMP is depicted in Figure 4.13, with Figure 4.13(a) showing both modulation spectra, and Figure 4.13(b) showing the resulting absolute value of impulsiveness. Hereby the resulting impulsiveness of the SI-operation has been defined as a reference value, thus denoting $IMP_{SI} = 1.0$. Operating the engine in HCCI increases the impulsiveness by $\approx 30\%$. This is due to the increased pressure rise rate, accompanied with cylinder peak pressure that is twice as much as during SI-operation. Moreover, the duration of

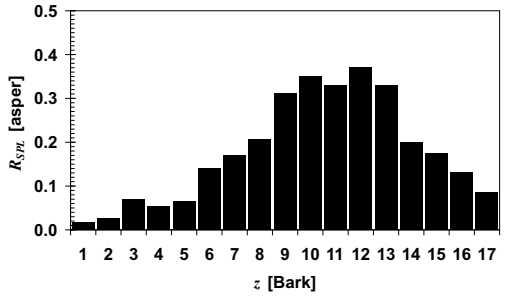

(a) Roughness R_{SPL} versus critical band z during SI combustion

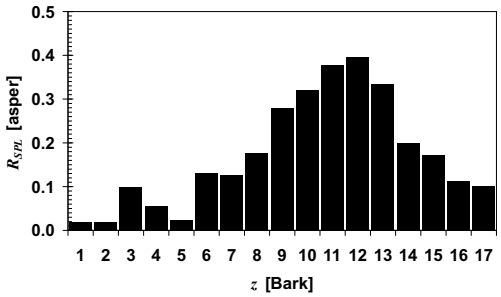

(b) Roughness R_{SPL} versus critical band z during HCCI combustion

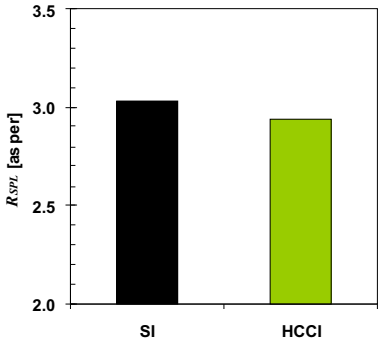

(c) Resulting roughness R_{SPL}- comparison of SI and HCCI operation (calculated from the data shown in the Figures 4.12(a) and 4.12(b))

Figure 4.12: Comparative analysis of the roughness during SI- and HCCI-operation at 2000rpm, 2bar BMEP

HCCI combustion at this point of operation is about five times shorter than for SI combustion. Note also the increase of the modulation frequencies of the half engine orders for HCCI. This is because of a higher cylinder to cylinder variability of the combustion. However, such a characteristic can only be achieved when each individual cylinder runs stable, i.e. with a low $p_{max}|_{SDM}$ and $B1090|_{SDM}$, but differs with its combustion characteristics relative to the other cylinders. Finally, Table 4.1 summarizes important combustion and noise and vibration data of both combustion modes at 2000rpm, 2bar BMEP operation.

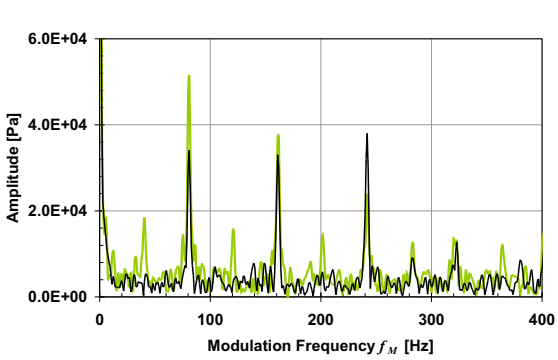

(a) Comparison of the narrow-band modulation spectra for SI- and HCCI-operation

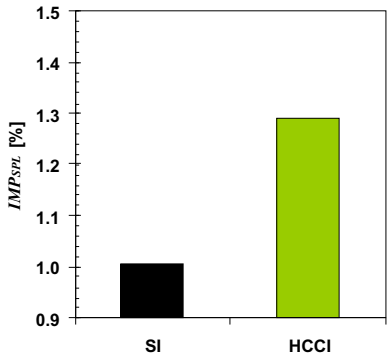

(b) Resulting impulsiveness for SI- and HCCI combustion

Figure 4.13: Comparative analysis of the impulsiveness IMP_{SPL} during SI- and HCCI-operation at 2000rpm, 2bar BMEP

Table 4.1: Comparison of the relevant combustion and noise related data of SI and HCCI-operation at 2000rpm, 2bar BMEP

	SI	HCCI
p_{max} [bar]	19.81	39.832
$p_{max}\|_{SDM}$ [bar]	1.829	1.464
location of p_{max} [deg]	10.4	6.77
$dp/d\alpha$ [bar/deg]	0.642	3.09
$dp/d\alpha\|_{SDM}$ [bar/deg]	0.145	0.483
$B1090$ [deg]	35.76	7.109
$B1090\|_{SDM}$ [deg]	4.224	0.795
$CA50$ [deg]	9.054	3.088
Radiated Noise [dB(A)]	75.7	81.2
Roughness [asper]	3.013	2.93
Impulsiveness [-]	1.0	1.3

4.2 Parametric Studies in HCCI-Mode

The reason for carrying out parametric studies in terms of interaction of combustion, emissions, control settings and noise and vibration is to gain a system identification of the engine hardware for the noise and vibration reduction and development. During this section the impact on noise and vibration of spark assisted HCCI, intake valve timing and intake manifold pressure on HCCI-operation will be shown. In addition the HCCI-operation can be controlled similarly as a conventional CI-engine. Hence parametric studies of different injection strategies were carried out. During these investigations the electro-mechanically actuated injector was revealed as a limiting factor because of its dynamic response characteristic. Most of the noise and vibration analysis were carried out using the prediction routine, derived in Chapter 3.1. Results, gained by measurements in parallel, are marked explicitly.

4.2.1 Spark assisted HCCI

To move the HCCI combustion without affecting the heat release, experiments were carried out to investigate the impact on engine acoustics. At 1500rpm, 2.62bar BMEP, with a start of injection at $280 degCA$ before combustion-TDC (BTDC), the spark during HCCI was first activated and during the second experiment the spark was switched off. The spark-angle in the first experiment was set to $29.9 degCA\ BTDC$. The resulting mass-fraction-burned (MFB) for both modes versus crank-angle is depicted in Figure 4.14. Spark assisted HCCI leads to an earlier start of the

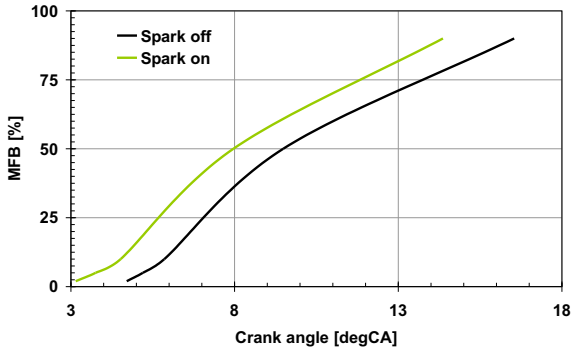

Figure 4.14: MFB of HCCI combustion with and without spark assist at 1500rpm, 2.62bar BMEP

combustion, but does not significantly affect its duration. Figure 4.15(a) shows the according combustion excitation spectrum. The difference in the total combustion

excitation level between the states is $198.8dB - 198.2dB = 0.6dB$. In addition Figure 4.15(b) shows the resulting radiated noise spectra. For operation with activated spark a radiated noise level of $78.8dB(A)$ was predicted. This is similar to the noise level for the operation with de-activated spark that was calculated to be $78.9dB(A)$. In order to investigate a possible impact on the sound-quality, the impulsiveness and

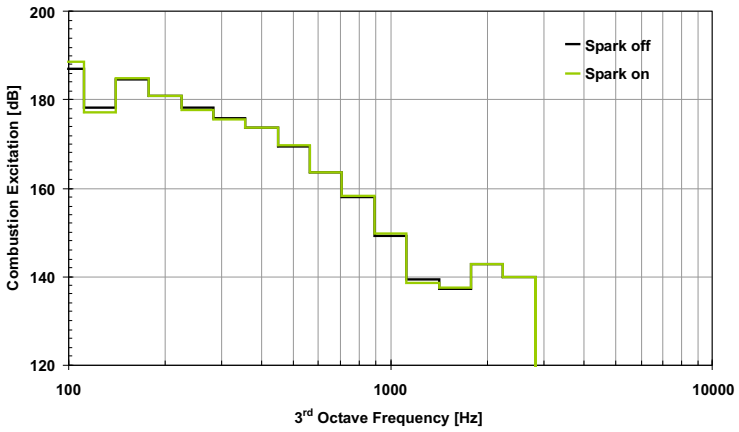

(a) Comparison of the combustion excitation - spark-on versus spark-off

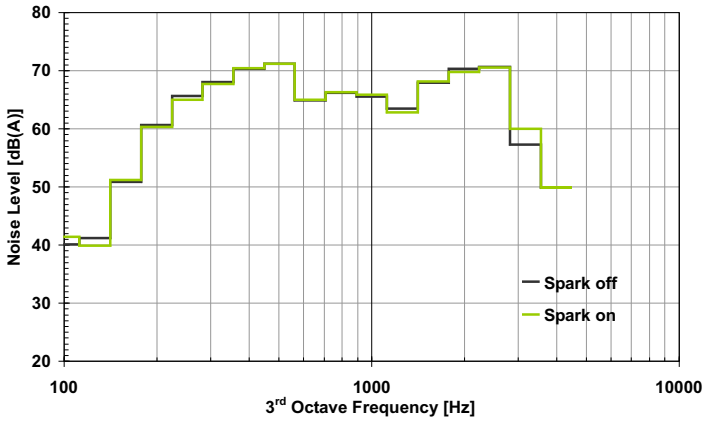

(b) Radiated noise spectrum for both strategies

Figure 4.15: Comparative analysis of the impact of HCCI with activated spark at 1500rpm, 2.62bar BMEP

the roughness have been analysed, too. According to the results shown in Figure 4.16 the HCCI with activated spark exhibits a slightly higher impulsiveness as well as the roughness. Thus, the relevant combustion data $B1090$ and $dp/d\alpha$ were calculated. In conclusion an overview of the test results is given while listing combustion and noise data in Table 4.2 . It can be concluded that only a slight trade-off for the HCCI

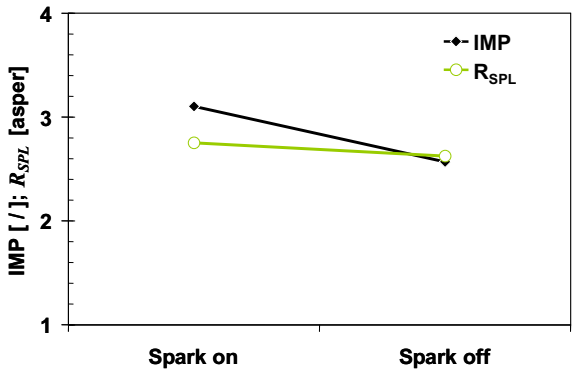

Figure 4.16: Impact of HCCI with activated spark on impulsiveness (IMP) and roughness (R_{SPL}) at 1500rpm, 2.62bar BMEP

Table 4.2: Characteristic data of both HCCI operation modes at 1500rpm, 2.62bar BMEP.

	Activated Spark	De-activated spark
p_{max} [bar]	36.1	34.3
location p_{max} [degCA]	11.3	12.6
$dp/d\alpha$ [bar/deg]	2.17	1.93
location $dp/d\alpha$ [degCA]	6.71	7.71
$B1090$ [degCA]	9.84	10.7
$CA50$ [degCA]	7.96	9.48
Radiated Noise [dB(A)]	78.8	78.9
R_{SPL} [asper]	2.7	2.6
IMP [-]	3.1	2.6

combustion with activated spark can be observed. Furthermore the trend to deliver a slight impulsive noise characteristic of HCCI combustion with activated spark is supported by the slightly higher pressure rise rate and shorter burn duration $B1090$. However, based on these findings spark assisted HCCI could offer an opportunity to phase or re-locate the combustion without any negative impact on the engine acoustics.

4.2.2 Intake Manifold Pressure

As mentioned at the beginning of this chapter a tonal noise of a low frequency, also called 'booming-noise' at the intake orifice was noted when running the engine in un-throttled HCCI mode. Such a noise can be associated with the negative-valve-overlap-strategy in conjunction with the un-throttled air-stream. To describe the characteristics of this noise, a microphone was located $14.4cm$ from the intake orifice at $45deg$ to its axis to measure the orifice noise at 2000rpm, 2bar BMEP. The engine was operated in HCCI using different positions of the throttle-flap. The following Figure 4.17 shows the measured noise level versus the different throttle flap opening angles. Referring to Figure 4.17, a significant lower level of the boom noise can be

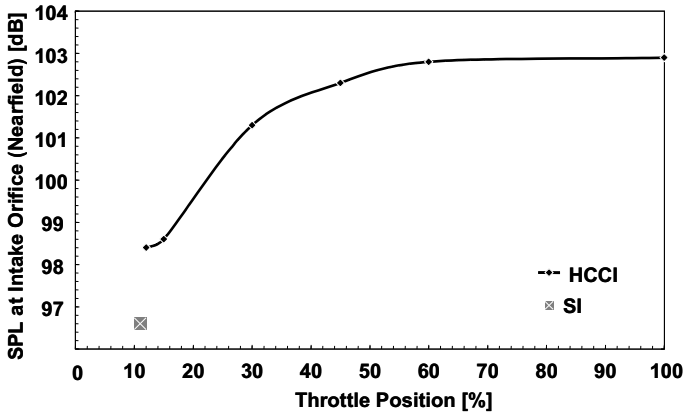

Figure 4.17: Nearfield sound pressure level at intake orifice for different positions of the throttle flap

achieved when establishing 12% throttle which is based on a angle of the throttle flap of $18deg$. Furthermore the characteristics of the noise curve follows the pressure versus throttle angle of an adiabatic throttle, as can be for instance taken from [9]. However, to exhibit the frequencies governing the booming noise, the following Figure 4.18 depicts the spectral analysis of the intake orifice noise during HCCI-mode, while showing the third octave bands versus throttle angle. The spectrogram exhibits a progressive rising slope of the $63Hz$ third octave band that converges above a throttle angle of 30%. In relation to the magnitude of the absolute radiated noise level as shown in Figure 4.17, the noise level at this particular frequency band dominates the noise level. Moreover, according to equation (4.1.1) this effect can be referred to an excitation frequency that again can be associated to the second engine order at the engine speed of 2000rpm. Hence, the booming noise can be explained by

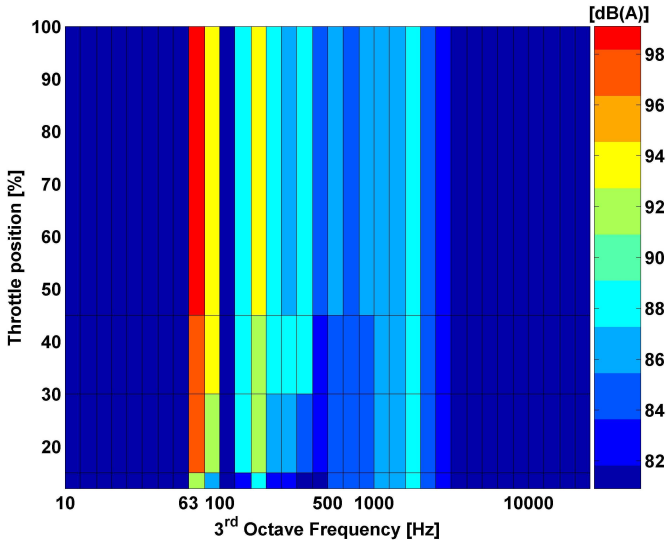

Figure 4.18: Spectrogram (third octave bandwidth) of the near-field sound pressure level at intake orifice for different throttle-angles during HCCI operation at 2000rpm, 2bar BMEP

pressure fluctuations, caused by pressure waves, reflected at a closed tube, thus the closed intake valve, and then in turn leading to a superimposition with a contrary pressure wave, evoked by the cylinder that is breathing consecutively. Because this effect happens twice per engine revolution on a four cylinder four stroke engine, it is associated with this particular frequency.

4.2.3 Intake-Camshaft Timing

To effect HCCI operation, the negative overlap valve timing strategy was enabled. During the investigation, carried out at 2000rpm, 2bar BMEP, the intake valve open (IVO) timing was varied within the range of 60degree to 90degree after top dead center (ATDC) of the re-compression. A microphone was positioned at the intake orifice as already mentioned in the previous chapter. The in-cylinder pressures with an interval of $\Delta\alpha = 1deg$ that is equal to a sampling rate of $f_s = 12kHz$ were measured, too. As aforementioned, the combustion excitation of the SI-mode at the same load and speed is lower than HCCI operation. Interesting to see is the variance of the maximum peak pressure and the spread of the duration of the combustion. Obviously the HCCI-mode has a lower variance at this point of operation than the SI-mode as already shown in Tab. 4.1. The different IVO chosen do not have an

impact on the HCCI combustion pressure traces. Thus no impact of the IVO on the combustion excitation was observed as it can be taken from Tab. 4.3. However, Fig-

Table 4.3: Characteristic combustion data of HCCI operation at 2000rpm, 2.0bar BMEP for different IVO-settings.

	IVO= $60 degCA$	IVO= $73 degCA$	IVO= $85 degCA$
p_{max} [bar]	37.74	38.45	37.84
location p_{max} [degCA]	11.19	10.75	10.97
$dp/d\alpha$ [bar/deg]	2.88	3.07	3.03
location $dp/d\alpha$ [degCA]	6.86	6.45	6.76
$B1090$ [degCA]	8.53	8.19	8.06
$CA50$ [degCA]	8.03	7.54	7.77

ure 4.19 shows the third octave spectral analysis of the measured intake orifice noise for three different timings of IVO. This was done because during the measurement

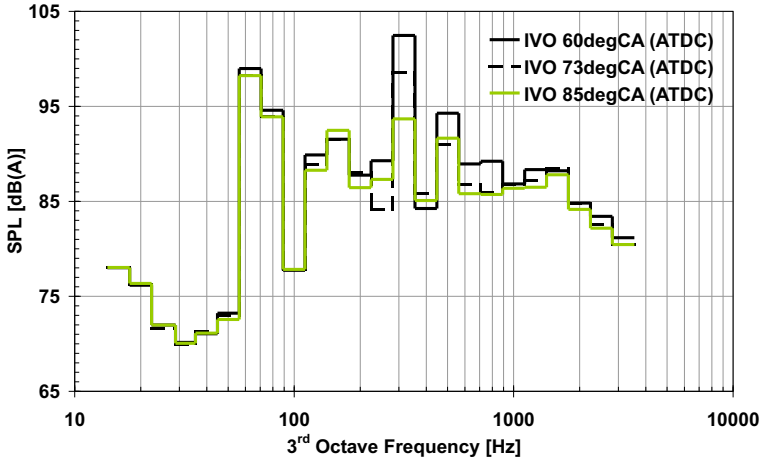

Figure 4.19: Interaction of sound pressure level at the intake orifice (near-field), IVO and the impact on engine roughness, governed by 315Hz-third octave band

an increase of the roughness of the radiated engine noise was observed while moving the IVO to earlier timings at $73 degCA$ and $60 degCA$. It can be seen that an increase of the $315 Hz$ third octave band clearly dominates the acoustics of the intake orifice. Because of that, the overall noise level increases from $96 dB$ at $85 degCA$ (ATDC) IVO up to $100.2 dB$ for the early IVO-timing at $60 degCA$ (ATDC) as well. The increase of the noise level of this particular band can be referred to a sensitivity of

the inlet-system on the 10^{th}-engine order, which is a harmonic of the second engine order, corresponding to 66Hz.

4.2.4 Timing of a Single-Injection Event

As it is known from compression ignition engines, the timing of the injection has an impact on the radiated noise and its impulsiveness. While keeping the injection quantity constant, an injection sweep using a single injection strategy, has been done while varying the injection from an early $333 degCA$ before ignition top dead center (BDTC) to a late $210 degCA$ BTDC. During the measurements, done at 1500rpm and a load of 2.62bar BMEP, the coolant outlet temperature was kept constant at $90°C$, and the air inlet temperature was constant at $22°C$. Figure 4.20 shows both the measured structure borne level and the calculated radiated noise level versus the start-of-injection (SOI). To avoid a tampered signal by local modes, the accelerometer was glued at a stiff location, evaluated by a modal analysis, on the crankcase. It can be seen that both noise levels increase progressively when the injection is

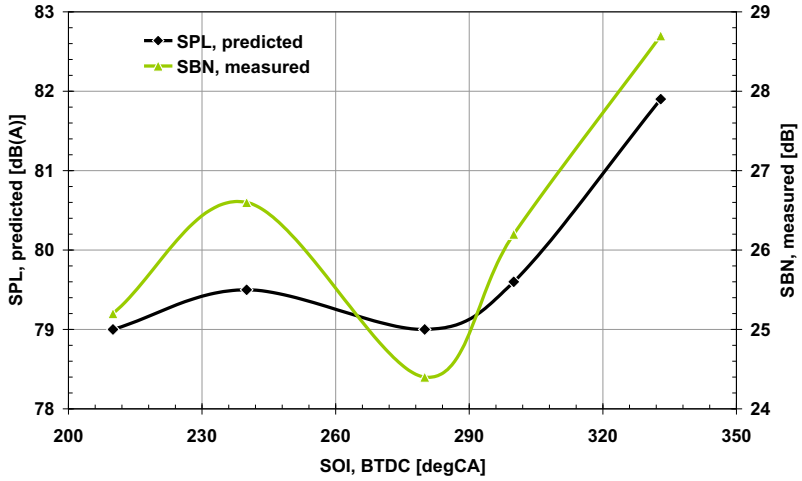

Figure 4.20: Radiated noise (calculated) and structure borne noise (measured) versus start-of-injection at 1500rpm, 2.62 bar BMEP

initiated early. If the injection takes place at the earliest possible location, id est immediately after the pre-compression, both noise levels reach a maximum. This is because the ignition delay for this setting allows a longer time for mixture formation, resulting in a sudden combustion, accompanied with maximum peak pressures occurring closer to TDC, higher pressure rise rates, and a shorter combustion dura-

tion, represented by $B1090$, as depicted in Figure 4.21. Moreover, this results in an increase of the impulsiveness, IMP, too. If the injection happens earlier, the tem-

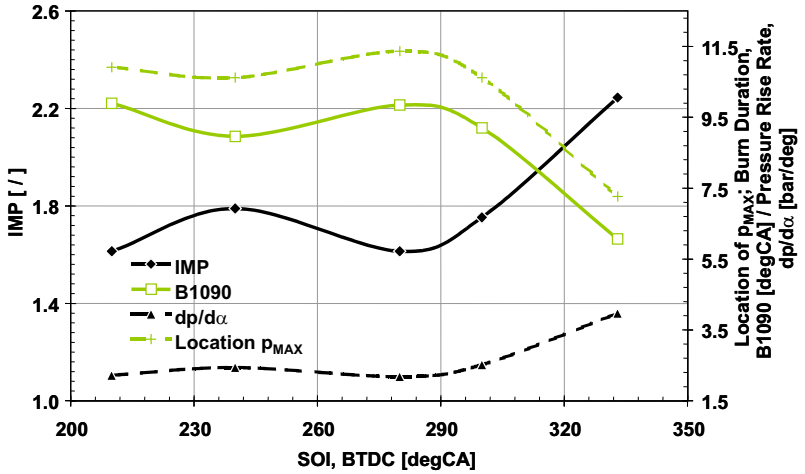

Figure 4.21: Impulsiveness (IMP) and combustion analysis versus start-of-injection at 1500rpm, 2.62 bar BMEP

perature and the pressure of the residual gas in the combustion chamber are lower because of the opened intake valve. However, because of the residuals, elevated in their temperature by the pre-compression, first chemical reactions can take place to let the main compression-ignition combustion take place suddenly and closer to combustion TDC [98]. Because of that the pressure rise rate will increase, accompanied by an earlier location of p_{max} and a shorter duration of combustion, $B1090$. However, what are the dominating modulation frequencies, leading to the higher magnitude of IMP for such combustion characteristics? The following Figure 4.22 shows the modulation spectrum, which forms the basis of the index IMP as derived in Chapter 3, versus SOI. Because of the four cylinder 4-stroke characteristics, the modulation frequencies f_M, representing the second and fourth engine order, dominate the spectrogram at $f_M = 50Hz$ and $f_M = 100Hz$. Thereby the modulation frequency f_M of an arbitrary chosen engine order can be similarly to equation (4.1.1) calculated by:

$$f_M = \frac{n \cdot N}{60}, \tag{4.2.1}$$

while taking $N = 2, 4$, and $n = 1500min^{-1}$. Moreover, as already depicted in Figure 4.21, at $SOI = 240degCA$ the increase of IMP is dominated by a slight increase of f_M at $50Hz$, evoked by a slightly higher pressure rise rate and an earlier and shorter

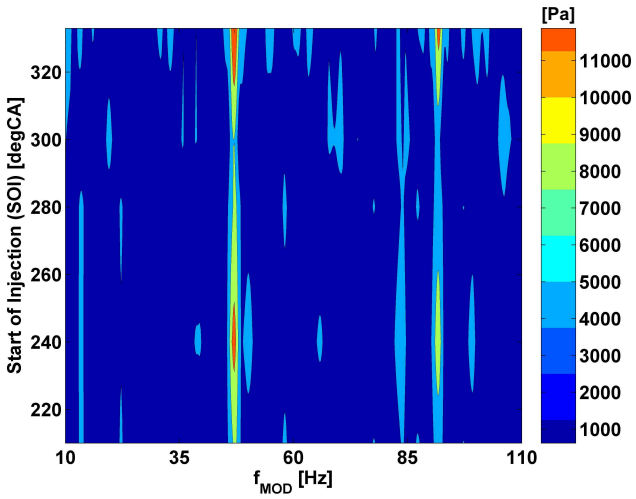

Figure 4.22: Modulation spectrum versus start-of-injection at 1500rpm, 2.62 bar BMEP

combustion at this particular operational point. Furthermore, the increase of IMP because of start-of-injection takes place early, is mostly based on the progressive increase of these particular modulation frequencies above $SOI = 310 degCA$ BTDC. Above all, the engine structure then will respond more harshly than at later injection settings. Figure 4.23 shows the calculated radiated noise spectrum versus SOI. It

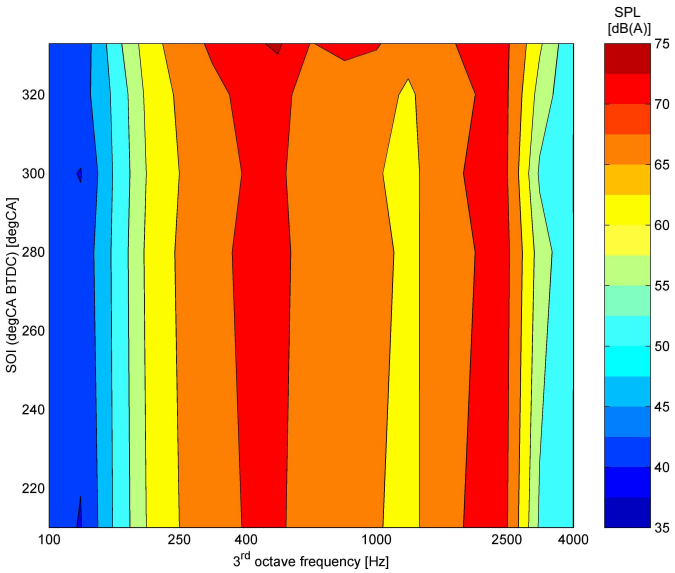

Figure 4.23: Third octave spectrum of the radiated noise (calculated) versus start-of-injection at 1500rpm, 2.62 bar BMEP

can be concluded that the earlier the start of injection is initiated, the more the spectrum is dominated by the frequency bands between 400 to $2500Hz$. This can be directly referred to the excitation models, as presented in Chapter 3, where the direct dependency of the forced response of the piston-pin-connecting rod dynamics was elaborated and analysed doing a parametric study, using a pressure rise sweep. Subsequently two settings were taken from the SOI-sweep for further analysis: the latest, which means SOI takes place at $210degCA$, and the earliest, thus SOI at $333degCA$. A comparison of the combustion excitation, piston side-force- and main-bearing excitation are shown as third octave spectra in Figure 4.24. The comparison of both combustion excitations, depicted in Figure 4.24(a) reveals a slightly higher excitation for the $SOI = 333degCA$ setting of the frequency bands that fall within the second and the fourth engine order. Because of the faster combustion and a higher pressure rise rate the early start of injection delivers a higher magnitude of the excitation at frequencies above $200Hz$. The resulting level of the combustion excitation increases from $198.8dB$ to $200.4dB$ for the SOI at $333degCA$. When looking at the excitation caused by the side forces and the secondary movement of the piston, as it is depicted in Figure 4.24(b), an early SOI leads to a higher magnitude of excitation in these frequency bands that can be associated with the integer and half engine orders ($N = 4.5, 5, 12$), which means for the in-line four cylinder four stroke engine used here the $125Hz$ and the $315Hz$ band, respectively. Because of the secondary movement of each piston between thrust- and anti-thrust side in the cylinder liner, occurring four times per piston for each cycle, the existence of such an order pattern can be generated. Moreover, this can be evoked by a high cylinder-to-cylinder deviation. This particular reason can be excluded here, because the validity of the individual measurements used for analysis, was proven to be below a certain target value, defined by the cylinder and average standard deviation of the indicated mean effective pressure [1]. However, using the SOI at $333degCA$ leads to a resulting excitation level of $51.6dB$ instead of $51.1dB$ for the late injection timing. Finally Figure 4.24(c) reveals the trade off regarding the main-bearing excitation. As this force has a similar shape as the combustion excitation and force, the increase of the individual third octave frequency bands is similar as in Figure 4.24(a). Because of the higher pressure rise rates, the early SOI setting shows an opposite trend to the late setting because of an increased $1250Hz$ frequency band. This can be associated

[1] The exact specific values are company confidential (Ford Motor Company).

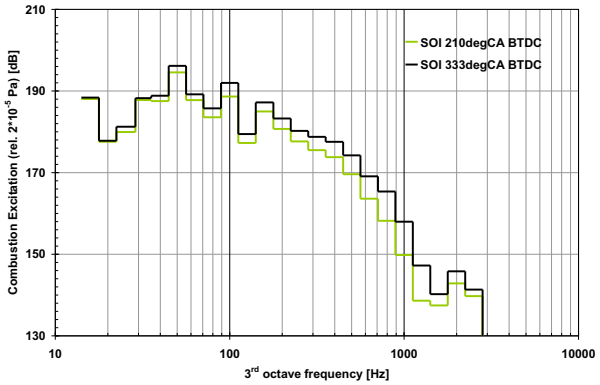

(a) Comparison of the combustion excitation for an early and a late start of injection

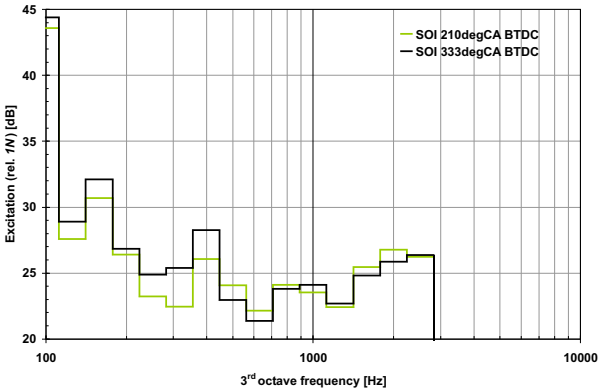

(b) Comparison of the piston side-force excitation for an early and a late start of injection

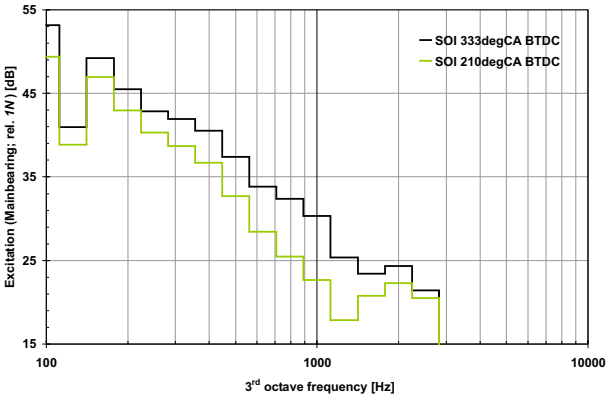

(c) Comparison of the main bearing excitation for an early and a late start of injection

Figure 4.24: Comparison of different excitation sources (third octave spectra) versus start-of-injection at 1500rpm, 2.62 bar BMEP

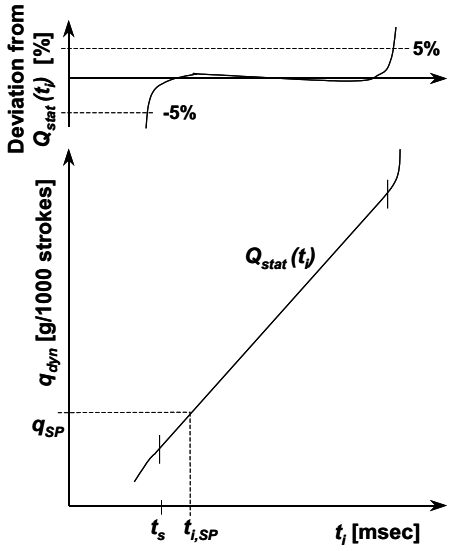

Figure 4.25: Flow rate q_{dyn} as a function of pulse-width t_i for a solenoid gasoline injector and deviation of flow rate versus pulse-width (upper graph)

with the eigenfrequency model as derived in Chapter 4 and is the contribution by the magnitude of the pressure rise rate. The absolute level of the excitation results in $56dB$ for the early SOI, and in $52.8dB$ for the late setting at $210degCA$. It can be concluded that the difference of the relevant structure excitation sources is mostly significant in the main bearing excitation.

4.2.5 Split-Injection

Hitherto single injection settings were considered. In order to support low-load and low speed operation the application of split-injection strategies during HCCI-operation can be useful [98]. When employing such a strategy a small amount of fuel is injected just before the pre-compression and the main injection is released similarly to stratified combustion strategies shortly before ignition TDC. On the hardware side this requires a high dynamic of the injector, and also a relative high precision to ensure linear mass flow characteristics. Also the injector driver must be capable to support such short pulse width to avoid non-linear flow during opening and closing. The engine used for the investigations here has outward opening multi-hole injectors of a solenoid design type. When choosing such injectors the characteristic of flow quantity through the opened injector is linear with the impulse width of the electrical current to open the injector. Such a flow characteristic as a function of pulse width is depicted in the lower graph in Figure 4.25. Because of the dynamics brought

with the system design itself, there is always a delay time t_s to open the injector in such a way that the flow increases linearly with longer opening times. In any case there could be a fuel below t_s, but this amount would not be controllable. This is why the pulse-width must be always longer than the delay time, thus $t_i > t_s$. The resulting linear flow is separated from the flow curve with a vertical line, denoting the minimum flow rate $q_{dyn}|_{min}$, and an upper second one, denoting the maximum flow rate $q_{dyn}|_{max}$. Between both the flow characteristics are linear. Furthermore, a set point (index sp) for reasons of specification, and to ensure comparability of different types of injectors is introduced. Hence on can write for the nominal static flow $Q_{stat}(t_i), [kg/min]$:

$$Q_{stat}(t_i) = \frac{60 \cdot [q_{dyn}(t_i) - q_{sp}(t_{i,sp})]}{t_i - t_{i,sp}}. \tag{4.2.2}$$

In order to better characterize an injector regarding its linearity of fuel flow, the *Dynamic-Flow-Range* (DFR) has been defined as the ratio of $q_{dyn}|_{max}$ and $q_{dyn}|_{min}$, [102]:

$$DFR = \frac{q_{dyn}|_{max}}{q_{dyn}|_{min}}. \tag{4.2.3}$$

The nominator and the denominator in equation (4.2.3) are both defined by the upper and lower end of the linear curve Q_{stat}. Both have a deviation from the flow function of $\pm 5\%$ as illustrated in the upper curve in Figure 4.25. Based on these characteristics the injector is then, beside other testing, proved regarding its dynamic repeatability and and static flow stability under different ambient conditions versus defined acceptance criteria. To achieve a better dynamic response the location of $q_{dyn}|_{min}$ should be mated with a pulse width as short as possible. However, this is again limited by the mechanical dynamics of the injector, governed by the mass of the needle (in conventional injectors it is in the range of 2.7 - 4.3g, [102]), and the injector driver, providing the current necessary to open and close the injector without bouncing effects of the needle in the valve seat. Such bouncing would lead to the undesired and un-metered injection of fuel, finally affecting the combustion characteristics.

It will be shown in the next paragraphs that the interaction of pulse width and the related flow can affect the split-injection characteristics, and thus influence the combustion characteristics.

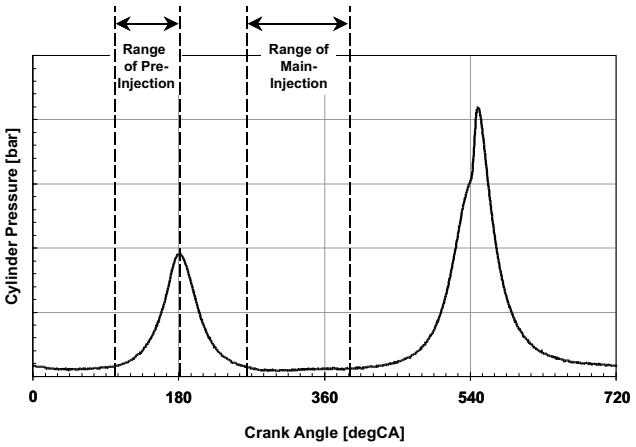

Figure 4.26: Sketch of the feasible range of the location of start-of-injection during HCCI-operation

4.2.5.1 Variation of the Amount for Pre- and Main-Injection

In order to establish low-load strategies, the usage of injectors allowing multiple injections prior to main-combustion is already known from CI-engines. As already mentioned solenoid injectors have a dynamic range that depends on the injector type and the amplifier and controls. The injectors applied on the engine here allowed one pre-, and a main injection. Subsequently tests were carried out varying the amount of fuel from a single main injection, which means a split rate of 100% down to a split rate of 78%. The 78% split rate was defined by the acceptance criteria for combustion stability and combustion knock-index at this speed and load. The range of the location of the start-of-injection for the pre- and the main-injection event is illustrated for a HCCI combustion in Figure 4.26. However, during the sweep of the split rate the timing of SOI and also the valve timing was kept constant at $405 degCA$ BTDC for the pre-injection, and at $245 degCA$ BTDC for the main-injection. The following Figure 4.27 shows the resulting radiated noise level evoked by the different settings of the split rates. It is clearly visible that above a split rate of 85.5% the noise level increases significantly. Moreover a significant rise of the impulsiveness of the radiated noise was observed which can be also taken from the shape of the graph representing IMP in Figure 4.28. Clearly the increased impulsiveness correlates with a shorter and earlier combustion, accompanied by an increased pressure rise rate, too. The shorter and earlier combustion for the split rates of 81.5% and 78% can be referred to an increased time for mixture preparation

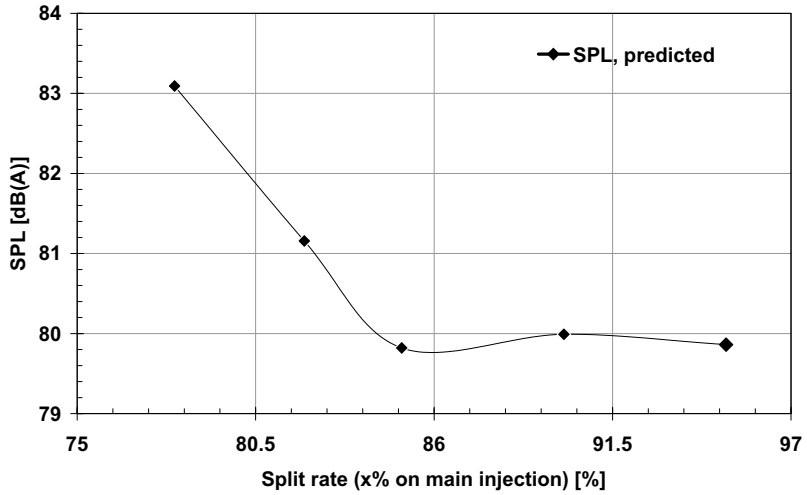

Figure 4.27: Calculated Noise level for a different split rates at 2000rpm, 2bar BMEP. A split rate lower 100% means attempting to increase the amount of fuel of the pre-injection

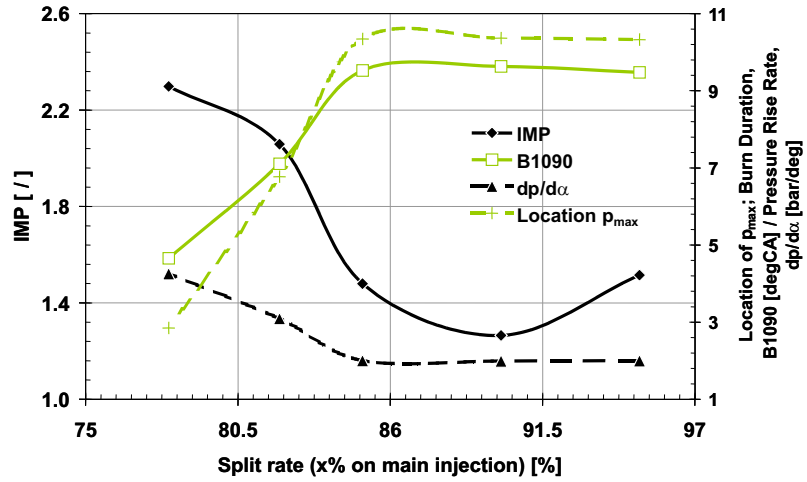

Figure 4.28: Interaction of Impulsiveness IMP and combustion data at 2000rpm, 2bar BMEP

and pre-reactions, initiated by pre-compression, thus allowing an earlier and faster combustion. In addition the sudden rise of the characteristics above 85% can be referred to the injector dynamic range, obviously limiting the pre-injection in the linear range for split rates below 85%. The Roughness of the engine noise versus split rate is depicted in Figure 4.29. Also the standard deviation of the maximum peak pressure $p_{max}|_{SDi}$ of each cylinder i has been included as a thermodynamic measure for the roughness. Because of the calculation procedure of the roughness R_{SPL},

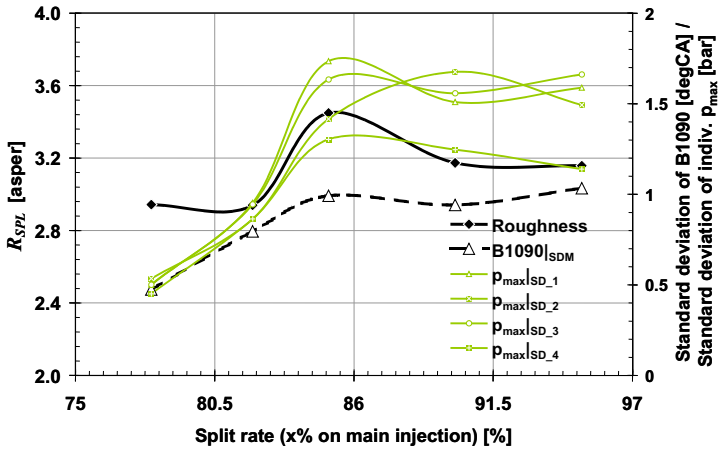

Figure 4.29: Interaction of Roughness R_{SPL} and combustion statistical-data at 2000rpm, 2bar BMEP

which was derived in Chapter 3.2.2.1, the higher the spread of the maximum pressure of each cylinder differs from the spread of the others, the higher is the roughness. This is also supported by the results depicted in Figure 4.29, where a larger difference of the individual standard deviations of the maximum peak pressures for a split rate higher than 85% is accompanied by a higher roughness R_{SPL}. Furthermore, it must be noted also that based on the calculation procedure of R_{SPL}, a high spread of the individual cylinders relative to the other cylinders supports a higher roughness, as shown at the split rate of 85%. This is supported by the results, gained from the operation with a the split rate of 95%, where indeed a large absolute spread of $p_{max}|_{SDi}$ can be observed, but except cylinder four, all other cylinders show a similar value of $p_{max}|_{SDi}$, then leading to a lower magnitude of R_{SPL}. In addition also a slight correlation of the averaged standard deviation of the burn duration $B1090$ can be noted.

4.2.5.2 Variation of the Timing of Main-Injection

Experiments were done at 2000rpm, 2bar BMEP with constant timing of the pre-injection, while varying the location of the main-injection from an early SOI of $280 degCA$ up to a late location at $180 degCA$. The amount of fuel injected during both injections was kept constant with a split rate of 78%. The valve timing was kept constant, too. The development of the predicted radiated noise versus the location of main-injection is shown in Figure 4.30. It can be concluded that the

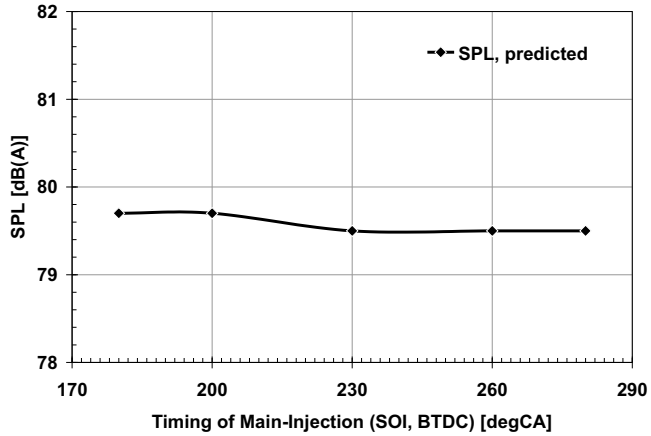

Figure 4.30: Radiated noise versus location of main-injection at 2000rpm, 2bar BMEP

timing of the main-injection does not have a significant impact on the level of the radiated noise. This is because the predicted noise level deviates just in a range of $0.3dB(A)$ which is below the repeatability of engine noise measurements. Similar characteristics are revealed when looking at the impulsiveness and the according combustion data as illustrated in Figure 4.32(b). Despite a slight increase of IMP

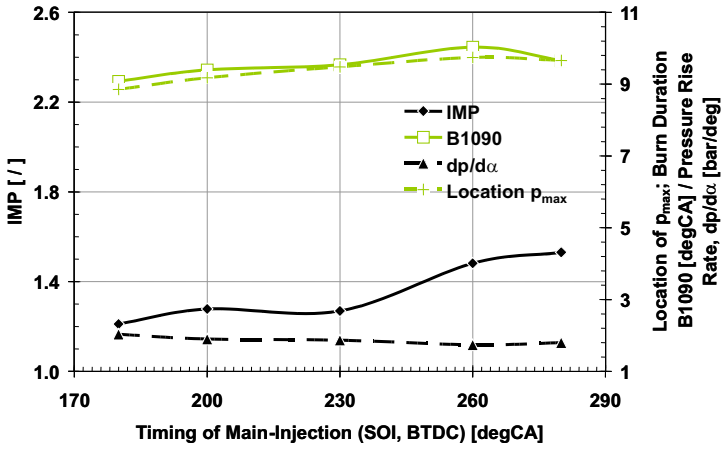

Figure 4.31: Sound-quality versus location of main-injection at 2000rpm, 2bar BMEP

of ≈ 0.4 for earlier main-injection timings, no significant impact can be noticed for the different settings. However, when correlating this sensitivity with the standard deviation of the maximum peak pressure, $p_{max}|_{SDi}$ one can observe that for the early setting of the main injection the spread of the standard deviation of the individual cylinders increases for the early setting of the main-injection at $280degCA$ BTDC

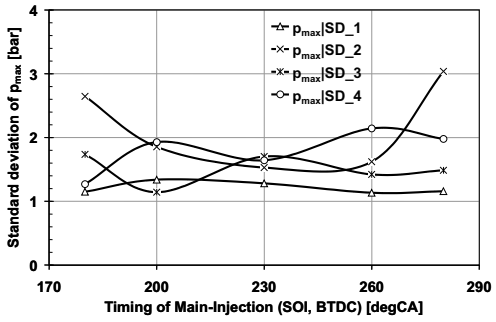

(a) Development of $p_{max}|_{SDi}$ versus main-injection setting

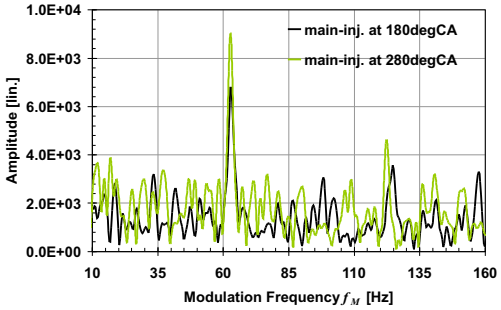

(b) Modulation spectra for the early- and the late main-injection setting

Figure 4.32: Impact of the standard deviation of p_{max} of the individual cylinders on the impulsiveness IMP_{SPL} for main-injection SOI at $180degCA$ and $280degCA$ BTDC at 2000rpm, 2bar BMEP

as shown in Figure 4.32(a). When looking at the individual modulation spectra as shown in Figure 4.32(b) the increase of the impulsiveness for the early setting can be referred to a higher magnitude of modulation of the main engine orders, thus the second and the fourth order at $66Hz$ and $132Hz$ respectively. Hence, caused by the higher spread of peak-pressure fluctuation, the level of the particular engine order rises even if the averaged maximum peak pressure p_{max} of both settings differ only $0.3bar$.

4.2.5.3 Variation of the Timing of Pre-Injection

In contrast to the experiment presented in the previous chapter, in this experiment the main-injection was kept constant at $245degCA$ BTDC, while the pre-injection timing (SOI) has been varied from $430degCA$ to $360degCA$, with $360degCA$ denoting that the SOI of the pre-injection happens at TDC of the pre-compression. The split rate was set to 78%. During all tests the valve timing was kept constant. Furthermore the engine speed was 2000rpm, the load was 2bar BMEP. The predicted level of the radiated noise is depicted in Figure 4.33. The change of the pre-injection timing does not have an impact on the level on the radiated noise nor it influences the combustion characteristics. When investigating the noise regarding its impulsiveness as it is illustrated in Figure 4.35(b), it can be summarized that only for the setting of $SOI = 360degCA$ a slight increase of the impulsiveness can be observed. In accordance with the findings presented in the previous chapter the interaction of

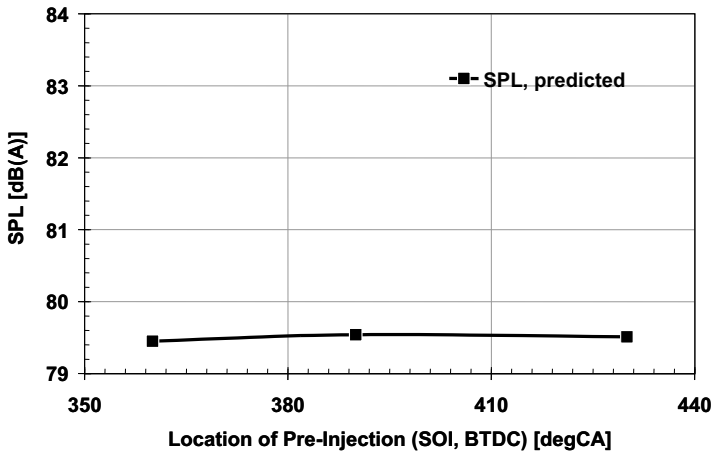

Figure 4.33: Radiated noise versus location of pre-injection at 2000rpm, 2bar BMEP

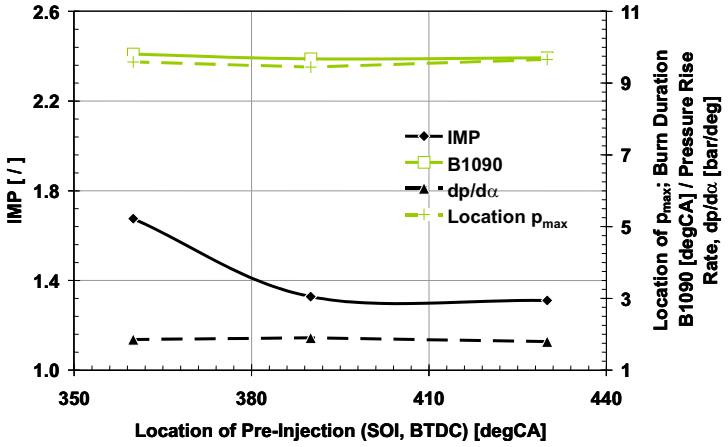

Figure 4.34: Noise-quality versus location of pre-injection at 2000rpm, 2bar BMEP

$p_{max}|_{SDi}$ and IMP was analysed similarly using statistical combustion data, represented by the standard deviation of the individual maximum peak pressures, as shown in Figure 4.35(a). The increase of the impulsiveness IMP can be rather referred to the higher variation of p_{max} of the individual cylinders at the particular setting, as here the difference of the average maximum peak pressure between both settings is just $0.2bar$. Thus, such characteristics can be again explained with the increased magnitude of the modulation frequency as shown in Figure 4.35(b), caused by the higher individual spread of the maximum cylinder pressures $p_{max}|_{SDi}$.

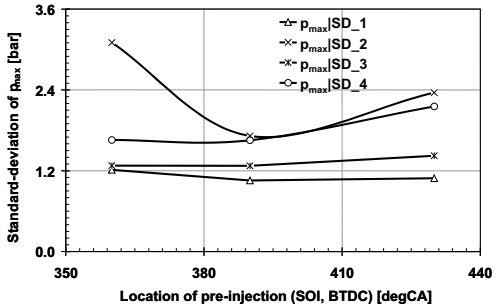

(a) Development of $p_{max}|_{SDi}$ versus pre-injection setting

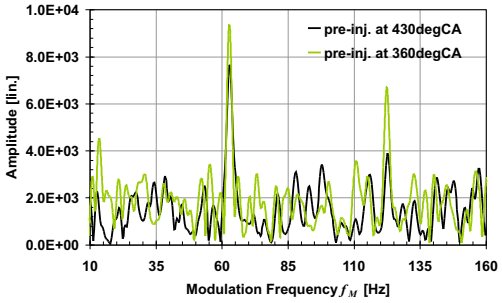

(b) Modulation spectra for the early- and the late pre-injection setting

Figure 4.35: Impact of the standard deviation of p_{max} of the individual cylinders on the impulsiveness IMP_{SPL} for pre-injection SOI at $360 degCA$ and $430 degCA$ BTDC at 2000rpm, 2bar BMEP

4.2.6 Fuel Quality

Operating an engine in SI-mode, there is always the task to prevent the engine from knocking at high load and also to ensure a stable and misfire free operation. In the SI-engine air and fuel are pre-mixed, ignited by the spark and then the heat release takes place in a turbulent flame front that propagates through the combustion chamber. To comply with the requirements of achieving an operation below the knock limit and fulfill the stability targets within certain limits of cyclic variation, during combustion system development mostly the ignition timing, valve timing, intake air flow and for gasoline direct injection engines the position of injector and spark plug are optimized in conjunction with the combustion chamber geometry itself. For instance the spark-timing, controlled by a knock sensor applied to the engine, can be used to control the combustion when burning fuels with different knock sensitivities, accordingly. In contrast, operating the engine in HCCI a compliance with similar requirements as in SI-mode needs to be achieved. But there is no spark timing available to control and phase the combustion as it is during SI-operation. However, even in HCCI knocking can occur when the pressure rise rate is unacceptably high and for example in an even worst scenario when the location of $CA50$ is just before combustion TDC. Thus the sensitivity of different fuel types should be investigated in terms of HCCI operation, as was carried out for instance in [154] where the impact of different research octane number RON and motored octane number MON has been investigated regarding combustion phasing ($CA50$). In any case, as already revealed in Chapters 4.2.4 and

4.2.5, the ignition delay influences the combustion noise, too. In addition it is known that the fuel sensitivity S ($S = RON - MON$) has an impact on the ignition delay of a fuel [9, 152, 154]. It has been also shown that in SI-operation above a load of approximately 80% a higher RON can lead to an increased level and roughness of the radiated noise [34]. Subsequently studies have been carried out to characterize the impact of three different fuel types on the noise and vibration characteristics, using specified fuel of RON numbers of 91, 95 and 98 at 1500rpm engine speed and a load of 2bar BMEP.

It is known that the RON affects the induction and autoignition time of a combustion [9]. Moreover one can assume for an end gas compression taking place in the time-span from $t = 0$ to $t = t_i$, at which autoignition occurs. According to Heywood the integral over the interval for the reciprocal value of τ, which denotes the induction time at the instantaneous temperature and pressure, is equal to one when autoignition occurs. Thus one can write generally:

$$\int_{t=0}^{t_i} \frac{1}{\tau} dt = 1. \tag{4.2.4}$$

However, a correlation, derived by Douaud and Eyzat, describes the induction time dependent on the octane number ON, [9]:

$$\tau = 17.68 \cdot \left(\frac{ON}{100}\right)^{3.402} \cdot p^{-1.7} \cdot \exp\left(\frac{3800}{T}\right). \tag{4.2.5}$$

The parameter ON denotes the octane number that can be derived from

$$ON = a(RON) + b(MON) + c. \tag{4.2.6}$$

Referring to Heywood it can be assumed that $a \approx b \approx 0.5$ with a good correlation to reality. However, a, b and c are normally derived from experiments [9]. If so called primary reference fuels (PRF), fulfilling the condition $RON = MON$, are used, the resulting ON is the same as the RON of the PRF [154]. However, in any case a high octane number ON leads to longer induction time τ at same pressure p and temperature T as can be derived from equation (4.2.4). But it is also known that the knock sensitivity of a fuel depends mostly on its amount of olefins, iso-paraffins and aromatics. The higher the amount of these ingredients, the higher is the knock resistance of a fuel [151][2]. However, the aforementioned theory is well

[2]Urlaub also states that by using molecules with more branches, as is the case for iso-octanes, the knock sensitivity could be increased, too.

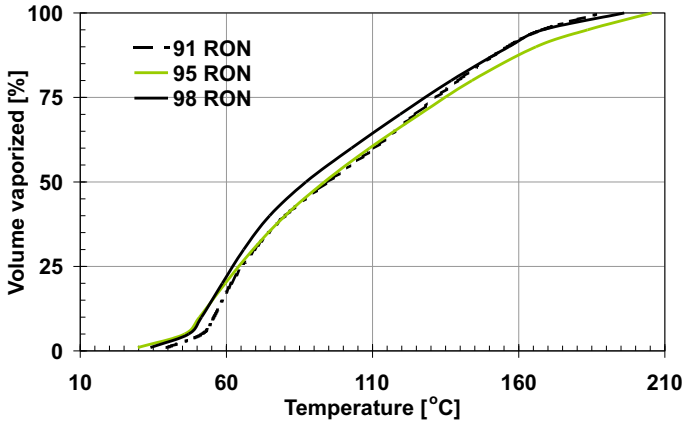

Figure 4.36: Volatility characteristics of the fuels used for the experiments.

correlated with SI combustion. Considering HCCI combustion, the volatility as a function of temperature could dominate the effect: a high volatility can then in turn lead to an early and short combustion, leading to an increased magnitude of the noise level and accompanied by a higher impulsiveness. The specification of the three fuels investigated are listed in Table 4.4. All three fuels have a similar

Table 4.4: Characteristic data of the fuels used for the tests.

	91RON	95RON	98RON
RON [-]	91.8	94.9	98.7
MON [-]	81.8	84.8	87.6
S [-]	10	10.1	11.1
Q_{LHV} $[MJ/kg]$	43.44	42.8	42.55

sensitivity S, but different lower heat values Q_{LHV}, thus to achieve the same heat release $\dot{Q}$ with the 98RON fuel as with 91RON, the fuel mass-flow $\dot{m}_F$ must be increased according to $\dot{Q} = \dot{m}_F \cdot Q_{LHV}$ of about 2%. Furthermore the individual volatility characteristics as measured by the fuel maker of the three fuels are shown in Figure 4.36. It can be concluded that the 98RON fuel used for the experiments has the highest volatility, whereby the 95RON fuel has a higher volatility at lower temperatures than 91RON, but then ascends with a lower slope than the 91RON fuel characteristics. The reference point for the experiments was the operation with base settings, consuming 95RON fuel. During the experiments with the other fuel

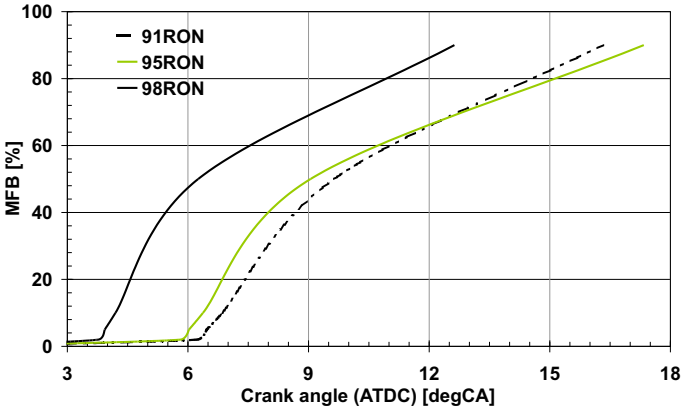

Figure 4.37: Mass-fraction-burned (MFB) of the fuels as characterized in Tab.4.4 and Figure 4.36 for the experiments at 1500rpm, 2bar BMEP.

types, the fuel mass flow was corrected via the injection time such that the same load was achieved as during the experiment with 95RON fuel. The start-of-injection (SOI) during all three experiments was kept constant at a split rate of 80% with SOI for the pre-injection at $381 degCA$, and main-injection occurring at $293 degCA$. The amount of fuel injected during pre-injection was kept constant by an injection duration of $0.195s$. The duration of the main-injection for 95RON was $0.98s$. The 91RON required a main-injection time of $0.964s$, and the 98RON operation was achieved with $0.992s$ main-injection time. It must be noted that the individual durations for the injection duration listed here were taken from calibrated values from the monitor of the engine controller, thus the opening time is represented by the solenoid current. The physical opening times of the injector are much shorter than shown here. However, all injection events were in the range of a linear fuel flow versus opening time. The experiments revealed that the 98RON has an early and fast heat release. In contrast, the mass-fraction-burned characteristics of the two other fuels are similar to the individual volatility characteristics, as is depicted in Figure 4.37. The resulting radiated noise level versus fuel-type is shown in Figure 4.38. Because of the earlier heat release the 98RON fuel operation results in slightly higher magnitude of the radiated noise level. However, analysing the impulsiveness, the dependency of the sound on the fuel type gets more significant, as shown in Figure 4.39(a). This is confirmed by the individual combustion data, too. For the fuel with the highest volatility the combustion lasts a shorter time ($B1090$), accompanied by an earlier location of the maximum peak pressure p_{max}, and a

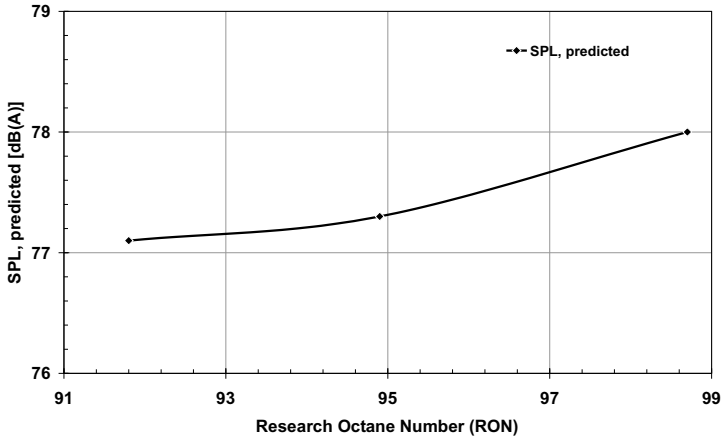

Figure 4.38: Radiated noise level versus the fuels as characterized in Tab.4.2.6 and Figure 4.36 at 1500rpm, 2bar BMEP.

higher pressure rise rate $dp/d\alpha$. According to Figure 4.39(b) it can be concluded that the impact of the fuels used here on the roughness is not significant at this point of operation.

In summary, during HCCI operation the volatility of a fuel has obviously a higher impact on the heat-release rate and thus the acoustics than its octane number or further ingredients increasing the induction time and hence the knock resistance. These factors do not become important for the acoustics until high load operation. However, further investigations are necessary to reveal the interaction of volatility and ignitability of fuel in HCCI.

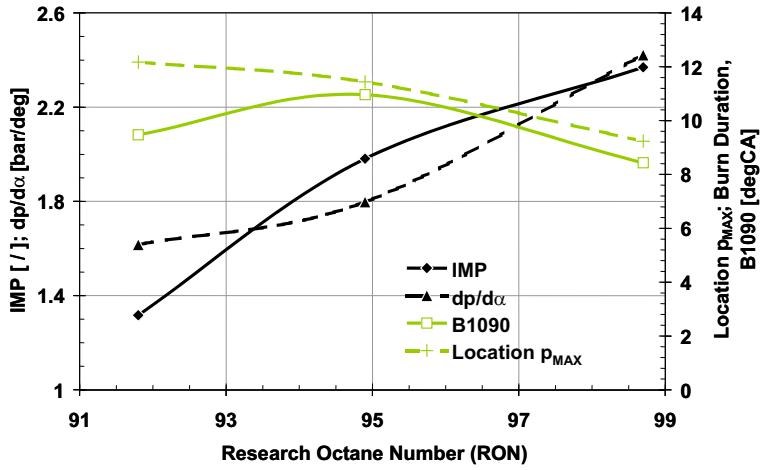

(a) Impulsiveness and its interaction with combustion data for the different fuels

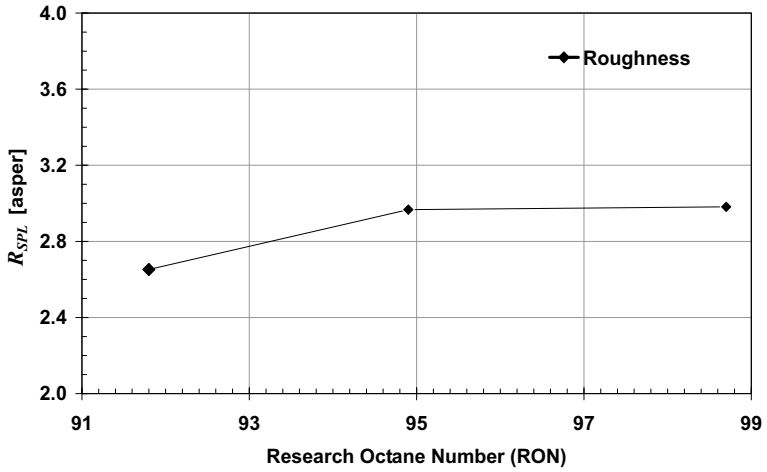

(b) Roughness versus fuel type

Figure 4.39: Impact of the fuel type on the sound-quality at 1500rpm, 2bar BMEP

Chapter 5

Combustion Mode-Change Acoustics

Applying steady state combustion control settings for both modes, the first few HCCI-cycles show unacceptable levels of cylinder peak-pressures and pressure rise-rates when switching from SI to HCCI-mode. In some cases this also corresponds to a sudden decrease or increase of the indicated-mean-effective-pressure (IMEP), causing fluctuations of torque. In addition, because of the higher peak pressures of the HCCI combustion, the level of vibrations increases, too. Moreover, due to the different modes of combustion, the noise characteristic can change. However, the noise characteristic of steady state HCCI operation and its sensitivity to control parameters was the subject of the previous chapter.

The following Figure 5.1 shows the cylinder pressure time history of a simple mode switch from SI to HCCI. The first row shows the measured cylinder pressures, the second row the first derivation of the cylinder pressures, and the third row the second derivation of the cylinder pressure. The analysis reveals higher pressure gradients and a higher contribution of the high frequency excitation of the engine structure. Moreover an increase of the signals can be noticed for the first few HCCI cycles immediately after SI-operation at around $t = 0.38s$. This can be referred to an excessively advanced HCCI combustion because of the hotter residual gases from the last SI combustion cycles. This effect results in a impulsive radiated noise event during the mode switch. Beside other important issues, as for example the engine out emissions, in summary the following tasks to achieve a smooth combustion mode switch can be formulated:

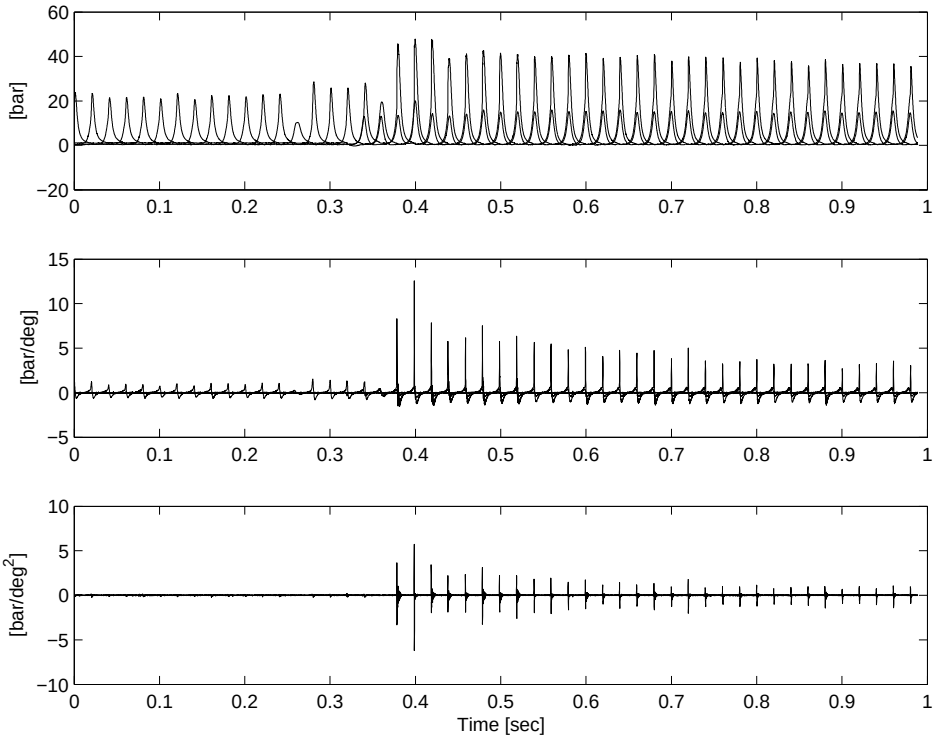

Figure 5.1: Cylinder pressure analysis (all four cylinders superimposed) of a mode switch from SI to HCCI at 1500rpm, 2.62bar BMEP. The mode switch command was initiated at $t = 0.34s$ (please note the first pre-compression, caused by the NVO valve-timing strategy).

- Achieve a constant and smooth engine noise characteristics by means of appropriate control of the HCCI combustion excitation. This is important because the HCCI-effected noise shall not differ significantly from SI-operation as HCCI operates in the low- and part-load operation range.
- Maintaining the fluctuations of torque during mode switch to prevent disturbing vibrations in the low frequency range of $1Hz$ to $32Hz$.
- When switching from SI to HCCI the early combustion characteristics of the first HCCI-cycles should be avoided using appropriate control settings.
- Because of the un-throttled operation in HCCI, combined with the negative valve overlap, during the mode switch pressure pulses in the inlet system can occur, leading to an impulsive noise at the mode switch.

The following sub-sections will give an overview from the perspective of acoustics on

a current state of SI-HCCI combustion mode changes. In addition, the effect of the throttle trigger and of different split rates of the injection on the acoustics is shown and quantified.

5.1 Intake System Acoustics during Mode Change

When opening the throttle quickly during the transition from SI- into HCCI-operation, a pressure fluctuation occurs. This results in a low frequency noise pulse that can be directly associated with the main firing order of the engine. This noise has been referred to a pressure fluctuation initiated by a wave which is reflected at the closed intake valve, propagating through the un-throttled intake runner and, due to the NVO-strategy to effect the first HCCI cycle, causing a short noise-pulse. However, to reduce the intensity of this pulse, the lift of the intake valve is switched to the lower cam-lift profile during the last SI combustion immediately before the mode transition to HCCI. This, in turn, will reduce the magnitude of the pressure fluctuation in the intake manifold, leading to a lower level of excitation. The comparative depiction of the absolute intake manifold pressure, measured closely before the throttle, is shown in Figure 5.2(a). Moreover, to assess the resulting effect of this strategy in detail, Figure 5.2(b)-(1) and 5.2(b)-(2) depict the frequency versus time characteristics for the base- and the low-lift-SI approach, both derived from processing the pressure pulsations that were measured 100mm before the throttle in the intake system. The mode switch from SI- into HCCI operation takes place around $t = 0.4s$ for both settings. It can be followed from Figure 5.2(a) that the pressure pulse is reduced by the low-lift-SI approach. Furthermore, this strategy also reduces the amplitudes of the airborne noise, associated with the even and odd engine firing orders during the combustion mode switch, as depicted in Figure 5.2(b)-(2), and detectable for example by the reduced excitation of the $66Hz$, $132Hz$ and $198Hz$ frequency band for the chosen engine speed of 2000rpm during this experiment. These frequencies can be obtained using equation (4.1.1), too.

5.2 Vibration Issues during Mode Change

Based on equations (3.1.28) and (3.4.21) the vibration excitation of the powertrain can be calculated. Hence the level of acceleration depends on the cylinder peak pressure, the moving masses involved, the inertia, and the crank train geometry,

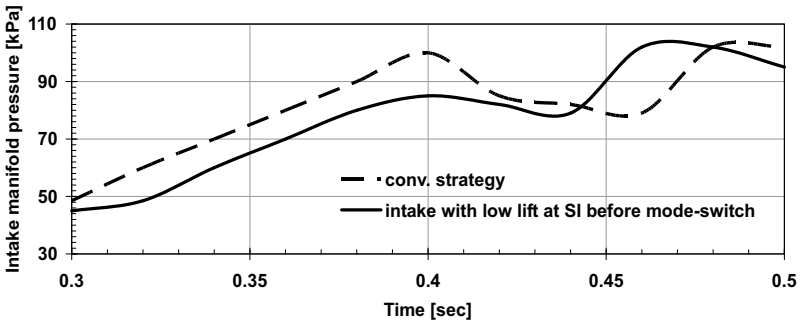

(a) Intake manifold pressure during mode switch for base setting (dotted line) and with low-lift operation during SI immediately before the mode switch to HCCI (solid line).

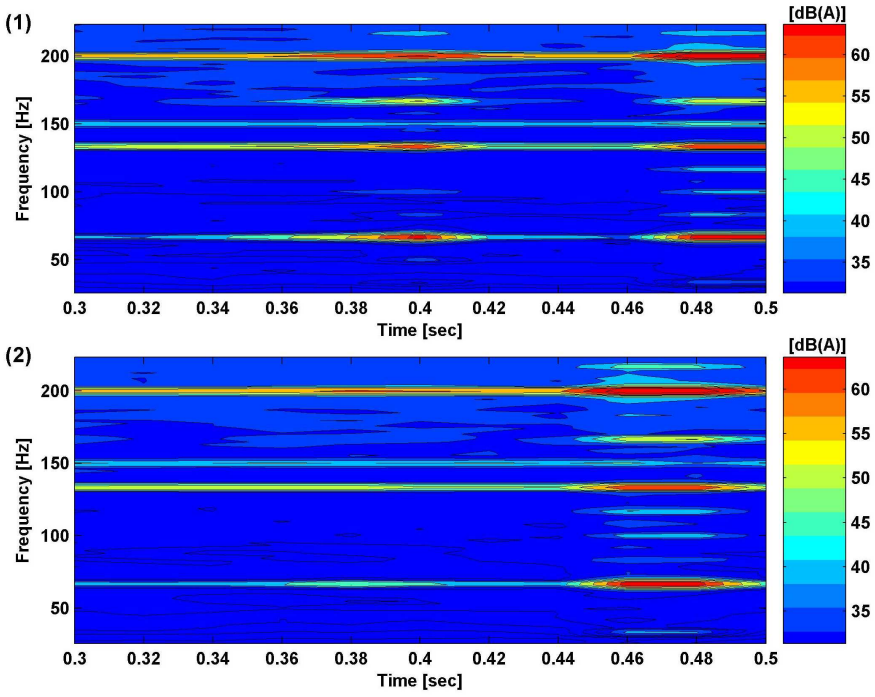

(b) Frequency versus time analysis of the intake manifold pressure fluctuation. Base setting in sub-figure (1), low-lift cam in SI immediately before mode switch in sub-figure (2).

Figure 5.2: Impact of low-lift cam operation in SI immediately before mode transition into HCCI at 2000rpm, 2bar BMEP. The mode switch into HCCI-operation takes place at $t = 0.4s$.

thus

$$a_{\ddot{\theta},RSS} \propto (p_{max}, IMEP, m_{OP}, I_i, \lambda) \tag{5.2.1}$$

However, considering just the variables affected by the combustion characteristics, relation (5.2.1) can be reduced:

$$a_{\ddot{\theta},RSS} \propto (p_{max}, IMEP) \tag{5.2.2}$$

The relationship (5.2.2) formulates the requirements of a combustion mode switch controller in terms of vibrations and jerks. If the peak pressures and the IMEP of both states of combustion are similar, the vibrations will be similar, too. As a consequence no jerk will occur. When considering cyclic variations of the combustion during one combustion mode, vibrations and jerks can evoked. This induces the request for individual cylinder control, thus promoting the use of gasoline direct injection. Investigations on the robustness and repeatability of combustion mode switches will be presented in the following sub-section. Moreover, the second sub-section presents factors which can be of use for controlling the mode switch in terms of vibration. The quality of the particular mode switches was assessed using the JLS-index as derived in chapter three. The value JLS_{MAX}, characterizing the peak level of the event, is primarily chosen to differentiate between 'good' and 'bad' switches. Secondly, if the individual JLS_{MAX} to be compared are on a similar level, the time of exposition, characterized by JLS_{INT} is additionally taken into account. It is worthwhile to mention that the use of certain settings of the control strategy has not delivered robust results as will be presented in the following sections. Moreover, the strategy used for the experiments is not developed completely yet. However, first statements on trends can be followed based on this (preliminary) outcome.

In general the mode switch used during the experiments is controlled in three phases. After a mode switch demand is recognized by the controller, the mode switch is initiated by setting a start signal triggered by the combustion of one cylinder. Firstly the SI combustion of each individual cylinder is made leaner by an according combination of throttle, fuel and spark timing, leading to $\lambda \approx 1.4$ to achieve lower temperatures in the combustion chamber. This is called *Phase 1.* During the second step the throttle is opened until ambient pressure conditions are achieved in the inlet system. Simultaneously the exhaust, and then the intake valve is switched to the lower lift and NVO-timing. This will effect the first HCCI cycles on each cylinder. This is called *Phase 2.* During the third phase (*Phase 3*) steady state settings for the HCCI will control the combustion accordingly.

5.2.1 Repeatability and Spread

Because of the higher temperature during operating in SI, there is a risk that the first cycles of HCCI operation can suffer from hot residuals, leading to early combustion. Moreover, misfire can also be observed, if for instance the amount or the composition of the residuals resulting from SI are not promoting HCCI. These effects can lead to a variability of the combustion mode switch and affect p_{max} and IMEP of individual cycles, leading to vibration and jerk issues during mode switch. Subsequently the variability of 14 consecutive mode switches from SI to HCCI operation at 1500rpm, 2.62bar BMEP has been investigated. This was done using split injection of a split rate of 78%, a main injection occurring at $260 degCA$ BTDC and pre-injection happening at $395 degCA$ BTDC. Firstly, both JLS_{MAX} and JLS_{INT} were calculated according to equations (3.4.11) and (3.4.13) for each individual run. The resulting individual bar charts for both are depicted in Figure 5.3(a) and Figure 5.3(b) respectively. Potential originators for a spread of the mode switch in terms

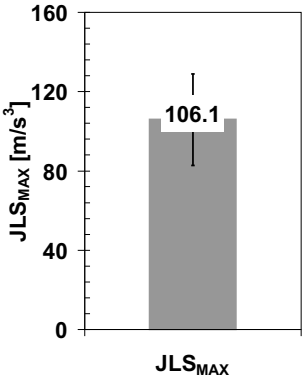

(a) Average and spread band (minimum and maximum value) of JLS_{MAX} for 14 consecutive mode switches from SI to HCCI

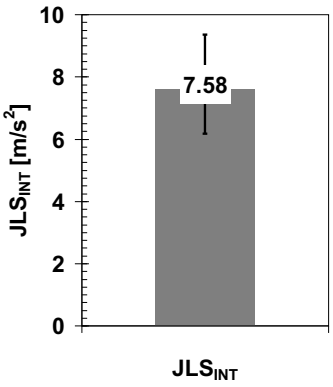

(b) Average and spread band (minimum and maximum value) of JLS_{INT} for 14 consecutive mode switches from SI to HCCI

Figure 5.3: Spread of JLS_{MAX} and JLS_{INT}, evaluated from 14 consecutive mode switches from SI to HCCI at 1500rpm, 2.62bar BMEP

of torque fluctuations and therefore vibrations can for example be the variability of trigger-setting for the cam profile switch on exhaust and inlet cam, caused by synchronization issues due to different sample rates of the individual sensors and controllers. It could also be the velocity of the valve-timing actuation, that depends

on the oil pressure, the temperature and the amount of air that can be entrapped in the oil. Furthermore, the opening and closing speed of the throttle and the dynamic range of the injectors can influence the repeatability. Therefore these deficiencies should be identified in advance while carrying out a detailed system identification that incorporates these parameters to build up a robust controller.

Choosing JLS_{MAX} and JLS_{INT} as the criterion, the best and the worst mode switch have been selected from the 14 switches. The following Figure 5.4 depicts from above the cylinder pressure and its first and second derivation of all cylinders superimposed during a switch from SI to HCCI combustion. The mode switch for both traces occurs approximately at $t = 0.9sec$. Both cylinder pressure traces, depicting all four cylinders superimposed, show a similar shape during operation in SI. The cylinder pressure trace during HCCI, leading to the worst case, is depicted in Figure 5.4(a). It exhibits a slope of the rise of the consecutive peak pressures during the switch period of approximately $15bar/cycle$, whilst the peak pressure rises from $18.5bar$ up to $55bar$. In contrast, the best case, as shown in Figure 5.4(b), ramps into HCCI with a lower slope of the consecutive peak pressures of approximately $7bar/cycle$ which is equivalent to a duration of five consecutive cycles. In turn this results in a lower slope of the acceleration level for the best case, as it will be revealed later. But both cases still show the increase of peak pressure and pressure rise rate caused by the hot residuals from the last SI cycles as mentioned earlier. However, a detailed analysis of both states using the JLS according to Chapter 3.4.3 is depicted in Figure 5.5. In accordance with the cylinder pressure traces of both states the resulting level of acceleration behaves similarly. However, the lower slope of the rise of the acceleration level from SI to HCCI for the best case in contrast to the worst case can be seen when comparing both Figure 5.5(a)-(b) and Figure 5.5(b)-(b). Consequently the latter mode switch will show a lower jerk, thus a lower value of JLS_{MAX} of $89.23m/s^3$ compared to $128.13m/s^3$. Furthermore the integrated value JLS_{INT} of the best case mode switch is $6.77m/s^2$ compared to $9.36m/s^2$ for the worst case [1].

[1] To get an impression of the sensitivity and height of JLS_{MAX} and JLS_{INT}, experiments were carried out, evaluating the effect of a single cylinder misfire on JLS_{MAX} and JLS_{INT} at 1500rpm, 2.62bar BMEP during HCCI: a single misfire during steady state HCCI operation leads to $JLS_{MAX} = 411.8m/s^3$ and $JLS_{INT} = 20.4m/s^2$. Such an event will lead to values four times higher than during a conventional mode switch from SI to HCCI. This would be clearly recognized by an average customer in the vehicle later on.

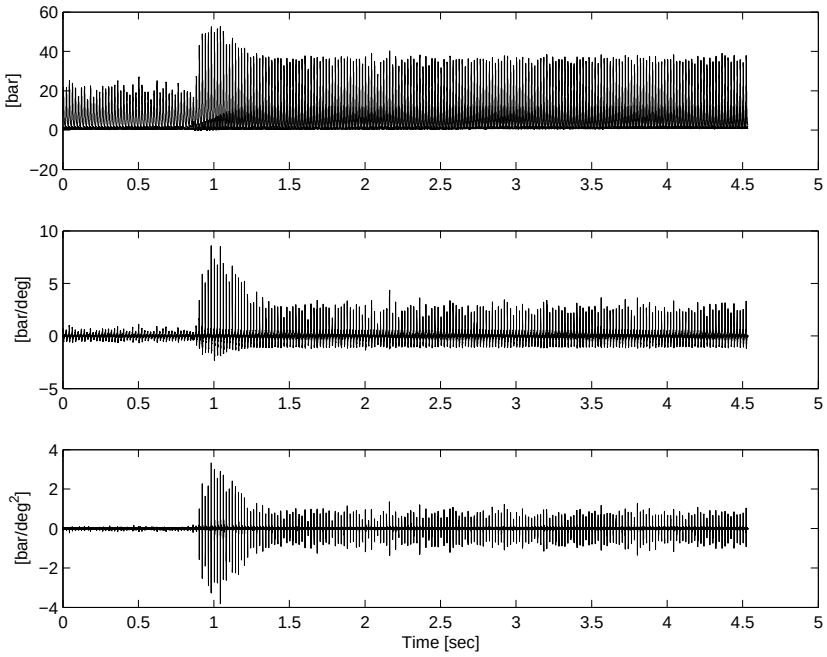

(a) Cylinder pressure characteristics for the worst mode switch SI to HCCI

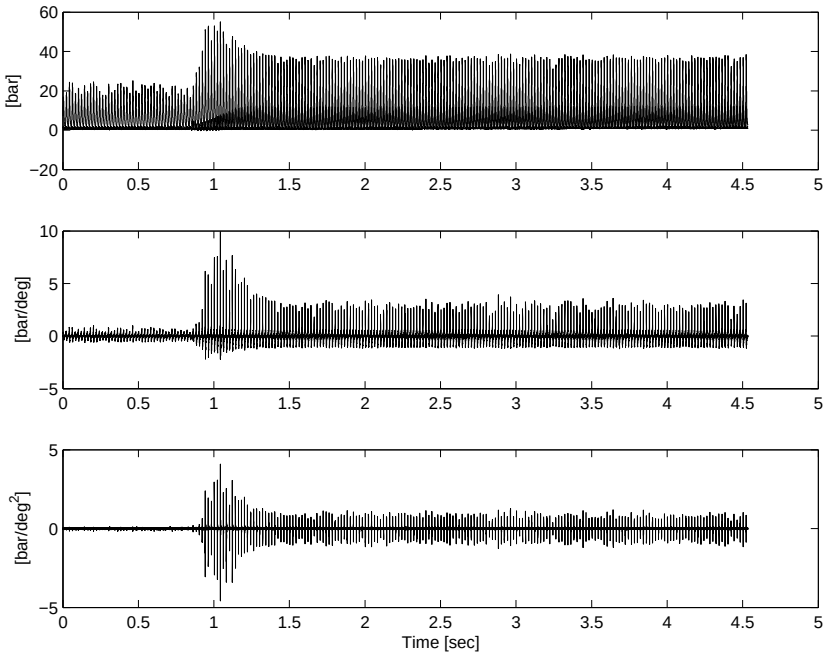

(b) Cylinder pressure characteristics for the best mode switch SI to HCCI

Figure 5.4: Cylinder pressure characteristics of all cylinders superimposed for the worst and the best mode switch from SI to HCCI at 1500rpm, 2.62bar BMEP

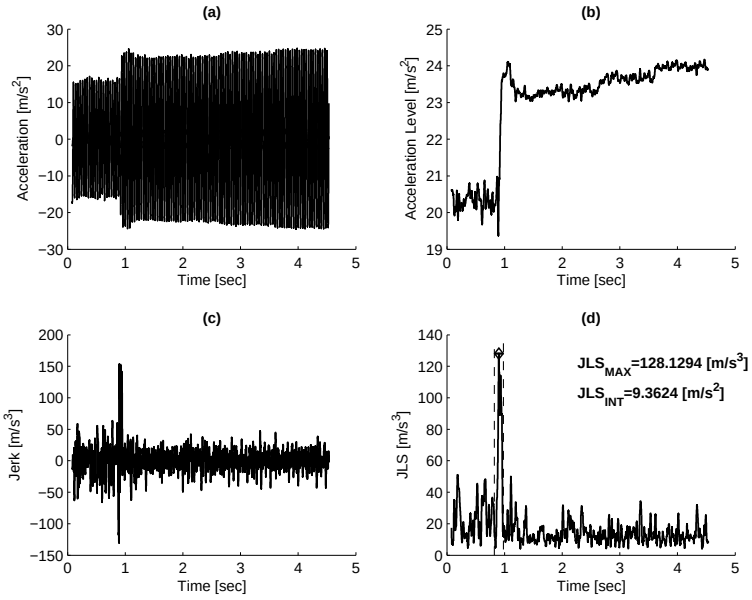

(a) Mode switch analysis SI to HCCI - worst case

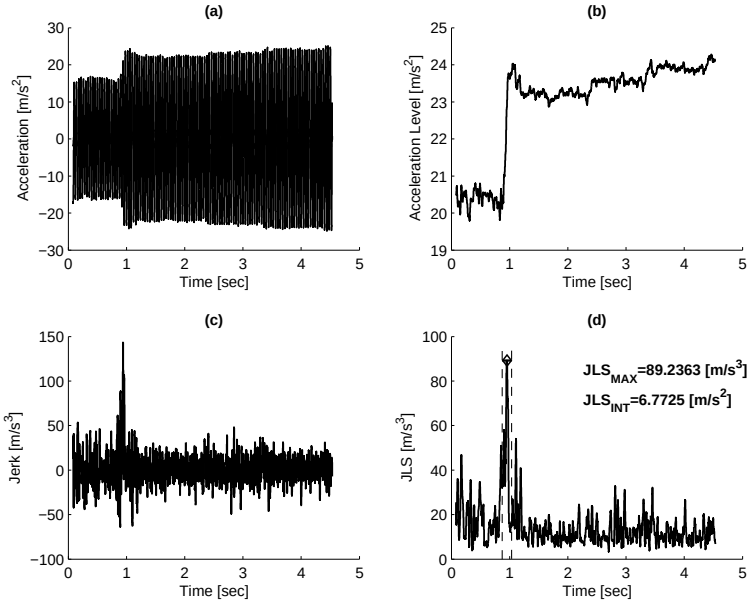

(b) Mode switch analysis SI to HCCI - best case

Figure 5.5: Mode switch analysis of the worst and the best mode switch from SI to HCCI at 1500rpm, 2.62bar BMEP. Please note the different scaling of the ordinate for the jerk and the JLS graphs.

5.2.2 Influence of the Throttle Trigger

To initiate lean SI and later on HCCI combustion the throttle is opened. However, the point in time for opening the throttle can be initiated at a desired point in time, triggered e.g. by a previous combustion event. Experiments were carried out at 1500rpm, 2.62bar BMEP using two different throttle trigger during *Phase 1* of the mode switch. During the first experiment the opening trigger was set at $305 degCA$ (early) after ignition-TDC of cylinder one, and during the second experiment the trigger was set at $585 degCA$ (late) after ignition-TDC of cylinder one. All other settings were kept constant. The experiments with both settings were repeated ten times to elaborate the individual spread of the chosen settings. Both JLS_{MAX} and JLS_{INT} were calculated according to equations (3.4.11) and (3.4.13) for each individual run. The resulting average values and the according spread of JLS_{MAX} and JLS_{INT} is comparatively depicted in Figure 5.6(a) and Figure 5.6(b). The

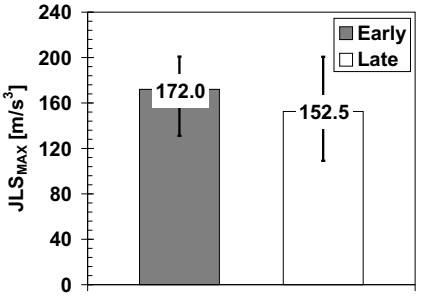

(a) Comparative analysis of the average and spread band of JLS_{MAX} for 10 consecutive mode switches from SI to HCCI

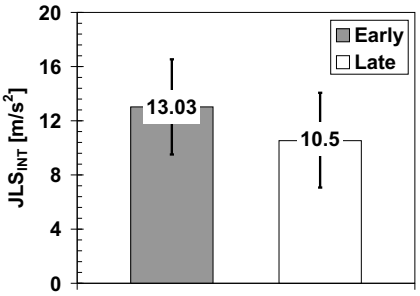

(b) Comparative analysis of the average and spread band of JLS_{INT} for 10 consecutive mode switches from SI to HCCI

Figure 5.6: Spread of JLS_{MAX} and JLS_{INT}, evaluated from 10 consecutive mode switches from SI to HCCI at 1500rpm, 2.62bar BMEP, using an early and late throttle trigger during *Phase 1* of the combustion mode switch.

late setting leads to lower values of JLS_{MAX} and JLS_{INT}. However, the spread of JLS_{MAX} increases when the the later setting is used. The cylinder pressure traces for the lowest (best) and highest (worst) JLS_{MAX} corresponding to the early setting are shown in Figure 5.7. Figure 5.8 depicts the cylinder pressure characteristics for the lowest and highest JLS_{MAX} for the late setting. Figure 5.7 shows for the best and the worst case two excessive peak pressures around $t \approx 0.25 sec$, just before the mode switch takes place. This can be referred to lean combustion cycles because of early throttle opening, but without an adapted amount of fuel. In contrast, this

effect is less pronounced for both cases with the late throttle trigger as it can be seen in Figure 5.8.

When looking at the slope of the peak pressure rise during mode switch, the early opening shows for the lowest and the highest JLS_{MAX} a similar slope. This means that for the early opening strategy the mode switch needs a similar number of cycles for both the lowest and highest JLS_{MAX}. Comparing this to the late trigger-setting, the picture is different. The worst case is characterized by a rise of the consecutive cylinder peak pressures of approximately $0.2sec$ compared to approximately $0.4sec$ for the best as it can be seen in Figure 5.8(a) and Figure 5.8(b); both switches start and end at similar peak pressures. Furthermore, it can be observed that the peak pressures of the HCCI cycles immediately after the switch are lower than for the best and the worst run when using the early trigger setting.

However, whilst the early setting delivers a constant mode switch duration, but higher JLS_{MAX} values, the late setting delivers a better averaged mode switch in terms of JSL_{MAX}, but has a higher spread in terms of mode switch duration, hence JLS_{INT}. Therefore Figure 5.9 depicts the comparative analysis of the best and worst mode switch in terms of the JLS_{INT} value of the case with the late-opening trigger. Based on Figure 5.9 it can be concluded that the higher value of JLS_{INT} is evoked by a shorter duration of the mode transition as already shown in Figure 5.8. Moreover, it is also caused by the higher peak pressures of the first few HCCI cycles. Therefore the worst case is characterized by a level of acceleration which is as twice as much (Figure 5.9(a)-(b)) as the best case immediately after the switch. In turn, this leads to a $50m/s^3$ higher peak of the jerk (Figure 5.9(a)-(c)), followed by a higher value of JLS_{INT} for this run.

Based on Figure 5.9 it can be concluded that the accelerations caused by lean operation during *Phase 1* are not dominating the mode switch quality in terms of vibrations. Note also the drift of the accelerations as shown for example in Figure 5.9(a)-(b). This is caused by the decreasing temperature of the combustion chamber during HCCI, leading to a later combustion (CA50 at $\approx 9.0degCA$ around $t = 4sec$ instead of $\approx 2.0degCA$ at $t = 1sec$), in turn leading to an higher level of IMEP that evokes an higher level of vibration. The (three) stages are caused by the torque controller of the dynamometer.

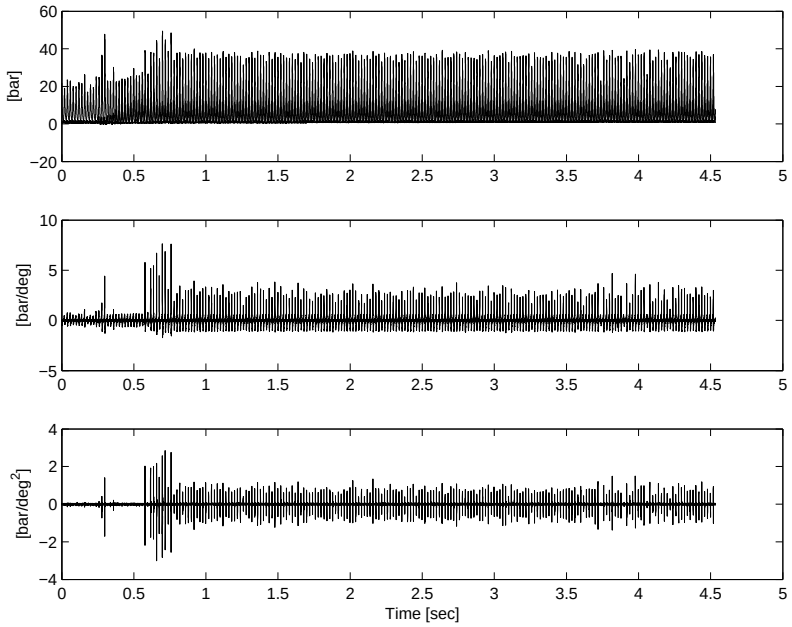

(a) Early trigger; cylinder pressure characteristics for the worst mode switch SI to HCCI.

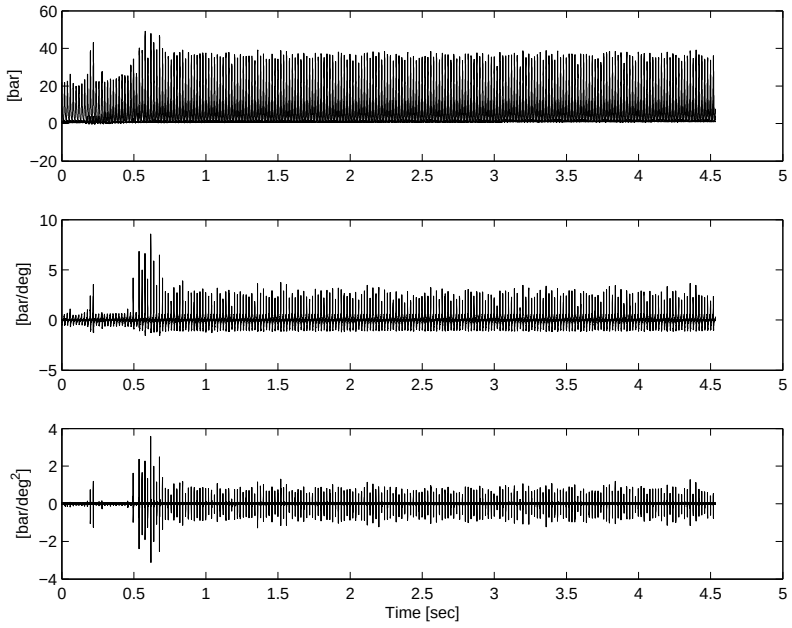

(b) Early trigger; cylinder pressure characteristics for the best mode switch SI to HCCI.

Figure 5.7: Early throttle trigger during *Phase 1* of the mode switch - cylinder pressure characteristics of all cylinders superimposed for the worst and the best mode switch from SI to HCCI at 1500rpm, 2.62bar. BMEP

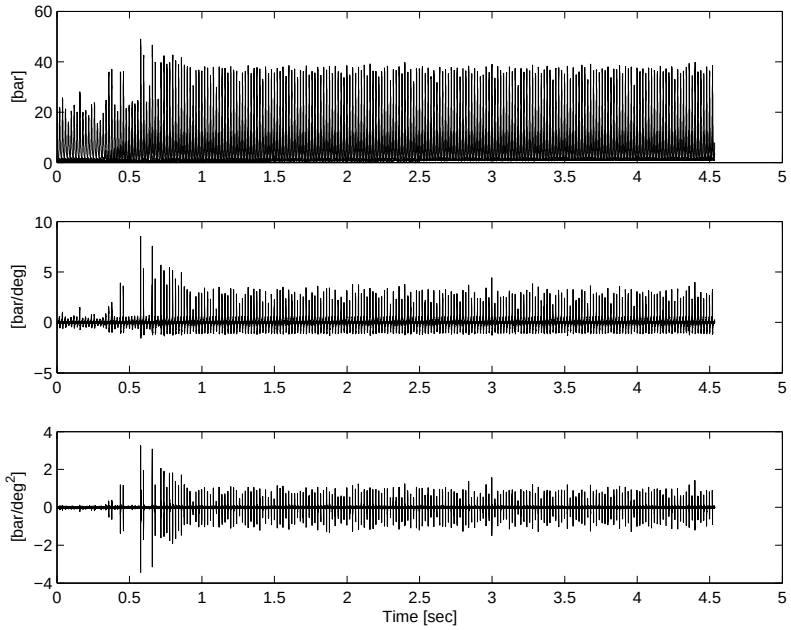

(a) Late trigger; cylinder pressure characteristics for the worst mode switch SI to HCCI

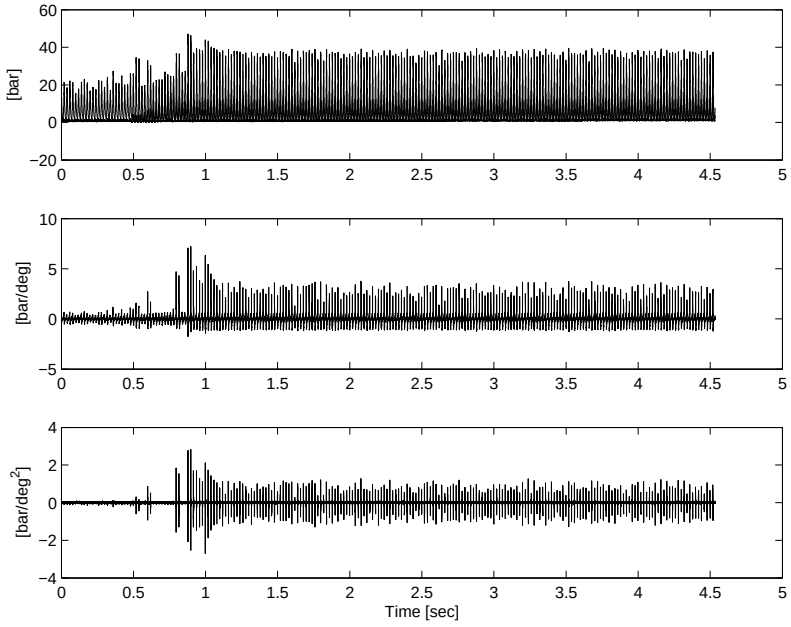

(b) Late trigger; cylinder pressure characteristics for the best mode switch SI to HCCI

Figure 5.8: Late throttle trigger during *Phase 1* of the mode switch - cylinder pressure characteristics of all cylinders superimposed for the worst and the best mode switch from SI to HCCI at 1500rpm, 2.62bar. BMEP

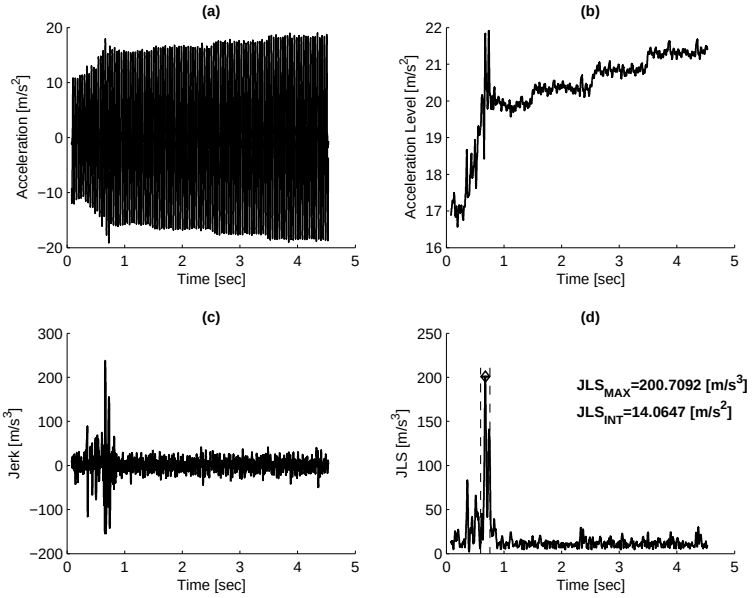

(a) Late trigger; vibration analysis of the worst ($JLS_{INT} = 14.06m/s^2$) mode switch SI to HCCI

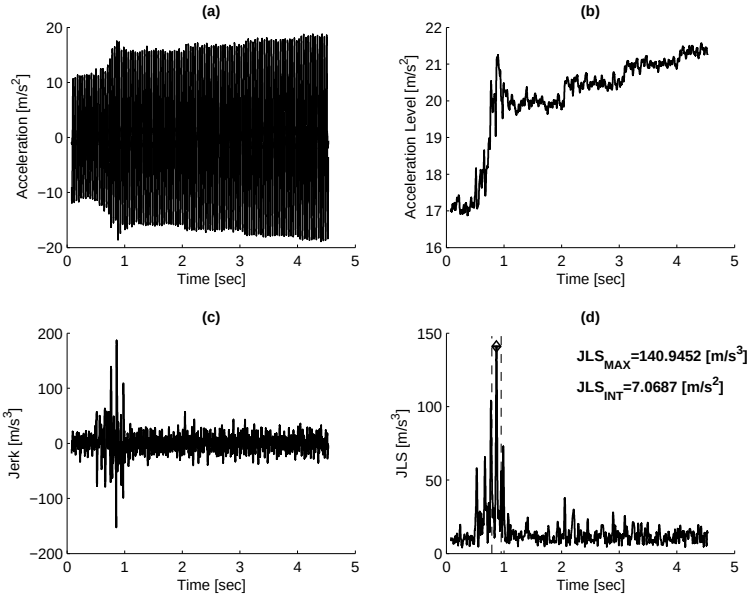

(b) Late trigger; vibration analysis of the best ($JLS_{INT} = 7.07m/s^2$) mode switch SI to HCCI

Figure 5.9: Late throttle trigger during *Phase 1* of the mode switch - vibration analysis of all cylinders superimposed for the worst and the best (JLS_{INT}) mode switch from SI to HCCI at 1500rpm, 2.62bar. BMEP

5.2.3 Injection Settings - Variation of the Split-factor

Using a low split rate for *Phase 2* of the mode switch, thus increasing the amount of fuel injected at the pre-compression, promises to cool by vaporization of the fuel the hot residuals of the previous SI-cycles. This is expected to result in lower peak pressures occurring during the first HCCI cycles in *Phase 2* because of a slower combustion effected by the lower temperature of the residuals. Two different experiments were carried out while doing a combustion mode switch from SI to HCCI at 1500rpm, 2.62bar BMEP. During the first experiment the split-factor of the fuel injection was set to 74% on the main injection during *Phase 2* of the mode switch, i.e. the first HCCI-cycles. During the second experiment the amount of fuel for the pre-injection was reduced, leading to a split factor of 82% during *Phase 2*. Both settings were elaborated in advance in steady-state setting, whereby a split rate of 74% was considered as the lower border in terms of combustion stability and knock. The split rate of 82% is defined by the injector's dynamic range as described in Chapter 4, when a split injection is still feasible with the solenoid injector type chosen for the experiments. The total amount of fuel was the same for both split rates. Each experiment was repeated 10 times. All other settings were kept constant.

The resulting average values and the according spread of JLS_{MAX} and JLS_{INT} is comparatively depicted in Figure 5.10(a) and Figure 5.10(b). Setting the split

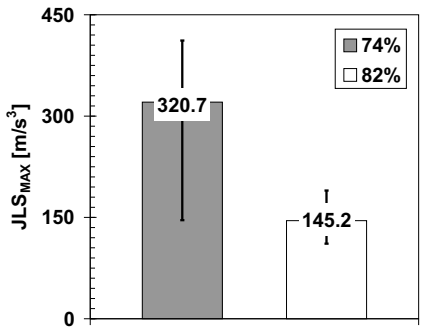

(a) Comparative analysis of the average and spread band of JLS_{MAX} for 10 consecutive mode switches from SI to HCCI

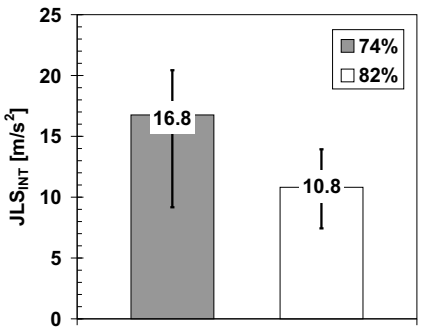

(b) Comparative analysis of the average and spread band of JLS_{INT} for 10 consecutive mode switches from SI to HCCI

Figure 5.10: Spread of JLS_{MAX} and JLS_{INT}, evaluated from 10 consecutive mode switches from SI to HCCI at 1500rpm, 2.62bar BMEP, using different split rates (74% and 82%) during *Phase 2* of the combustion mode switch.

rate to 74%, the average and the total spread of JLS_{MAX} and JLS_{INT} increases

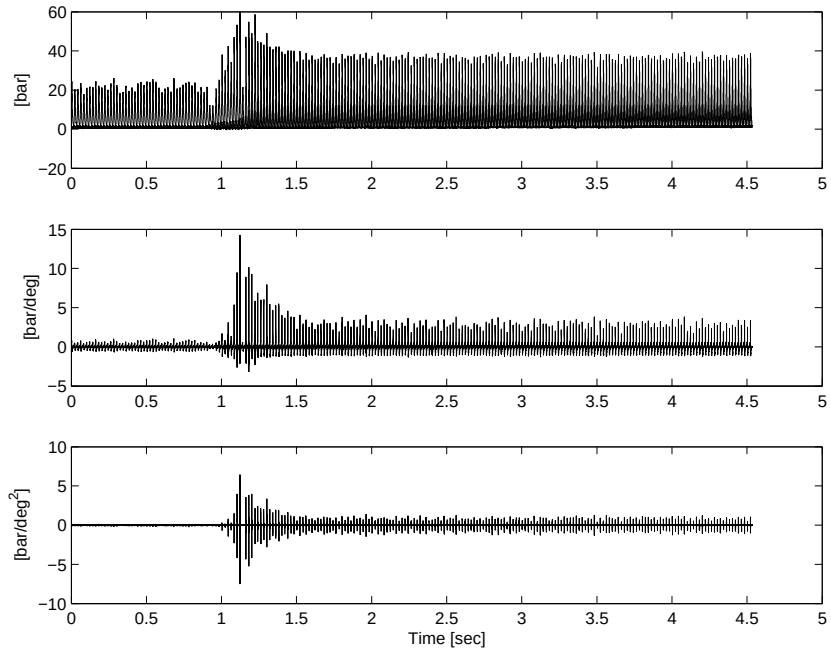

Figure 5.11: Split rate of 74% during *Phase 2* of the mode switch - cylinder pressure characteristics of all cylinders superimposed for the worst mode switch from SI to HCCI at 1500rpm, 2.62bar.

enormously compared to a split rate of 82%. While the average JLS_{MAX} is as twice as much than for example using an early throttle trigger as depicted earlier in Figure 5.6(a), the average value of JLS_{INT} does not show such an exaggerated level, although a high spread is visible. The reason for this can be obtained from Figure 5.11 that shows the cylinder pressure characteristics of the worst mode switch achieved with the split rate of 74%. The cylinder pressure characteristic exhibits a single misfire, occurring during *Phase 2* before switching to steady state settings. In addition, the cylinder pressure characteristics during *Phase 2* show high peak pressures, accompanied by high pressure rise rates. These characteristics were revealed for all switches, contributing to the upper half of the spread-band. The according analysis of JLS_{MAX} is shown in Figure 5.12 for the best and worst mode switch. The misfire immediately after mode switch leads to the high value of $JLS_{MAX} = 411.8 m/s^3$ for the worst mode switch. However, both switches show a sudden drop of the accelerations immediately before switching to HCCI at $t \approx 1 sec$. This is caused by a drop the IMEP, thus the generated torque. Taking the effect of the misfire out of consideration, the peak of the JLS-curve in Figure 5.12(b)-(d) effected by mode

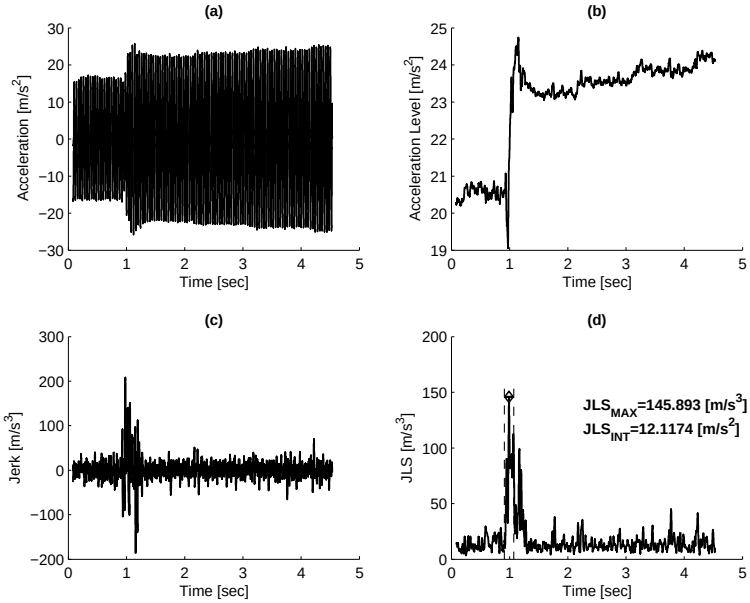

(a) Split rate of 74% during *Phase 2* - vibration analysis of the best ($JLS_{MAX} = 145.9m/s^3$) mode switch SI to HCCI

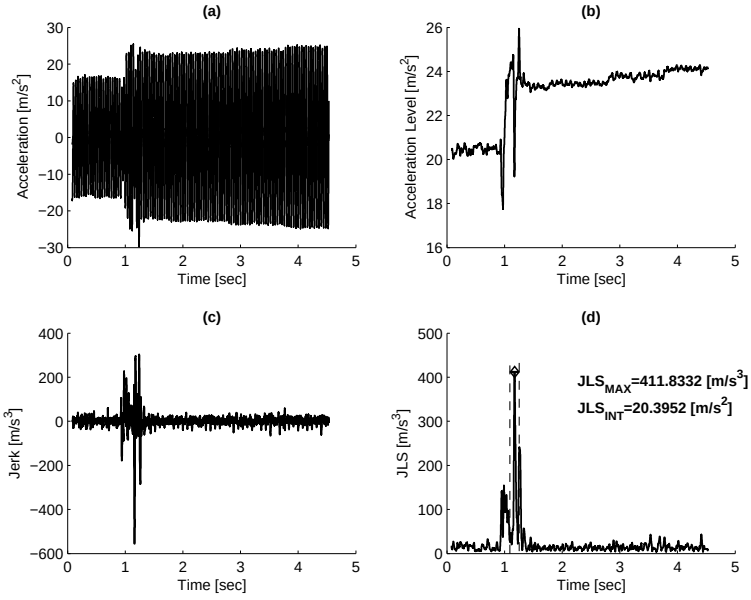

(b) Split rate of 74% during *Phase 2* - vibration analysis of the worst ($JLS_{MAX} = 411.8m/s^3$) mode switch SI to HCCI

Figure 5.12: Split rate of 74% during *Phase 2* of the mode switch - vibration analysis of all cylinders superimposed for the best and worst (JLS_{MAX}) mode switch from SI to HCCI at 1500rpm, 2.62bar. BMEP

switch itself shows a similar height of approximately $150 m/s^3$ as the corresponding peak shown in Figure 5.12(a).

The vibration analysis of the best and the worst switch, using a split rate of 82%, is depicted in Figure 5.13. The best run shows a less pronounced drop in the acceleration immediately before the switch. Although the overshoot of the acceleration just after the switch is similar to the worst run, this leads to a lower value of JLS_{MAX} of $111.08 m/s^3$. In contrast, JLS_{MAX} of the run rated worst is caused by the larger absolute difference of the acceleration from the drop-in before the switch until the first HCCI combustion, showing a high peak pressure.

In summary, a split rate of 82% is obviously even more beneficial to achieve low JLS_{MAX} values. However, it does not cure the mode switch from the cycles with excessive advanced combustion. Potential causes for the variability of this setting can be tolerances of the cylinder individual solenoid injectors, fuel pressure fluctuations and synchronization effects between controller and sensors.

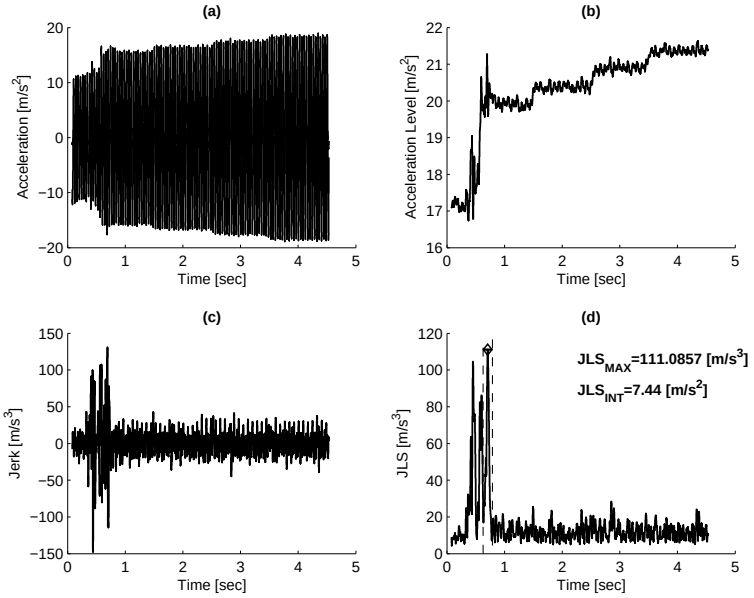

(a) Split rate of 82% during *Phase 2* - vibration analysis of the best ($JLS_{MAX} = 111.1m/s^3$) mode switch SI to HCCI

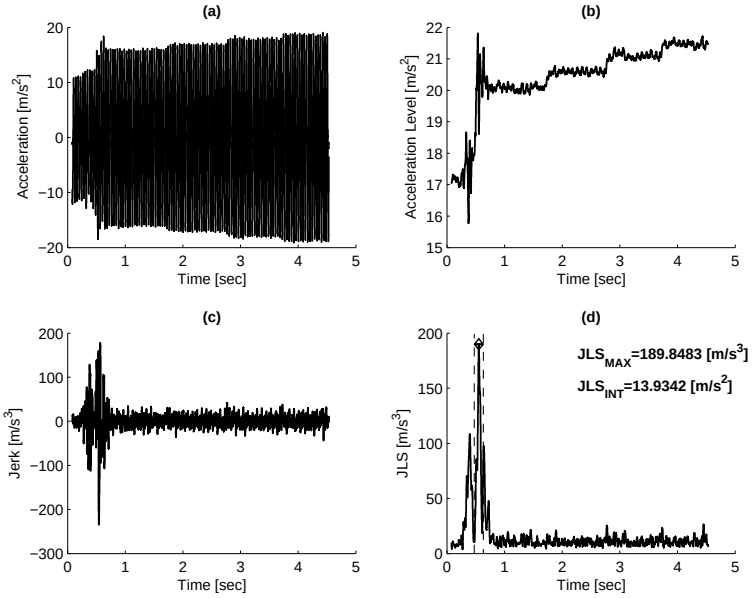

(b) Split rate of 82% during *Phase 2* - vibration analysis of the worst ($JLS_{MAX} = 189.8m/s^3$) mode switch SI to HCCI

Figure 5.13: Split rate of 82% during *Phase 2* of mode switch - vibration analysis of all cylinders superimposed for the best and worst (JLS_{MAX}) mode switch from SI to HCCI at 1500rpm, 2.62bar. BMEP

Chapter 6

Conclusion and Outlook

6.1 Conclusion

The results of the research presented in this thesis are two innovative methodologies to analyse and predict noise and vibrations emitted from dual-combustion-mode internal combustion engines, operated in non semi-anechoic conditions. Both allow to obtain early statements on engine acoustics even during the pre-development phase of the combustion system and controller. They contribute to reduction of development-time of new internal combustion engines, and also support reduction of development costs. The methods were used to investigate the impact of gasoline HCCI operation on engine acoustics. Firstly, a conclusion of the development and usage of the radiated-noise prediction method is given. Secondly, a conclusion of the results obtained using the method to evaluate combustion mode-switches is given.

The radiated-noise prediction methodology showed an error of less than 10% with measurements. Therefore it was used to analyse and quantify the impact of steady state gasoline HCCI operation on the radiated noise and its characteristics. Moreover, because of the advantageous usage of already correlated methods for the psychoacoustic indices, the correlation with the according combustion characteristics is possible now. In detail, furthermore, the development of the methodology generated the following expertise:

- A piston slap model was refined to achieve a better correlation with measured results. This was done by the introduction of a more realistic elliptical contact pattern model between piston and liner.

- The modal analysis of the piston-pin-connecting rod revealed different eigen-frequencies than its assembly. A forced response study using cylinder pressures of similar peak pressures but different pressure rise rates showed correlation with the frequencies visible on the engine structure when a certain pressure rise rate was exceeded. The improvement of the piston-pin-connecting rod according to these findings can lead to less clattering noise characteristics of compression-ignition engines.

When accompanying the combustion system and controls development of gasoline HCCI using the radiated-noise prediction method, the following findings were obtained:

- The steady state operation of HCCI leads to an increase of the radiated noise compared to SI at same load and speed. Because of a faster and earlier combustion, the character of the radiated noise is perceived as rough and impulsive. In addition, the application of the NVO-strategy led to tonal noise effects in the inlet system. Detailed parametric studies were carried out to describe the sensitivity of these noises on control parameters in order to support best settings in terms of acoustics.

- Supporting the HCCI combustion with spark, the combustion can be phased. No significant impact on the combustion excitation spectra was observed. This parameter can be used when switching between both combustion operation modes. However, the controller used for the mode switches during the present research was not able to support such a strategy.

- The variation of the start of injection, different split rates between main- and pre-injection and timings in HCCI have shown that a very early injection timing and increased fuel-rate at pre-injection will lead to a rough and clattering sound of the engine. Sensitivity maps to describe the noise trade-off while considering the noise-related thermodynamic characteristics as such as peak pressure, pressure gradient and B1090 versus injection-settings were developed.

- Using fuels of different RON and volatility revealed that the combustion characteristics in HCCI are obviously associated with the volatility of the fuel. The higher the volatility, the faster and shorter is the combustion. This affects rather the Impulsiveness than the level of the radiated noise.

In addition, a correlation of the Roughness R and Impulsiveness IMP with combustion data and -statistics was carried out. It was revealed that the 'Roughness' is proportional to the individual standard deviation of the height and location of the cylinder peak pressures and pressure rise rates. The higher the standard deviation SD of the combustion of the individual cylinder i to each other, the higher the Roughness R, thus:

$$R \propto \left(max\left[p_{max}(\alpha)|_{SDi}\right] - min\left[p_{max}(\alpha)|_{SDi}\right]\right),$$

and

$$R \propto \left(\left[dp/d\alpha_{max}|_{SDi}\right] - \left[dp/d\alpha_{min}|_{SDi}\right]\right).$$

Furthermore, it was demonstrated that a high Impulsiveness is generated by an early combustion with a maximum peak pressure close to TDC. Moreover, an early center of gravity of the combustion (CA50), a short duration (B1090), and a high pressure rise rate is favourable to a high Impulsiveness. Thus it can be written:

$$IMP \propto f\left(p_{max}(\alpha), \frac{dp}{d\alpha}(\alpha), CA50^{-1}, B1090^{-1}\right).$$

The application of the different relationships can be viable for example when optimizing the combustion system and its controls, as is possible by using the Design of Experiments-method (DoE).

The mode switch evaluation methodology was used to evaluate the quality of different combustion mode switch strategies from SI to HCCI in terms of powertrain vibration. This new methodology is able to analyse height (JLS_{MAX}) and duration (JLS_{INT}) of the excitation. Based on this methodology, the acceleration and the jerk occurring during mode switch are associated with the cylinder peak pressure and torque fluctuations. In general, the following main issues in terms of noise and vibration can be associated with the switch:

- An increase of noise and vibration can be noticed especially for the first few HCCI cycles. This can be referred to an excessively advanced HCCI combustion because of hotter residuals from the last SI combustion.
- Using a low-lift cam for the last SI cycles before a mode switch, noises in the inlet system, which are caused by reflected waves, can be avoided. A similar effect can be achieved when closing the throttle slightly during steady state HCCI operation.

Investigations of mode switches under the consideration of repeatability using different settings were carried out.

- Spread analysis: the quality of the mode switch in terms of noise and vibration depends on the rise rate of the consecutive peak pressures during the switch from SI to HCCI. In addition, the constancy of the torque generated (IMEP) affects the quality. The experiments revealed that the worst mode switch had a peak-pressure rise rate that was twice as much as for the best case. Furthermore, the variability of IMEP was lower in this run.

- Throttle trigger: an early opening of the throttle during the last lean SI cycles effects higher vibrations. This is caused by a higher overshoot of vibrations caused by the first few HCCI cycles.

- Split rate: to reduce the early combustion characteristics of the first few HCCI cycles, an increase of fuel during the pre-ignition phase of the intermediate HCCI combustion during mode-transition was investigated. It was found out that the higher the amount of fuel in the pre-injection, the higher were the vibrations and jerk. Moreover, misfires were detected with such a setting, leading to values of JLS_{MAX} that are four times higher than provoked by a misfire-free switch.

Based on these findings, the quality in terms of noise and vibration of a combustion mode switch can be referred to the combustion characteristics as follows:

$$JLS_{MAX} \propto f\left[p_{max}, \Delta p_{max} = \left(p_{max,i+1} - p_{max,i}\right), \left(IMEP_{i+1} - IMEP_i\right)\right],$$

with the index i denoting an individual engine cycle, and $i+1$ the consecutive cycle of the following firing cylinder.

6.2 Outlook

The following items may be subject to further research and development.

Enhancement of the noise prediction method. This may include e.g. clutch-systems, transmissions and a detailed modelling of the powertrain mount characteristics. This would then allow an incorporation of the predicted excitations into vehicle noise prediction models.

Interaction of combustion and clattering noise. Further research into the interaction of piston-pin-connecting rod dynamics and combustion characteristics. Likewise, detailed investigations on the interaction of combustion-chamber cavity-modes, piston slap and structure excitation would be worthwhile. This may help to explain the half-order structure of the clatter-noise of compression ignition engines, that was observed even when the pressure-rise rates and peak-pressures were of a certain consistency.

Fuels and volatility. A further investigation using fuels with different volatility would contribute to a further understanding of the effects, observed during the experiments presented in Chapter 4.2.6 .

Hardware and Controls. A further development of the combustion mode switch strategy is desireable. However, the current investigations have shown that the hardware can be a limiting factor. Hence, the advance of the development may also include piezo-electric-injectors and full variable valve trains (EVA). This may improve the repeatability of the mode switches, and may avoid the fast burning HCCI cycles immediately after the combustion mode switch with the help of an improved cylinder individual combustion-control.

Bibliography

[1] N.N.: Press Release - UNFCCC Executive Secretary calls for speedy and decisive international action on climate change. Paris, 2 February 2007: `http://unfccc.int/files/press/news_room/press_releases_and_advisories/application/pdf/070202press_rel_paris_en.pdf`; (Last access: 18 March 2007).

[2] Intergovernamental Panel on Climate Change (*IPCC*): *'Report on Climate Change 2007 - The Physical Science Basis'.* Report for Policymakers. Paris, 5 February 2007: `http://ipcc-wg1.ucar.edu/wg1/docs/WG1AR4_SPM_Approved_05Feb.pdf`; (Last access: 06 April 2007)

[3] N.N.: Commission Recommendation of 5^{th} February 1999 on the reduction of CO_2 emissions from passenger cars. Official Journal of the European Communities 1999/125/EC; `http://www.acea.be/ACEA/24072000.html`.

[4] Turner, J.W.G.; Pearson, R.J.; Kenchington, S.A.: *'Concepts for improved fuel economy from gasoline engines'.* Int. J. Engine Res., Vol. 6, pp. 137-157. IMechE, London, 2005.

[5] Altvater, E.: *'Das Ende des Kapitalismus'.* Blätter für deutsche und internationale Politik, Vol. 2, 2006, pp. 171-182. Blätter Verlagsgesellschaft mbH, Bonn, Berlin, 2006.

[6] Schäfer, A.; Jacoby, H.D.: *'Vehicle technology under CO_2 constraint: a general equilibrium analysis'.* Energy Policy, Vol. 34, 2006, pp. 975-985. Amsterdam, Elsevier Science, 2006.

[7] Wirth, M. et al.: *'The Next Generation of Gasoline Direct Injection: Improved Fuel Economy and Optimized System Cost'.* 12^{th} Aachen Colloquium on Automotive- and Engine Design, 2003.

[8] Fuerhapter, A. et al.: *'The new AVL CSI Engine - HCCI Operation on a Multi Cylinder Gasoline Engine'.* 2004 SAE World Congress, Detroit, MI, 2004. SAE-Paper 2004-01-0551, Society of Automotive Engineers, Warrendale, U.S.A., 2004.

[9] Heywood, J.B.: *'Internal Combustion Engine Fundamentals'.* New York, McGraw-Hill, 1988.

[10] Fahy, F.: *'Foundations of Engineering Acoustics'.* London - Academic Press, 2001.

[11] Fahy, F.; Walker, J. (Edrs.): *'Fundamentals of Noise and Vibration'.* London, New York - Spon Press, 1998.

[12] Crighton, D.G.; Dowling, A.P.; Ffowcs Williams, J.E.; Heckl, M.; Leppington, F.G.: *'Modern Methods in Analytical Acoustics'.* Lecture Notes. London, Springer Verlag, 1992.

[13] Dowling, A.P.; Ffowcs, J.E.: *'Sound and Sources of Sound'.* Chichester, Ellis Horwood Publishers, 1982.

[14] Hickling, R.; Kamal, M.M.: *'Engine Noise - Excitation, Vibration and Radiation'.* New York, London - Plenum Press, 1982.

[15] DeJong, R.G.: *'Using Vibration Transmission Analyses in the Design of Quiet Engines'.* in [14], pp.123-146. New York, London - Plenum Press, 1982.

[16] Griffin, M.J.: *'Handbook of Human Vibration'.* London, Academic Press, 1990.

[17] Stoffels, H.; Collings, N.: *'Effect of gasoline homogeneous charge compression ignition on engine acoustics and vibration'.* Proc. IMechE, Part JER: Journal of Engine Research, Vol. 8, No. 1, pp. 51-62. IMechE, London, 2007.

[18] Maeda, O.; Meakawa, Y.; Nomura, K.: *'Development of an Engine Noise Meter'.*, SAE Paper 870965, Society of Automotive Engineers, Warrendale, U.S.A., 1987.

[19] Okamura, H.; Furubayashi, M.: *'Experiments on Cylinder Pressure Pulsation and Distribution in a Swirl-Chamber-Type Automotive Diesel Engine: Idling Knocking Noise Induced by Non-Uniformly Distributed Cylinder Pressure Pulsation'.* SAE Paper 831329. In: 'A Worldwide View of Diesel Combustion Emissions and Analysis', pp. 137 - 149; Publication P-130. Society of Automotive Engineers, Warrendale, U.S.A., 1983.

[20] Hughes, M.: *'Subjective Evaluation of Diesel Idle Noise Using Simulation Techniques'.* ISVR, University of Southampton. Consultation Report No. 816/94 for the Ford Motor Company, 1994.

[21] Champagne, A.J.; Shiau, N.-M.: *'Commercial Van Diesel Idle Sound Quality'.* SAE Paper 971980, Society of Automotive Engineers, Warrendale, U.S.A., 1997.

[22] Schmillen, K.: *'Geräuschanalyse und Rechentechniken im Motorenbau II'.* Technical University of Aachen, Lecture Notes, 1997.

[23] Baxa, D.E.: *'Noise Control in Internal Combustion Engines'.* New York, London - John Wiley and Sons, 1982.

[24] Hempel, W.; Pflaum, W.: *'Geräuschverteilung bei Dieselmotoren I+II'.* FVV Vorhaben Nr.34, Hefte 55-1 + 55-2. Forschungsvereinigung Verbrennungskraftmaschinen e.V., Frankfurt a.M., 1965.

[25] Wodiczka; Huber, E.W.: *'Verbrennungsgeräusch bei Dieselmotoren'.* FVV Vorhaben Nr.71, Heft 123. Forschungsvereinigung Verbrennungskraftmaschinen e.V., Frankfurt a.M., 1971.

[26] Essers, U.; Gutzmer, P.; Phillip, U.: *'Körperschallanregung in den Kurbelwellengrundlagern eines Verbrennungsmotors'.* Heft 369. Forschungsvereinigung Verbrennungskraftmaschinen e.V., Frankfurt a.M., 1985.

[27] Haake, B.; Hanses, G.; Rebbert, M.: *'Verbrennungsgeräusch Ottomotor I'.* FVV Vorhaben Nr.645, Heft 670. Forschungsvereinigung Verbrennungskraftmaschinen e.V., Frankfurt a.M., 1998.

[28] Heuer, S.; Ademes, N.; Wiehagen, N.; Salber, W.: *'Verbrennungsgeräusch Ottomotor II'.* FVV Vorhaben Nr.731, Heft 721. Forschungsvereinigung Verbrennungskraftmaschinen e.V., Frankfurt a.M., 2001.

[29] Schelenz, R.; Steffens, C. et al.: *'Motor-Getriebe-Akustik II'.* FVV Vorhaben Nr.747, Heft 739. Forschungsvereinigung Verbrennungskraftmaschinen e.V., Frankfurt a.M., 2002.

[30] Essers, U.; Werkmann, M.; Denker, D.: *'Rauher Motorlauf'.* FVV Vorhaben Nr.567, Heft 610. Forschungsvereinigung Verbrennungskraftmaschinen e.V., Frankfurt a.M., 1995.

[31] Heuer, S.: *'Verbrennungsgeräusch der direkteinspritzenden Hubkolbenmaschine'.* PhD Thesis. University of Technology, Aachen, Germany, 2001.

[32] Wolschendorf, J.: *'Zyklische Schwankungen im Verbrennungsgeräusch von Dieselmotoren und ihre Ursachen'.* PhD Thesis. University of Technology, Aachen, Germany, 1990.

[33] HEAD Acoustics: *Artemis, Release 7.0, User Manual.* Herzogenrath, Germany, 2005.

[34] Stoffels, H.: *'Combustion Noise Investigation on a Turbocharged Spray Guided Gasoline Direct Injection I4-Engine'.* SAE N&V Conference 2005, Traverse City, MI, 2005. SAE-Paper 2005-01-2527, Society of Automotive Engineers, Warrendale, U.S.A., 2005.

[35] Stoffels, H.: chapter 10 *'Geräuschemissionen'*, in v. Basshuysen, R. (Ed.): *'Ottomotor mit Direkteinspritzung'.* Wiesbaden, Vieweg Verlag, 2007.

[36] Stoffels, H., Schröer, M.: *'NVH Aspects of a Downsized Turbocharged Gasoline Powertrain with Direct Injection'.* SAE N&V Conference 2003, Traverse City, MI. Transactions of the SAE 2003. SAE-Paper 2003-01-1664, Society of Automotive Engineers, Warrendale, U.S.A., 2003.

[37] Stoffels, H.: *'Untersuchungen zur Verminderung von Torsionsschwingungen in PKW Antriebsträngen'.* VDI Berichte 1493. Düsseldorf, VDI Verlag, 2001.

[38] Knoll, G.; Keßler, K.; Träbing, C.: *'Kurbelgehäusedynamik'.* FVV Vorhaben Nr.692, Heft 716. Forschungsvereinigung Verbrennungskraftmaschinen e.V., Frankfurt a.M., 2001.

[39] Knoll, G.; Reiners, W.: *'Kolbenhydrodynamik I'.* FVV Vorhaben Nr.287, Heft 434. Forschungsvereinigung Verbrennungskraftmaschinen e.V., Frankfurt a.M., 1984.

[40] Lang, O.R.; Steinhilper, W.: *'Gleitlager'.* Konstruktionsbücher Band 31, 1.Auflage; Berlin, Göttingen, Heidelberg. Springer Verlag, 1978.

[41] Khonsari, M.M.; Booser, E.R.: *'Applied Tribology'.* New York, Weinheim, Brisbane, Singapore, Tokio. John Wiley and Sons, Inc., 2001.

[42] Knoll, G.; Pischinger, F.: *'Kolben-Zylinder-Dynamik I+II'.* FVV Vorhaben Nr.528, Heft 489. Forschungsvereinigung Verbrennungskraftmaschinen e.V., Frankfurt a.M., 1996.

[43] Künzel, R.: *'Die Kolbenbewegung in Motorquer- und Motorlängsrichtung. Teil 1: Einfluß fertigungsbedingter Bauteilunsymmetrien'.* Motortechnische Zeitschrift, MTZ. 56. Jahrgang, Nr.4, 1995. Stuttgart, Franckh-Kosmos Verlag, 1995.

[44] Fiedler, R.G.: *'Ermittlung der Pleuelquerbewegung in Verbrennungsmotoren'.* PhD Thesis, University of Stuttgart. Renningen, Expert-Verlag, 2001.

[45] Ryan, J., Wong, W.V., Lyon, R.H. et al.: *'Engine Experiments on the Effects of Design and Operational Parameters on Piston Secondary Motion and Piston Slap'.* SAE-Paper 940695, Society of Automotive Engineers, Warrendale, U.S.A., 1994.

[46] Knoll, G.D.; Peeken, H.J.: *'Hydrodynamic Lubrication of Piston Skirts'.* Journal of Lubrication Technology, Vol. 104, No. 4, pp. 504 - 508. ASME, October 1982.

[47] Woschni, G.; Wachtmeister, G.; Zeilinger, K.: *'dp/dt-Einfluß - Einfluß der Druckanstiegsgeschwindigkeit auf die Bauteilbelastung'.* FVV Vorhaben Nr.351, Forschungsvereinigung Verbrennungskraftmaschinen e.V., Frankfurt a.M., 1987.

[48] Aouichi, A.; Herrmann, M.: *'Diesel Engine Noise and Internal Excitation Mechanisms'.* International SAE Congress and Exposition, 1989, Detroit. SAE-Paper 890132, Society of Automotive Engineers, Warrendale, U.S.A., 1989.

[49] Stoffels, H.: *'On the Impact of the Pressure Rise Rate on Piston and Connecting Rod Dynamics in Internal Combustion Engines'.* Submitted to the Proceedings of the IMechE, Part K, Journal of Multi-body Dynamics, May 2007.

[50] Roy, P.K.; Ganesan, N.: *'Transient response of a cantilever beam subjected to an impulse load'.* pp. 873 - 890. Journal of Sound and Vibration, Vol. 183(5), 1995.

[51] Wang, D.; Keith, T.G.; Yang, Q.; Vaidyanathan, K.: *'Lubrication Analysis of a Connecting-Rod Bearing in a High-Speed Engine. Part I: Rod and Bearing Deformation'.* Tribology Transactions 47, pp. 280 - 289. STLE/ASME, 2004.

[52] Shenoy, P.S.; Fatemi, A.: *'Dynamic analysis of loads and stresses in connecting rods'.* pp. 615 - 624. Proc. IMechE Vol.220, Part C, J. Mechanical Engineering Science, 2006.

[53] Goudas, I.; Natsiavas, S.: *'Non-linear dynamics of engine mechanisms with a flexible connecting rod'.* Proc. Instn. Mech. Engrs., Vol. 218, Part K: Journal of Multi Body Dynamics, pp. 67 - 80. IMechE, 2004.

[54] Fung, R.-F.: *'Dynamic Responses of the Flexible Connecting Rod of a Slider-Crank Mechanism with Time-Dependent Boundary Effect'.* Computers and Structures, Vol.63, No. 1, pp. 79 - 90. Elsevier Sciences, 1997.

[55] Carlucci, A.P., Chiara, F.F.; Laforgia, D.: *'Analysis of the relation between injection parameter variation and block vibration of an internal combustion diesel engine'.* pp. 141 - 164. Journal of Sound and Vibration, Vol. 295, 2006.

[56] Kim, T.; Jung, I.; Bae, D-H.; Yeo, S-D.: *'NVH Optimization of the New 2.5L HSDI Diesel engine with Common Rail'.* SAE-Paper 2003-01-0056, Society of Automotive Engineers, Warrendale, U.S.A., 2003.

[57] Miura, Y.; Kojima, N.: *'Noise Generating Mechanism at Idling for a Four-cylinder In-line Diesel Engine'.* SAE-Paper 2003-01-1720, Society of Automotive Engineers, Warrendale, U.S.A., 2003.

[58] Pollack, M.; Govindswamy, K.; Hartwig, M.: *'Cold Start Engine Clatter Noise Evaluations'.* SAE-Paper 2005-01-2455, Society of Automotive Engineers, Warrendale, U.S.A., 2005.

[59] Alt, N.; Sonntag, H-D.; Heuer, S.; Thiele, R.: *'Diesel engine Cold Start Noise Improvement'.* SAE-Paper 2005-01-2490, Society of Automotive Engineers, Warrendale, U.S.A., 2005.

[60] Ishida, S. et al.: *'Development of Technique to Measure Stress on Connecting-Rod during Firing Operation'.* SAE-Paper 951797, Society of Automotive Engineers, Warrendale, U.S.A., 1997.

[61] Wang, D. et al.: *'Lubrication Analysis of a Connecting-Rod Bearing in a High-Speed Engine. Part 1: Rod and Bearing Deformation'.* Tribology Transactions 47, pp. 280-289. STLE/ASME Tribology Conference 2003. Society of Tribologists and Lubrication Engineers, 2004.

[62] Schäfer, F.; v. Basshuysen, R.: *'Reduced Emissions and Fuel Consumption in Automobile Engines'.* Springer Verlag, Wien, New York / SAE Society of Automotive Engineers, Inc. Warrendale, PA., USA, 1995.

[63] Suh, I-S.; Lyon, R.H.: *'An Investigation of Valve Train Noise for the Sound Quality of I.C. Engines'.* SAE-Paper 1999-01-1711, Society of Automotive Engineers, Warrendale, U.S.A., 1999.

[64] Phlips, P.; Schamel, A.; Meyer, J.: *'An Efficient Model for Valvetrain and Spring Dynamics'.* SAE-Paper 890619, Society of Automotive Engineers, Warrendale, U.S.A., 1989.

[65] Walgrave, S.C.; Ehlbeck, J.M.: *'Understanding Modal Analysis'.* SAE-Paper 780695, Society of Automotive Engineers, Warrendale, U.S.A., 1978.

[66] Bronstein, I.N.; Semendjajev, K.A.: *'Taschenbuch der Mathematik'.* page 325. 24. Edition, Leipzig, Teubner Verlag, 1989.

[67] Ewins, D.J.: *'Modal Testing: Theory and Practice'.* London, New York. Research Studies Press Ltd., 1988.

[68] Døssing, O.: *'Structural Testing Part 1 & 2'.* Brüel & Kjæer Primers. BR 0458-11 and BR 0507-11, Nærum, Denmark, 2001.

[69] Newland, D.E.: *'Mechanical Vibration Analysis and Computation'.* pp. 326 - 329. Unabridged re-publication of the 1989 edition by Dover, New York, 2006.

[70] Natke, H.G.: *'Einführung in Theorie und Praxis der Zeitreihen- und Modalanalyse'.* Serie 'Grundlagen und Fortschritte der Ingenieurwissenschaften'. Dritte Auflage. Vieweg-Verlag, Wiesbaden, 1992.

[71] Cremer, L.: *'Vorlesungen über Technische Akustik'.* Berlin, Heidelberg, New York. Springer Verlag, 1971.

[72] Müller, H.W.; Langer, W.; Richter, H.P.; Storm, R.:*'Praxisreport Maschinenakustik'.* Forschungshefte des Forschungskuratorium Maschinenbau, Heft 102. FKM, Frankfurt a.M., 1983.

[73] Trendelenburg, F.: *'Einführung in die Akustik'.* Berlin. Springer Verlag, 1939.

[74] von Békésy, G.: *'Experiments in Hearing'.* New York, McGraw-Hill, 1960.

[75] Zwicker, E.; Fastl, H.: *'Psychoacoustics'.* 2^{nd} updated edition. Berlin, Heidelberg, New York. Springer Verlag, 1999.

[76] Zwicker, E.: *'Direct Comparisons between the Sensations Produced by Frequency Modulation and Amplitude Modulation'.* J. Acoust. Soc. Am., Vol. 34, No. 8, Part 2, pp. 1425-1430, September 1962.

[77] Zwicker, E.; Terhardt, E.: *'Analytical expressions for critical-band rate and critical bandwidth as a function of frequency'.* J. Acoust. Soc. Am., Vol. 68, No. 5, pp. 1523-1525, November 1980.

[78] Houtgast, T.: *'Frequency selectivity in amplitude-modulation detection'.* J. Acoust. Soc. Am., Vol. 85, No. 4, pp. 1676-1680, April 1989.

[79] Terhardt, E.: *'Acoustic Roughness and Fluctuation Strengh'.* Acustica, Vol. 20, pp. 215-224 (in german), 1968.

[80] Vogel, A.: *'On the Relation Between Roughness and Degree of Modulation'.* Acustica, Vol. 32, pp. 300-306 (in german), 1975.

[81] Aures, W.: *'A Procedure for Calculating Auditory Roughness'.* Acustica, Vol. 58, pp. 268-281 (in german), 1985.

[82] Terhardt, E.: *'Akustische Kommunikation'.* Berlin, Heidelberg, New York. Springer Verlag, 1998.

[83] Eguíluz, V.M.; Ospeck, M.; Choe, Y.; Hudspeth, A.J.; Magnasco, M.O.: *'Essential Nonlinearities in Hearing'.* Physical Review Letters, Vol. 84, Number 22, pp. 5232-5235, 29. May 2000.

[84] Bodden, M. et al.: *'Diesel Sound Quality Engineering'.* Fortschritte der Akustik - DAGA 2006.

[85] Genuit, K.: *'The sound quality of vehicle interior noise: a challenge for the NVH-engineers'.* Int. Journal Vehicle Noise and Vibration, Vol. 1, Nos. 1/2, pp. 158-168, 2004.

[86] Ruffell, C.M.; Griffin, M.J.: *'Effects of 1-Hz and 2Hz transient vertical vibration on discomfort'.* J. Acoust. Soc. Am., Vol. 98, No. 4, pp. 2157-2164, October 1995.

[87] Onishi, S.; Jo, S.H.; Shoda, K. et al.: *'Active Thermo-Atmosphere Combustion (ATAC)'.* SAE-Paper 790840, Society of Automotive Engineers, Warrendale, U.S.A., 1979.

[88] Najt, P.M.; Foster, D.E.: *'Compression-Ignited Homogeneous Charge Combustion'.* SAE-Paper 830264, Society of Automotive Engineers, Warrendale, U.S.A., 1983.

[89] Thring, R.: *'Homogeneous-charge Compression Ignition (HCCI) Engines'.* SAE-Paper 892068, Society of Automotive Engineers, Warrendale, U.S.A., 1989.

[90] Lavy, J. et al.: *'Innovative Ultra-low NO_x Controlled Auto-Ignition Combustion Process for Gasoline Engines'.* SAE-Paper 2000-01-1026, Society of Automotive Engineers, Warrendale, U.S.A., 2000.

[91] Law, D. et al.: *'Controlled Combustion in an IC-engine with a fully variable valve train'.* SAE-Paper 2000-01-0251, Society of Automotive Engineers, Warrendale, U.S.A., 2000.

[92] Allen, J.; Law, D.: *'Variable Valve Actuated Controlled Auto-Ignition: Speed Load Maps and Strategic Regimes of Operation'.* SAE-Paper 2002-01-0422, Society of Automotive Engineers, Warrendale, U.S.A., 2002.

[93] Fraidl, G.K.; Piock, W.F.; Wirth, M.: *'Gasoline Direct Injection: Actual Trends and Future Strategies for Injection and Combustion Systems'.* SAE Paper 960465, Society of Automotive Engineers, Warrendale, U.S.A., 1996.

[94] Bücker, C.; Krebber-Hortmann, K; Mori, S.: *'Evaluation of different operation strategies for the Controlled Auto Ignition Combustion process'.* (in german). Transactions of the Conference 'Controlled Auto Ignition', HdT, Essen, 20 - 21 October 2005.

[95] Zhao, F. (Ed.): *'Homogeneous Charge Compression Ignition (HCCI) Engines'.* SAE Book PT-94. Society of Automotive Engineers, Warrendale, U.S.A., 2003.

[96] Zhao, F. (Ed.): *'Automotive Gasoline Direct-Injection Engines'.* SAE Book R-315. Society of Automotive Engineers, Warrendale, U.S.A., 2002.

[97] Koopmans, L.; Ström, H. et al.: *'Demonstrating a SI-HCCI-SI Mode Change on a Volvo 5-Cylinder Electronic Valve Control Engine'.* SAE-Paper 2003-01-0753, Society of Automotive Engineers, Warrendale, U.S.A., 2003.

[98] Koopmans, L.; Ogink, R.; Denbratt, I.: *'Direct Gasoline Injection in the Negative Valve Overlap of a Homogeneous Charge Compression Ignition Engine'.* SAE-Paper 2003-01-1854 / JSAE 20030195, Society of Automotive Engineers, Warrendale, U.S.A., 2003.

[99] Schäflein, J.: *'Beitrag zur Steuerung der Kompressionszündung in Ottomotoren'.* Fortschritt Berichte VDI, Reihe 12, Nr.611. Düsseldorf, VDI-Verlag, 2005.

[100] Ogink, R.: *'Computer Modeling of HCCI combustion'.* PhD Thesis, Chalmers University of Technology. Göteborg, Sweden, 2004.

[101] Schneider, M.; Schmillen, K.; Pischinger, F.: *'Regularities of Cylinder Pressure Oscillations and their Effects on the Combustion Process and Noise'.* Truck and Bus Meeting and Exposition, Dearborn, MI, 1987. SAE-Paper 872248, Society of Automotive Engineers, Warrendale, U.S.A., 1987.

[102] Greiner, M; Romann, P.; Steinbrenner, U.: *'Bosch Fuel Injectors - New Developments'.* SAE-Paper 870124, Society of Automotive Engineers, Warrendale, U.S.A., 1987.

[103] Warnatz, J.; Maas, U.; Dibble, R.W.: *'Verbrennung'.* Third edition. Berlin, Heidelberg, New York, Springer Verlag, 2001.

[104] Oppenheim, A.K.: *'Combustion in Piston Engines'.* Berlin, Heidelberg, New York. Springer Verlag, 2004.

[105] Kontarakis, G.; Collings, N.; Ma, T.: *'Demonstration of HCCI Using a Single Cylinder Four-Stroke SI Engine with Modified Valve Timing'.* International Fall Fuels and Lubrication Meeting and Exposition, Baltimore, Maryland, 2000. SAE-Paper 2000-01-2870, Society of Automotive Engineers, Warrendale, U.S.A., 2000.

[106] Rayleigh, J.W.S.: *'The Theory of Sound, Vol.1'.* Unabridged Second Edition, Dover Publications, New York, 1945.

[107] Taylor, C.F.: *'The Internal Combustion Engine in Theory and Practice, Vol.1'.* Revised Edition, The MIT Press, Cambridge, Massachusetts, U.S.A., 1985.

[108] Taylor, C.F.: *'The Internal Combustion Engine in Theory and Practice, Vol.2'.* Revised Edition, The MIT Press, Cambridge, Massachusetts, U.S.A., 1985.

[109] Ricardo, H.R.: *'Der schnellaufende Verbrennungsmotor'.* Dritte Auflage, Berlin, Göttingen, Heidelberg. Springer Verlag, 1954 (translation of the 4^{th} edition of 'The High-speed Internal-combustion Engine', Blackie and Son Ltd., 1953).

[110] Pye, D.R.: *'The Internal Combustion Engine, Vol.I: Principles'.* Second edition. Engineering Science Series, Oxford University Press. Oxford, 1937.

[111] Pye, D.R.: *'The Internal Combustion Engine, Vol.II: The Aero-Engine.'* Engineering Science Series, Oxford University Press. Oxford, 1943.

[112] Judge, A.W.: *'Aircraft Engines, Vol. I & II.'* Second Edition. London, Chapman & Hall, 1947.

[113] Löhner, K.; Müller, H.: *'Gemischbildung und Verbrennung im Ottomotor'.* Series 'Die Verbrennungskraftmaschine', Vol.6. Wien, New York, Springer Verlag, 1967.

[114] Schmidt, F.A.F.: *'Verbrennungskraftmaschinen'.* Berlin, Heidelberg, New-York, Springer Verlag, 1967. Also published as: *'The Internal Combustion Engine'.* London, Chapman and Hall, 1965.

[115] Schmidt, F.A.F.: *'Benzinmotoren mit Kraftstoffeinspritzung und Funkenzündung'.* Motortechnische Zeitschrift, MTZ. 11.Jahrgang, Nr. 6, 1950. Stuttgart, Franckh'sche Verlagshandlung, 1950.

[116] Scherenberg, H.: *'Rückblick über 25 Jahre Benzin-Einspritzung in Deutschland'.* Motortechnische Zeitschrift, MTZ. 16.Jahrgang, Nr. 9, 1955. Stuttgart, Franckh'sche Verlagshandlung, 1955.

[117] Pischinger, A., Cordier, O.: *'Gemischbildung und Verbrennung im Dieselmotor'.* Wien, Springer Verlag, 1939.

[118] v. Gersdorff, K.; Grasmann, K.; Schubert, H.: *'Flugmotoren und Strahltriebwerke'.* 3. Auflage, Bonn, Bernhard und Graefe Verlag, 1995.

[119] Rubbra, A.A.: *'Rolls-Royce Piston Aero Engines - a designer remembers'.* Historical Series No.16. Rolls-Royce Heritage Trust, Derby, England, 1990.

[120] Ludvigsen, K.: *'Classic Racing Engines'.* Haynes Publishing, Sparkford, U.K., 2001.

[121] Sass, F.: *'Kompressorlose Dieselmaschinen'.* 1.Auflage, Wien, Springer Verlag, 1929.

[122] Küntscher, V.: *'Kraftfahrzeugmotoren - Auslegung und Konstruktion'.* Dritte Auflage, Verlag Technik GmbH, Berlin, 1995.

[123] Hoag, K.L.: *'Vehicular Engine Design'.* Wien, New-York, Springer Verlag, 2005.

[124] Bensinger, W.-D.; Meier, A.: *'Kolben, Pleuel und Kurbelwelle bei schnellaufenden Verbrennungsmotoren'.* Konstruktionsbücher Band 6, 2.Auflage; Berlin, Göttingen, Heidelberg. Springer Verlag, 1961.

[125] Prescher, K.-H.: *'Messungen der Bewegung und Beanspruchung von Kolben in schnellaufenden Verbrennungskraftmaschinen'.* PhD Thesis, TU Berlin, 1971.

[126] Zima, S.: *'Motorkolben'.* Vieweg Verlag, Wiesbaden, 2005.

[127] Meier, A.: *'Zur Kinematik der Kolbengeräusche'.* Automobiltechnische Zeitschrift - ATZ, Nr. 6, 54. Jahrgang, pp.123-128. Franckh'sche Verlagshandlung, Stuttgart, 1952.

[128] Nakada, T.: *'Piston Slap Noise Analysis by using Numerical Piston Secondary Motion Simuation'.* JSAE-Paper 9833881. JSAE VOL. 52, No. 3, 1998.

[129] Becker, G.: *'Leichtmetallkolben'.* Verlag von M.Krayn, Berlin, 1929.

[130] Reipert, P.; Voigt, M.: *'Simulation of the Piston/Cylinder Behavior for Diesel Engines'.* SAE-Paper 2001-01-0563, Society of Automotive Engineers, Warrendale, U.S.A., 2001.

[131] Neugebauer, G.H.: *'Kräfte in den Triebwerken schnellaufender Kolbenkraftmaschinen'.* Konstruktionsbücher Band 2; Springer Verlag, Berlin, 1939.

[132] Schwaiger, K.: *'Entwerfen und Berechnen neuzeitlicher Nutzkraftwagen-Motoren mit besonderer Berücksichtigung der Fahrzeug-Diesel-Maschine'.* Automobiltechnische Bibliothek, Band XIV. Verlag von M. Krayn, Berlin, 1934.

[133] Lang, O.: *'Triebwerke schnellaufender Verbrennungsmotoren'.* Konstruktionsbücher Band 22; Berlin, Heidelberg, New York. Springer Verlag, 1966.

[134] Mahle, E. et al.: *'Mahle Kolbenkunde'.* Zweite Auflage; Stuttgart, Bad Cannstatt. Mahle Komm.-Ges., 1964.

[135] Austen, A.E.; Priede, T.: *'Origins of Diesel Noise'.* SAE National Diesel Engine Meeting, 1959, Chicago, Il. SAE-Paper 590127, Society of Automotive Engineers, Warrendale, U.S.A., 1959.

[136] Stout, J.: *'Concept Level Powertrain Radiated Noise Analysis'.* SAE N&V Conference 1999, Traverse City, MI. SAE-Paper 1999-01-1746, Society of Automotive Engineers, Warrendale, U.S.A., 1999.

[137] Brunt, M.F.J.; Emtage, A.L.:*'Evaluation of IMEP Routines and Analysis Errors'.* International SAE Congress and Exposition, 1996, Detroit. SAE-Paper 960609, Society of Automotive Engineers, Warrendale, U.S.A., 1996.

[138] Brunt, M.F.J.; Rai, H.; Emtage, A.L.: *'The Calculation of Heat Release Energy from Engine Cylinder Pressure Data'.* International SAE Congress and Exposition, 1998, Detroit. SAE-Paper 981052, Society of Automotive Engineers, Warrendale, U.S.A., 1998.

[139] Brunt, M.: *'Gasoline Engine Knock Analysis using Cylinder Pressure Data'.* International SAE Congress and Exposition, 1998, Detroit. SAE-Paper 980896, Society of Automotive Engineers, Warrendale, U.S.A., 1998.

[140] Priede, T.: *'In Search of Origins of Engine Noise - An Historical Review'.* International SAE Congress and Exposition, 1980, Detroit. SAE-Paper 800534, Society of Automotive Engineers, Warrendale, U.S.A., 1980.

[141] Lalor, N.; Grover, E.C.; Priede, T.: *'Engine Noise due to Mechanical Impacts at Pistons and Bearings'.* International SAE Congress and Exposition, 1980, Detroit. SAE-Paper 800402, Society of Automotive Engineers, Warrendale, U.S.A., 1980.

[142] Jang, S.; Cho, J.: *'Effects of Skirt Profiles on the Piston Secondary Movements by the Lubrication Behaviors'.* Int. J. of Automotive Technology, Vol. 5, No. 1, pp. 23 - 31 (2004).

[143] Mansouri, S.H.; Wang, V. W.: *'Effects of piston design parameters on piston secondary motion and skirt-liner friction'.* Proc. IMechE, Vol. 219, pp. 435 - 449, Part J: J. Engineering Tribology, 2005.

[144] Kuratle, R.: *'Motorenmeßtechnik'.* 1. Auflage, Würzburg. Vogel Verlag, 1995.

[145] Quiring, S.; Stoffels, H.: *'Schwingungs- und Einflußgrößenanalyse an Fahrzeugen mit Start-Stopp Funktionalität'.* HdT-Conference 'Systemanalyse in der Antriebstechnik III'. Haus der Technik Fachbuch Bd.44. Renningen, Expert-Verlag, 2005.

[146] D'Anna, T.; Govindswamy, K. et al.: *'Aspects of Shift Quality With Emphasis on Powertrain Integration and Vehicle Sensitivity'.* SAE N&V Conference 2005, Traverse City, MI, 2005. SAE-Paper 2005-01-2303, Society of Automotive Engineers, Warrendale, U.S.A., 2005.

[147] Brohmer, A.; Joerres, M.; Kemmerling, J.: *'Influence of Gasoline-DI-Technology on Engine NVH'.* 10^{th} Aachen Colloquium on Automotive- and Engine Design, 2001.

[148] Nehl, J.: *'Economic, clean and silent! Engine noise prediction as an integral part of combustion system development'.* FEV Spectrum, Vol.21, p.6, Aachen, 2002.

[149] N.N.: *'AVL Combustion Noise Meter'. http://www.avl.com*; AVL GmbH, Graz, 2005.

[150] Schwarz, C.; Schünemann, B.; Durst, B.; Fischer, J.; Witt, A.: *'Potentials of the Spray-Guided BMW DI Combustion System'.* SAE-Paper 2006-01-1265, Society of Automotive Engineers, Warrendale, U.S.A., 2006.

[151] Urlaub, A.: *'Verbrennungsmotoren'.* 2. Edition, pp. 261 - 262. Berlin, Heidelberg, New York. Springer Verlag, 1994.

[152] Stiesch, G.: *'Modeling Engine Spray and Combustion Processes'.* Series 'Heat and Mass Transfer'; Berlin, Heidelberg, New York. Springer Verlag, 2003.

[153] Baumgarten, C.: *'Mixture Formation in Internal Combustion Engines'.* Series 'Heat and Mass Transfer'; Berlin, Heidelberg, New York. Springer Verlag, 2006.

[154] Kalghatgi, G.T.; Head, R.A.: *'Combustion limits and efficiency in a homogeneous charge compression ignition engine'.* Int. J. Engine Res., Vol. 7, pp. 215 - 236. IMechE, 2006.

[155] Johnson, K.L.: *'Contact Mechanics'.* Ninth printing, Cambridge; Cambridge University Press, 2003.

[156] Kiencke, U., Nielsen, L.: *'Automotive Control Systems'.* Berlin, Heidelberg, New York. Springer Verlag, 2000.

[157] Guzzella, L., Onder, C.H.: *'Introduction to Modeling and Control of Internal Combustion Engine Systems'.* Berlin, Heidelberg, New York. Springer Verlag, 2004.

[158] Gipser, M: *'Systemdynamik und Simulation'.* Stuttgart, Leipzig. Teubner Verlag, 1999.

[159] Koopmans, L.: *'HCCI combustion by Retaining Residuals'.* PhD Thesis, Chalmers University of Technology. Göteborg, Sweden, 2005.

[160] Affenzeller, J., Gläser, H.: *'Lagerung und Schmierung von Verbrennungsmotoren'.* Serie 'Die Verbrennungskraftmaschine', neue Folge, Vol.8. Wien, New York, Springer Verlag, 1996.

[161] Floberg, L.: *'The two groove journal bearing considering cavitation'.* Trans. Chalmers University of Technology, Gothenburg, Sweden, No. 232; 1960.

[162] Gerges, S.N.Y.; de Luca, J.C.; Lalor, N.: *'The Influence of Cylinder Lubrication on Piston Slap'.* Journal of Sound and Vibration, No.257, pp. 527 - 557. Elsevier Science Ltd., Academic Press, 2002.

[163] Haddad, S.D.; Kek-Tjen, T.: *'An Analytical Study of Offset Piston and Crankshaft Designs and the Effect of Oil Film on Piston Slap Excitation in a Diesel Engine'.* Journal of Mechanical Machine Theory, Vol.30, No.2, pp. 271 - 284. Elsevier Science Ltd., Pergamon Press, 1995.

[164] Resch, T.; Klarin, B.: *'Analysis of Engine Dynamics Under Transient Run-Up Conditions'.* International SAE Congress and Exposition, Detroit, MI, 2004. SAE-Paper 2004-01-1454, Society of Automotive Engineers, Warrendale, U.S.A., 2004.

[165] Göhringer, V.; Philipp, U.; Bargende, M.: *'Verbrennungsgeräusch - Ermittlung und Optimierung'.* 10. Symposium Dieselmotorentechnik. TAE, Esslingen, 2006.

[166] Priebsch, H.H.; Affenzeller, J.; Kuipers, G.: *'Structure Borne Noise Prediction Techniques'.* International SAE Congress and Exposition, Detroit, MI, 1990. SAE-Paper 900019, Society of Automotive Engineers, Warrendale, U.S.A., 1990.

[167] Yawata, Y.; Crocker, M.J.: *'Identification of Internal Noise Sources in Diesel Engines'.* International Off-Highway Meeting and Exposition, Milwaukee, WI, 1983. SAE-Paper 831330, Society of Automotive Engineers, Warrendale, U.S.A., 1983.

[168] Maass, H., Klier, H.: *'Kräfte, Momente und deren Ausgleich in der Verbrennungskraftmaschine'.* Serie 'Die Verbrennungskraftmaschine', neue Folge, Vol.2. Wien, New York, Springer Verlag, 1981.

[169] Rassweiler, G.M.; Withrow, L.: *'Motion Pictures of Engine Flames Correlated with Pressure Cards'.* SAE Technical Paper Series. Originally presented January 14, 1938. Reprinted 1980 as SAE paper 800131. Society of Automotive Engineers, Warrendale, U.S.A., 1980.

[170] Curry, S.: *'The Relationship Between Flame Propagation and Pressure Development During Knocking Combustion'.* Automotive Engineering Congress and Exposition, Detroit, MI, 1963. SAE-Paper 630095, Society of Automotive Engineers, Warrendale, U.S.A., 1963.

[171] Eggerath, G. et al.: *'Switchable Valve Train Components Solutions for the Future'.* Motortechnische Zeitschrift - MTZ Worldwide, 07.2005. Wiesbaden, Vieweg Verlag, 2005.

Patents

1. *'Verfahren und Vorrichtung zur quantitativen Auswertung von Vibrationen in einem Kraftfahrzeug'. ('Procedure and device for the evaluation of vibrations in automotive vehicles'.)* Applicant: Harald Stoffels. Submitted by Ford Motor Company. German Patent Office, Munich, 13 September 2006. Reference number 10 2006 043 440.4.

2. *'Verfahren und Vorrichtung zur Reduzierung von Geräuschen und Schwingungen in einem Hybrid-SI-HCCI Verbrennungsmotor'. ('Procedure and device to reduce noise and vibrations of a hybrid SI-HCCI combustion engine'.)* Applicants: Harald Stoffels, Jens Wojahn, Dr Anthemios Petridis; Ford Motor Company. German Patent Office, Munich, 15 September 2006. Reference number 10 2006 042 868.4.

Appendix A

Engine Technical Data

The investigations were made on a spray-guided direct injection in-line four cylinder engine [7] with twin-independent camshaft timing on both inlet and exhaust-side. Both cam-drives were equipped with a hydraulic actuated cam-profile-switch (CPS) to effect the two different valve lifts [171]. The basic technical data of the engine are provided in Table A.1. The camshafts on both intake and exhaust side were

Table A.1: Research Engine Technical Data

Displacement $[cm^3]$:	1998.00
Nr. of Cylinders:	4
Bore $[mm]$:	87.5
Stroke $[mm]$:	83.1
λ [bore/stroke]:	0.2841
Compression Ratio:	12.1
Combustion System:	Spray Guided Gasoline DI
Valve-train:	DOHC, independent variable timing, two-stage lift

equipped with two different profiles to enable two different lifts of the valves. Both camshafts with the two different profiles are shown in Figure A.1. This Figure also contains on its right half a cross-section through the cylinder head to illustrate the switchable tappets that connect the valves to the specific actual activated cam-profile. In addition, the cam-drive was suited with hydraulic actuated timing phasers on both camshafts, as shown in Figure A.2.

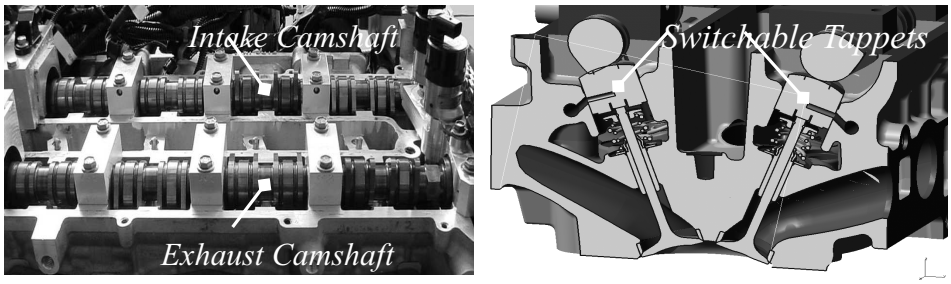

Figure A.1: Hardware necessary to release Cam-Profile switching

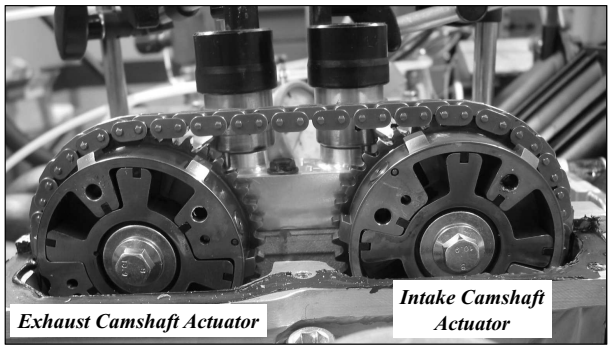

Figure A.2: Hydraulic actuated cam-phasers (cover removed)

A.1 Dynamometer Environment

Two similar engines were driven on either the dynamometer at the Cambridge University Engineering Department (CUED), Hopkinson Laboratory, or on a dynamometer at Ford Motor Company, Testing Department, Merkenich, Germany. On both test beds the in-cylinder pressure indication was carried out using Kistler transducers, adapted to an AVL-Indimaster. The analysis of the cylinder pressures, such as for example heat release and statistical data, was then processed based on the Ford Motor Company specifically owned 'LUCID'- program [137, 138, 139]. Further details of the heat-release calculation are presented in section A.2. All experiments were done with 90^oC coolant out temperature, using 95RON fuel type if not otherwise mentioned.

A.2 Combustion Data Analysis

The combustion data were gained from the LUCID program system. The heat release rate and the parameters that followed from it, for example B1090, CA50, were processed according to the Rassweiler and Withrow method [169], and as applied by Brunt et al. in [137]. Its application is also described for instance in [144]. To calculate the heat release dQ_H/dt the first law can be written:

$$\frac{dQ_H}{dt} = \frac{dU}{dt} + p \cdot \frac{dV}{dt}. \tag{A.2.1}$$

Alternatively one can write with the consideration of the heat losses dQ_W/dt the burn rate dQ_B/dt:

$$\frac{dQ_B}{dt} = \frac{dU}{dt} + p \cdot \frac{dV}{dt} + \frac{dQ_W}{dt}. \tag{A.2.2}$$

In equation (A.2.1) the fraction dU/dt denotes the energy of the gas, thus $dU/dt = c_v \cdot m \cdot dT/dt$. The variable dT/dt denotes the temperature gradient, $p \cdot dV/dt$ the work at the piston, m the mass of the cylinder charge, and c_v the specific heat at a constant volume. However, choosing a high sample rate corresponding for example to $1deg$ crank angle, both equations can be solved numerically with a sufficient accuracy [144]. Hence the incremental pressure rise Δp due to combustion between the crank angle locations i and j with the according cylinder volumes V_i and V_j can be approximated by:

$$\Delta p = \left[p_j - p_i \cdot \left(\frac{V_i}{V_j} \right)^n \right]. \tag{A.2.3}$$

The actual cylinder volume can be calculated as a function of crank angle α, considering a potential offset of either piston and pin, or crankshaft:

$$V(\alpha) = \frac{D^2\pi}{4} \cdot \left[r \cdot (1 - \cos\alpha) + l \cdot \left(1 - \sqrt{1 - \left(\lambda \cdot \sin\alpha - \frac{\Delta - q}{l} \right)^2} \right) \right] + V_c. \tag{A.2.4}$$

In equation (A.2.4) r is the radius of the crank, l the acting length of the connecting rod, λ the ratio of r/l, D is the diameter of the piston, Δ denotes the piston to pin offset corresponding to Figure 3.4, q the crankshaft offset, and V_c denotes the compression volume that obeys the following equation:

$$V_c = \frac{V_H}{\epsilon - 1}, \tag{A.2.5}$$

with V_H denoting the displacement, and ϵ denoting the compression ratio. However, a discussion of equation (A.2.4) with regard to the position of the crank, and with

$\Delta = q = 0$ means that it is $V = V_c$ for $\alpha = 0 \wedge 180 deg$. If for example p_i is known, e.g. the ambient pressure during opened inlet valve, the pressure rise can be calculated. Hereby the related cylinder volume V_i is based on the crank geometry and crank angle position. In addition, the polytropic index n is defined as follows:

$$n = 1 + \frac{R}{c_v}. \tag{A.2.6}$$

In equation (A.2.6) R denotes the gas constant, defined as $R = 287 J/kg \cdot K$. Because c_v depends strongly on the temperature and hence influences n significantly, it can be approximated as a function of temperature T by an empiric formula [144]:

$$c_v = 0.7 + T \cdot 10^{-3} \cdot (0.155 + A). \tag{A.2.7}$$

The variable A has the value of $A = 0.1$ for the Otto-cycle [144]. Once the pressure rise Δp is known, the corresponding incremental rise of the temperature ΔT can be calculated assuming ideal gas relationships, too:

$$\Delta T = \frac{\Delta p \cdot V_j}{m \cdot R}. \tag{A.2.8}$$

Applying the first law to a constant volume process one can write

$$\Delta Q_H = m \cdot \Delta U = m \cdot c_v \cdot \Delta T. \tag{A.2.9}$$

The combination of equations (A.2.3), (A.2.6) and (A.2.9) yields the approximate rate of heat release ΔQ_H:

$$\Delta Q_H = \frac{c_V}{R} \cdot V_j \cdot \left[p_j - p_i \cdot \left(\frac{V_i}{V_j} \right)^n \right]. \tag{A.2.10}$$

Implying the calculation of the cumulative combustion pressure rise terms using equation (A.2.3), the mass fraction burned (MFB) as a function of the crank-angle α can be calculated:

$$MFB(\alpha) = \frac{\Delta p \cdot V(\alpha) - (\Delta p \cdot V)|_I}{(\Delta p \cdot V)|_f - (\Delta p \cdot V)|_I}. \tag{A.2.11}$$

The index I denotes the value at ignition, and f the final value at the estimated end of combustion (EEOC). Thus, the value of MFB before ignition is set to 0%, while it is set to 100% at EEOC. The EEOC is calculated while writing the product of $p \cdot V_i^m$ with m denoting an index set to a value slightly less than the lowest polytropic expansion index expected. Values of $m = 1.2$ are recommended. The product of

$p \cdot V_i^m$ is then calculated for each degree crank angle, starting from approximately TDC to exhaust valve opening (EVO). Applying an averaging algorithm over 11 consecutive values, this process is continued until $20 deg CA$ after EVO. The EEOC is then set to the corresponding crank angle at which the maximum value occurred. Note that the evaluation of the statistical combustion data was done according to the appendix of [138].

A.3 Coefficients for SAE-Oil Types

Table A.2: Coefficients a, b and c for different SAE-oil specifications in accordance with Vogel's equation (3.1.67)

SAE-classification	$a \cdot 10^8$	b	c
10W and 10W/10	0.0850	820.723	93.625
10W/20	0.1034	773.810	93.153
10W/30	0.2020	737.690	89.900
10W/40	0.1165	1033.340	120.800
10W/50	0.0952	1304.170	155.220
20W and 20W/20	0.1350	737.810	77.700
20W/30	0.1441	811.962	93.458
20W/40	0.1671	793.329	83.931
20W/50	0.0948	1146.250	124.700
30	0.1531	720.015	71.123

Appendix B

Acoustic Data Acquisition and Analysis

For the NVH measurements either a BEQII - 2 channel measurement device by HEAD Acoustics or the HEAD SQ-LabIII front-end was used. This device allows a maximum sample rate of 48kHz both for airborne and structure-borne noise measurements.
For the structure-borne measurements a sample rate of 24kHz was chosen. The sensors were both so-called ICP-sensors, which can be employed without an external charge amplifier. Alternatively conventional accelerometers were glued on the engine structure, type Brüel & Kjær 4393. For the airborne measurement at the intake orifice an ICP-microphone was used. The position of the microphone was perpendicular to the orifice with a distance of $0.1m$ from the orifice. The sample rate was set to 48kHz linked to a binaural filter, which is part of the BEQII-device. The data gained from SQ-LabIII and BEQII were evaluated using the HEAD-Artemis software, version 7.0. The further processing of the recorded cylinder pressure data was done using the programs as derived in Chapter 3 of this thesis. Both analysis routines are programmed in MatLab, Vers.7.0.1. Other data analyses were carried out using IMC-Famos. The wavelet analysis of the combustion excitation was carried out using the HEAD-Artemis software, version 7.0.

B.1 Modal Analysis

The modal analysis was carried out using accelerometers of the type Brüel & Kjær 4374. A Kistler impact-hammer, type 9724A2000 was used with an aluminium shoe. The data were recorded with a HEIM front end. The post-processing of the data was done using LMS CADA-X. The frequency response curves depicted in Chapter 3.1.4 of the investigated structures were taken from the individual resulting universal files ($*.unv$, Universal file 55).

B.2 Pressure Indication

The cylinder pressures at both the Cambridge University dynamometer and the Ford-Merkenich dynamometer were measured with transducers of the type Kistler 6123. These transducers were fitted onto each of the four cylinders of both engines. At Cambridge the cylinder pressure data were fed into an AVL-Indimaster 671. The post-processing of the data was carried out using AVL Concerto. At Ford-Merkenich, the cylinder pressure data were fed into a FEV-CAS system. The post-processing was done using the Ford Motor Company specifically developed 'LUCID' system. Here as well, two Kistler absolute pressure transducers of the type 4073A were fitted onto the intake duct to measure the pressure pulsation before and after the throttle, both connected to a Kistler 4643 amplifier. All data signals were fed into the dSpace device for further analysis and were also available on the break-out box for the further pick-up by either the HEAD SQ-LabIII or the HEAD BEQII front end.